

CEST MRI for the characterisation of human brain tumours

by

Fotios Savvopoulos

Supervisors: Professor Dorothee Auer, Professor Richard Grundy

Internal Assessor: Professor Alan Perkins

Thesis submitted to The University of Nottingham for the degree of Doctor of Philosophy

September 2017

Contents

Contents **2**

Nomenclature 9

Abstract **14**

Acknowledgements **18**

List of Tables **20**

List of Figures **21**

0.1 Disclaimer on figures used throughout the thesis 36

1 MRI principles **37**

1.1 Introduction 38

1.2 Nucleus inside a magnetic field 39

1.2.1 Origins of magnetism 39

1.2.2 Magnetic properties of hydrogen 41

1.2.2.1 Spin 41

1.2.2.2 Magnetic moment 43

1.2.2.3 Magnetic susceptibility 46

1.2.3 Energy states and Zeeman splitting 47

1.2.4 Net magnetisation 49

1.2.5 Precession and resonance 52

1.2.6 Chemical shift . . . 55
1.2.7 J-coupling . . . 56
1.3 Bloch equations . . . 57
1.3.1 Solutions for static $\vec{B}$ excluding relaxation . . . 59
1.3.2 Solutions for static $\vec{B}$ including relaxation . . . 60
1.3.2.1 Longitudinal relaxation . . . 60
1.3.2.2 Transverse relaxation . . . 61
1.3.3 Rotating frame of reference . . . 63
1.3.3.1 Bloch equations in the rotating frame . . . 65
1.3.3.2 On resonant radio-frequency irradiation in the rotating frame . . . 66
1.3.3.3 Off resonant radio-frequency irradiation in the rotating frame . . . 67
1.4 The MR signal . . . 68
1.4.1 Echo formation . . . 68
1.4.1.1 Spin echo . . . 68
1.4.1.2 Gradient echo . . . 70
1.4.1.3 Hahn echo and stimulated echo . . . 70
1.5 Spatial localisation . . . 72
1.5.1 Slice selection (G_z) . . . 73
1.5.2 Frequency encoding (G_x) . . . 74
1.5.3 Phase encoding (G_y) . . . 75
1.6 Shimming . . . 76
1.6.1 Passive shimming . . . 77
1.6.2 Active shimming . . . 78
1.6.3 Dynamic shimming . . . 80
1.6.4 Multi-coil shimming . . . 83

2 CEST: mechanism, optimisation and clinical applications 85

2.1 Mechanism . . . 85

2.1.1 CEST mechanism and underlying processes . . . 85

2.1.1.1 Direct contributions to the MR signal . . . 85

2.1.1.2 Indirect contributions to the MR signal . . . 87

2.1.1.3 Magnetisation transfer pathways . . . 88

2.1.1.4 Contrast generation in MT and CEST . . . 90

2.1.1.5 The basic saturation transfer experiment . . . 91

2.1.1.6 Conditions for detecting chemical exchange. . . . 95

2.1.1.7 Saturation transfer in tissue . . . 97

2.2 CEST: optimisation techniques . . . 99

2.2.1 Bloch equations . . . 99

2.2.1.1 Two pool model (water - solute with one exchange proton group) . . . 99

2.2.1.2 Three pool model (water - solute with two exchange proton groups) . . . 100

2.2.1.3 Three pool model (water - solute in the presence of MT) . . . 101

2.2.1.4 Multi-pool systems . . . 102

2.2.1.5 Numerical solutions . . . 103

2.2.1.6 Pulsed CEST . . . 108

2.2.2 Quantifying CEST effects . . . 110

2.2.2.1 Proton Transfer Ratio (PTR) . . . 110

2.2.2.2 Labelling efficiency . . . 110

2.2.2.3 Simplified PTR and asymmetry . . . 112

2.2.2.4 Isolating CEST from MT and spillover effects . . . 113

2.2.2.5 Calculating the proton exchange rate, k_{sw} . . . 114

2.2.3 CEST effect dependence on experimental variables . . . 115

2.2.3.1 Water relaxation times . . . 116
2.2.3.2 Magnetic field strength . . . 116
2.2.3.3 B_1 power . . . 117
2.2.3.4 Pulsed CEST . . . 117
2.2.4 Sequences for CEST imaging . . . 119
2.3 Endogenous CEST . . . 121
2.3.1 Amines (NH_2) . . . 122
2.3.1.1 Glutamate . . . 122
2.3.1.2 Creatine . . . 124
2.3.2 Hydroxyl (-OH) . . . 125
2.3.2.1 Glycogen . . . 125
2.3.2.2 GAGs . . . 126
2.3.2.3 Myo-inositol . . . 128
2.3.2.4 Glucose . . . 129
2.3.2.5 Lactate . . . 134
2.3.3 Amides (NH) . . . 138
2.3.3.1 Absolute pH mapping . . . 138
2.3.3.2 Cerebrovascular stroke . . . 141
2.3.3.3 Brain Tumours . . . 141

3 CEST: In-silico optimisation 153
3.1 Introduction . . . 153
3.2 Materials and Methods . . . 155
3.3 Results . . . 159
3.4 Discussion . . . 170
3.5 Conclusion . . . 175

4 pH mapping using exogenous CEST contrast agents: in vitro feasibility assessment 176

4.1 Introduction . . . 177
4.2 Materials and Methods . . . 180
4.3 Results . . . 182
4.3.1 Visipaque . . . 182
4.3.2 Niopam . . . 186
4.3.3 Ultravist . . . 190
4.4 Discussion . . . 194
4.5 Conclusion . . . 199

5 Pulsed CEST at 3T. Comparison between single slice and 3D acquisitions. 200

5.1 Introduction . . . 201
5.2 Materials and methods . . . 202
5.2.1 Sequences . . . 202
5.2.2 Phantoms . . . 206
5.2.3 Scanning . . . 206
5.2.4 Data analysis . . . 207
5.3 Results . . . 208
5.3.1 Distilled water . . . 208
5.3.2 Ultravist . . . 209
5.3.3 Creatine . . . 215
5.3.4 Creatine plus glutamate . . . 218
5.4 Discussion . . . 225
5.5 Conclusion . . . 229

6 Glioma characterisation with CEST MRI at 7T 230

6.1 Introduction . . . 231
6.2 Materials and Methods . . . 233
6.2.1 Recruitment process . . . 233

6.2.2 Patient demographics . . . 234
6.2.2.1 Histological notes . . . 236
6.2.3 7T scanning protocol . . . 237
6.2.4 Data analysis . . . 238
6.2.4.1 3T clinical data and ADC maps . . . 238
6.2.4.2 Registrations . . . 239
6.2.4.3 ROI definitions . . . 241
6.2.5 Quantitative APT and NOE maps . . . 242
6.3 Results . . . 244
6.3.1 APT and NOE maps in tumours and controls . . . 244
6.3.1.1 Quality of fitting . . . 244
6.3.1.2 APT and NOE colour-maps for all patients . . . 245
6.3.1.3 Statistical analysis of all ROIs . . . 248
6.3.2 APT and NOE signal correlation with ADC . . . 250
6.3.2.1 APT - ADC correlations in low grades . . . 251
6.3.2.2 APT - ADC correlations in high grades . . . 251
6.3.2.3 NOE - ADC correlations in low grades . . . 252
6.3.2.4 NOE - ADC correlations in high grades . . . 253
6.3.2.5 Summary of correlations . . . 254
6.4 Discussion . . . 256
6.5 Conclusion . . . 259

7 Discussion **260**

Appendix A Matrix exponential solution to Bloch equations **269**

Appendix B Simulation parameters **270**

Appendix C Patient recruitment documents **272**

Appendix D Lorentzian pool fitting parameters **277**

Bibliography **278**

Nomenclature

1.5T: 1.5 Tesla

2DG: 2-deoxy-D- glucose

3T: 3 Tesla

7T: 7 Tesla

AACID: Amine and Amide Concentration Independent Detection

ADC: Apparent Diffusion Coefficient

APEX: Amine Proton Exchange

APT: Amide Proton Transfer

AREX: Apparent Exchange-dependent Relaxation

ATP: Adenosine-5-triphosphate

BOLD: Blood Oxygen Level Dependent

BW: Bandwidth

CBF: Cerebral blood flow

CBV: Cerebral blood volume

CEST: Chemical Exchange Saturation Transfer

CHESS: Chemical Shift Selective Saturation

Cr: Creatine

CrCEST: Creatine Chemical Exchange Saturation Transfer

CT: Computed Tomography

CW-CEST: Continuous wave CEST

DC Direct current

DICOM: Digital Imaging and Communications in Medicine

dnsAREX: Downfield Nuclear Overhauser Effect Suppresed Aparent Relaxation

DTI: Diffusion Tensor Imaging

EMF: Electromotive force

EPI: Echo Planar Imaging

eV: Electron Volt

FA: Fractional anisotropy

FDG-PET: Fludeoxyglucose Positron Emission Tomography

FISP: Fast Imaging with Steady State Precession

FLAIR: Fluid-attenuated Inversion Recovery

FLIRT: Linear Image Registration

fMRI: Functional Magnetic Resonance Imaging

FOV: Field of View

FWHM: Full Width at Half Maximum

GAG: Glycosaminoglycan

gagCEST: Glycosaminoglycan Chemical Exchange Saturation Transfer

GBM: Glioblastoma

Gd: Gadolinium

GE: General Electric

GluCEST: Glutamate Chemical Exchange Saturation Transfer

glucoCESL: Glucose Chemical Exchange Spin Lock

glucoCEST: Glucose Chemical Exchange Saturation Transfer

GM: Grey Matter

GRASE: Gradient and Spin Echo

GRE: Gradient Recalled Echo

Hz: Hertz

IVD: Intervertebral disc

LATEST: Lactate Chemical Exchange Saturation Transfer

LBM: Label Transfer Module

LDH: Lactate Dehydrogenase

LGG: Low Grade Glioma

MC: Multi-coil

MICEST: Myo-inositol Chemical Exchange Saturation Transfer

mIns: Myo-inositol

MPRAGE: Magnetization Prepared Rapid Gradient Echo

MRI: Magnetic Resonance Imaging

MRS: Magnetic Resonance Spectroscopy

MT: Magnetisation Transfer

MTR(REX): Spillover-corrected Magnetisation Transfer Ratio

MTRasym: Magnetisation Transfer Ratio Asymmetry

MTT: Mean transit time

NAA: N-acetylaspartate acid

NMR: Nuclear Magnetic Resonance

NOE: Nuclear Overhauser Effect

PCr: Phosphocreatine

PET: Positron Emission Tomography

ppm: Parts per Million

PSR: Pool Size Ratio

PTR: Proton Transfer Ratio

R1p: Longitudinal Relaxation Rate in the Rotating Frame

R2ρ: Transverse Relaxation Rate in the Rotating Frame

RARE: Rapid Acquisition with Relaxation Enhancement

RF: Radio Frequency

ROI: Region of Interest

SAR: Specific Absorption Rate

SDP: Standard Deviation of Precision

SH: Spherical Harmonic

sigma: Standard deviation

SL: Spin Lock

SNR: Signal to noise ratio

SWI: Susceptibility Weighted Imaging

T1: Longitudinal Relaxation Time

T2: Transverse Relaxation Time

TE: Echo Time

TFE: Turbo Field Echo

TMS: Tetramethylsilane

TMZ: Temozolomide

TR: Repetition Time

TSE: Turbo Spin Echo

VAPOR: Variable Pulse Power and Optimised Relaxation Delays

WEX: Water Exchange Spectroscopy

WM: White Matter

Abstract

Chemical Exchange Saturation Transfer (CEST) is a novel MRI technique that amplifies the detection of otherwise undetectable compounds. Under certain physico-chemical and experimental conditions, CEST allows the detection of compounds containing amide, amine and hydroxyl proton groups, that are in chemical exchange with free water molecules. The main focus of this work is to gain an understanding of the underlying principles of CEST, both in-vitro and in-vivo.

After introducing essential MRI principles in chapter 1, chapter 2 contains a review of the CEST theory, optimisation techniques and applications of CEST, mainly in characterising brain tumours.

Chapter 3 studies the impact of experimental parameters in generating and quantifying the APT signal, in-silico. The parameters investigated were: the B_1 irradiation power, the APT pool size, the saturation length and finally the SNR. For each of those parameters, the relationship between the parameter and APT signal was derived and its implications in optimising CEST experiments were discussed. For the model under investigation, it was found that the optimal parameters were: B_1 = 1μT, APT pool size of 0.01 and saturation time of 3 seconds, at most. Furthermore, it is shown that the presence of noise diminishes the ability to quantify the APT effect accurately and that this loss varies linearly with SNR. In conclusion, the model studied here should be imaged with an SNR of ~70 so that the percentage error and relative accuracy in the measurements is ~10% and 0.8, respectively.

Chapter 4 contains a feasibility comparison of measuring extracellular pH with

CEST, by using three clinically approved iodinated contrast agents, at 7T, in-vitro. The contrast agents tested were: Iodixanol (brand name - Visipaque, GE Healthcare), Iopamidol (brand name - Niopam, Bracco UK Ltd) and Iopromide (brand name - Ultravist, Bayer Healthcare). Phantoms of the agents, in phosphate buffer and at different pH levels were prepared and subsequently scanned using a 2D gradient echo CEST sequence. The CEST effect was calculated by asymmetry analysis and pH maps were derived on a pixel by pixel basis. In addition, calibration curves were determined by fitting the in-vitro CEST signal of all three agents, against pH. Under the experimental conditions used, Niopam and Ultravist showed two, while Visipaque showed one, CEST exchange peaks. Consequently, Visipaque was found unsuitable in determining pH, by ratiometric CEST analysis. On the contrary, Niopam and Ultravist showed great potential in determining extracellular pH, as the ratiometric analysis produced linear calibration curves, for both agents. Moreover, Ultravist showed superior linearity to Niopam (R^2 = 0.99, R^2 = 0.88). Next steps could involve, measuring the CEST effects, of both Niopam and Ultravist, in-vivo. First, on a pre-clinical model and second, in humans. The latter will be at 3T, instead of 7T. Patients could be immediately scanned after routine CT procedures, where either of these contrast agents is used. Before assessing the pH, calibration curves, of both agents, will be derived at 3T, in-vitro, with experiments similar to those reported at 7T.

Chapter 5 contains the comparison between a modified single slice and volumetric CEST gradient echo sequences, in generating CEST contrast, in a series of phantoms, at 3T. The single slice sequence was successfully modified by myself, whereas the volumetric sequence was prepared by a team from Institute of Psychiatry, Psychology and Neuroscience in King's College, London. Besides allowing for different spatial excitation, the two sequences also differ in the pre-saturation pulse type. The latter is a Fermi pulse, in the 2D sequence and a Gaussian pulse, in the 3D sequence. A common limitation of both sequences is the maximum allowed pulse duration, which is in the order of milli-seconds. However, CEST effects were successfully measured in phantoms of the

iodinated contrast agent, Ultravist, creatine and glutamate, under physiological conditions (pH =7). Asymmetry analysis was used to quantify the CEST effect, in all cases. Despite post-processing corrections for B_0 inhomogeneities, some datasets were noisy. This is perhaps due to small sample size and inefficient shimming. The Gaussian pulse of the 3D sequence was found to produce a 2-fold increased CEST effect in Ultravist and a 7-fold CEST effect increase in creatine, as compared to the Fermi pulse of the 2D sequence. Furthermore, increasing the duty-cycle of the 2D sequence did not result in greater CEST effect magnitude. Analysis of the main field homogeneity, after linear and high order shimming, showed that the latter results in frequency shifts within ± 0.5 ppm, whereas the shifts, after linear shimming, extended beyond that range. As the CEST effect is highly sensitive on frequency shifts, a high order shimming is more beneficial, especially when characterising CEST effects in-vivo. Future work could include studying the pH dependence of Ultravist and Niopam, in-vitro. Even if only one CEST peak, instead of the two found at 7T, can be measured at 3T, calibration curves can still be derived by implementing an RF power based ratiometric method. Subsequent translation, of measuring pH, in patients that have received iodinated contrast injection, will require further ethical approval. Besides measuring pH, typical CEST acquisitions could be optimised in more complex phantoms, in-vitro. For example, the CEST effects of three-pool model phantoms (agar gel + creatine or ammonium chloride) could be tested, using the 3D gradient echo CEST sequence. Existing analysis tools could be updated to allow for Lorentzian fitting separation of co-existing CEST effects. New tools, allowing fitting of Bloch equations to CEST data, should also be developed. In addition, besides B_0 inhomogeneity corrections, the impact of RF inhomogeneity effects, on CEST signals, should be studied. The latter correction might be crucial in detecting weaker CEST effects at 3T. It would also be interesting to measure the relaxation compensated CEST effect at 3T. That would be possible if our sequences allow for a pre-saturation time in the order of seconds ($t_{sat} >> T_{1w}$). Ultimately, the efficacy of the 3D CEST sequence could be tested in healthy volunteers and finally in brain

tumour patients, after acquisition of appropriate ethical approval.

Chapter 6 contains the details of a CEST study, of cerebral gliomas at 7T, where the APT and NOE signals, between low and high grade brain tumours and normal white matter, are compared. In addition, the correlation between, APT and NOE signals with apparent diffusion coefficient (ADC), is also investigated. More specifically, a 3D CEST MRI scan, targeting amide and aliphatic protons, was acquired, at 7T, in seven untreated glioma patients, who had previously undergone routine clinical 3T MRI. APT and NOE maps were produced by Lorentzian fitting of the CEST data. Significantly higher tumour APT signal was found in both low grades and glioblastomas, as compared to healthy white matter. In addition, the APT signal, was 3 to 4-fold elevated in glioblastoma versus low grades. On the contrary, significantly lower tumour NOE was found in both low grades and glioblastomas, as compared normal tissue, with the latter being ~7-fold decreased in GBMs. Further, investigation of the correlation of the APT and NOE, tumour and control signals, with ADC, did not show any particular trend, with the exception of the NOE - ADC signals in controls, which showed a weak, negative correlation. Further analysis of our data could include asymmetry analysis, as a comparison to Lorentzian fitting, in cerebral gliomas. Also, quantification of the conventional magnetisation transfer (MT), along with APT and NOE effects, in oedema, necrotic and haemorrhagic regions, that often accompany gliomas.

Chapter 7 contains an overall discussion of the work on this thesis, how it relates to the literature and presents some ideas on what should be done next.

Acknowledgements

I would like express my deep gratitude to my main supervisor, Professor Dorothee Auer, for her invaluable, scientific and otherwise, guidance, continuous support, patience, motivation and understanding. I'm also grateful to my secondary supervisor, Professor Richard Grundy and Cancer Research UK, for giving me the opportunity to study in Nottingham. Dr Henryk Faas for his scientific input, support and advice and Professor Alan Perkins for his guidance, in times of need. Dr Olivier Mougin for his advice on experimental and analysis methods. My colleagues, at the department of Radiological and Imaging Sciences, for helpful discussions and overall support with trivial and non-trivial issues. Finally, the University of Nottingham's student support services, for proving me with a helping hand and assistance, regarding personal issues.

My former flatmate, Joey, for being a true friend and the best drummer I've played with. Our music will live forever.

Last but not least, I would like to thank my parents, for their unconditional love. We will meet again, some sunny day.

‘‘Body, against mind

I forgot, what is mine’’

List of Tables

1.1 Composition of nuclei that can or can't be used in MRI experiments. . . 43

1.2 γ values of commonly used nuclei. Notice that the electron γ value is 3 orders of magnitude larger than the γ of the other nuclei [7]. 45

1.3 Examples of diamagnetic, paramagnetic and ferromagnetic materials [149]. 46

2.1 The source of the MRI signal. 86

2.2 The 6 basic relaxation mechanisms affecting the T_1 and T_2 times of the measured MR signal 89

3.1 Simulation parameters of the 2-pool model. 156

3.2 2-pool model parameter variation for fitting the noisy Z-spectra. k_{APT} and f_{APT} denote the exchange rate and pool size of the APT pool respectively. 157

4.1 Spectroscopic and imaging methods of measuring pH. 178

6.1 Inclusion and exclusion criteria for recruiting brain glioma patients . . 234

6.2 Pathology of the patients scanned at 7T. 234

6.2 Pathology of the patients scanned at 7T. 235

List of Figures

1.1 Spinning tops and magnets 37

1.2 The magnetic field lines of a positive charge moving 'through' the page. A moving electron will produce similar but counter-clockwise field lines. 40

1.3 The magnetic field lines of a nucleus are equivalent that of a magnetic dipole. In other words, a nucleus behaves like a tiny magnet. 40

1.4 Classic, single electron orbit, view of the hydrogen atom (left). Quantum microscope image of the atom's wave function (right). Image taken from Stodolna et al [181]. 41

1.5 Angular momentum of a rotating object. 42

1.6 A simple analogy between a spinning top and a spinning nucleus. . . . 43

1.7 The magnetic moment $\vec{\mu}$ of a rotating charge q. 44

1.8 How the magnetic susceptibility of a material affects the intensity of the local magnetic field. The blue arrows indicate the orientation of the internal magnetic field. 47

1.9 Classic, simplified, view of the spin-up and spin-down proton states (left). The 2 states have the same energy when $B_0 = 0$. Zeeman splitting occurs when $B_0 \neq 0$. The anti-parallel or spin-down state has higher energy than the spin-up state (right). 49

1.10 In the absence of a magnetic field the random orientation of the spins averages out the net magnetisation (left). Within a strong magnetic field however, a small excess of spins orients parallel to B_0. The ensemble of such spins is described through the magnetisation vector $\vec{M}$, that is also collinear to B_0 (right). The spins are not static, but move in a circular path as explained in the next paragraph. 50
1.11 Precession of a spinning nucleus.. 52
1.12 Precession of a magnetic moment $\vec{\mu}$ around B_0. 53
1.13 The application of a rotating B_1 at ω_0 causes $\vec{M}$ to drop at the xy plane. Motion as viewed from the lab (left) and rotating (right) frame. 54
1.14 Brain proton spectrum measured at 7T. The resonant peaks of major brain metabolites are also shown [74]. 56
1.15 Through bond coupling of 2 nuclei. The 4 possible configurations lead to a double resonant peak. Note that the electron spins in the bond must follow Pauli's exclusion principle. 57
1.16 Longitudinal and transverse relaxation after a 90° RF pulse. T_1 = 1.3 sec, T_2 = 0.8 sec for white matter at 3T [220]. The plots were generated in Matlab using custom written code. 62
1.17 Rotating (blue) and laboratory (black) frame. 63
1.18 Quadrature RF transmit coil. 64
1.19 The RF pulse is a rotating magnetic vector, on a plane perpendicular to B_0. 65
1.20 Flipping of the magnetisation by an on resonant RF pulse. 66
1.21 The effective field around which the magnetisation precesses when the RF pulse is applied off-resonance. 67
1.22 Rephrasing of the spins during the application of a 90^0- 180^0 pair of pulses. 69
1.23 RF pulses for a spin echo. 69

1.24 Gradient echo sequence. The echo is formed by reversing the polarity of the frequency encoding gradient. The slice selection and phase encoding gradients have been omitted for clarity. 70
1.25 Formation of a Hahn echo. 71
1.26 Slice selection gradient orientation. 72
1.27 Selecting slices having different thickness. 73
1.28 A simple nine pixel slice. 74
1.29 Effect of G_x gradient on spin precession. 75
1.30 Using the G_y gradient, allows for individual identification of all the spins. 75
1.31 The superposition of the inherent and shim fields improves magnetic field homogeneity. Image taken from [38]. 77
1.32 First and second order shim examples. Images taken from [224]. 80
1.33 Human in-vivo 2nd order Global Shimming versus 2nd order Dynamic Shimming field homogeneity measures: field standard deviation, central 80% pixel value range and fraction of non-zero field value pixels greater than 50 Hz. The data was acquired at 7T, with the shim ROI box being propagated to all slices. Image taken from [163]. 82
1.34 Comparison between global spherical harmonic shimming and multi-coil shimming across six slices in the human brain at 7T. Image taken from [95]. 83

2.1 The spectral lines of pool A (free protons) and pool B (bound protons) . 90

2.2 Contrast enhancement in MT and CEST experiments. Under normal conditions (left) the magnetisation exchange does not affect the contrast. After selective saturation (flip) of the macromolecular magnetisation (middle) and subsequent transfer of the inverted spins to free water (right) the measured signal drops. This signal difference between the macromolecular containing tissue and an another one that does not contain the macromolecule increases the contrast between the tissues. *Image taken from* [21] 91
2.3 Basic saturation transfer experiment. The protons of interest are saturated with a continuous hard pulse before a typical acquisition scheme, including excitation, slice selection and encoding, is implemented. . . . 92
2.4 Acquisition of a full Z-spectrum is achieved by the application of a saturating RF pulse at multiple resonant frequencies. Image taken from [242] 93
2.5 Z-spectrum showing the amide resonance peak at +3.5 ppm from the water peak (0 ppm). Image taken from [208]. 94
2.6 WEX spectra for perfused RIF-1 cancer cells for different mixing times (time allowed for the magnetisation to diffuse before the imaging sequence is applied). The inset image is just the aliphatic region, enlarged. Similar spectra have been obtained for a rat brain study as well. Image taken from [209]. 95
2.7 The three cases of the two proton exchanging pools. Only the first one is of interest for CEST experiments. An additional condition is that the exchange rate should be greater than the relaxation rate in order for any magnetisation to be transferred. Image taken from [144]. 96

2.8 Potential pathways of magnetisation transfer/chemical exchange in a typical off-resonance irradiation experiment. **Left:** chemical exchange (red) and dipolar relaxation, NOE (blue), in mobile proteins **Right:** Both intermolecular and intramolecular NOE along with chemical exchange contribute to the magnetisation pathways in semi-solid proteins. The latter pathways make up of what is known as magnetisation transfer (MT). Image taken from [208]. 97

2.9 Z-spectra obtained in corpus callosum (CC), cortex and cerebrospinal fluid. The two exchange peaks at the positive offsets correspond to chemical exchange, while the peak at the negative offsets to NOE. The effect of MT isd indicated as an overall down-shift of the spectrum for the CC and the cortex. Image taken from [84]. 98

2.10 Two, three and four-pool systems that can be described by the numerical solution of the Bloch equations as proposed by [97]. $k_{ij}$is the proton exchange rate between the pools. Arrows also denote the direction of the exchange. Image taken from [97]. 103

2.11 Simulation of a two pool system containing bulk water and amides. The system is more efficiently saturated at low RF power. The parameters of the simulation are listed in Appendix B. 104

2.12 Simulation of a two pool system containing bulk water and amides. The CEST effect increases with increasing exchange rate. The parameters of the simulation are listed in Appendix B. 105

2.13 Simulation of a two pool system containing bulk water and amides. The CEST effect increases with increasing amide concentration. The parameters of the simulation are listed in Appendix B 105

2.14 Simulation of a three pool system containing bulk water and two additional proton exchanging pools. RF spillover effects prevent the detection of the +4.2 ppm for RF power more than 2μT. The parameters of the simulation are listed in Appendix B. 106
2.15 Simulation of a three pool system containing bulk water and two additional proton exchanging pools. As the exchange rate is increased the peak at +5.5 ppm violates the slow exchange condition. Thus its CEST effect vanishes. The parameters of the simulation are listed in Appendix B. 107
2.16 Simulation of a three pool model including bulk water, amides and a semi-solid component. The effect of the MT is evident as an overall downward shift of the Z-spectrum. This shift is more pronounced at hight RF pulse powers.The parameters of the simulation are listed in Appendix B 108
2.17 Pulsed CEST simulation for a two-pool system (bulk water, amides). The optimal flip angle for the maximum CEST effect is between 180 and 360 degrees.The parameters of the simulation are listed in Appendix B. 109
2.18 **Left:** Labelling efficiency dependence on irradiation power and magnetic field for amides and amines. **Right:** Labelling efficiency dependence on chemical shift and irradiation power amides. Images taken from [242]. 111
2.19 **Left:** The dependence of spectral line-width Γ, for amides and amines, on B_1 pulse power. **Right:** Relationship between labelling efficient and spectral line-width. Increasing the labelling efficiency is detrimental for selectivity. Images taken from [242]. 111
2.20 CEST contrast dependence on magnetic field strength. The effect is more pronounced at higher fields. Image taken from[99]. 116

2.21 Exchange rate normalised B_1 power as a function of chemical shift and magnetic field strength. Image taken from [99]. 117
2.22 Dependence of the $B_{avg\ power}$ and $B_{avg\ field}$ on the RF flip angle and duty cycle. $B_{avg\ power}$ (left), remains relatively constant with varying flip angle and duty cycle. Image taken from [275]. 118
2.23 Pulsed CEST contrast dependence on $B_{avg\ power}$ and flip angle. The maximum contrast is generated at a 180° flip angle. Image taken from [275]. 119
2.24 Amide (-NH), amine (NH_2) and hydroxyl (-OH) proton group properties. Table taken from [106]. 121
2.25 GluCEST maps of a rat brain tumour model acquired pre-injection and at 1, 1.5 and 2.0 h following the injection of the glutamate solution. A gradual increase of GluCEST was found within 2 hours of injection. Image taken from [10]. 122
2.26 **A.** CEST contrast of Cr, PCr and ATP. **B.** CrCEST contrast linear dependence on concentration. Image taken from [62]. 124
2.27 CrCEST in human calf muscles at 7T. During exercise, CrCEST signal rapidly increases, before returning to its baseline ~14 minutes after the onset of the exercise. Image taken from [140]. 125
2.28 Glycogen depletion over time is reflected as decreased glycoCEST signal in perfused mouse liver at 4.7T. Image taken from [212]. 126
2.29 gagCEST signal decrease, in the medial side of the patellofemoral human knee joint, indicating loss of GAG, at 3T. Image taken from [122]. 127
2.30 **Left to right:** B_0 and B_1 corrected gagCEST maps at 3T, 7T and the corresponding asymmetry plot. Image taken from [174]. 127
2.31 Higher grade of intervertebral discs degeneration results in decreased gagCEST contrast. Image taken from [109]. 128

2.32 MICEST map of white and gray matter. White matter shows elevated MICEST signal, indicating a higher concentration of myo-inositol. Image taken from [61]. 128
2.33 **Left:** MICEST signal in wild type mouse. **Right:** Elevated MICEST signal in the Alzheimer's disease mouse model, indicating glial cell proliferation. Image taken from [63]. 129
2.34 **Left to right:** Anatomical image showing the location of the tumours, pre D-glucose infusion CEST, post D-glucose infusion CEST and post infusion FDG-PET. Image taken from [12]. 130
2.35 Uptake of 2DG in healthy rat brain. The first image serves as a baseline. Image taken from [147]. 131
2.36 T_{2w}, Gd-T_{1w} and glucoCEST images of patient with anaplastic astrocytoma acquired at 7T. The subscripts in the glucoCEST images denote time in seconds. Image taken from [236]. 133
2.37 Comparison of the difference between pre and post glucose injection CEST signal in tumour and normal tissue. Image taken from [219]. . . 133
2.38 Glucose Contrast Enhanced MRI, Anatomical MRI and FDG-PET images of a tumour patient. Image taken from [219]. 134
2.39 **Top row:** Lactate asymmetry spectrum and concentration dependence. **Bottom row:** Lactate asymmetry spectrum and pH dependence. Image taken from [24]. 135
2.40 **Left:** Anatomical, pre and post pyruvate LATEST images. **Middle:** pre and post infusion LATEST asymmetry curves **Right:** pre and post infusion LATEST contrast comparison. Image taken from [24]. 136
2.41 LATEST images of human calf muscle 3 minutes post exercise. The signal falls back to the baseline in about 18 minutes after exercise cessation. Image taken from [24]. 136

2.42 Z-spectra of various EuDO3A complexes measured at 9.4T, in-vitro. **Black line**:50 mM EuDO3A+50 mM lactate, **Red line**:50 mM EuDO3A+ 50 mM (NaH2PO4+ Citric acid+ NaHCO3+Lactate) **Blue line**: 50 mM EuDO3A+50 mM Citric acid. **Green line**: 50 mM EuDO3A in 4% HSA. **Purple line**: 50 mM EuDO3A +50 mM lactate in cell culture medium. Image taken from [253]. 137

2.43 CEST image of a mouse bladder showing the presence of the intact lactate·EuDO3A complex at 45 min post injection. Image taken from [253]. 138

2.44 **Left:** pH weighted MTR_{asym} map. **Right:** absolute pH map of ischaemic rat model at 4.7T. Image taken from [198]. 139

2.45 Endogenous ratiometric absolute pH maps (AACID), in rat brain at 9.4T, 2 and 5 hours after middle cerebral artery occlusion. Image taken from [138]. 140

2.46 Various MR images for a patient with meningioma. For the APT image the mean and the standard error of the APT values were -0.1 ± 0.04 (tumour), -3.3 ± 0.2 (CNAWM), -2.8 ± 0.04 (INAWM), and -2.0 ± 0.08 (oedema). Image taken from [88]. 142

2.47 Multimodal MRI of a low grade glioma. In the APT image, the tumour is indistinguishable from healthy tissue. Image take from [266]. 143

2.48 Comparison between radiation necrosis and glioma in two brain tumour rat models. Necrosis is hypo-intense on APT images. Image taken from [267]. 144

2.49 Grade III astrocytoma at 3T. **Left:** non enhancing Gd-T_1 image **Right:** APT image, showing high signal intensity in tumour (red arrow) and low signal intensity in oedema (orange arrow). Image taken from [259]. 144

2.50 Conventional MRI and APT CEST images from a 49-year-old man with tumour progression. The patient had a new contrast-enhancing lesion, 1 month after completion of chemoradiation. Image taken from [132]. . 145

2.51 Conventional MRI and APT CEST images from a 65-year-old man with pseudo-progression. Indications of new lesion can be seen on conventional MRI images. On the other hand, the lesion appears iso-intense to contralateral healthy brain, on the APT image. Image taken from [132]. 145

2.52 APT CEST, of a rat tumour model at 4.7T. **Top:** Z-spectra and asymmetry curves for $B_1 = 0.6\mu T$. **Bottom:** Z-spectra and asymmetry curves for $B_1 = 2.1\mu T$. Image taken from [269]. 148

2.53 Left frontal glioblastoma of a 59 year old patient at 3 Tesla. **A:** Gd-T_1 **B:** T_2 weighted and **C:** NOE-mediated CEST images. As NOE effects drop in tumours, MTR_{asym} is increased. Image taken from [153]. . . . 149

2.54 Correlations of MTR_{asym}, AREX(APT) and AREX(NOE), with water relation rates R_1 and R_2, pool size ratio (PSR) and chemical exchange rate (k_{mf}). Red squares represent the mean values of each tumour, and the blue circles are the mean values of each region of interest (ROI) of contralateral normal tissue. The Spearman's rank correlation coefficient (r) and p value of each correlation, along with the linear regression line, are also shown. Image taken from [235]. 150

2.55 Various MRI images of a glioblastoma patient, acquired at 7T. **A:** Gd-T_1 **B:** MTR_{asym} **C:** Amide Lorentzian difference **D:** NOE Lorentzian difference **E:** AREX-APT **F:** AREX-NOE. Image taken from [247]. . . . 151

2.56 Gd-T_1, T_2-FLAIR, AREX and AREX (dnsAREX) images of a glioblastoma patient at 7T. Even though the tumour enhancing ring is identified on the AREX image, the signal size is also similar to the contralateral region. On the contrary, the contrast on the dnsAREX image shows a significantly higher intensity in the enhancement region compared with contralateral white matter. Image taken from [249]. 152

3.1 Dependence of the APT CEST signal on B_1 power. 159

3.2 Relationship between the measured APT signal and B_1 power. 160

3.3 Dependence of the APT CEST signal on APT pool size. 161

3.4 Linear relationship between the measured APT signal and APT pool size. 161

3.5 Dependence of the APT CEST signal on saturation time. 162

3.6 Relationship between the measured APT signal and saturation time. The CEST effect plateaus at 3s and beyond. 163

3.7 Noise-free spectrum. The benchmark for analysing the effects of SNR on the APT peak. 164

3.8 Fitting the benchmark Z-spectrum with the 2-pool model equations while SNR = 100. The noise-free and fitted spectra match one another. 165

3.9 Fitting the benchmark Z-spectrum with the 2-pool model equations for an intermediate SNR = 50. Evidently, the fitted APT peak differs from the ideal one. 165

3.10 Fitting the benchmark Z-spectrum with the 2-pool model equations for SNR = 10. The fitted APT peak can no longer be quantified. 166

3.11 Fitted APT magnitude at +3.5ppm for each one of the SNR values tested in this study. To the aid visual interpretation of the result, a magnified version of the circled area is also shown. 167

3.12 The relationship between the CEST effect and SNR for the 2-pool model studied here is linear. 167
3.13 Relationship between percentage error and SNR. 168
3.14 Relationship between relative accuracy and SNR. 169

4.1 Glucose metabolism in mammalian cells [255]. 177
4.2 Chemical formulas of Visipaque (A), Niopam (B) and Ultravist (C). . . . 180
4.3 Z-spectrum and asymmetry curves for Visipaque. 182
4.4 Visipaque CEST peak pH dependence. The bars indicate standard deviation.. 184
4.5 Pixel by pixel asymmetry maps for Visipaque. The images were cropped using an elliptical mask during post-processing. 185
4.6 Z-spectrum and asymmetry curves for Niopam. 186
4.7 Pixel by pixel asymmetry maps for the 4.2 ppm peak of Niopam. The images were cropped using an elliptical mask during post-processing. . 187
4.8 Pixel by pixel asymmetry maps for the 5.4 ppm peak of Niopam. The images were cropped using an elliptical mask during post-processing. . 187
4.9 Signal ratio of the 4.2 ppm over the 5.4 ppm peak against pH for Niopam. The bars indicate the standard deviation. 188
4.10 95% prediction bounds in the calibration curve for Niopam. 189
4.11 Z-spectrum and asymmetry curves for Ultravist. 190
4.12 Pixel by pixel asymmetry maps for the 4.2 ppm peak of Ultravist. The images were cropped using an elliptical mask during post-processing. . 191
4.13 Pixel by pixel asymmetry maps for the 5.6 ppm peak of Ultravist. The images were cropped using an elliptical mask during post-processing. . 191
4.14 Signal log ratio of the 4.2 ppm over the 5.6 ppm peak against pH for Ultravist. The bars indicate the standard deviation. 192
4.15 95% prediction bounds in the calibration curve for Ultravist. 193

5.1 The 2D gradient echo (left) and the 3D spoiled gradient echo (right) sequences that were modified for CEST imaging. 202
5.2 Time domain graphs of the Fermi (left) and Gauss (right) RF pulses used for CEST imaging. 203
5.3 Fermi pulse addition to the 2D gradient echo sequence. The pulse is generated on the 'rho' sequencer of the scanner (**left**). Code example of incorporating the Fermi pulse in the pulse sequence (**right**). 204
5.4 Gauss pulse addition to the 3D gradient echo sequence. The pulse is generated on the 'rho' sequencer of the scanner. 205
5.5 Single slice water Z-spectrum for three RF bandwidths. 208
5.6 Water Z-spectrum of the middle slice using the 3D sequence. 209
5.7 Z-spectrum and asymmetry curves for Ultravist for three RF pulse durations. 210
5.8 Single slice Z-spectrum for Ultravist using three and four 20 ms pre-pulses. 211
5.9 Single slice asymmetry curves for Ultravist, using three and four 20 ms pre-pulses. 212
5.10 Z-spectrum and asymmetry curves of the second slice, for Ultravist. . 213
5.11 Z-spectra and asymmetry curves for Ultravist acquired using the single and multislice sequences. 214
5.12 Single slice Z-spectra and asymmetry curves for 50mM of creatine and three different pulse widths. 215
5.13 Z-spectra and asymmetry curves of the second slice for the 50mM creatine phantom. Data have been acquired at two B_1 powers and durations. 216
5.14 Z-spectra and asymmetry curves, for creatine, acquired using the single and multislice sequences. 217

5.15 Hardcoded saturation scheme for the 2D CEST sequence (**left**). Externally read saturation scheme for the 3D CEST sequence. In this example the scheme for creatine is shown (**right**) 218
5.16 Internal B0 shift maps after high order shimming for four datasets. . . 219
5.17 Internal B0 shift maps after linear shimming for four datasets. 220
5.18 Z-spectrum and asymmetry curves, for every slice of dataset 4, after high order shimming. 221
5.19 Z-spectrum and asymmetry curves, for every slice of dataset 4, after linear shimming. 222
5.20 Z-spectrum and asymmetry curves, for every slice of dataset 2, after high order shimming. 223
5.21 Z-spectrum and asymmetry curves, for every slice of dataset 2, after linear shimming. 224

6.1 Clinical patient scans at 3T. **Top row:** (left to right): T_2-FLAIR image of LGG, T_2- FLAIR image of LGG, Gd-T_1 image of GBM, Gd-T_1 image of an early GBM. **Bottom row:** (left to right): Gd-T_1 image of GBM, Gd-T_1 image of GBM, T_2-FLAIR image of LGG. 236
6.2 Schematic diagram of the CEST sequence (pulsed per-saturation module + TFE readout) [145]. 238
6.3 ADC maps of a low grade left insular glioma (left) and a right temporal GBM (right). 238
6.4 Registering 3T - 7T images flowchart. 239
6.5 Example of assessing the registrations: In this case: 7T MPRAGE to Gd-T_1 3T. Image #1 is the base Gd-$T_1$and the subsequent images sequentially reveal the registered MPRAGE on the base image. 240
6.6 Haemorrhagic tumour components on 7T SWI images. **Top row:** Original images. **Bottom row:** ROIs of haemorrhagic components. 242

6.7 Z-spectra in white, grey matter, tumour and control for the ROIs shown on the images. 244
6.8 Z-spectra in white and grey matter for the ROIs shown on the images. 245
6.9 APT and NOE maps for #1 (LGG) and #2 (LGG). 246
6.10 APT and NOE maps for #3 (LGG) and #4 (GBM). 246
6.11 APT and NOE maps for #5 (GBM) and #6 (GBM). 247
6.12 APT and NOE maps for #7 (LGG). 247
6.13 Mean APT values and standard deviation of controls, low grade gliomas (LGG) and GBMs. The mean difference and 95% confidence interval is also provided. The non-parametric Wilcoxon test indicated that both mean differences of low grade gliomas and GBMs and controls, were significantly different ($p<0.01$). 249
6.14 Mean NOE values and standard deviation of controls, low grade gliomas (LGG) and GBMs. The mean difference and 95% confidence interval is also provided. The non-parametric Wilcoxon test indicated that both mean differences of low grade gliomas and GBMs and controls, were significantly different ($p<0.01$). 250
6.15 Joint scatter-plots of APT - ADC between tumour and healthy control regions in low grade gliomas. Red indicates tumour and blue indicates controls. 251
6.16 Joint scatter-plots of APT - ADC between tumour and healthy control regions in high grade gliomas. Red indicates tumour and blue indicates controls. 252
6.17 Joint scatter-plots of NOE - ADC between tumour and healthy control regions in low grade gliomas. Red indicates tumour and blue indicates controls. 253

6.18 Joint scatter-plots of NOE - ADC between tumour and healthy control regions in high grade gliomas. Red indicates tumour and blue indicates controls. 253
6.19 Summary of the APT - ADC and NOE - ADC correlations in tumours and controls for all glioma cases. 255

0.1 Disclaimer on figures used throughout the thesis

Unless otherwise stated, all figures have been created using Inkscape 0.91 (GNU General Public Licence) or Matlab (The MathWorks Inc., Natick, MA, 2000).

Chapter 1

MRI principles

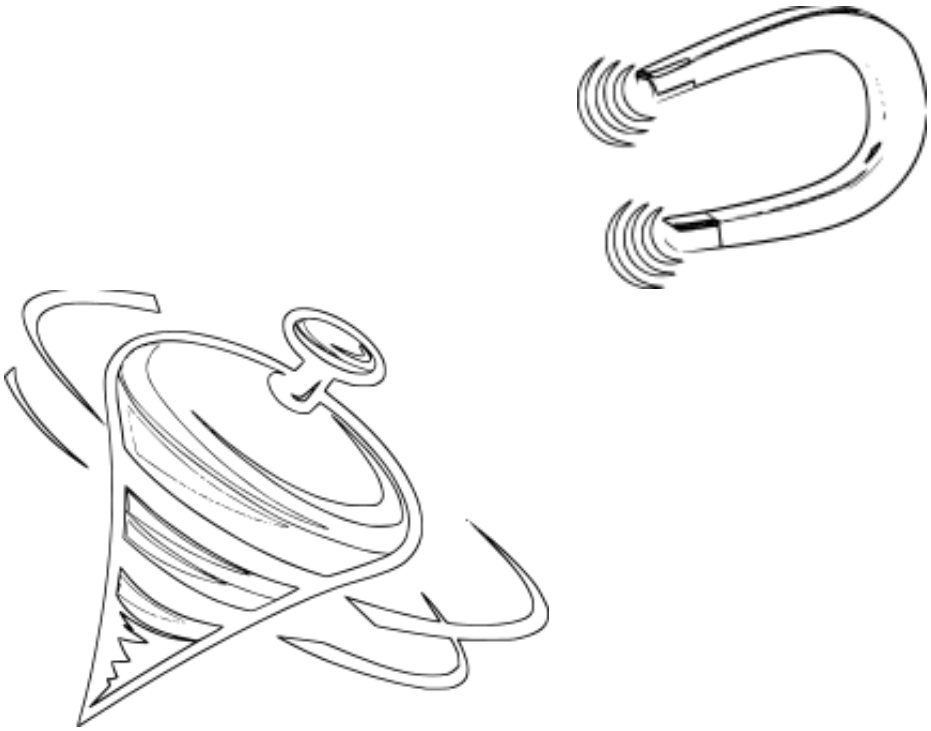


Figure 1.1: Spinning tops and magnets

1.1 Introduction

Magnetic resonance imaging (MRI) is a medical imaging modality capable of producing tomographic images (slices) that are highly sensitive to the micromagnetic properties of the tissues present on the location of interest. Similarly to computed tomography (CT) the production of MRI images depends on the interaction between electromagnetic radiation and matter. However, MRI is devoid of the risks using ionising radiation as the modality is based on detecting electromagnetic signals within the non-ionising radiofrequency part (~MHz) of the electromagnetic spectrum.

The contrast in MRI is highly dependent on not only the tissue composition, as is the case with the X and γ-ray based imaging modalities, but also on the tissue relaxation properties. This renders the modality capable of reporting on additional physicochemical tissue properties, but also complicates its interpretation. Furthermore, even though MRI is concerned with energies that are a billion electron-volt (eV) less than the ones used in X or γ-ray based modalities, its spatial resolution is comparable to the latter (~1 mm or less for higher magnetic fields). The reason behind this remarkable fact is the amount of protons, to which the MR signal depends on, that reside within an imaging voxel. A simple calculation assuming a $2 \times 2 \times 5$ mm = 0.02 ml and a field of 1.5T gives 6.02×10^{15} protons or 6 million billion sources of signal!

The basic principle of MRI is closely related to that of Nuclear Magnetic Resonance (NMR). In fact, NMR was discovered first, paving the way for the development of one today's most useful medical imaging techniques. A brief timeline of the discoveries leading to the development of MRI is presented below:

- **1937**: Isidor Rabi described how nuclei could have their magnetic orientation disturbed by the use of an oscillating magnetic field.
- **1945**: Felix Bloch and Edward Purcell independently described the energy absorption and signal generation by water/paraffin nuclei inside a magnetic field.

- **1971**: Raymond Damandian demonstrated that cancer cells have longer T_1 and T_2 relaxation times than healthy cells and produced the first NMR based image.
- **1973**: Paul Lauterbur produced one dimensional projections of the NMR signal by rotating magnetic field gradients.
- **1973**: Peter Mansfield demonstrated the localisation of the NMR signal by a linear magnetic field gradient on a slice by slice basis.

The latter discovery forms the foundation of the spatial encoding techniques used in modern MRI scanners for signal localisation through the use of 3 orthogonal linearly varying magnetic field gradients.

1.2 Nucleus inside a magnetic field

1.2.1 Origins of magnetism

Magnetism is the result of moving electric charges (usually electrons) and is a fundamental property of matter just like mass and electric charge. There are 2 types of magnetism namely atomic and nuclear magnetism. Atomic magnetism is the result of the orbital movement of the surrounding electrons which as moving charged particles create both an electric and a magnetic field that orient perpendicularity to each other. The strength of the magnetic field is proportional to the amplitude of the moving charge and its velocity. The direction of the magnetic field can be found using the right hand rule (Figure 1.2).

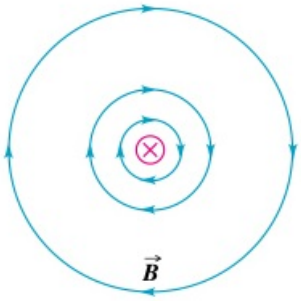


Figure 1.2: The magnetic field lines of a positive charge moving 'through' the page. A moving electron will produce similar but counter-clockwise field lines.

The magnetic fields of the orbital electrons orient randomly through the space around the atom and in non-magnetic materials cancel out (this is the case for an even number of electrons). However, when the number of electrons is odd then a magnetic field can be sustained rendering the material magnetic.

Nuclear magnetism is the result of the spin angular momentum of a nucleus as a whole. Both the positively charged protons and the uncharged neutrons (due to the internal quarks) precess under the effects of an external magnetic or gravitational field. The result of precession is movement of charged particles and therefore creation of magnetic fields. Again, an odd number of uncoupled spins is required for a magnetic field to be sustained.

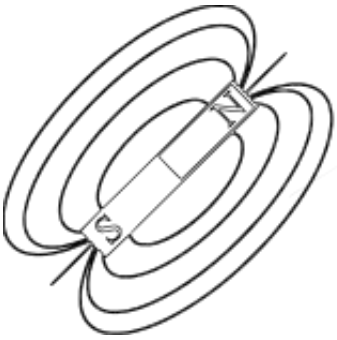


Figure 1.3: The magnetic field lines of a nucleus are equivalent that of a magnetic dipole. In other words, a nucleus behaves like a tiny magnet.

MRI is based on nuclear magnetism and the most commonly used nucleus in MRI experiments is hydrogen ^{1}H. Since hydrogen consists of only one proton in its nucleus the MRI signal is commonly referred to as signal arising from protons. Nevertheless, when higher atomic number elements such as ^{23}Na or ^{31}P are used for MRI experiments then the equivalency between the terms nucleus and proton breaks down. The nuclei of the latter chemical elements contain multiple protons and neutrons and thus in these cases nucleus $\neq$ proton.

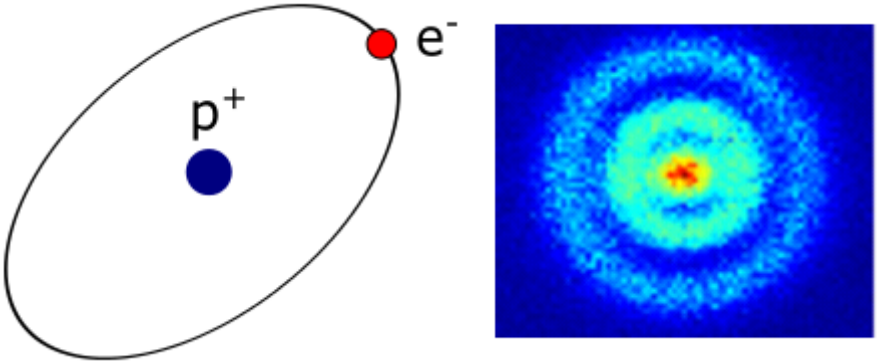


Figure 1.4: Classic, single electron orbit, view of the hydrogen atom (left). Quantum microscope image of the atom's wave function (right). Image taken from Stodolna et al [181].

1.2.2 Magnetic properties of hydrogen

1.2.2.1 Spin

In classical physics, an object of mass m, rotating in an orbit of radius $\vec{r}$, having a tangential speed $\vec{u}$ is described by a vector quantity called angular momentum $\vec{L}$:

$$\vec{L} = \vec{r} \times \vec{p} = \vec{r} \times m\vec{u} \tag{1.2.1}$$

The vector $\vec{L}$ is perpendicular to the plane of rotation as indicated in Figure 1.5.

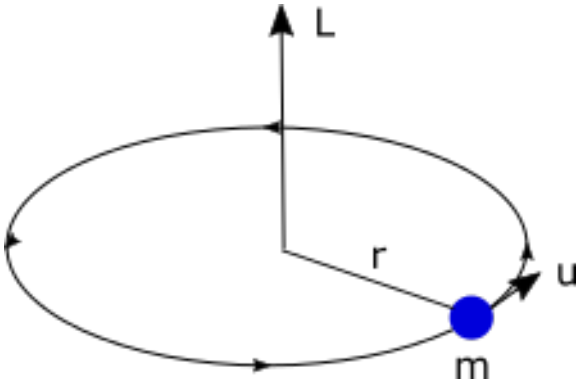


Figure 1.5: Angular momentum of a rotating object.

Spin (represented with S for electrons or I for nuclei) is the corresponding quantity of the classical angular momentum for atomic and sub-atomic particles. It is an inherent property of matter that represents an intrinsic angular momentum. Charged (protons, electrons), uncharged particles like neutrons (due to the internal quarks) and also nuclei, all posses spin. Furthermore, just as angular momentum interacts with gravitational fields, spin interacts with electromagnetic fields. However, unlike angular momentum, spin can only take a discrete set of values, or in other words, the magnitude of spin quantised. For example the number N of eigenstates for a nucleus with spin = $\vec{I}$ is:

$$N = 2I + 1 \tag{1.2.2}$$

In the special case of hydrogen (^{1}H) that has I = 1/2 there are:

$$2(\frac{1}{2}) + 1 = 2$$

possible spin states.

In quantum mechanic formulation these states are written as:

$$\left|+\frac{1}{2}\right\rangle \text{ or } \left|-\frac{1}{2}\right\rangle$$

and referred to as 'spin up' or 'parallel' and 'spin down' or 'anti-parallel' respectively.

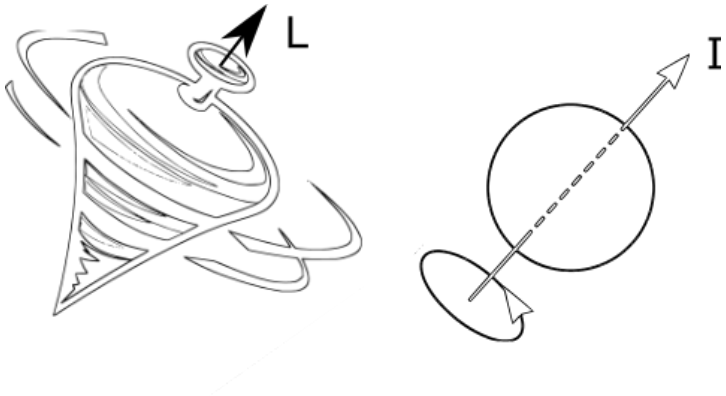


Figure 1.6: A simple analogy between a spinning top and a spinning nucleus.

Being quantised, spin, can only take discrete integer of half integer values (0, $\frac{1}{2}$, 1, $\frac{3}{2}$, 2, $\frac{5}{2}$, ...). Nucleons and electrons have spin = $\frac{1}{2}$ whereas the spin of nuclei across the periodic table ranges from I = 0 to I = 8. Not all nuclei can be used in MRI experiments. As described in the following table, the nuclei relevant to MRI are the ones having an odd/even or even/odd number of protons and neutrons. Hydrogen not only obeys the previous rule but also is very abundant in the human body, as $\frac{2}{3}$ of the latter is composed of water.

# protons & neutrons	Examples	Used in MRI
Even/even	^{4}He, ^{12}C	No
Odd/odd	^{2}H, ^{6}Li ^{10}B	No
Odd/even or even/odd	^{1}H, ^{13}C, ^{19}F, ^{23}Na, ^{31}P	Yes

Table 1.1: Composition of nuclei that can or can't be used in MRI experiments.

1.2.2.2 Magnetic moment

The magnetic moment $\vec{\mu}$, of a nucleus, is a vector quantity that measures the tendency of the nucleus to interact with an external magnetic field. Assuming a charge q, rotating in an orbit of radius $\vec{r}$ with speed $\vec{u}$ (Figure 1.7) then the magnetic moment $\vec{\mu}$ of the charge is:

$$\vec{\mu} = iA \tag{1.2.3}$$

where

i: the circulating current at the boundary of the area A

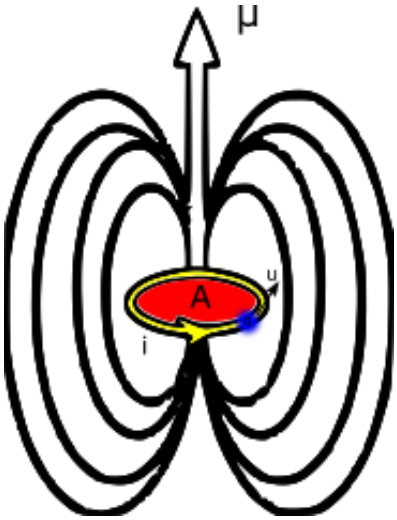


Figure 1.7: The magnetic moment $\vec{\mu}$ of a rotating charge q.

The period of rotation t of the charge q is:

$$t = \frac{\text{circumference}}{\text{speed}} = \frac{2\pi r}{u} \tag{1.2.4}$$

and the equivalent current i can be shown to be:

$$i = \frac{q}{t} = \frac{qu}{2\pi r} \tag{1.2.5}$$

From equations 1.2.1, 1.2.3 and 1.2.5 the magnetic moment $\vec{\mu}$ of the charge q can be shown to be:

$$\vec{\mu} = \left(\frac{q}{2m}\right)\vec{L} \tag{1.2.6}$$

where

m: the mass of the charge q

Consequently, the magnetic moment $\vec{\mu}$ is proportional to the angular momentum $\vec{L}$. The constant of proportionality is called gyromagnetic ratio, γ:

$$\gamma = \left(\frac{q}{2m}\right)$$

Using γ, equation 1.2.6 can be written as:

$$\vec{\mu} = \gamma\vec{L} = \gamma\vec{I} \tag{1.2.7}$$

where

$\vec{I}$: the total spin of the nucleus

The equivalent relationship that relates the magnetic moment $\vec{\mu}$ to the quantised angular momentum or spin reads:

$$\vec{\mu} = \gamma\hbar\vec{I} \tag{1.2.8}$$

where

$\hbar$: the reduced Planck's constant, $\frac{h}{2\pi} = \frac{6.62\times10^{-34}}{2\pi}$ J sec

We conclude this section by providing the γ values of nuclei used in MRI experiments and also the γ value of the electron . A negative gyromagnetic ratio indicates that the magnetic moment $\vec{\mu}$ and $\vec{I}$ are aligned in an anti-parallel orientation.

Nucleus/particle	**gyromagnetic ratio, γ, in MHz/T**
^{1}H	42.5
electron	-28024
^{13}C	10.705
^{19}F	40.052
^{23}Na	11.26
^{31}P	17.235

Table 1.2: γ values of commonly used nuclei. Notice that the electron γ value is 3 orders of magnitude larger than the γ of the other nuclei [7].

1.2.2.3 Magnetic susceptibility

Magnetic susceptibility, χ, describes the extend to which a material becomes magnetised when placed inside a magnetic field. As stated before, hydrogen behaves like a tiny magnet and therefore a large number of hydrogen atoms within a material define an internal magnetic field. When the latter is formed in the same direction as the external magnetic field then the material has positive χ. This type of material attracts the external magnetic field lines. On the other hand, when the internal magnetic field is formed in the opposite direction from the external magnetic field, then χ is negative. In this case the external magnetic field lines are dispersed around material lowering the local field (Figure 1.8).

Type	Susceptibility	Behaviour	Examples
Diamagnetic	$\chi<0$	Slightly repelled by magnets	Hydrogen, copper
Paramagnetic	$\chi>0$	Weak interaction with magnets	Oxygen, manganese
Ferromagnetic	$\chi>1$	Easily magnetised	Iron, Gadolinium

Table 1.3: Examples of diamagnetic, paramagnetic and ferromagnetic materials [149].

Since χ affects the local magnetic field it is an important parameter in MRI experiments as variabilities in tissue susceptibility is a common source of artefacts in MRI. Depending on their susceptibility, materials are classified as diamagnetic, paramagnetic or ferromagnetic as summarised in the previous table (1.3).

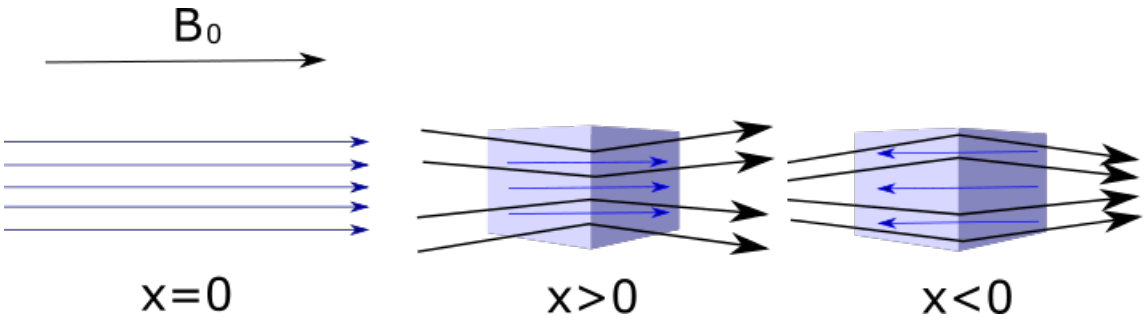


Figure 1.8: How the magnetic susceptibility of a material affects the intensity of the local magnetic field. The blue arrows indicate the orientation of the internal magnetic field.

1.2.3 Energy states and Zeeman splitting

As described previously (equation 1.2.2), the number of eigenstates of a nucleus with spin $\vec{I}$ is:

$$N = 2I + 1.$$

For ^{1}H:

$$I = \frac{1}{2}$$

and thus N = 2.

In quantum mechanic formulation these states are written as:

$$\left|+\frac{1}{2}\right\rangle \text{ or } \left|-\frac{1}{2}\right\rangle$$

and referred to as 'spin up' or 'parallel' and 'spin down' or 'anti-parallel' respectively.

The physical separation of the 2 spin states is only observable when the nucleus is inside an external magnetic field. In other words, in the absence of an external magnetic field the two states are said to be degenerate.

However, the situation is completely different in the presence of an external magnetic field. In this case, the interaction between the magnetic moment $\vec{\mu}$ and the mag-

netic field causes a splitting of the system's energy states and was first observed by Zeeman as splitting of optical spectral lines by a magnetic field. The energy difference between the two states (Figure 1.9) is given by:

$$\Delta E = \gamma \hbar B_0 \tag{1.2.9}$$

where

γ: the proton gyromagnetic ratio, 42.5 $\frac{MHz}{T}$

$\hbar$: the reduced Planck's constant, $\frac{h}{2\pi} = \frac{6.62\times10^{-34}}{2\pi}$ J sec

B_0: the magnitude of the external magnetic field

Starting from equation 1.2.8 and replacing the nuclear spin $\vec{I}$ with the proton spin $\vec{S}$, equation 1.2.9 is derived as follows:

$$\vec{\mu} = \gamma \hbar \vec{S} \tag{1.2.10}$$

Considering that $\vec{S} = \pm\frac{1}{2}$, the magnetic potential energy of the proton inside a field B_0 is:

$$E = -\mu B_0 = -\gamma \hbar \left(\frac{1}{2}\right) B_0 \tag{1.2.11}$$

for the spin-up state and

$$E = -\mu B_0 = -\gamma \hbar \left(-\frac{1}{2}\right) B_0 \tag{1.2.12}$$

for the spin-down state.

Subtracting equation 1.2.11 from equation 1.2.12 yields:

$$\gamma \hbar \left(\frac{1}{2}\right) B_0 - \left(-\gamma \hbar \left(\frac{1}{2}\right) B_0\right) = \gamma \hbar B_0 \tag{1.2.13}$$

which corresponds to equation 1.2.9 regarding the energy difference between the two proton spin states.

Finally, it is also evident from equation 1.2.12 that the spin down state has higher energy than the spin up state, as indicated in figure 1.9.

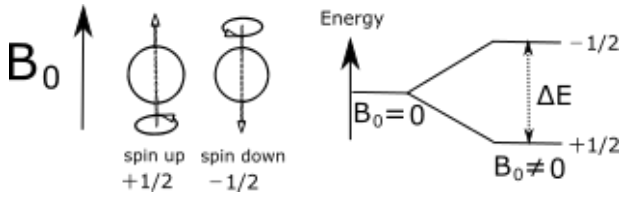


Figure 1.9: Classic, simplified, view of the spin-up and spin-down proton states (left). The 2 states have the same energy when $B_0 = 0$. Zeeman splitting occurs when $B_0 \neq 0$. The anti-parallel or spin-down state has higher energy than the spin-up state (right).

Figure 1.9 presents a simplified description of the two proton spin states that is somewhat inaccurate. What is known from the quantum mechanic description of the spin is that the latter does not exist on either the up or down state. More precisely, the spin exists in a linear combination (superposition) of the up and down states. In the most general case, this state of superposition can be expressed through a complex spin state vector $|A\rangle$:

$$|A\rangle = \alpha \left|+\frac{1}{2}\right\rangle + \beta \left|-\frac{1}{2}\right\rangle \tag{1.2.14}$$

where α and β are the components of the complex vector $|A\rangle$ along the basis directions defined as spin-up and spin-down.

Furthermore, $|\alpha|^2$ and $|\beta|^2$ give the probabilities of observing the spin on either the up or down state. This is because the process of measuring the spin state causes the 'collapse' of the wave-function, resulting in a single spin state.

1.2.4 Net magnetisation

Net magnetisation or simply magnetisation, $\vec{M}$, is a vector that expresses the density of the individual nuclear magnetic moments within a volume element:

$$\vec{M} = \frac{1}{V}\sum_i \vec{\mu_i} \tag{1.2.15}$$

where

$\vec{\mu_i}$: the elementary magnetic moment

V: the unit volume element

The fundamental relationships in MRI are simplified through the use of the $\vec{M}$ vector. This is because the vast (in the range of million billions) number of spins present in the sample undergoing MRI can be represented by a simple vector that obeys the laws of classical physics. A further consequence of the latter is the establishment of a fully classical formulation of MRI principles without any quantum mechanical assumptions.

In the absence of an external magnetic field the orientation of the nuclear magnetic moments is totally random. As a consequence, there is no net magnetisation that can describe the ensemble of spins. Nevertheless, when the spins reside within an external magnetic field then the preferential orientation of the magnetic moments or spins is the one that is parallel to the external magnetic field. In other words, most (but not all) spins will align with the external magnetic field.

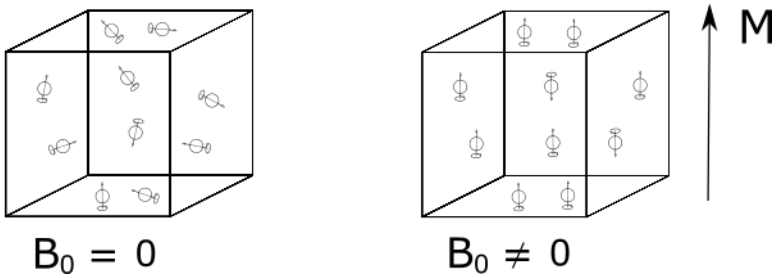


Figure 1.10: In the absence of a magnetic field the random orientation of the spins averages out the net magnetisation (left). Within a strong magnetic field however, a small excess of spins orients parallel to B_0. The ensemble of such spins is described through the magnetisation vector $\vec{M}$, that is also collinear to B_0 (right). The spins are not static, but move in a circular path as explained in the next paragraph.

In the previous paragraph it was shown that the parallel (spin-up), to the external B_0, orientation of the spins corresponds to the low energy spin state. The natural preference of occupying the lowest possible energy state is seen throughout all natural

phenomena and is not an exclusive feature of spin physics. If this the case, then what prevents the perfect alignment of all spins with the external field?

The answer here is that the spins also posses kinetic energy due to the local temperature. This so called thermal motion is a competing process to the magnetic alignment that works to equalise the 2 spin states. Assuming that the population of the spin-up state is $N^+$and the population of the spin-down state is N^-, then the arrangement of the spins can be described by the Boltzmann distribution:

$$\frac{N^+}{N^-} = e^{-\frac{\Delta E}{kT}} \tag{1.2.16}$$

where

ΔE: the energy difference between the states

k: the Boltzmann constant, $1.38\times10^{-23}\frac{J}{^oK}$

T: the temperature measured in ^{o}K.

The equilibrium magnetisation M_0, which is the available magnetisation at the start of an MRI experiment is given by [51]:

$$M_0 = \frac{N(\gamma\hbar)^2 B_0}{4kT} \tag{1.2.17}$$

where

N: the total number of spins

γ: the proton gyromagnetic ratio, 42,5 $\frac{MHz}{T}$

$\hbar$: the reduced Planck's constant, $\frac{h}{2\pi} = \frac{6.62\times10^{-34}}{2\pi}$ J sec

k: the Boltzmann constant, $1.38\times10^{-23}\frac{J}{^oK}$

T: the temperature measured in ^{o}K.

B_0: the magnitude of the external magnetic field

From equation 1.2.17 it is evident that a large number of available spins and a stronger B_0 will increase the MRI signal.

1.2.5 Precession and resonance

The spins that were presented in Figure 1.10 are not perfectly aligned parallel or anti-parallel with B_0 and are certainly not static. In fact, they move in a circular path (Figure 1.11) under the effects of a twisting force from the magnetic field. This type of movement is called precession.

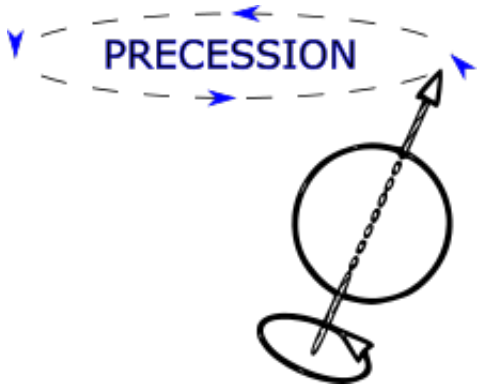


Figure 1.11: Precession of a spinning nucleus..

The force causing the precession acts perpendicularly to both the magnetic field and the magnetic moment and is called torque, $\vec{\tau}$:

$$\vec{\tau} = \vec{\mu} \times \vec{B} \tag{1.2.18}$$

where

$\vec{\mu}$: the magnetic moment of the nucleus

$\vec{B}$: the external magnetic field

The rate of precession, $d\varphi$ and the rate of change of the angular momentum $d\vec{L}$, caused by the torque, are illustrated in the following graph.

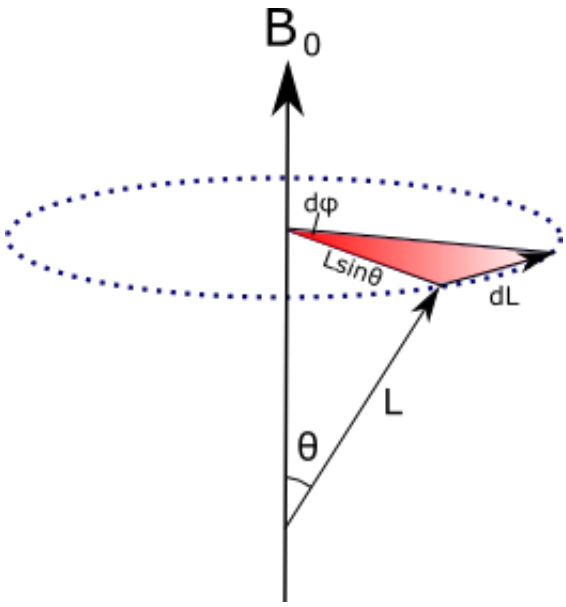


Figure 1.12: Precession of a magnetic moment $\vec{\mu}$ around B_0.

From Figure 1.12 the torque can be expressed as:

$$\vec{\tau} = \frac{dL}{dt} = \frac{Lsin\theta d\varphi}{dt} \tag{1.2.19}$$

Equating equations 1.2.18 and 1.2.19 gives:

$$\begin{aligned} \vec{\mu} \times \vec{B} &= \frac{Lsin\theta d\phi}{dt} \\ |\mu B sin\theta| &= \frac{Lsin\theta d\phi}{dt} \\ \mu B &= \frac{Ld\varphi}{dt} \end{aligned} \tag{1.2.20}$$

From the definition of the angular frequency, ω:

$$\omega = \frac{d\varphi}{dt}$$

and equation 1.2.7:

$$\gamma = \frac{\mu}{L}$$

equation 1.2.20 yields:

$$\omega_0 = \gamma B_0 \tag{1.2.21}$$

where

γ: the proton gyromagnetic ratio, 42.5 $\frac{MHz}{T}$

B_0: the magnitude of the external magnetic field measured in Tesla

Equation 1.2.21 is called the Larmor equation and ω_0 gives the precessional frequency of protons measured in MHz.

Even though at equilibrium the individual spins precess around B_0 with ω_0, the net magnetisation vector $\vec{M}$, does not (see also section 1.3.1). In this case, $\vec{M}$ is simply aligned with B_0. Nevertheless, when $\vec{M}$ is tipped from its equilibrium condition then it will precess around B_0. This is achieved with the application of an additional magnetic field, B_1, rotating near the Larmor frequency ω_0. The latter condition is necessary for resonance to occur. During resonance there is efficient energy transfer from the rotating magnetic field B_1 to the precessing spins (and equivalently to $\vec{M}$) resulting in a downward spiral motion of $\vec{M}$, as illustrated in the following graph.

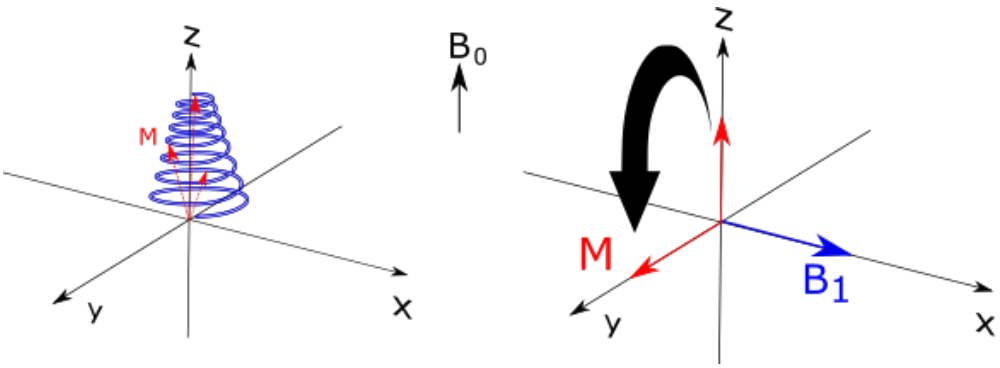


Figure 1.13: The application of a rotating B_1 at ω_0 causes $\vec{M}$ to drop at the xy plane. Motion as viewed from the lab (left) and rotating (right) frame.

The description of resonance is simplified by the use of the so called rotating frame.

This frame rotates around the z axis with ω_0 just as $\vec{M}$ does. This results in a simple drop of $\vec{M}$ to the xy plane as indicated in Figure 1.13.

The angle, θ, by which $\vec{M}$ is tipped by the application of B_1 is called the flip angle. In Figure 1.13 $\theta = 90^o$ or $\frac{\pi}{2}$.

In the most simple case of a rectangular hard pulse the flip angle is given by:

$$\theta = \gamma B_1 t \tag{1.2.22}$$

where

γ: the proton gyromagnetic ratio, 42.5 $\frac{MHz}{T}$

B1: the amplitude of the B_1 field

t: the duration of the B_1 pulse

1.2.6 Chemical shift

The chemical shift, δ (or σ), is a dimensionless constant that provides information about the chemical environment of a nucleus. Not all nuclei inside the same B_0 precess at the same frequency ω. This is because the local, to these nuclei, magnetic field depends on the interaction between the external B_0 and opposing, B_i fields created by the electrons orbiting the nuclei. This so called electron shielding results in a local field different than B_0. The relationship between these fields can be expressed as:

$$B_{local} = B_0 - B_i = B_0 (1 - \delta) \tag{1.2.23}$$

Chemical shift is measured in parts per million (ppm) and reflects the frequency separation of a nucleus from a standard reference:

$$\delta = \frac{(f_{sample} - f_{reference})}{f_{reference} \times 10^{-6}} \tag{1.2.24}$$

Typically, TMS {tetramethyl-silane - $(CH_3)_4Si$} is used as the reference and its single

resonance peak is assigned at 0 ppm in the proton spectrum. All other resonant frequencies are assigned in comparison to the TMS peak.

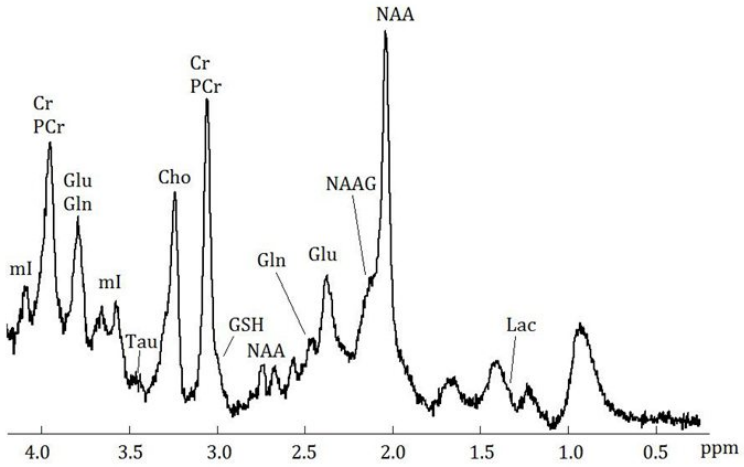


Figure 1.14: Brain proton spectrum measured at 7T. The resonant peaks of major brain metabolites are also shown [74].

Proton spectroscopy aims in detecting very low concentrations of organic chemical compounds. Typically, the peaks of these compounds are many orders of magnitude lower than the peaks of abundant compounds such as water and lipids. Water suppression techniques like CHESS and VAPOR or other inversion suppression pulses are commonly used in proton spectroscopy experiments in order to minimise the contamination of the spectrum from the water and fat signal.

1.2.7 J-coupling

J-coupling refers to the possible energy configuration states between coupled (interacting) nuclei. This coupling can occur either via the chemical bonds between the nuclei or simply 'through' space. In either case, due to quantum interactions the nuclear magnetic energy levels are split leading to double (e.g Lactate), triple or multiple resonant peaks.

The following is a simple classical explanation of the J-coupling.

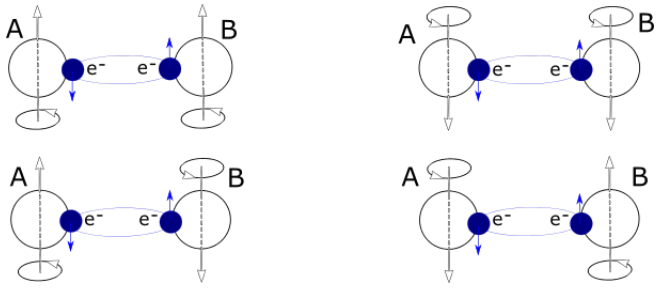


Figure 1.15: Through bond coupling of 2 nuclei. The 4 possible configurations lead to a double resonant peak. Note that the electron spins in the bond must follow Pauli's exclusion principle.

Consider a two spin system, coupled through a chemical bond, as indicated in Figure 1.15. Furthermore, nucleus B has an equal probability of being in a parallel or anti-parallel spin state. Then nucleus A will be split into two equal peaks. The peak of nucleus A, that is coupled to nucleus B, parallel to B_0 will have a higher frequency than the peak of nucleus A coupled to nucleus B anti-parallel to B_0. The most possible configurations of the spins are those where they are anti-parallel, since these states correspond to lower energy. Assuming that the probability of transitioning between parallel and anti-parallel configurations is equal, the energy corresponding to these configurations is slightly different. The latter results in the splitting of the resonant peak of nucleus A into two peaks of equal intensity.

Using Lactate as example, the CH_3 nucleus at 1.31 ppm is coupled to the CH nucleus at 4.10 ppm. This results in the CH_3 nucleus being split into two equal peaks, having a 6.9 Hz chemical shift [34].

1.3 Bloch equations

The following sections are based on the lectures given by Josef Granwehr and Paul Glover in autumn 2010 [51].

The Bloch equations is a set of first order differential equations that describe the evolution of the magnetisation vector $\vec{M}$. These equations can be derived by consulting Newton's second law of motion:

$$\frac{d\vec{p}}{dt} = \vec{F}$$

where

$\vec{p}$: the linear momentum

$\vec{F}$: the force acting on the system

A similar equation is valid for rotational motion:

$$\frac{d\vec{L}}{dt} = \vec{\tau}$$

where

$\vec{L}$: the angular momentum

$\vec{\tau}$: the torque acting on the system

From the last equation and the previously introduced equations 1.2.7 and 1.2.18 one obtains:

$$\frac{d\vec{\mu}}{dt} = \gamma\vec{\mu} \times \vec{B}$$

Using equation 1.2.15 the previous result is written as:

$$\frac{d\vec{M}}{dt} = \gamma\vec{M} \times \vec{B} \tag{1.3.1}$$

where

$\vec{M}$: the net magnetisation

Equation 1.3.1 represents a system of three coupled linear differential equations:

$$\begin{aligned}\frac{dM_x}{dt} &= \gamma\left(M_y B_z - M_z B_y\right)\\ \frac{dM_y}{dt} &= \gamma\left(M_z B_x - M_x B_z\right)\\ \frac{dM_z}{dt} &= \gamma\left(M_x B_y - M_y B_x\right)\end{aligned} \tag{1.3.2}$$

These equations are valid for an arbitrary field $\vec{B}$ that is homogeneous over the whole volume of interest.

1.3.1 Solutions for static $\vec{B}$ excluding relaxation

Assumptions:

a) $\vec{B} \parallel \vec{z}$, $B_x = B_y = 0$, $B_z = B_0$

b) $M_y(0) = 0$

Equations 1.3.2 are simplified to:

$$\begin{aligned}\frac{dM_x}{dt} &= \gamma M_y B_0\\ \frac{dM_y}{dt} &= -\gamma M_x B_0\\ \frac{dM_z}{dt} &= 0\end{aligned} \tag{1.3.3}$$

Therefore

$M_z(t) = M_z(0) = \text{constant}$

Moreover, by taking the first derivative of the first equation in 1.3.3 and substituting the expression for $\frac{dM_y}{dt}$ we find:

$$\frac{d^2M_x}{dt^2} = -\left(\gamma B_0\right)^2 M_x$$

which is a harmonic differential equation with solution (for $M_y(0) = 0$)

$$M_x = M_x(0)\cos(\omega_0 t)$$
$$M_y = M_x(0)\sin(\omega_0 t)$$
$$M_z = M_z(0)$$

where

ω_0 : the Larmor frequency

In this case, the magnetisation vector $\vec{M}$, precesses around the magnetic field direction as indicated in Figure 1.11. Depending on the sign of ω_0, the precession is clockwise for $\omega_0 > 0$ and anti-clockwise for $\omega_0 < 0$.

1.3.2 Solutions for static $\vec{B}$ including relaxation

After tipping the magnetisation $\vec{M}$ from its equilibrium state, the vector precesses around the magnetic field direction and its three components M_x, M_y, and M_z evolve as described in the previous section. Nevertheless, the precession cannot be maintained indefinitely. Energy is lost due to various interactions and processes and $\vec{M}$ gradually returns to the equilibrium state where it is $\parallel$ to $\vec{B}$. These processes are collectively called relaxation.

There are two types of relaxation. Longitudinal relaxation, which describes the growth of the M_z component towards the $\vec{z}$ axis and transverse relaxation which describes the decay of the transverse magnetisation components M_x and M_y. Both processes progress exponentially.

1.3.2.1 Longitudinal relaxation

Molecular translations, rotations, vibrations and changes in local resonant frequencies due to electron shielding affect the interactions between magnetic moments. This in turn affects the interactions of the magnetisation vector $\vec{M}$, with its immediate envir-

onment. During the longitudinal relaxation, energy is transferred from the spins to the surrounding lattice in the form of heat. This loss of energy results in the exponential return of the longitudinal relaxation M_z to its equilibrium state M_0.

The process is described by the following differential equation:

$$\frac{dM_z}{dt} = -\frac{M_z - M_0}{T_1} \tag{1.3.4}$$

The solution of 1.3.4 is:

$$M_z(t) = M_0 + (M_z(0) - M_0)\, e^{-\frac{t}{T_1}} \tag{1.3.5}$$

where

T_1 : the characteristic time constant termed longitudinal relaxation time

1.3.2.2 Transverse relaxation

Transverse relaxation is also an exponential process and is characterised by the time constant T_2. It describes the exponential decay of the transverse magnetisation components M_x and M_y. The latter is expressed as:

$$M_x(t) = M_x(0)\cos(\omega_0 t)e^{-\frac{t}{T_2}} \tag{1.3.6}$$

$$M_y(t) = M_x(0)\sin(\omega_0 t)e^{-\frac{t}{T_2}} \tag{1.3.7}$$

in the case where $B_x = B_y = 0$ and $M_y(0) = 0$.

Transverse relaxation is the result of the spin phase dispersion in the transverse plane. This loss of phase coherence determines the acquisition window during which a measurable MR signal can be detected. Both T_1 and T_2 relaxation occur at the same time, with the latter being faster than the former. Finally, additional spin phase dispersion in the transverse plane due to magnetic field inhomogeneities results in an even

faster than T_2 relaxation. This process is termed T_2^* relaxation and is given by:

$$\frac{1}{T_2^*} = \frac{1}{T_2} + \frac{1}{T_2'}$$

where

T_2 : relaxation due to spin-spin interactions

T_2' : relaxation due to magnetic field inhomogeneities

In summary, by combining the equations presented in the sections 1.3.1 and 1.3.2 the Bloch equations including relaxations terms are written as:

$$\begin{aligned}
\frac{dM_x}{dt} &= \gamma(M_y B_z - M_z B_y) - \frac{M_x}{T_2} \\
\frac{dM_y}{dt} &= \gamma(M_z B_x - M_x B_z) - \frac{M_y}{T_2} \\
\frac{dM_z}{dt} &= \gamma(M_x B_y - M_y B_z) - \frac{M_z - M_0}{T_1}
\end{aligned} \tag{1.3.8}$$

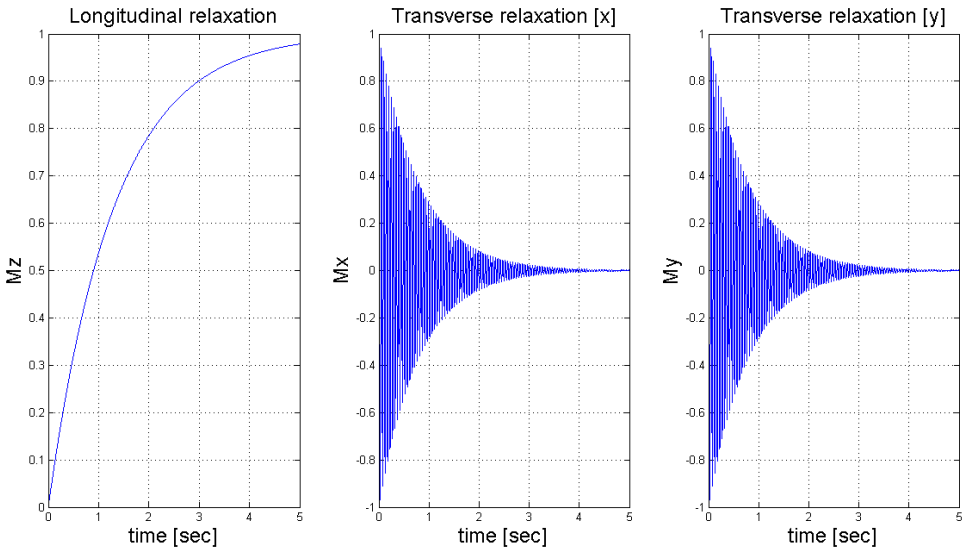


Figure 1.16: Longitudinal and transverse relaxation after a 90° RF pulse. T_1 = 1.3 sec, T_2 = 0.8 sec for white matter at 3T [220]. The plots were generated in Matlab using custom written code.

1.3.3 Rotating frame of reference

The rotating frame of reference is a coordinate system that simplifies the description of the evolving $\vec{M}$, especially under the effects of radio-frequency pulses. Essentially, it is a Cartesian coordinate system that rotates around $\vec{z}$ (assuming that $B_0 \parallel \vec{z}$), at the Larmor frequency ω_0, as illustrated in the following graph (Figure 1.17).

The magnetisation vector in the rotating frame, $\vec{M}^r$, can be obtained as:

$$\vec{M}^r = T\vec{M}$$

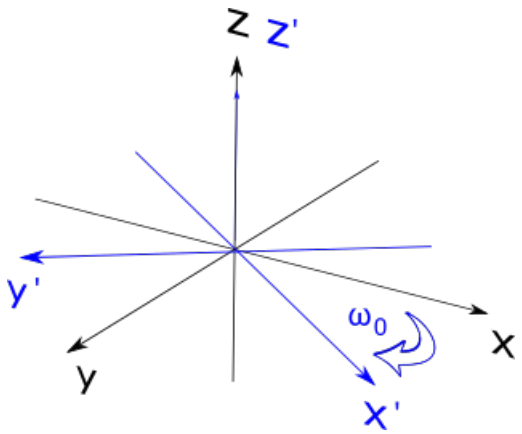


Figure 1.17: Rotating (blue) and laboratory (black) frame.

with T the transformation matrix:

$$T = \begin{bmatrix} \cos(\omega_{rf}t) & \sin(\omega_{rf}t) & 0 \\ -\sin(\omega_{rf}t) & \cos(\omega_{rf}t) & 0 \\ 0 & 0 & 1 \end{bmatrix}$$

where

ω_{rf}: the frequency of the applied radio-frequency pulse

Using the last result the relations of the magnetisation components in the two frames can be shown to be:

$$M_x^r = M_x\cos(\omega_{rf}t) + M_y\sin(\omega_{rf}t) \qquad M_x = M_x^r\cos(\omega_{rf}t) - M_y^r\sin(\omega_{rf}t)$$
$$M_y^r = -M_x\sin(\omega_{rf}t) + M_y\cos(\omega_{rf}t) \qquad M_y = M_x^r\sin(\omega_{rf}t) + M_y^r\cos(\omega_{rf}t)$$
$$M_z^r = M_z \qquad M_z = M_z^r$$

At this point the concept of the radio-frequency (RF) pulse, which is an integral part of all MRI experiments, will be described.

Consider two Helmholtz coil pairs arranged in a quadrature configuration as shown in Figure 1.18. When the sinusoidal current running through the coils has a 90° phase difference between the two pairs then the vector sum of the two magnetic fields results in a rotating vector.

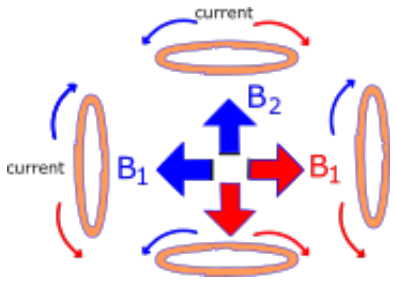


Figure 1.18: Quadrature RF transmit coil.

This result occurs because the magnetic fields of the coils are 90° out of phase and perpendicular to each other. In other words, when one magnetic field is at its maximum, the other one is zero. This is further illustrated in the following graph.

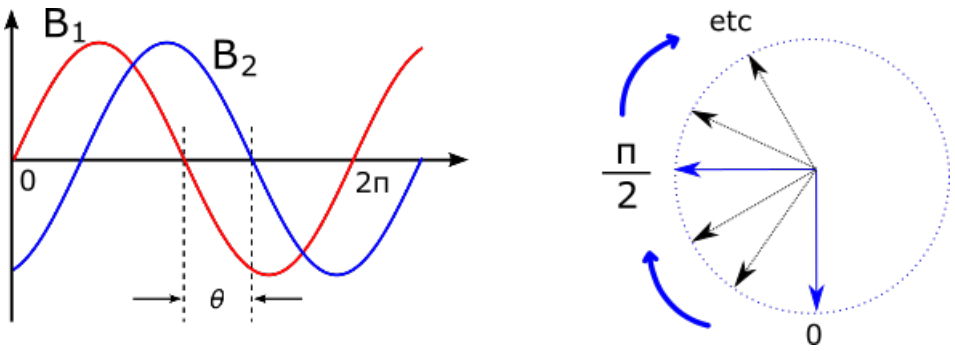


Figure 1.19: The RF pulse is a rotating magnetic vector, on a plane perpendicular to B_0.

Mathematically, the rotating magnetic vector of the RF pulse is given by:

$$\vec{B}_1(t) = B_1 \left(\cos\left(\omega_{rf} t\right) \vec{e}_x + \sin\left(\omega_{rf} t\right) \vec{e}_y\right)$$

The different pulse shapes used in MRI experiments are achieved by pulsing the RF field modulation envelope, $\vec{B_1}(t)$, for very short times (200 µs to 5 ms) [7]. Within this short time-frame T_1 and T_2 relaxation can be neglected and therefore a cumulative effect (e.g excitation) of the RF on the magnetisation can be attained.

1.3.3.1 Bloch equations in the rotating frame

In the rotating frame, the effective precession frequency is given by:

$$\Omega = \omega_0 - \omega_{rf}$$

and Bloch equations can be shown to be:

$$\begin{aligned}
\frac{dM_x^r}{dt} &= -M_y^r \left(\omega_0 - \omega_{rf}\right) - \frac{M_x^r}{T_2} \\
\frac{dM_y^r}{dt} &= M_x^r \left(\omega_0 - \omega_{rf}\right) + M_z \gamma B_1 - \frac{M_y^r}{T_2} \\
\frac{dM_z^r}{dt} &= -M_y^r \gamma B_1 - \frac{\left(M_z - M_0\right)}{T_1}
\end{aligned} \tag{1.3.9}$$

1.3.3.2 On resonant radio-frequency irradiation in the rotating frame

In this case, B_1 rotates around $\vec{z}$ (assuming that $B_0 \parallel \vec{z}$) with $\omega_{rf} = \omega_0$. Since the frame rotates with ω_0, just like the magnetisation does, the latter appears to be static. This means that $\vec{M}$ does no longer "feel" the effect of the main magnetic field B_0. In addition, even though B_1 is also static in this frame it affects the magnetisation.

Considering the on resonant condition $\omega_{rf} = \omega_0$ equations 1.3.9 give:

$$\begin{aligned}\frac{dM_x^r}{dt} &= 0\\ \frac{dM_y^r}{dt} &= \gamma B_1 M_z\\ \frac{dM_z^r}{dt} &= -\gamma B_1 M_y^r\end{aligned}$$

and the solutions can be shown to be:

$$\begin{aligned}M_y^r(t) &= -M_0 \sin(\theta)\\ M_z^r(t) &= M_0 \cos(\theta)\end{aligned}$$

where

θ: the flip angle of the RF pulse, equal to $\gamma B_1 t$

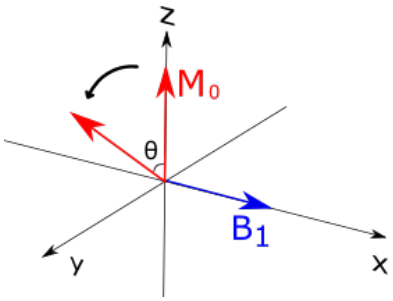


Figure 1.20: Flipping of the magnetisation by an on resonant RF pulse.

1.3.3.3 Off resonant radio-frequency irradiation in the rotating frame

The assumption $\omega_0 = \omega_{rf}$ is experimentally usually not fulfilled. In this case, $\omega_0 \neq \omega_{rf}$ and the effects of the B_0 field do not completely disappear. In fact, there is a residual longitudinal field given by:

$$B' = B_0 - \frac{\omega_{rf}}{\gamma}$$

In this case, the existing fields, $\vec{B}_1$ and $\vec{B'}$, are vectorially added together to produce an effective field $\vec{B}_{eff}$. The magnitude of the $\vec{B}_{eff}$ is given by:

$$| B_{eff} | = \sqrt{B_1^2 + B'^2}$$

and the magnetisation precesses in cone around $\vec{B}_{eff}$, as shown in the following graph (Figure 1.21).

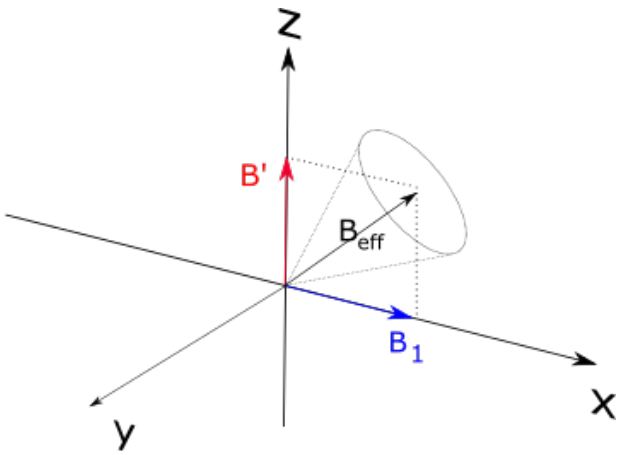


Figure 1.21: The effective field around which the magnetisation precesses when the RF pulse is applied off-resonance.

1.4 The MR signal

According to Faraday's Law of induction:

$$\vec{\nabla} \times \vec{E} = -\frac{\partial \vec{B}}{\partial t}$$

changing magnetic flux through a surface results in a circulating electric field, $\vec{E}$, at the boundary of the surface. The latter is the driving force of a measurable electric current. In MRI, the transverse magnetisation, M_{xy}, is the changing magnetic field that creates a voltage in the receiver coils. Measuring the latter leads to the MR signal.

The signal is recorded during certain relaxation times and typically when the spins in the traverse plane are in phase. In other words, the signal is recorded during an echo. The different ways of generating an echo are summarised in the following paragraphs.

1.4.1 Echo formation

1.4.1.1 Spin echo

A spin echo is formed at time TE (echo time) after the application of a 90° and a 180° RF pulse, separated by a time interval of $\frac{TE}{2}$. The effect of the pulses on the spins is illustrated below.

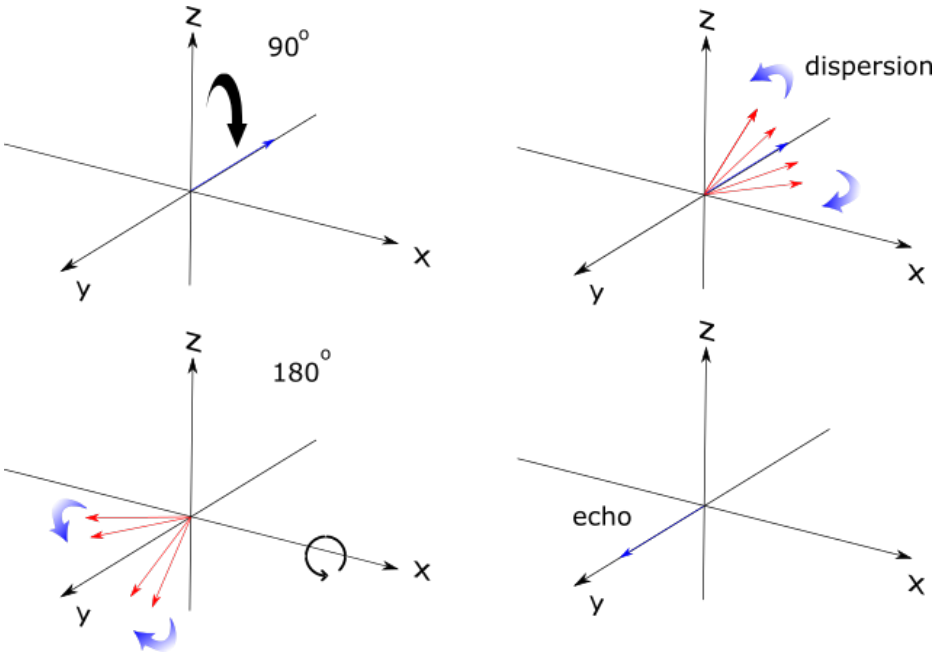


Figure 1.22: Rephrasing of the spins during the application of a 90^0- 180^0 pair of pulses.

After an initial 90^0 excitation, the 180^0 pulse flips the spins about the $\vec{x}$ axis. This results in an echo when the spins meet again at the positive $\vec{y}$ axis. The 180^0 pulse corrects for phase dispersion due to main magnetic field inhomogeneities and therefore spin-echo sequences are T_2 weighted and have higher signals than gradient echo sequences. Despite generating higher signals, the former have increased repetition times (TR) and thus take longer than the latter.

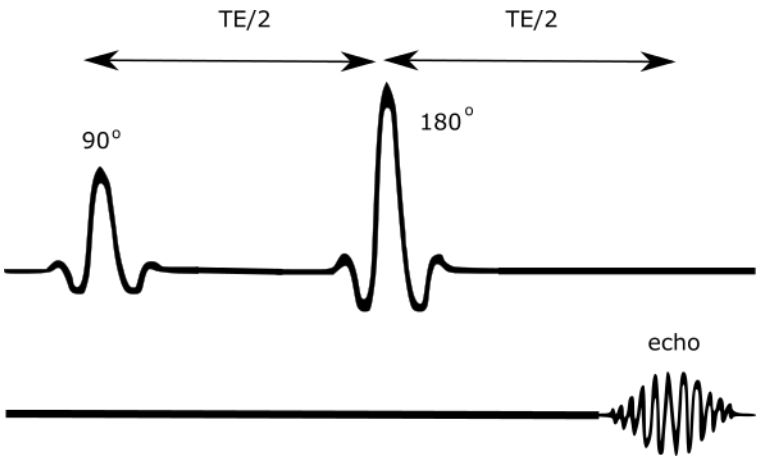


Figure 1.23: RF pulses for a spin echo.

1.4.1.2 Gradient echo

A gradient echo is formed without using an 180^0 RF pulse. In this case, a certain spin phase dispersion is introduced and immediately reversed by the frequency encoding gradient. The dephasing and rephasing gradient areas have the same magnitude but opposite polarities, as illustrated in the graph below. This gradient reversal, forces the spins to eventually rephase and thus to form an echo. Due to the absence of the 180^0 pulse, the gradient echo sequences are T_2^* weighted and have shorter repetition times. Since these sequences are sensitive to magnetic field inhomogeneities they are often used for acquisition of susceptibility weighted images.

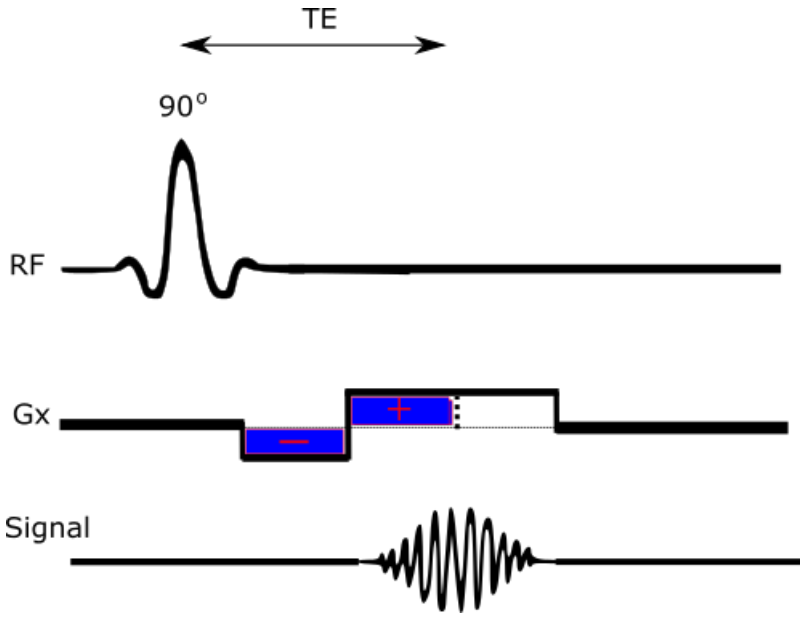


Figure 1.24: Gradient echo sequence. The echo is formed by reversing the polarity of the frequency encoding gradient. The slice selection and phase encoding gradients have been omitted for clarity.

1.4.1.3 Hahn echo and stimulated echo

A Hahn echo is observed during the application of two 90^0 RF pulses. If the pulses are separated by a time interval t, then the echo is formed at time 2t (Figure 1.25).

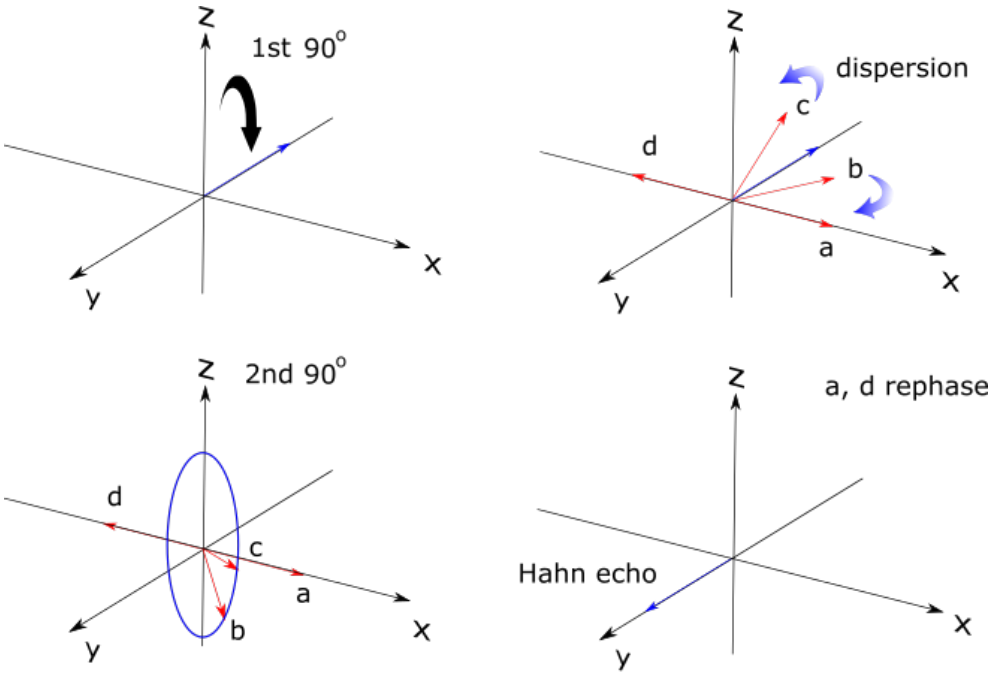


Figure 1.25: Formation of a Hahn echo.

The first 90^0 pulse tips the spins into the transverse plane initiating the transverse phase dispersion. Spins that are aligned with the $\vec{x}$ axis when the second RF pulse is applied will remain unaffected (a and d). However, slower spins like b and c will be flipped another 90^0 by the second RF pulse, into the yz plane. At this point, both b and c, can be described by their components on the $\vec{y}$ and $\vec{z}$ axis. Even though the z components will not rephase, since they are parallel to B_0 (and $B_0 \| \vec{z}$), the y components will rephase, but later than the a and b, forming a smaller echo.

The signal generated by a Hahn echo is half as large as the one obtained by a 90^0-180^0 pair. More specifically, it is reduced by a factor of: $\sin(\theta_1)\sin^2(\frac{\theta_2}{2})$, where θ_1 and θ_2 are the flip angles of the RF pulses.

Application of a third 90^0 RF pulse will tip the z components of spins b and c back into the transverse plane. There, after precessing and rephasing, these components will form another form of echo called stimulated echo.

In practice, the situation is more complicated, as any combinations of RF pulses will lead to numerous primary, secondary, and stimulated echoes. For example, applic-

ation of three RF pulses leads to five echoes: three primary, one secondary and one stimulated echo. This simple example illustrates the problem of echo contamination during an MRI experiment. Not all of the echoes generated are useful, especially when they overlap with desired signals.

1.5 Spatial localisation

A prerequisite of creating clinically relevant MRI images is the ability to precisely localise the source of the signal. This is achieved by the use of three additional magnetic fields, called gradients. These gradients induce linear variations in the magnitude of the main magnetic field proportional to the distance from the centre of the magnet (isocentre). It is important to note that the gradient magnetic fields are oriented in such a way as to always have their magnetic vector parallel to $\vec{B}_0$. This is achieved by using a Helmholtz coil for the z gradient and saddle coils for the x and y gradients.

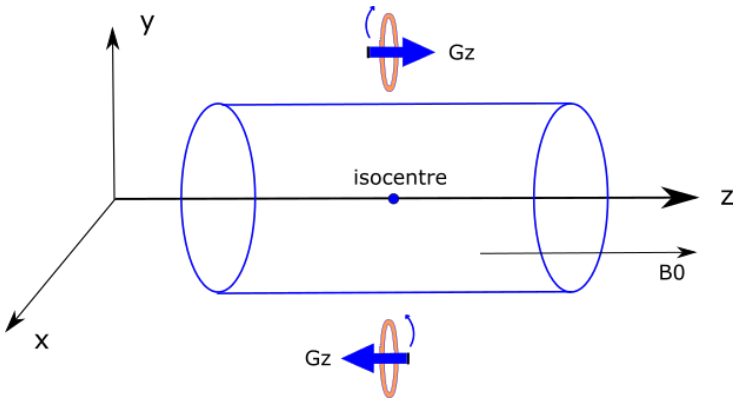


Figure 1.26: Slice selection gradient orientation.

The two most important gradient properties are the peak amplitude and the slew rate. The former defines how steep the gradient can be and is measured in milli-Tesla per meter ($\frac{\mathrm{mT}}{\mathrm{m}}$). Generally, higher amplitudes mean smaller FOVs and thinner slices. The slew rate is measured in $\frac{\mathrm{mT}}{msec}$ (milli-Tesla per msec) and determines how fast the gradient can be turned on. Obviously, this affects the imaging speed, with higher slew rates resulting in shorter echo and repetition times.

1.5.1 Slice selection (G_z)

Slice selection is accomplished by the simultaneous application of an RF pulse and a gradient (G_z) which causes a linear variation of the spin resonant frequencies across the $\vec{z}$ axis. Subsequently, the RF pulse excites groups of spins on either side of its centre frequency depending on its bandwidth.

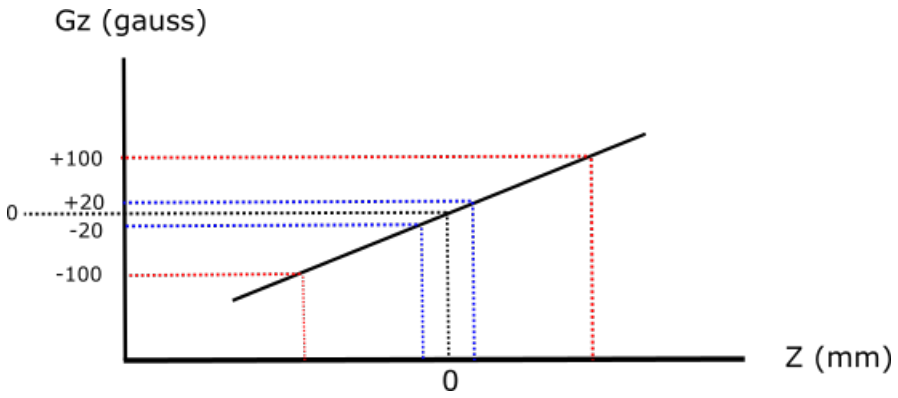


Figure 1.27: Selecting slices having different thickness.

As illustrated in Figure 1.27, the slice thickness can be determined by either the RF bandwidth or the slope of the gradient. More specifically:

$$\Delta z = \frac{BW_t}{G_z} \tag{1.5.1}$$

where

Δz: the slice thickness

BW_t: the bandwidth of the transmitted RF pulse

G_z: the gradient strength

In the previous example the centre frequency of the RF pulse matches the Larmor frequency ω_0. However, this is not always necessary. In general, the location of a slice can simply be determined by changing the centre frequency of the RF pulse to a value $\neq \omega_0$.

1.5.2 Frequency encoding (G_x)

The second magnetic field used for within slice spatial localisation is termed frequency encoding gradient (G_x) and is applied along the $\vec{x}$ axis. Nevertheless, its magnetic vector is still parallel to $\vec{B}_0$. Just like G_z, the frequency encoding gradient changes the spin precessional frequencies in the $\vec{x}$ direction. This is better illustrated with an example.

Consider the selection of a slice containing only nine pixels and that each pixel contains only one spin, as illustrated below.

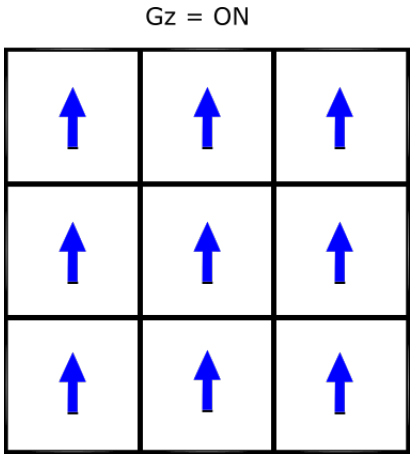


Figure 1.28: A simple nine pixel slice.

The precession of the spins in Figure 1.28 can be described by:

$$\sin(\omega t + \phi)$$

where

ω: the precessional frequency

ϕ: the phase of the precession

If now G_x is turned on, then the spins right (+$\vec{x}$ axis) of the central column (isocentre) will precess faster and the spins left of the central column will precess slower. This is indicated with ω_+ and ω_- respectively, in Figure 1.29.

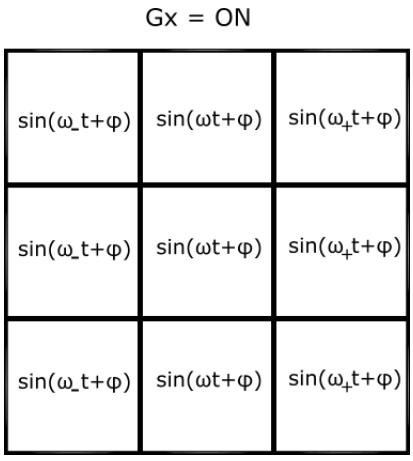


Figure 1.29: Effect of G_x gradient on spin precession.

At this point there are three precessional frequencies: ω, ω_+ and ω_-. This modification allows, at most, to differentiate the spins column-wise, but obviously, this classification is not optimal. However, by applying another gradient, along the $\vec{y}$ axis this time, the spins can be identified individually (see next paragraph).

1.5.3 Phase encoding (G_y)

The frequency changes introduced by the G_x gradient persist, after the gradient is turned off. By applying now a third gradient along the $\vec{y}$ axis, the phase of the spins can also be changed, as illustrated below.

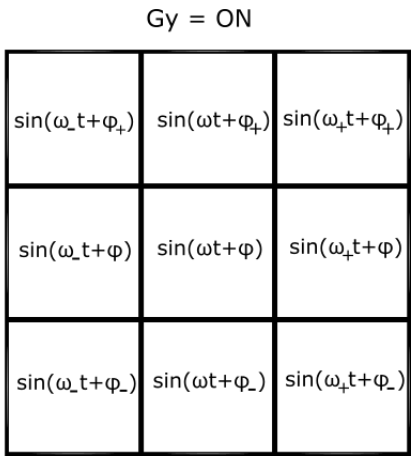


Figure 1.30: Using the G_y gradient, allows for individual identification of all the spins.

Again, the spins above the middle row (isocentre) gain phase (φ_+) and the spin be-

low lag behind (φ_-). Now, all the spins have unique precessional characteristics that depend on their location. This is a very important diagnostic aspect as being able to identify the exact correspondence between frequency and location is absolutely crucial in producing images that contain the right information (signal) from the correct and corresponding areas.

1.6 Shimming

Magnetic field inhomogeneities destroy the linear variation of the Larmor frequency and spatial location, leading to misplaced MRI signal and thus image distortions. The inhomogeneities are caused by manufacturing imperfections (coil winding variations, mechanical and electrical tolerances, surrounding structures) and inevitably, by the sample placed inside the magnet. Even if it was possible to create a perfectly homogeneous magnet, placing a sample of varying susceptibility within its field, would lead to distortions. For example, when scanning the human brain, differences in susceptibility occur between brain tissue and air in the nasal and auditory cavities. These susceptibility variations result in image distortions in the frontal cortex and temporal lobes. Mathematically, the distorting field that is caused by a volume element dV near tissue-air boundaries can be calculated by [216]:

$$B(\bar{r}) = (\chi_{tissue}(\bar{r}) - \chi_{air}) * (\frac{B_0}{4\pi} \cdot \frac{3z^2 - r^2}{r^5} dV) \tag{1.6.1}$$

where

χ: the magnetic susceptibility of tissue/air

B_0: the main magnetic field

Equation 1.6.1 shows that the magnitude of the distorting field increases linearly with B_0. This means that the problem of field inhomogeneity is more severe at higher magnetic fields. In addition, the more complex the geometric arrangement of tissue-air elements is, the more complex the disturbance of B_0 becomes.

Shimming is the process of minimising magnetic field inhomogeneities prior an MRI scan. Just like the total gravitational field (from a number of masses) and the total electric field (from a number of charges) is derived from the principle of superposition, the total magnetic field (from a number of coils) also obeys the same principle. Consequently, the total magnetic field present during an MRI experiment can be manipulated by the use of additional magnetic fields (apart from the main magnet). Ideally, the additional shimming fields, exactly resemble the existing magnetic field variations in both shape and amplitude, but have an opposite polarity.

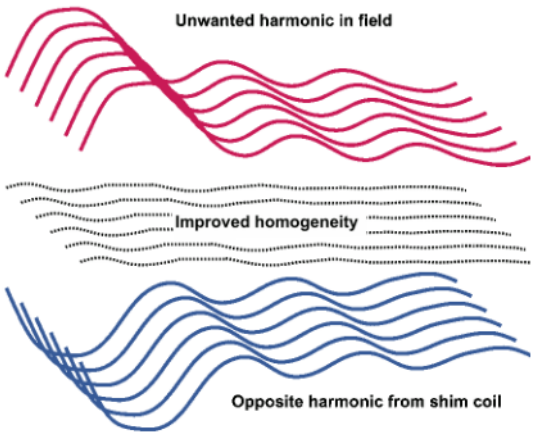


Figure 1.31: The superposition of the inherent and shim fields improves magnetic field homogeneity. Image taken from [38].

1.6.1 Passive shimming

Passive shimming is performed during the installation of an MRI scanner by placing pieces of metal (iron or steel) at the inner bore of the main magnet. For a typical cylindrical superconducting magnet, the shim elements are placed symmetrically around the $z-\mathrm{axis}$ of the magnet along its circumference. During the shimming process, the field homogeneity is repeatedly measured and the shimming elements are adjusted/tweaked accordingly to improve homogeneity.

Passive shimming mostly addresses inhomogeneities caused by hardware and environmental components and can provide an excellent field homogeneity, but that is

only when the bore is empty. It is time consuming and lacks flexibility as it is impractical for patient-by-patient implementation. A further disadvantage is the dependence of the passive shim induced fields on temperature (higher temperature→higher thermal energy→less available magnetisation) [179]. Thus, increased temperature during scanner operation might compromise the magnetic distribution caused by the passive shims, which in turn is detrimental for the acquired image quality.

1.6.2 Active shimming

Active shimming is performed with coils similar to gradient coils. The magnetic field produced by the former, is proportional to the current running through them and thus, by adjusting the current, the desired shimming field is produced.

The distribution of the magnetic field is given by the Laplace equation:

$$\nabla^2(B_x, B_y, B_z) = 0 \tag{1.6.2}$$

However, maximising the field homogeneity in the $z - \mathrm{direction}$ requires only the solution of:

$$\nabla^2 B_z = 0 \tag{1.6.3}$$

We note here that in most shimming techniques the non-uniform field is approximated and decomposed in an orthogonal basis set of spherical harmonic (SH) functions. These functions are defined on the surface of the sphere and can be used to solve differential equations such as equation 1.6.3. In spherical coordinates the solutions of 1.6.3 are [216]:

$$B_z(r, \theta, \phi) = \sum_{n=0}^{N} \sum_{m=-n}^{n} A_{n,m} r^n S_n^m(\theta, \phi) \tag{1.6.4}$$

where

N: the maximum spatial order of the harmonic decomposition

n: the shim order

m: the degree of one of the (2n +1) linearly independent functions associated with order n

$S_n^m(\theta, \phi)$: complex spherical harmonic functions derived as the product of the Legendre polynomial $P_n^m(\cos\theta)$ and $e^{im\phi}$.

How good the shimming can be, depends on how accurate the model of the magnetic field to be optimised is. For example, equations 1.6.4 can be expanded in the form of a Taylor series like so [224]:

$$B_0 + 3\ linear\ terms\ + 5\ 2^{nd}\ order\ terms\ + 7\ 3^{rd}\ order\ terms\ + \ldots \quad (1.6.5)$$

Equation 1.6.5 describes a magnetic field that results from the superposition of the main magnetic field (B_0) and additional fields in the x, y, z directions (first order shim), $xy, zx, yz, z^2, x^2 - y^2$ (second order shim) and $zxy, z(x^2 - y^2), x^3 - y^2x, y^3 + x^2y$ directions (third order shim: a comprehensive list of directions can be found in reference [78]). In other words, the first and higher order terms in equation 1.6.5 represent the shimming magnetic fields that have the same amplitude, but opposite direction (inverted sign) from the field distortions, in order to eliminate them. Three graphical examples of shimming fields are presented below:

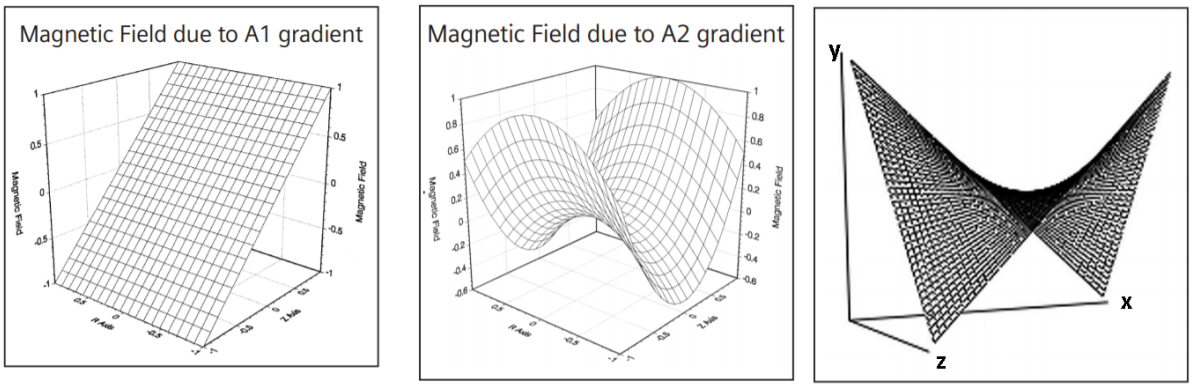


Figure 1.32: First and second order shim examples. Images taken from [224].

Active shimming offers a robust, user independent and quick method for correcting magnetic field distortions. Being orthogonal, the spherical harmonic functions can be adjusted independently simply by driving an appropriate current through the shim coils. In theory, more spherical harmonic function modelling allows for a more accurate field correction but in practice, due to space and cost restrictions (even though linear shimming can be achieved by the gradient coils, high order shimming requires additional dedicated equipment), most human MRI scanners can accommodate shimming up to the third order. The latter is problematic when a highly localised field distribution is present (such as in the human prefrontal cortex). In this case, the complexity of the magnetic field distribution cannot be adequately compensated by low order active shimming [96].

1.6.3 Dynamic shimming

The need for obtaining maximum field homogeneity across the whole human brain can be addressed by dynamic shimming, among other strategies (intra-oral passive shimming [225, 18], external passive shimming [92], electrical non-spherical harmonic shimming [93]). Dynamic shimming is based on the principle that any complex field distribution can be approximated by a number of lower order functions over smaller regions of interest. As such, as opposed to global static shimming, dynamic shim-

ming optimises the magnetic field homogeneity on a slice by slice basis. This means that the currents driven through the shim coils need to be updated before each new slice/volume is acquired, with the update time being as short as possible so as to have minimum impact on the total scanning time. In dynamic shimming an improved homogeneity, over the entire region/volume of interest, is achieved through the individual improvements of the fields in all sub-regions.

Dynamic shimming is not perfect as it is still compromised by the shallowness of the low order spherical harmonic fields that are inadequate to compensate for the higher-order inhomogeneities that are typical in-vivo. Despite that, an increased B_0 homogeneity would still be beneficial for applications such as fat suppression ([141]) and frequency specific detection like MRS [102] and CEST [264].

Even though field homogeneity is improved by the use of higher order spherical harmonic functions, in both static and dynamic shimming strategies, dynamic shimming offers better field homogeneity as compared to static shimming [163]). Figure 1.33 shows the field homogeneity gains in human in-vivo data at 7T of a 2nd order dynamic shim versus a 2nd order global shim. Dynamic shimming was found to be superior in all three measures of homogeneity, namely field standard deviation, central 80% pixel value range and fraction of non-zero field value pixels greater than 50 Hz for both axial and coronal orientations. 2nd order dynamic shimming performed the best even when compared to 3rd order global shimming and a combined 3^{rd}order global + 1^{st}order dynamic shim. Unsurprisingly, 1st order global shim was found to have the greatest residual inhomogeneity, while 2nd order global shim was superior to 1st order dynamic shim (results not shown, [163]).

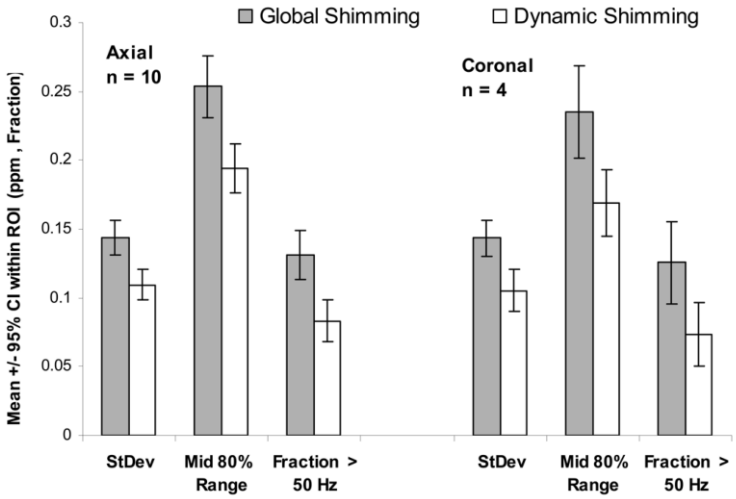


Figure 1.33: Human in-vivo 2nd order Global Shimming versus 2nd order Dynamic Shimming field homogeneity measures: field standard deviation, central 80% pixel value range and fraction of non-zero field value pixels greater than 50 Hz. The data was acquired at 7T, with the shim ROI box being propagated to all slices. Image taken from [163].

Dynamic shimming comes with its own challenges. First of all, it requires dedicated electronics/shim coils, similarly to high order active shimming. Second, the implemented pulse sequence must be programmed to allow for updating the coil current right after a k-space acquisition and before the next RF excitation. Finally, the rapid switching of the shim/gradient coils results in short and long lived eddy currents, which in turn create unwanted magnetic fields that affect the main B_0 in a spatial and temporal manner. Active shielding can be used to minimise eddy currents (from linear shimming), but a successful implementation of high order dynamic shimming requires pre-emphasis (”overshoot”) and B_0 compensation ([22]). The latter involves driving currents of appropriate amplitude and decay characteristics in the gradient and shim coils in an attempt to offset the eddy currents. In other words, the shim coil induced transient fields are being counteracted by the extra shim field offsets of pre-emphasized current waveforms. In the case of multiple channel shim coils, the cross coupling terms between all channels must be taken into account during the design of the pre-emphasized waveforms. Eddy current field perturbations and channel coup-

ling can be modelled as described in reference [93] and their spatial characteristics can be measured with 1D projections along the z-axis in a spin echo experiment, as described in reference [202].

1.6.4 Multi-coil shimming

Multi-coil (MC) shimming methods utilise a number of shim coils that are independently driven by DC currents. As opposed to the methods described in the previous sections, multi-coil shim arrays generate non-orthogonal shim fields with the trade off being the ease of construction (loop shaped geometries placed in close proximity to the anatomy of interest). The simple coil design offers the following advantages: 1) low inductance of the coil loops (and subsequent low EMF) allows for the use of low voltage amplifiers, 2) adequate separation from bore structures (and subsequent reduced eddy current generation) and 3) generation of MRI-relevant magnetic fields by a linear combination of a generic set of localized coils. The latter allows for simultaneous spatial encoding and shimming that could account for signal losses and spatial distortions frequently encountered in EPI [207].

Figure 1.34 compares a 1st-3rd order global spherical harmonic shimming with a 48 channel MC shim array (termed DYNAMITE [95]) in the human brain at 7T. The colour-maps show the standard deviation of the main field offsets (ΔB_0) in Hz.

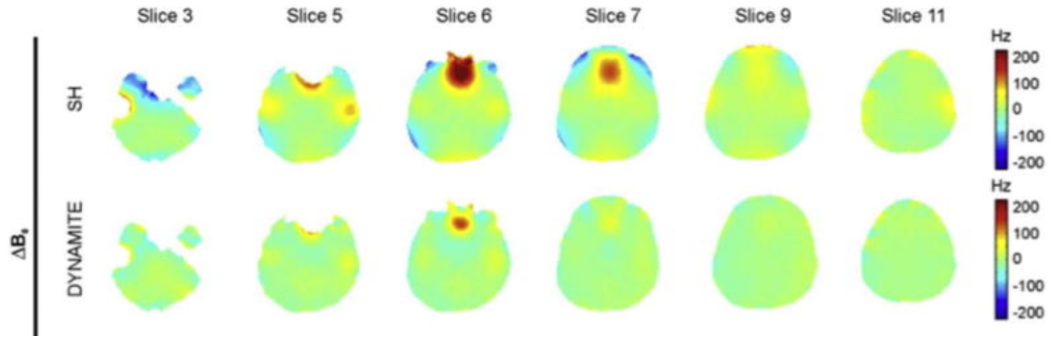


Figure 1.34: Comparison between global spherical harmonic shimming and multi-coil shimming across six slices in the human brain at 7T. Image taken from [95].

Even though global spherical harmonic shimming does improve homogeneity ($\sigma = 32.3$Hz) by removing smoothly-varying B_0 components, its efficacy is inferior, for steep B_0 changes (frontal lobes), to multi-coil shimming ($\sigma = 13.3$Hz) [95].

A practical problem when using multi-coil shim arrays is to how best integrate them with the transmit-receive RF coil arrays. Both arrays benefit from not only using as many elements as possible (increased parallel imaging performance and cancellation higher order B_0 inhomogeneities), but also from close placement to the anatomy of interest (high B_1 sensitivity and SNR and high ΔB_0 shim field efficiency). Nevertheless, the space within the bore is limited and a 48 shim coil array (100 turns per coil) leaves about 10cm in the middle, enough to fit 8 transmit-receive RF coils [94]. To overcome space restrictions combined shim-RF coils have been developed [59, 180].

The practical utility of multi-coil arrays can be further enhanced by reducing the number of amplifiers used. Instead of driving each separate element by a dedicated amplifier, elements can be connected in 'clusters' and be driven by a single amplifier, without compromising the variety of the field shapes generated. In this case, a switching circuit must be designed to perform the following two functions: 1) connecting every coil element to all terminals of every other coil element and 2) connecting every terminal of each coil element with every terminal of every amplifier. The purpose of the switching circuit is simply to switch between different configurations of the coil elements depending on the desired field shapes. Even though process of switching is time consuming, the number of required switches can be limited to only those essential for the application at hand [110, 111].

Chapter 2

CEST: mechanism, optimisation and clinical applications

2.1 Mechanism

2.1.1 CEST mechanism and underlying processes

2.1.1.1 Direct contributions to the MR signal

Magnetic Resonance Imaging has evolved from exploiting contrast due to differences in intrinsic tissue properties (proton density, spin-lattice relaxation - T_1 time, spin-spin relaxation - T_2 time) to utilising contrast mechanisms based on tissue susceptibility differences, molecular diffusion, perfusion and flow, nuclear chemical shifts and finally endogenous or exogenous contrast agents.

The largest and most important source of signal in MRI comes from the protons found 'free' water molecules That is, highly unstructured water molecule populations that can easily perform translations and rotations. It is exactly due to this motional independence that 'free' water is characterised by long T_1 and T_2 relaxation times (a few seconds at low magnetic fields). Cerebrospinal fluid is a very good example of a structure almost exclusively composed of such kind of protons. Additionally, high

concentrations of this water species can be found in cytosol and cellular interstitium.

The second important direct contribution to MR signal comes from protons in tissues containing fat/lipids (e.g. skeletal muscle, adipose tissue, bone marrow). These protons are more restricted than water protons and therefore have shorter (but measurable) T_1 (hundreds of msec) and T_2 (a few msec) relaxation times.

Biological tissues however are vastly complex structures, characterised by internal micro-structures containing water (internally or in hydration layers) and a plethora of macromolecules (proteins, phospholipids, polysaccharides, fat) that are distributed non-uniformly and within additional compartments. Macromolecular protons are highly restricted ('bound' on macromolecules) and are therefore characterised by very short T_2 relaxation times (μsec). Moreover, their concentrations are in the milli-molar range. The practical implication of the very low relaxation times and concentrations is that macromolecular protons cannot be detected directly by an MRI experiment. Table 2.1 presents a summary of which protons can or cannot directly be detected by MRI.

Proton origin	Description	Directly detectable
'Free' water	Rapidly translating and rotating protons. Relaxation times ~sec	Yes
Fat/lipids	More restricted than free water protons. Relaxation times ~msec	Yes
Macromolecules (proteins)	Highly restricted ('bound'). Relaxation times ~μsec	No
Macromolecular hydration layer	Restricted. Relaxation times ~μsec/msec	No

Table 2.1: The source of the MRI signal.

2.1.1.2 Indirect contributions to the MR signal

As was mentioned in the previous section, the macromolecular protons (in proteins/peptides) cannot directly be detected by MRI (Table 2.1). This is because of their very short T_2 relaxation times and milli-molar concentrations. However, proteins and peptides play an important role in various physiological processes like metabolism, DNA manipulation, and signal transmission, cell division and catabolism among others. Additionally, they are tumour specific molecules. Consequently, being able to measure them would be beneficial for a number of reasons, including, possible, earlier detection of disease, more accurate determination of the spatial distribution of the lesions and overall better characterisation of the pathology. Furthermore, the ability to generate contrast based on endogenous compounds would reduce the use the potentially toxic exogenous paramagnetic contrast agents like ^{3}Gd. The latter, has been used in clinical practice for more than 20 years and has been proven a very useful diagnostic tool in characterising active tumour parts. However, it is not an efficient contrast enhancing mechanism in low tumour grades as the uptake of the agent in these tumours is low.

In order to overcome the limitation of MRI to directly measure endogenous proteins, an alternative contrast mechanism, based on the exchange of magnetisation between proteins and 'free' water (that dominates the MR signal) has been developed. This contrast mechanism is termed Magnetisation Transfer (MT) and together with its variation, Chemical Exchange Saturation Transfer (CEST) allows the indirect measurement and quantification of endogenous proteins with MRI.

Even though the technique has successfully been used in numerous human in vivo studies during the last few years, the physical phenomenon of magnetisation exchange was initially studied more than half a century ago. Those early NMR spectroscopy studies were investigating the different resonant frequency shifts of protons in ethyl-alcohol and their dependence on temperature [5]. Soon after, similar experiments investigated the proton resonant frequencies in a variety of aqueous solutions

(acetic acid, sulphuric acid, potassium nitrate, potassium sulphate, sodium chloride [57]), followed by mathematical efforts to describe these processes, by modifying the Bloch equations to include the chemical shift dependence of magnetisation [135, 227]. In 1963, the first study to quantitatively measure the proton lifetimes between exchanging systems (a mixture of Salicylaldehyde and ^{2}Hydroxyacetophenone) was performed [42]. In the years that followed, spectroscopy was applied to other nuclei as well, apart from protons. Phosphorus (^{31}P), carbon (^{13}C) and fluorine (^{19}F) along with ^{1}H-MRS, provided important information regarding biochemical processes significantly improving the diagnostic effectiveness of magnetic resonance imaging. The realisation that the process of the chemical exchange could provide an increase in the sensitivity enhancement of the acquired signals came after a landmark in-vivo study, in 1989 [229]. While similar studies followed [54], the idea of using exogenous paramagnetic contrast agents, that utilise the chemical exchange, started developing. In 2000, an important study [222] showed the feasibility of using a large number of compounds (sugars, amino-, Imino-, and Barbituric acids) as CEST based MRI contrast agents. In addition, studies on cationic-anionic polymers like poly-l-lysine (PLL) and polyuridilic acid (poly(rU)) showed very high sensitivity enhancement factors allowing the detection of concentrations in the molar range [50, 175]. Thankfully, such high sensitivity enhancement factors can be achieved by using endogenous proteins and peptides, as demonstrated in 2003 [264, 263]. This novel endogenous contrast agent, termed amide proton transfer (APT), has been used, since then, to provide physiological information for assessing brain tumours [263, 210, 88, 266, 165, 223, 172, 271] and other pathologies like multiple sclerosis [145].

2.1.1.3 Magnetisation transfer pathways

Magnetisation transfer (MT) and Chemical Exchange Saturation Transfer (CEST) is the result of cross relaxation effects between protons in interacting molecular environments. However, the internal complexity of the biological tissues does not allow for

a single universal quantitative description of the relaxation processes. Instead, there are 6 accepted relaxation pathways leading to a variety of simultaneous processes affecting the measured MR signal. Table2.2 presents a summary of these relaxation mechanisms.

Mechanism	Description
Dipole-Dipole interaction	This is the dominant mechanism for ^{1}H relaxation. It is a 'through space' interaction where the fluctuations of the magnetic field of one nucleus (dipole) change the relaxation properties of another
Chemical Shift	Electron clouds magnetically shield a nucleus changing its resonant frequency and relaxation rates
Translation/Flow/ Diffusion	Molecular translation due to electro-chemical or gravitational gradients, blood flow or random thermal displacements (Brownian motion)
Chemical Exchange	Physical exchange of protons between molecules
J-coupling	Similar to dipole-dipole interaction but only for spins belonging to the same molecule (and chemical bond). The orientation of one spin determines the orientation of the other and overall the energy of the system. J-coupling is also responsible for peak splitting e.g lactate
Electric-quadrupole coupling	Nuclei with spins I$\geqslant$1 do not have spherical charge distribution like ^{1}H has. These nuclei relax by strong interactions of their quadrupolar moment with nearby electric fields (electron clouds)

Table 2.2: The 6 basic relaxation mechanisms affecting the T_1 and T_2 times of the measured MR signal

Magnetisation transfer and chemical exchange are based on well defined physical and chemical processes. Furthermore, since biological tissues can have very different macromolecular compositions, the MR signal based on magnetisation transfer and chemical exchange can greatly vary. The bigger the variations the larger the contrast between the tissues. The nature of the two contrast mechanisms can be summarised as:

- Magnetisation transfer is based on dipole-dipole interactions between proton spins
- CEST refers to the physical exchange of protons between molecules

Therefore, spin proximity and relative motion are two important factors that determine the effectiveness of magnetisation transfer (drops with $\frac{1}{r^6}$ where r is the distance between the spins and as the relative motion of the nuclei increases. MT and chemical exchange occur simultaneously shortening both T_1 and T_2 (at a much greater extent) times.

2.1.1.4 Contrast generation in MT and CEST

Let us consider the simple case of two proton species. Protons that belong to 'free' water (pool A) and protons 'bound' to macromolecules (pool B). Pool A and pool B have different spectral characteristics. More specifically, protons of pool A are less restricted than protons in pool B and therefore have longer T_2 relaxation times (~100ms as opposed to $T_2 \leqslant$0.1msec). This means that the free protons are characterised by a narrow spectral FWHM, whereas the bound ones by a wide spectral FWHM ($FWHM = \frac{1}{T_2}$) as can be seen in the following figure 2.1.

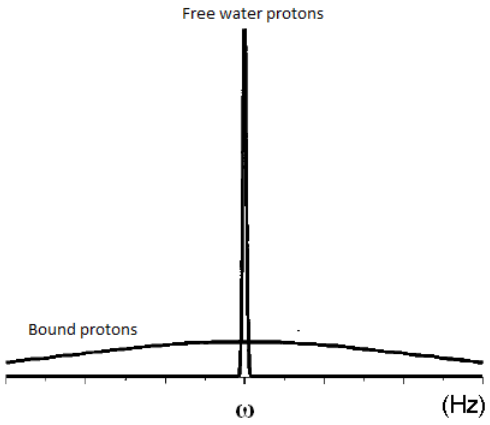


Figure 2.1: The spectral lines of pool A (free protons) and pool B (bound protons)

Under normal conditions magnetisation is exchanged between the 2 pools until an equilibrium state is achieved. An MRI measurement at this point will produce the same result as in the case of a single isolated free proton pool, i.e bound protons are undetectable.

However, in the case of MT and CEST experiments a special condition is established. That is, the bound protons are selectively saturated with specific RF pulses before an MRI measurement is performed. This initial saturation followed by the typical exchange of the (saturated now) magnetisation results in the reduction of the available longitudinal magnetisation and therefore a reduction in the measured signal. Why would a drop in the measured MR signal be beneficial? That is because it is accompanied by an increase contrast between the tissue containing the macromolecular bound protons and a tissue that does not. Figure 2.2 presents a more intuitive explanation of the contrast enchantment in MT and CEST experiments.

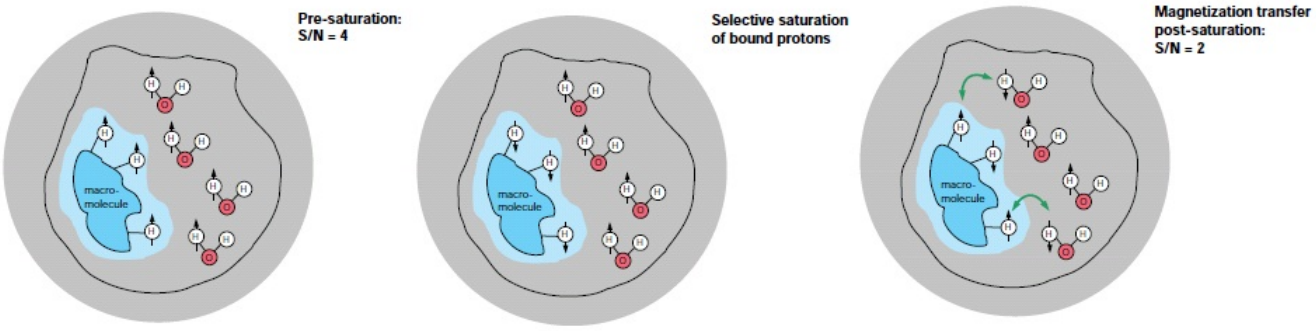


Figure 2.2: Contrast enhancement in MT and CEST experiments. Under normal conditions (left) the magnetisation exchange does not affect the contrast. After selective saturation (flip) of the macromolecular magnetisation (middle) and subsequent transfer of the inverted spins to free water (right) the measured signal drops. This signal difference between the macromolecular containing tissue and an another one that does not contain the macromolecule increases the contrast between the tissues. *Image taken from* [21]

2.1.1.5 The basic saturation transfer experiment

As described in the previous figure (2.2), CEST is a contrast enhancement technique allowing the indirect detection of metabolites having exchangeable protons. Unlike contrast mechanisms such as T_1, T_2 and diffusion weighted imaging, CEST probes molecular targets in a frequency-specific manner. As a result, a number of molecu-

lar species including amides (-NH), hydroxyl (-OH) and amines (-NH_2), can be potential candidates for CEST imaging and even be detected simultaneously [204] [125]. Contrary to magnetic resonance spectroscopy (MRS), CEST, as a non-spectroscopic method, is characterised by higher spatial resolution and sensitivity. The latter is due to an amplification in contrast after the occurrence of a large number of saturation exchange instances between a milli-molar sized proton pool and a much larger (in the molar range) proton pool (free water). Finally, unlike the radioactive isotopes used in the extremely sensitive positron emission tomography (PET), the molecular contrast agents relevant to CEST are devoid of ionising radiation.

At its most simplest, a saturation transfer experiment involves the application of a pre-saturation RF pulse, followed by a typical acquisition scheme as implemented in all magnetic resonance imaging experiments (Figure 2.3).

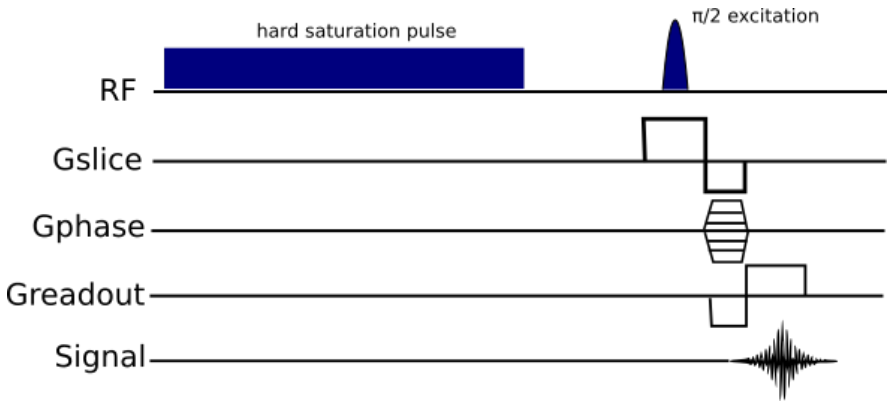


Figure 2.3: Basic saturation transfer experiment. The protons of interest are saturated with a continuous hard pulse before a typical acquisition scheme, including excitation, slice selection and encoding, is implemented.

The important thing to note here is that the pre-saturation pulse is applied multiple times, having a different frequency in each pass. This way, the sample under investigation is affected by a resonant frequency sweep resulting in the acquisition of one image per frequency as illustrated in the following figure (Figure 2.4).

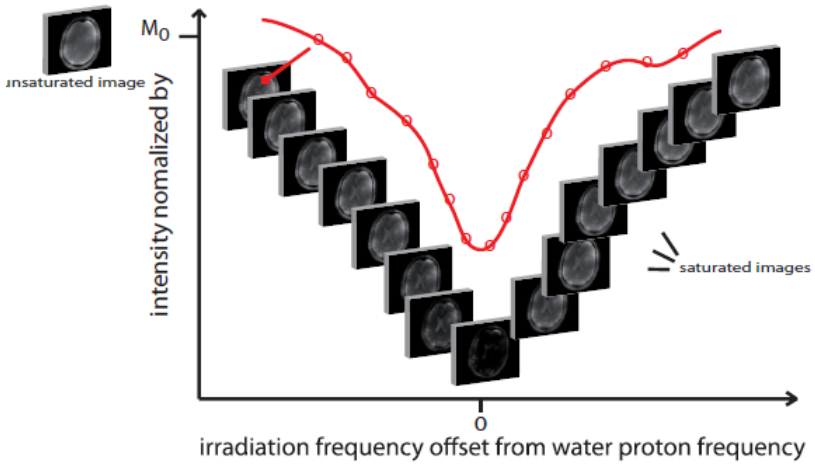


Figure 2.4: Acquisition of a full Z-spectrum is achieved by the application of a saturating RF pulse at multiple resonant frequencies. Image taken from [242]

Figure 2.4 describes the dependence of the measured signal from the irradiating frequency and is called the Z-spectrum. The Y axis describes the measured signal, while the X axis represents the irradiating frequency, ω (in Hz or ppm). The Z-spectrum provides information on the total magnetisation transfer processes that occur and cannot selectively describe only one of them. In addition, the nature of the magnetisation transfer process, and therefore the shape of the Z-spectrum, can not only be affected by factors like pH, temperature and ionic composition [55] (sample parameters) but also by experimental parameters (type of saturation pulse, saturation duration, RF amplitude, number of pre-pulses, and duty cycle) [99] as will be explained in later sections.

The collapse of the measured signal at the centre of the spectrum (0 ppm) corresponds to direct water saturation. This is the dominant peak of the spectrum and often complicates the detection of proton groups resonating within a range of ± 1 ppm from the saturated water peak. As the CEST experiment probes molecular targets in a frequency-specific manner, any other molecular species having exchangeable protons will also appear, on the Z-spectrum, as distinct peaks at their specific resonant frequency. An example showing the amide (-NH) resonant peak in the Z-spectrum is

presented in Figure 2.5. Depending on the sample composition, other peaks can also be present on the Z-spectrum. These peaks arise from hydroxyl or amine proton carrying compounds. Finally, underlying dipolar relaxation transfer mechanisms such as magnetisation transfer or Nuclear Overhauser Effect can also affect the shape of the Z-spectrum and complicate the detection of the molecular compounds of interest.

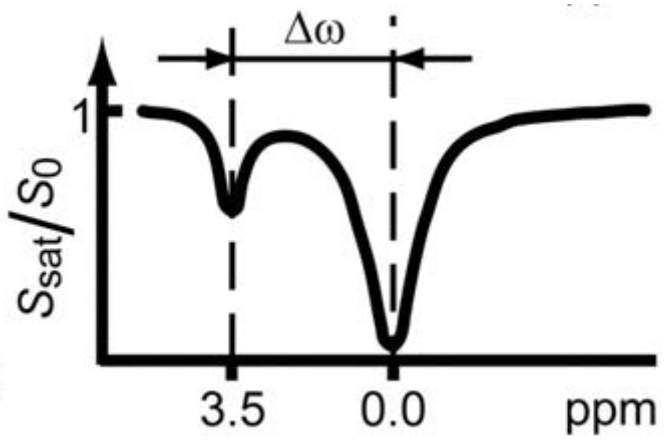


Figure 2.5: Z-spectrum showing the amide resonance peak at +3.5 ppm from the water peak (0 ppm). Image taken from [208].

The Z-spectrum resembles the spectrum acquired by conventional proton spectroscopy. It is however, shifted by 4.7 ppm relative to the scaled used in proton MRS. Water exchange (WEX) experiments have been used for the confirmation of macromolecular peaks, such as the ones arising from amides [209]. These experiments are exactly the opposite of a conventional magnetisation transfer experiment. The difference lies in the fact that, in a WEX experiment the free water protons are selectively saturated, instead of the bound ones. Then the magnetisation diffuses, from the free water to the bound one, following intra and intermolecular pathways, as well as chemical exchange. An example proton spectra derived from such experiments is presented Figure 2.6.

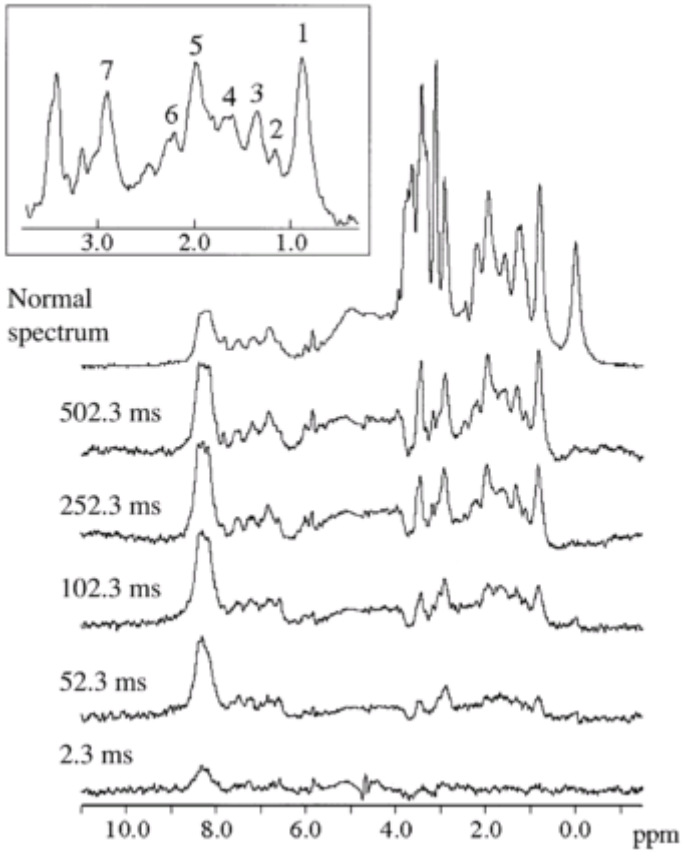


Figure 2.6: WEX spectra for perfused RIF-1 cancer cells for different mixing times (time allowed for the magnetisation to diffuse before the imaging sequence is applied). The inset image is just the aliphatic region, enlarged. Similar spectra have been obtained for a rat brain study as well. Image taken from [209].

The composite resonance in the proton spectrum which is centred at 8.3 ppm (from ~ 7.8 - 8.8 p.p.m) has been attributed to mobile macromolecular amide protons [209] as it is narrow (immobile macromolecules have broad line-shape) and arises from molecules having proton exchange rates within the range of 10-40 Hz [121]. In a CEST experiment, the amide resonant peak at +3.5 ppm corresponds to the to the peak measured at 8.3 ppm in the WEX proton spectroscopy.

2.1.1.6 Conditions for detecting chemical exchange.

Let's examine now the conditions under which the exchange of magnetisation between two pools of protons can be detected by an NMR experiment. Generally, what is desir-

able is that there is adequate chemical shift ($\Delta\Omega$) between the two pools, in order for them to be distinguishable and also possible to be irradiated without overlaps. This chemical shift should be greater than the proton exchange rate, k (s^{-1}), in order for the system to be in the slow proton exchange scheme. If this is the case, then in the acquired spectrum, a peak from each pool can be identified. If the proton exchange between the two pools is fast ($k>\Delta\Omega$) then the two pools cannot be distinguished. Therefore, only one peak is visible on the spectrum. Finally, if $k\sim\Delta\Omega$ and the two pools are not adequately separated then the result is a broad peak on the acquired spectrum (intermediate exchange). Obviously, only the first case, of slow exchange (Figure 2.7), is of interest in CEST applications because only then there is clear influence of the bound pool to the free water signal. In addition, the exchange rate, k, should be greater than the relaxation rate e.g. $1/T_1$, otherwise the magnetisation will decay in time T_1 without being transferred first. Consequently, the conditions under which a CEST experiment is performed should include both $k<\Delta\Omega$ and at the same time $k>1/T_1$.

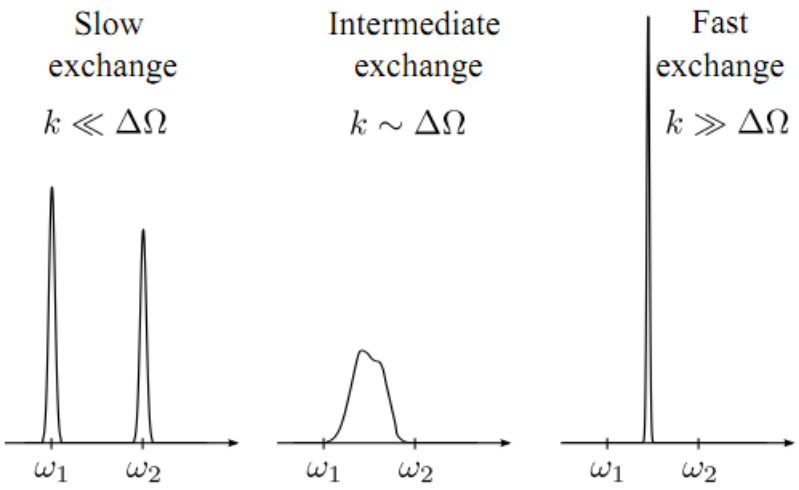


Figure 2.7: The three cases of the two proton exchanging pools. Only the first one is of interest for CEST experiments. An additional condition is that the exchange rate should be greater than the relaxation rate in order for any magnetisation to be transferred. Image taken from [144].

2.1.1.7 Saturation transfer in tissue

Owning to the intrinsic complex compartmentalisation and structure of tissues, saturation transfer experiments in-vivo are complicated by simultaneous underlying magnetisation exchange mechanisms. Protons can be found outside, around the protein, in various water hydration layers, but also 'buried' inside the protein (internal water molecules). In addition, a protein can contain other proton carrying compounds like hydroxyl, amines, amides that can exchange protons with bulk water.

Dipolar cross relaxation (MT, NOE) and physical proton exchange are the possible magnetisation transfer pathways that have been described in-vitro, by measuring the relaxation dispersion of ^{1}H, ^{2}H and ^{17}O nuclei. In short, these experiments have measured the variation of the relaxation rates of the previous nuclei with varying magnetic field strength (or frequency). Fitting of the acquired data then provided quantitative information about the various parameters of relaxation dispersion equations that describe the observed relaxation [152][230][104][103][27][26][215][105].

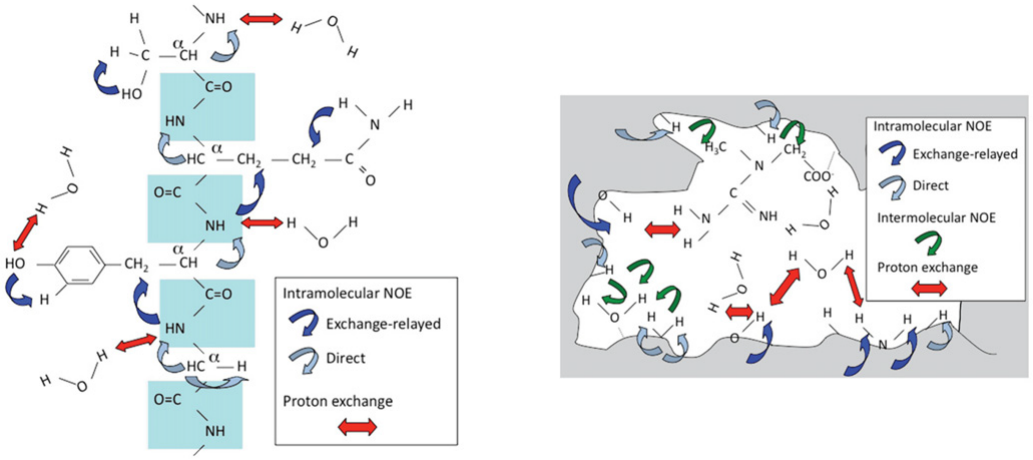


Figure 2.8: Potential pathways of magnetisation transfer/chemical exchange in a typical off-resonance irradiation experiment. **Left:** chemical exchange (red) and dipolar relaxation, NOE (blue), in mobile proteins **Right:** Both intermolecular and intramolecular NOE along with chemical exchange contribute to the magnetisation pathways in semi-solid proteins. The latter pathways make up of what is known as magnetisation transfer (MT). Image taken from [208].

The main conclusions of the previous studies were that in the magnetisation transfer processes the internal water molecules and the labile protein protons play the most important role. Moreover, water molecules from the hydration layer, around the protein, were found to be highly mobile. This renders the chemical exchange with free water inefficient and therefore this mechanism is thought of minimum importance. A summary of the potential pathways of magnetisation transfer/chemical exchange is presented in Figure 2.8.

In-vivo all three magnetisation transfer pathways (MT, NOE, CEST) are simultaneously present (Figure 2.9).

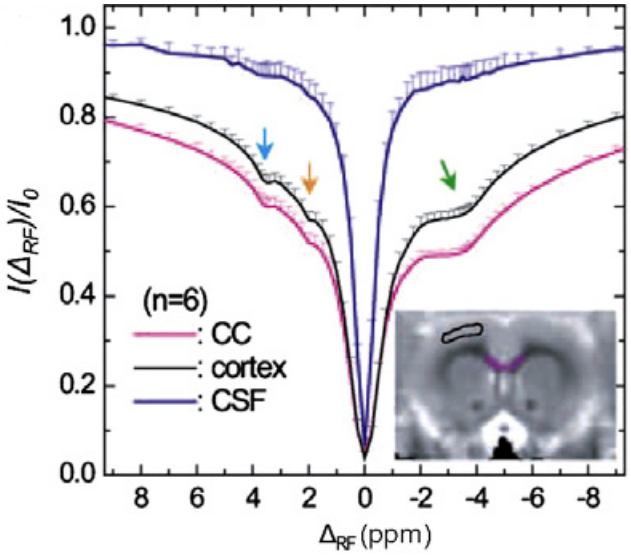


Figure 2.9: Z-spectra obtained in corpus callosum (CC), cortex and cerebrospinal fluid. The two exchange peaks at the positive offsets correspond to chemical exchange, while the peak at the negative offsets to NOE. The effect of MT isd indicated as an overall down-shift of the spectrum for the CC and the cortex. Image taken from [84].

In fact, MT always accompany CEST in-vivo [116]. MT originates from semi-solid components, having short T_2 times, via cross relaxation and chemical exchange processes. The very broad line-shape of such immobile macromolecules (~ kHz) leads to an overall down-shift of the Z-spectrum as the saturation is transferred to bulk water (Figure 2.9). NOE and CEST, on the other hand, have a more frequency specific effect on the Z-spectrum as their presence is indicated by specific resonant peaks. CEST

effects appear on the positive side [264], while NOE effects appear on the negative side of the Z-spectrum [122]. NOE effects arise from macromolecules containing -CH and -CH_2 groups and and might overlap with lipid artefacts also present at the negative side of he Z-spectrum [189]. CEST effects are caused by labile protons of exchangeable groups such as amides, amines and hydroxyl. The magnitude of the effect depends mainly on the concentration of the metabolite protons relative to bulk water protons and the pH and temperature dependent proton exchange rate, k, [264]. Various endogenous macromolecules have been used for in-vivo CEST experiments including macromolecular amides [264, 266], creatine [108], glucose [12], glutamate [10], myo-inositol [61] and s (GAG) [60]. A more detailed overview of the clinical applications is presented in a following section.

2.2 CEST: optimisation techniques

2.2.1 Bloch equations

2.2.1.1 Two pool model (water - solute with one exchange proton group)

The time dependent Bloch equations in the two-pool exchange model for CEST are given by [228]:

$$\begin{aligned}
\frac{dM_x^a}{dt} =& \Delta\omega_a M_y^a(t) - R_2^a M_x^a(t) - k_a M_x^a(t) + k_b M_x^b(t) \\
\frac{dM_x^b}{dt} =& \Delta\omega_b M_y^b(t) - R_2^b M_x^b(t) - k_b M_x^b(t) + k_a M_x^a(t) \\
\frac{dM_y^a}{dt} =& -\Delta\omega_a M_x^a(t) - R_2^a M_y^a(t) - k_a M_y^a(t) + k_b M_y^b(t) + \omega_1 M_z^a(t) \\
\frac{dM_y^b}{dt} =& -\Delta\omega_b M_x^b(t) - R_2^b M_y^b(t) - k_b M_y^b(t) + k_a M_y^a(t) + \omega_1 M_z^b(t) \\
\frac{dM_z^a}{dt} =& -\omega_1 M_y^a(t) - R_1^a [M_z^a(t) - M_0^a] - k_a M_z^a(t) + k_b M_z^b(t) \\
\frac{dM_z^b}{dt} =& -\omega_1 M_y^b(t) - R_1^b [M_z^b(t) - M_0^b] - k_b M_z^b(t) + k_a M_z^a(t)
\end{aligned} \tag{2.2.1}$$

In 2.2.1, the subscripts a and b, refer to the two exchanging proton pools. In this case, bulk water (a) and solute (b). For example, $M_x^a(t)$ denotes the x component of the magnetisation in bulk water at time t. k_a and k_b refer to the exchange rates from pool a to b and from b to a respectively. These rates are measured in s^{-1}. M_0^a and M_0^b denote the thermal equilibrium magnetisation of each pool. $\Delta\omega_a$ and $\Delta\omega_b$ are calculated as ω_a- ω and ω_b- ω respectively, where ω_a and ω_b are the resonant frequencies of pools a and b respectively. Finally, ω, is the frequency of the RF irradiation and $\omega_1$the RF pulse power.

2.2.1.2 Three pool model (water - solute with two exchange proton groups)

The time dependent Bloch equations in the three-pool exchange model for CEST are given by [228]:

$$\begin{aligned}
\frac{dM_x^a}{dt} &= -(\omega_a - \omega)M_y^a - k_{2a}M_x^a + C_b M_x^b + C_c M_c^x \\
\frac{dM_x^b}{dt} &= -(\omega_b - \omega)M_y^b - k_{2b}M_x^b + C_{ab}M_x^a \\
\frac{dM_x^c}{dt} &= -(\omega_c - \omega)M_y^c - k_{2c}M_x^c + C_{ac}M_x^a \\
\frac{dM_y^a}{dt} &= (\omega_a - \omega)M_x^a - k_{2a}M_y^a + C_b M_y^b + C_c M_c^c - \omega_1 M_z^a \\
\frac{dM_y^b}{dt} &= (\omega_b - \omega)M_x^b - k_{2b}M_y^b + C_{ab}M_y^a - \omega_1 M_z^b \\
\frac{dM_y^c}{dt} &= (\omega_c - \omega)M_x^c - k_{2c}M_y^c + C_{ac}M_y^a - \omega_1 M_z^c \\
\frac{dM_z^a}{dt} &= \frac{M_0^a}{T_{1a}} - k_{1a}M_z^a + C_b M_z^b + C_c M_z^c + \omega_1 M_y^a \\
\frac{dM_z^b}{dt} &= \frac{M_0^b}{T_{1b}} - k_{1b}M_z^b + C_{ab}M_z^a + \omega_1 M_y^b \\
\frac{dM_z^c}{dt} &= \frac{M_0^c}{T_{1c}} - k_{1c}M_z^c + C_{ac}M_z^a + \omega_1 M_y^c
\end{aligned} \tag{2.2.2}$$

As before the subscripts a (bulk water), b and c denote each proton pool. Furthermore,

$$k_{1a} = \frac{1}{T_{1a}} + C_a$$
$$k_{2a} = \frac{1}{T_{2a}} + C_a$$
$$C_{ab} = (\frac{M_0^b}{M_0^a})C_b$$
$$C_{ac} = (\frac{M_0^c}{M_0^a})C_c$$
$$C_a = C_{ab} + C_{ac}$$

where:

$T_{1a,2a}$: the relaxation times of pool A

ω_a : the resonant frequency of pool A

C_a : the transition rate of spins leaving pool A

C_{ab} :the transition rate of pool A protons in leaving pool A and entering pool B

C_{ac} :the transition rate of pool A protons in leaving pool A and entering pool C.

Similar definitions apply for pools B and C.

We note here that this model does not take into account the proton exchange between pools B and C.

2.2.1.3 Three pool model (water - solute in the presence of MT)

Based on the model described in the previous paragraph Desmond et al. [29] have described a three pool model involving bulk water, a CEST pool and an MT pool. In the time dependent Bloch equations, only the longitudinal component of the MT pool was take into account as it was assumed that the net transverse dipole-dipole interaction was negligible. The MT term also included the RF absorption profile of the semi-solid component as a Lorentzian line-shape [160]. For semi-solid structures in living tissue a super-Lorentzian line-shape defined as:

$$g(2\pi\Delta) = \int_0^{\pi/2} d\theta sin\theta \sqrt{\frac{2}{\pi}} \frac{T_{2c}}{|3cos^2\theta - 1|} exp[-2(\frac{2\pi\Delta T_{2c}}{|3cos^2\theta - 1|})^2] \quad (2.2.3)$$

has also been used [248].

2.2.1.4 Multi-pool systems

In the case of many interacting proton pools, more complicated models have to be used in order to describe the various magnetisation transfer pathways. This is especially important for in-vivo studies, where the signal from the macromolecules of interest is contaminated by the presence of underlying MT and NOE effects. What is more, when the exchange between different CEST pools in not negligible then the Bloch equations have to be appropriately modified.

A four pool model similar to what was described in the previous sections has been reported by Li et al. [115]. The pools that were modelled include bulk water, macromolecular MT and two proton exchange sites on a PARA-CEST agent. The MT line-shape was modelled as being a super-Lorentzian (2.2.3).

As expanding the Bloch equations to describe multi-pool systems is tedious, Sun et al. [183] proposed a simplified and scalable numerical solution by modifying the classic two-pool model. Their approach was to replace the multi-pool system with a number of two-pool systems and correcting for the simplistic linear superposition of the CEST effects. From [183] the multi-pool CEST MRI contrast was shown to be:

$$CESTR(\omega_1, \Delta\omega) = \sum_i CESTR_i(\omega_1, \Delta\omega_{si}) - \sum_{i>j} [CESTR_i(\omega_1, \Delta\omega_{si}) CESTR_j(\omega_1, \Delta\omega_{sj}) * (2 - CESTR_i(\omega_1, \Delta\omega_{si}) - CESTR_j(\omega_1, \Delta\omega_{sj}))]$$

where

CESTR($\omega_1, \Delta\omega_s$): the magnetisation transfer ratio of the solute minus the magnetisation transfer ratio of bulk water (direct water saturation).

An alternative but also simple and fast method was proposed by Murase [97]. In this case the Bloch equations were first reduced to a homogeneous linear differential equation and then the numerical solution for the ($R_{1\rho}$) and transverse relaxation rate in the rotating frame ($R_{2\rho}$) was calculated using a matrix operation and Kronecker tensor product. The model was used to describe various pool configurations as summarised in the following figure (Figure 2.10).

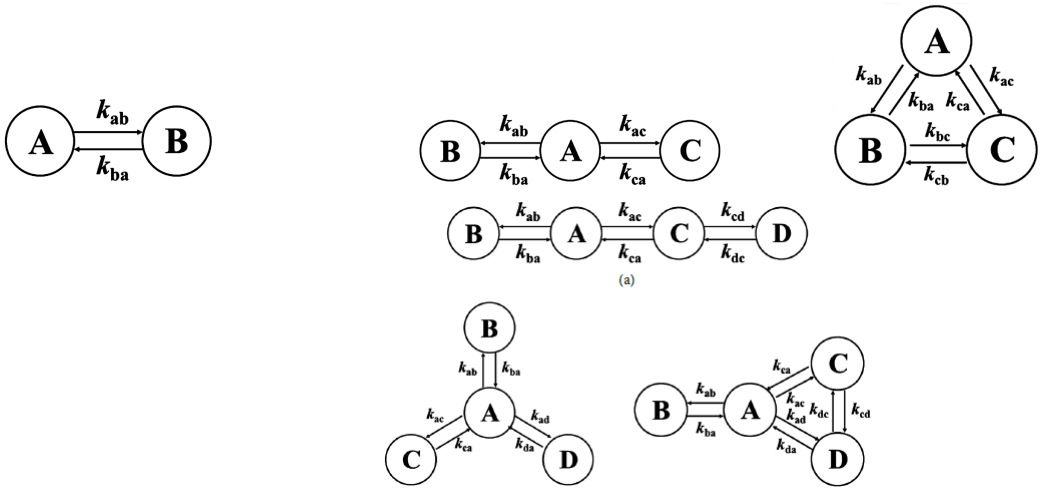


Figure 2.10: Two, three and four-pool systems that can be described by the numerical solution of the Bloch equations as proposed by [97]. $k_{ij}$is the proton exchange rate between the pools. Arrows also denote the direction of the exchange. Image taken from [97].

2.2.1.5 Numerical solutions

For simulating the CEST effects, the time dependent Bloch equations can be numerically solved by either using the Runge Kutta approximation [228] (ode45 in Matlab) or the matrix exponential (expm in Matlab) [146].

The following simulations of various proton exchanging systems have been performed using the latter and the procedure described in [146]. The matrix A for the two and three pool system is given in the Appendix A.

In its most simple case a CEST experiment aims to indirectly measure the signal from a milli-molar concentrated macromolecular species via the dominant water signal. Amides on mobile endogenous proteins have a resonant frequency of +3.5 ppm from water and are of interest in brain pathologies such as ischaemia [120] and cancer [267, 266]. In the case of two proton exchanging pools the amide CEST effect depends on the RF irradiation power, exchange rate and concentration.

Figure 2.11 shows the dependence of the amide Z-spectrum on the RF irradiation power. As will be explained in later sections, the saturation efficiency of exchangeable protons reaches a plateau at a certain pulse power and further power increase leads to spill-over effects reducing the CEST effect. For this two pool system, a low saturation of 0.5μT yields the highest CEST effect.

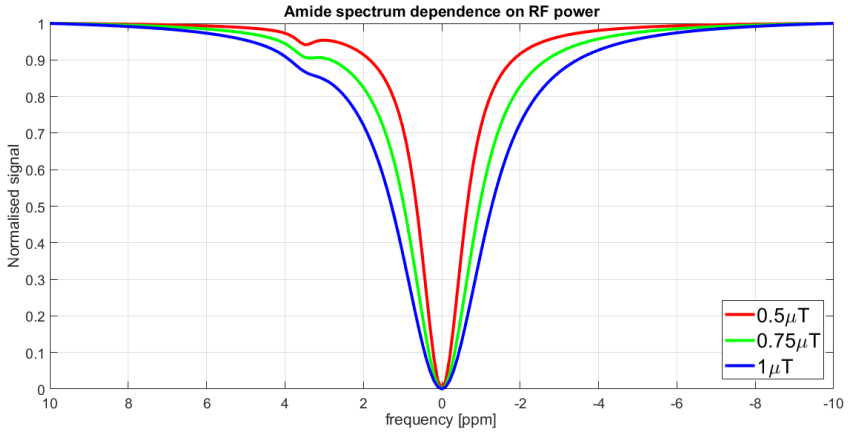


Figure 2.11: Simulation of a two pool system containing bulk water and amides. The system is more efficiently saturated at low RF power. The parameters of the simulation are listed in Appendix B.

Section 2.1.1.6 introduced the condition of slow exchange ($k \ll \Delta\omega$) as a mandatory requirement for CEST. As it can be seen in Figure 2.12, the simulated system satisfies this condition up until an exchange rate of ~200 s^{-1}. Further increases of the exchange rate do not correspond in higher CEST effect, as the spectral peaks of the two pools start to overlap and therefore cannot be adequately distinguished.

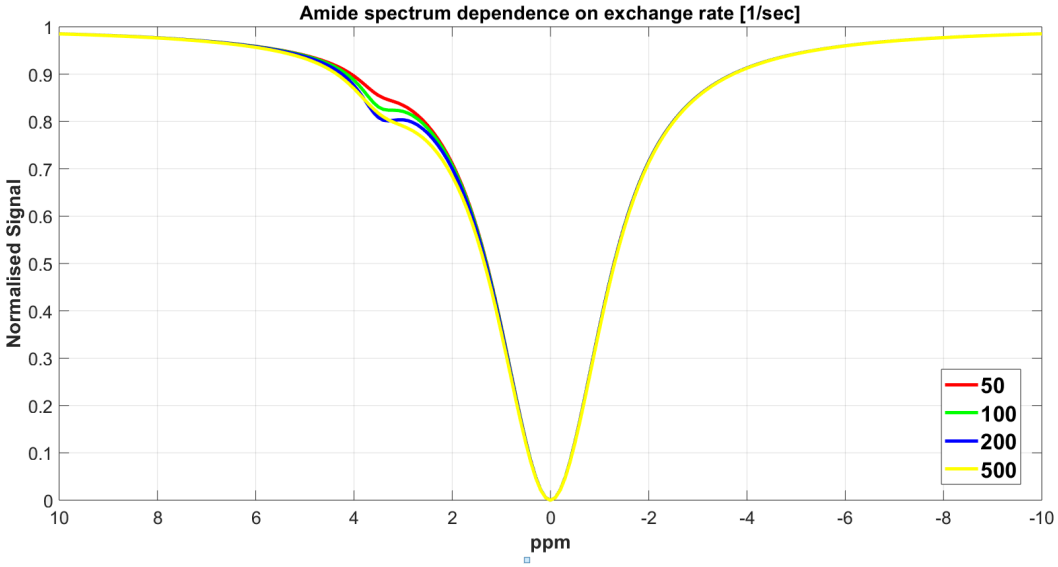


Figure 2.12: Simulation of a two pool system containing bulk water and amides. The CEST effect increases with increasing exchange rate. The parameters of the simulation are listed in Appendix B.

Figure 2.13 shows the dependence of the amide Z-spectrum on the amide proton concentration. Even though such a concentration might be unrealistic in-vivo, the graph clearly demonstrates that the higher the macromolecular concentration the higher the CEST effect.

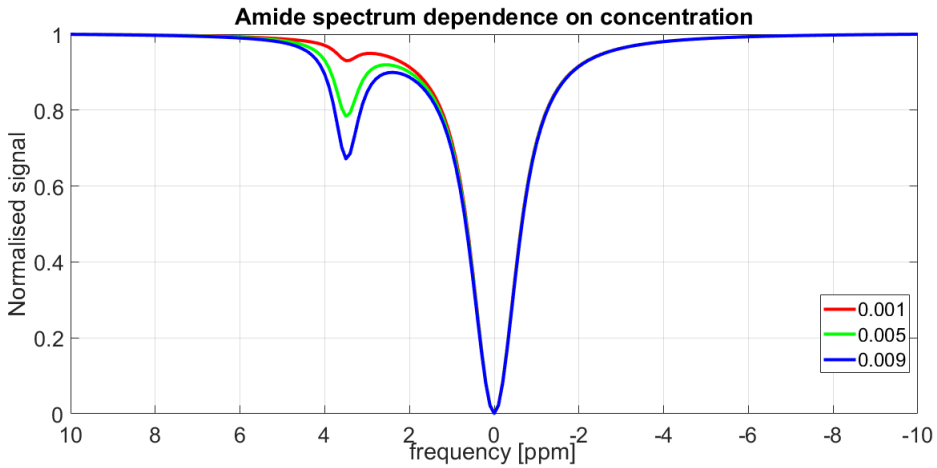


Figure 2.13: Simulation of a two pool system containing bulk water and amides. The CEST effect increases with increasing amide concentration. The parameters of the simulation are listed in Appendix B

For the simulation of a three-pool system, the matrix A of the matrix exponential solution[146] of the Bloch equations is given in Appendix A. This system comprises of bulk water and two pools with resonant frequencies at +4.2 ppm and +5.5 ppm. The exchange between the two proton pools is considered negligible in this simulation.

Figure 2.14 shows that only at low (~1μT) RF pulse power both peaks are detected. Strong saturation allows for spillover effects, resulting in the efficient saturation of the distant (from water) resonant peak.

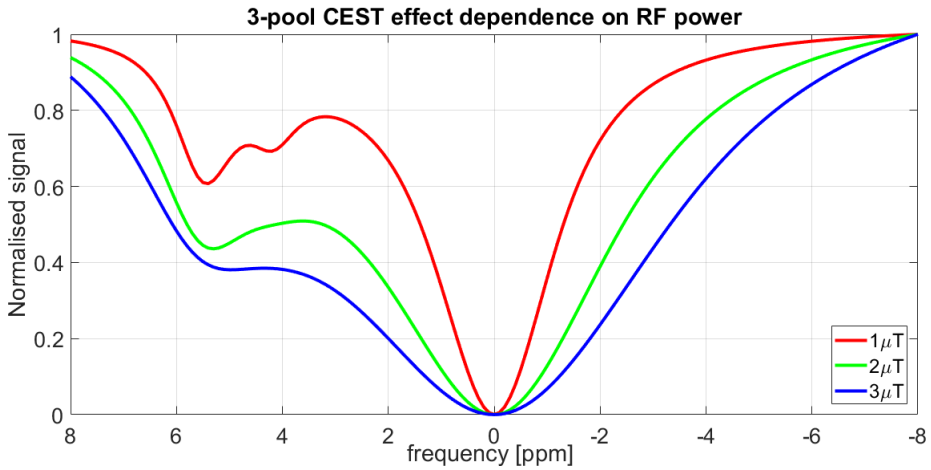


Figure 2.14: Simulation of a three pool system containing bulk water and two additional proton exchanging pools. RF spillover effects prevent the detection of the +4.2 ppm for RF power more than 2μT. The parameters of the simulation are listed in Appendix B.

An increase in the exchange rate has an opposite effect on the CEST contrast of the two proton pools (Figure 2.15). The +4.2 ppm peak gets amplified, while the +5.5 ppm peak is diminished. Taking into account that he simulation was performed under the assumption that the +5.5 ppm pool (pool C) has a six times higher exchange rate than the +4.2 ppm peak (pool B) and that the main field was chosen to be 3T, then the corresponding chemical shifts for pool C and B were ~ 700 Hz and ~530 Hz. As the exchange rate is gradually increased from 50 - 100 -150 s^{-1}, pool B continuously satisfies the slow exchange condition of [exchange rate << chemical shift]. On the other hand, the exchange rates of pool C violate the latter condition as they become far greater than the 700 Hz chemical shift. Consequently, the CEST effect of pool C is

vanished from the spectrum.

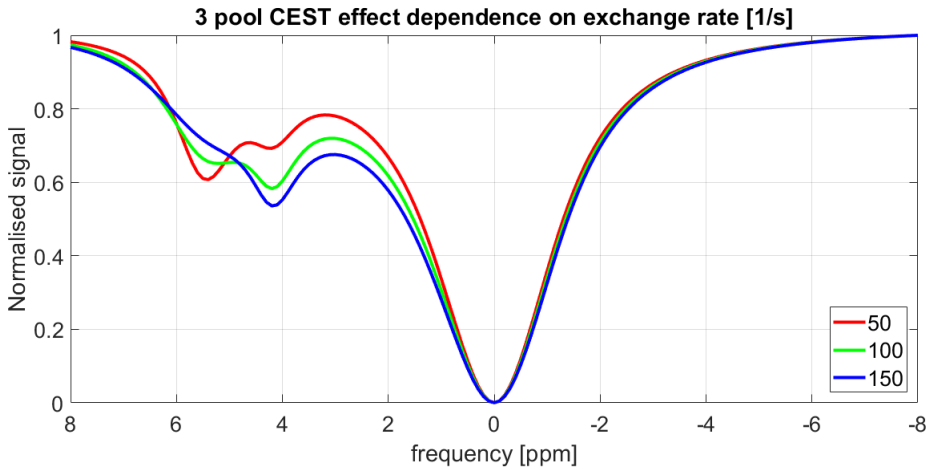


Figure 2.15: Simulation of a three pool system containing bulk water and two additional proton exchanging pools. As the exchange rate is increased the peak at +5.5 ppm violates the slow exchange condition. Thus its CEST effect vanishes. The parameters of the simulation are listed in Appendix B.

Finally, an increase in the concentration of the proton exchanging pools will lead to a similar amplification of the CEST effect of both peaks. This result similar to the one shown for the two-pool system (Figure 2.13) and is therefore omitted from this discussion.

We conclude this section by showing the influence of semi-solid MT on the Z-spectrum. A three pool model including bulk water, amides and a semi-solid component (MT) was used similar to [29]. The MT line-shape incorporated into the Bloch equations was chosen to be super-Lorentzian (2.2.3). The numerical solution was calculated using again the matrix exponential [146].

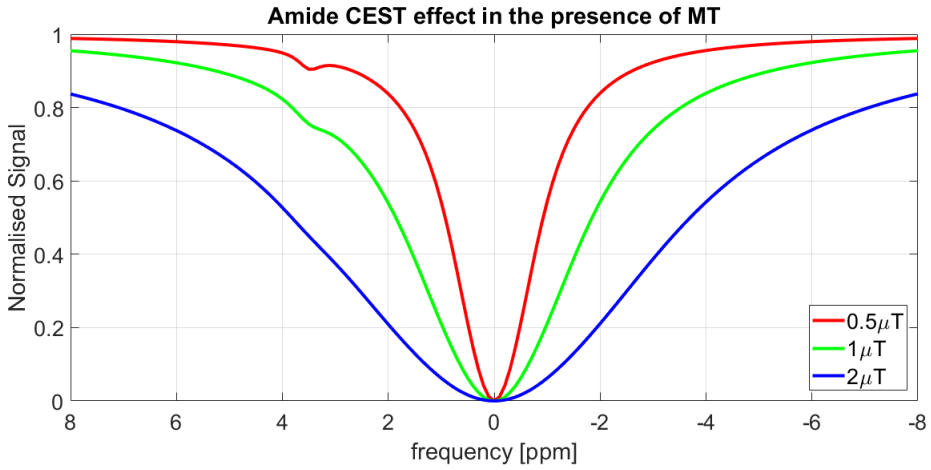


Figure 2.16: Simulation of a three pool model including bulk water, amides and a semi-solid component. The effect of the MT is evident as an overall downward shift of the Z-spectrum. This shift is more pronounced at hight RF pulse powers.The parameters of the simulation are listed in Appendix B

As it can be seen in Figure 2.16, the higher the RF power used the more pronounced the effect of the MT is. As a competing mechanism, MT always accompanies CEST, in-vivo, complicating the detection of the latter. Experimental and post processing methods used for the separation of the two competing effects will be discussed in later sections.

2.2.1.6 Pulsed CEST

The previous simulation examples were performed for a continuous RF B_1 power. Continuous-wave CEST however, cannot be used clinically due to the SAR restrictions. In this case, pulsed CEST can be implemented to study saturation transfer effects in-vivo.

Simulating pulsed-CEST only requires the discretisation of the RF pulse. In other words, the constant B_1 power is replaced by a time varying amplitude. For example from [197] the time varying B_1 amplitude can be modelled as:

$$B_1(i)_{|i=1:N} = \frac{\phi}{\gamma} \frac{\exp(-(i\frac{\tau_p}{N} - \frac{\tau_p}{2})^2/c^2)}{\sum_{i=1:N} \exp(-(i\frac{\tau_p}{N} - \frac{\tau_p}{2})^2/c^2)\frac{\tau_p}{N}}$$

where

ϕ: the RF pulse flip angle

N: the discretisation steps of the RF pulse

$c = \frac{\tau_p}{2\sqrt{-\ln(tl)}}$, with tl the truncation level

To solve the time dependent Bloch equations, Xiao et al. [234] have proposed an iterative matrix algorithm for a fast numerical solution of pulsed CEST experiments. For a two pool system (bulk water and amides) and using a discrete Gaussian pulse (number of steps = 64) and 15 ms duration the Z-spectra for various RF flip angles is presented in Figure 2.17.

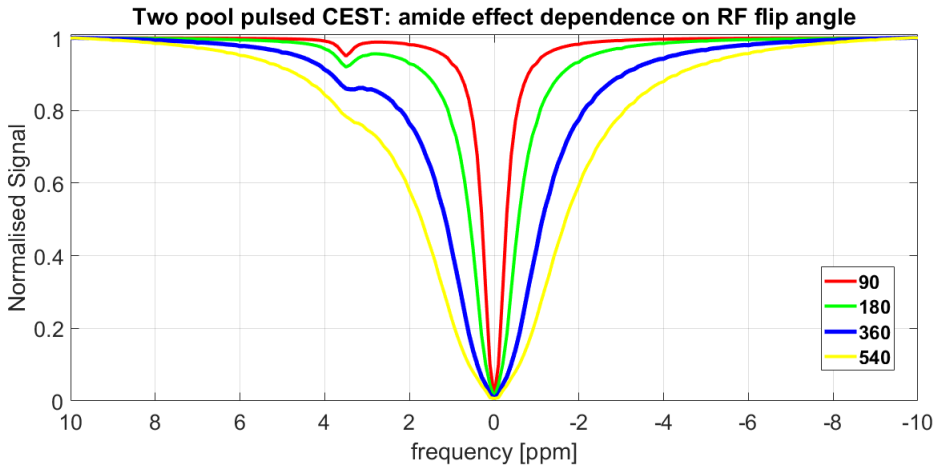


Figure 2.17: Pulsed CEST simulation for a two-pool system (bulk water, amides). The optimal flip angle for the maximum CEST effect is between 180 and 360 degrees.The parameters of the simulation are listed in Appendix B.

The optimal flip angle for the maximum CEST effect is between 180 and 360 degrees as also shown in [197].

2.2.2 Quantifying CEST effects

2.2.2.1 Proton Transfer Ratio (PTR)

The analytical solution of the two-pool CEST model [265] yields the most straightforward CEST metric, termed proton transfer ratio (PTR):

$$PTR = \frac{k_{sw} a M_s^0}{(R_{1w} + k_{ws}) M_w^0} (1 - e^{-(R_{1w}+k_{ws})t_{sat}}) \tag{2.2.4}$$

where

k_{sw} : exchange rate of solute $\rightarrow$water

k_{ws} : exchange rate of water $\rightarrow$solute

M_s^0: thermal equilibrium magnetisation of solute

M_w^0: thermal equilibrium magnetisation of water

R_{1w} :the relaxation rate of water

$t_{sat:}$ the saturation time

a: the labelling efficiency, taking values between 0 and 1

2.2.2.2 Labelling efficiency

Labelling efficiency is a crucial parameter in CEST experiments. As reported by Woessner et al. [228], optimal labelling is achieved when the solute exchange rate matches the saturation pulse's frequency (k_{sw}= ω_1). Figure 2.18 shows the dependence of the labelling efficiency on the RF irradiation amplitude, main magnetic field and chemical shift. It can be seen that different proton exchanging groups have different labelling profiles. For amides, the optimal efficiency is achieved at ~ 1.5μT, whereas for amines at ~ 7μT. In general higher exchange rates require higher B_1 power for efficient saturation [188] [228]. However, as illustrated in Figure 2.18 (right), increasing B_1 also leads to broader peak width and subsequent overlap of the CEST effects.

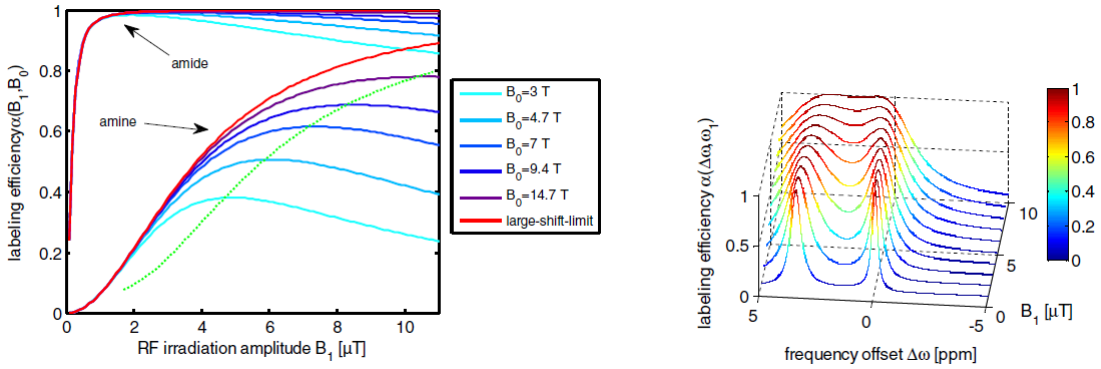


Figure 2.18: **Left:** Labelling efficiency dependence on irradiation power and magnetic field for amides and amines. **Right:** Labelling efficiency dependence on chemical shift and irradiation power amides. Images taken from [242].

Furthermore, as shown by Zaiss and Bachert [242], it's not only the labelling efficiency but also the spectral selectivity of a CEST experiment that strongly depends on B_1. By modelling the CEST effects having a Lorentzian line-shape of width Γ, the authors described three selectivity regimes: narrow, intermediate and broad [242] depending on the values of B_1. Higher B_1 values result in wider line-shapes reducing this way the spectral selectivity of the experiment. This is summarised in Figure 2.19. It can be seen that both the amide and amine line-widths increase with increasing B_1. The border indicates the separation between the narrow and intermediately selective regime (Figure 2.19, left). Increasing the labelling efficiency is also detrimental for selectivity as indicated in Figure 2.19, (right).



Figure 2.19: **Left:** The dependence of spectral line-width Γ, for amides and amines, on B_1 pulse power. **Right:** Relationship between labelling efficient and spectral line-width. Increasing the labelling efficiency is detrimental for selectivity. Images taken from [242].

2.2.2.3 Simplified PTR and asymmetry

Assuming instant labile proton saturation without any direct water saturation and negligible back exchange (a $\simeq$1, $k_{ws} \simeq 0$), equation 2.2.4 is simplified as:

$$PTR = k_{sw}\frac{[solute]}{[water]}T_{1w}(1 - e^{t_{sat}/T_{1w}}) \tag{2.2.5}$$

From equation 2.2.5 it can be concluded that PTR:

1. is directly proportional to the concentration of the solute
2. is directly proportional to the solute $\rightarrow$ water proton exchange rate, k_{sw}. This is valid as long as k_{sw} remains much smaller that the chemical shift of the solute proton pool
3. is increased as T_{1w} is increased .e.g higher magnetic fields

Direct measurement the proton transfer ratio (2.2.5) is not possible in-vivo, as the the presence of competing underlying mechanisms such as conventional MT and direct water saturation contaminates the measured signal. However, the CEST signal can be separated by any competing saturation transfer mechanisms by performing an asymmetry analysis [264, 263].

For solute protons undergoing slow to intermediate exchange, the CEST effect can be calculated as:

$$MTR_{asym}(\Delta\omega) = \frac{S_{sat}(-\Delta\omega) - S_{sat}(+\Delta\omega)}{S_0} \tag{2.2.6}$$

where

$S_{sat}(-\Delta\omega)$: the up-field measured signal

$S_{sat}(+\Delta\omega)$: the down-field measured signal

S_0: unsaturated signal

Equation 2.2.6 is valid in-vitro, where the conventional MT and direct water saturation effects are symmetric around the water resonance, thus cancelled out in the

calculation. However, in-vivo that might not be the case. As discussed by Hua et al. [76], the presence of conventional MT, within a ± 5 ppm range results in negative values of MTR_{asym}. Had the conventional MT being symmetric, then the MTR_{asym} would have been positive, as the down-field signal ($S_{sat}(\Delta\omega)$), is lower than the up-field, ($S_{sat}(-\Delta\omega)$), signal due the presence of amide proton groups. Even though, MTR_{asym}, will be contaminated by the conventional MT effects, it is still a useful metric to quantify the difference in CEST contrast between tissues, under the assumption that the MT effect is constant [192] [257, 263, 271].

An alternative definition of the MTR_{asym} given as:

$$MTR_{asym} = 1 - \frac{S_{sat}(\Delta\omega)}{S_{sat}(-\Delta\omega)} \tag{2.2.7}$$

has been used for the in-vivo quantification of the amide CEST effect at +2ppm [10]. In this case, the MTR_{asym} is normalised according to the signal contamination by the conventional MT and direct water saturation. Using this definition the calculated asymmetry is higher than the one calculated from 2.2.6 and is thought to be accurate in reporting on the CEST contrast within the same tissue.

2.2.2.4 Isolating CEST from MT and spillover effects

A post-processing, semi-quantitative method for isolating the CEST effects from conventional MT and direct water saturation involves the fitting of the experimental data with a number of Lorentzian [142] curves. Each curve has a unique amplitude, width and frequency offset [125, 120, 244, 90]. The idea here is to decompose the Z-spectrum to a number of separate components and then quantify the CEST effect by comparing the difference of the experimental data from the fitted Lorentzian curves [30]. An alternative approach to Lorentzian curve fitting, termed qCEST, involves a polynomial fitting procedure of the experimental Z-spectrum. The CEST effect is quantified again by calculating the difference between the original and fitted data [260]. Other met-

rics, based on the equivalency of CEST and spin locking include, the spillover and MT corrected inverse difference (MTR_{Rex}) [245] and the spillover, MT and T_1 corrected AREX contrast [246]. However, the later is only valid for systems driven to the steady state ($t_{sat} > T_{1w}$) or at the very least $t_{sat} \approx T_{1w}$. Finally, the APT contribution can be isolated, from fitting the 2-pool conventional magnetisation transfer model [160], to acquired data, and then subtracting the fitted curve from the data or a simulated 3-pool model [67, 69, 68].

Additional approaches involve the use of special irradiation schemes that generate images insensitive to the conventional MT, direct water saturation and B_0 inhomogeneities. For example, SAFARI [167], utilises a two frequency irradiation scheme by the application of an alternating frequency pulse train, whereas in LOVARS [234], a variation of the experimental parameters during the acquisition determines the magnitude of the various saturation transfer processes. Both techniques have be demonstrated in-vivo. However, in the former approach, the generated images suffer from low SNR, while the maps produced by latter technique are less sensitive to the CEST proton concentration and exchange rate, as compared with the conventional MTR_{asym} generated maps. A simpler method involving a three offset measurement (at the CEST peak's resonant frequency and its two boundaries) was also demonstrated in-vivo at 9.4T. This method does not require any special pulse sequences modifications. It relies strongly however on the clear delineation of the CEST peaks [85].

2.2.2.5 Calculating the proton exchange rate, k_{sw}

The proton exchange rate, k_{sw}, can be calculated by utilising the dependence of the PTR (equation 2.2.4) on the saturation time and B_1 power by measuring the CEST signal while varying the latter two parameters. k_{sw} can then me calculated by fitting the data to numerical or analytical solutions of the Bloch equations. A separate experiments is also required in order to determine the longitudinal relaxation time of water, also present in 2.2.4. This method of determining k_{sw} is termed QUEST or QUESP

depending on whether the saturation time or pulse power is the parameter of experimental variation [137]. This method is limited by the need to somehow determine the solute concentration and the severe implications of not carefully chosen fitted parameters. An extension of the latter method, aiming to reduce the dependence of the quality of the fit on experimental parameters (T_1,T_2, B_1) was reported in [185]. It is a ratio-metric method that normalises the magnetization transfer ratio at the labile and reference frequencies, eliminating this way the confounding relaxation and RF spillover effects.

In the omega-plot approach, the steady state water magnetisation is plotted against $\frac{1}{w_1^2}$, with the x intercept of the plot being equal to $-\frac{1}{k_{sw}^2}$ [32]. This is a concentration independent method but not clinically useful as it is only valid under the assumption of negligible MT and direct water saturation contamination. A more clinically relevant approach was reported in [276]. In this study, the exchange rate k_{sw} was successfully separated from being dependent on the solute concentration and the $T_{1,2}$ relaxation times. In this ratio-metric method, the CEST signal was shown as having an oscillating [~cos(θ)] component, where θ is the pre-saturation pulse's flip angle. This oscillating component was shown via numerical simulations to be dependent only on k_{sw}. Furthermore, the technique was demonstrated for pulsed saturation and therefore might be useful in clinical applications, where the use of continuous wave acquisitions is limited.

2.2.3 CEST effect dependence on experimental variables

CEST experiments require careful experimental considerations, as the measured CEST signal depends, not only on the CEST agent specific properties (concentration, exchange rate, relaxation rate), but also, on a number of experimental variables including, the RF pulse power/flip angle, type of pre-saturation (continuous or pulsed) and magnetic field strength. The CEST effect dependence on the agent's concentration and its exchange rate was previously described in section 2.2.1.5, for two and three

pool models. In the following sections the effect's dependence on other experimental parameters is briefly discussed.

2.2.3.1 Water relaxation times

CEST effect strongly depends on the T_{1w} due to the fact that efficient saturation transfer (from solute $\rightarrow$ water) is counterbalanced by the water longitudinal relaxation time. Low T_{1w} times are detrimental for sufficient CEST signal generation [222].

Similarly, a low T_{2w} means a wider water spectral line-shape width. As CEST is a frequency specific technique, a clear spectral peak separation is required for a successful identification of proton exchanging compounds. Thus, a low T_{2w} time increases the spill-over effects on the measured signal [188].

2.2.3.2 Magnetic field strength

As shown in Figure 2.20, the CEST effect is more pronounced at higher fields. This is because of the prolonged T_{1w} times and wider chemical shifts induced by an increasing magnetic field. The only downside of measuring the CEST effect on a high field is the increased SAR of the RF pulses (SAR ~ square of the field strength).

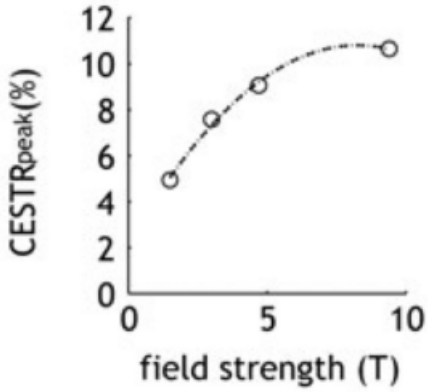


Figure 2.20: CEST contrast dependence on magnetic field strength. The effect is more pronounced at higher fields. Image taken from[99].

2.2.3.3 B_1 power

Weak RF pulse power results in a weak CEST signal, while strong RF pulse power results in non-negligible spill-over effects, detrimental for the detection of a CEST signal. An empirical solution for the optimal RF pulse power is reported in [188] and [99]. In general, the CEST contrast increases with B_1, reaches a plateau, and finally diminishes due to saturation spill-over effects. The optimal RF power depends on the proton exchange rate, chemical shift and magnetic field strength. Higher exchange rates require stronger RF pulses for efficient saturation [228]. In addition, the optimal RF pulse power is higher for stronger magnetic fields and higher chemical shifts (Figure 2.21). Low RF pulse power has also been shown to decrease conventional MT and direct water saturation effects [89].

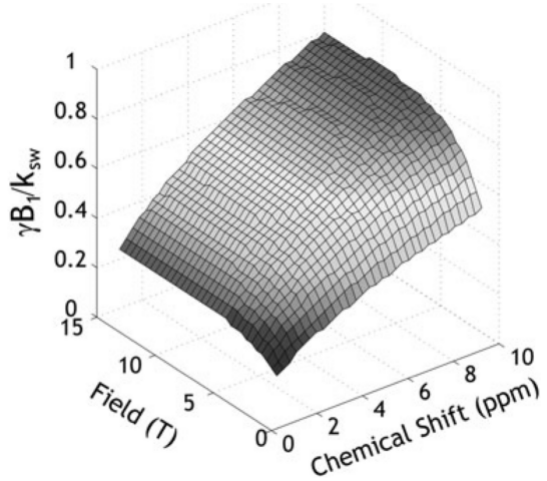


Figure 2.21: Exchange rate normalised B_1 power as a function of chemical shift and magnetic field strength. Image taken from [99].

2.2.3.4 Pulsed CEST

Even thought continuous wave CEST (CW-CEST) has a more straightforward theoretical and experimental implementation, its use clinically is limited by safety concerns over the absorbed RF power. In this case, pulsed CEST can be implemented without any significant compromises on the generated CEST signal. In pulsed CEST, the saturation pulse's amplitude is time varying, as opposed to CW-CEST. Furthermore, in

order to reduce the SAR absorption, a train of short in duration pulses is implemented instead of a long continuous pulse.

Optimising pulsed CEST involves a few extra considerations as opposed to CW-CEST [197] [49] [193] [275]. For example, the RF pulse shape, flip angle and duty cycle need to be taken into account during optimisation. Luckily, at least one parameter, namely the pulsed RF irradiation power, can directly be inferred from a continuous wave scheme [197, 193], for exchange rates up to 50 s^{-1}. In this case the, RF amplitudes of the pulsed and continuous scheme are linearly related and the pulsed CEST contrast is approximately 95% of the CW-CEST contrast. Alternatively, by using an analytical solution for CW-CEST, two parameters, namely, average irradiation power ($B^2_{\text{avg power}}$) and mean irradiation field ($B_{\text{avg field}}$) can be used to relate the CW-CEST to the pulsed CEST RF power [274]. It was concluded that the former is a more meaningful metric for pulsed CEST, as it is independent from the pulse's flip angle and the implemented duty cycle (Figure 2.22).

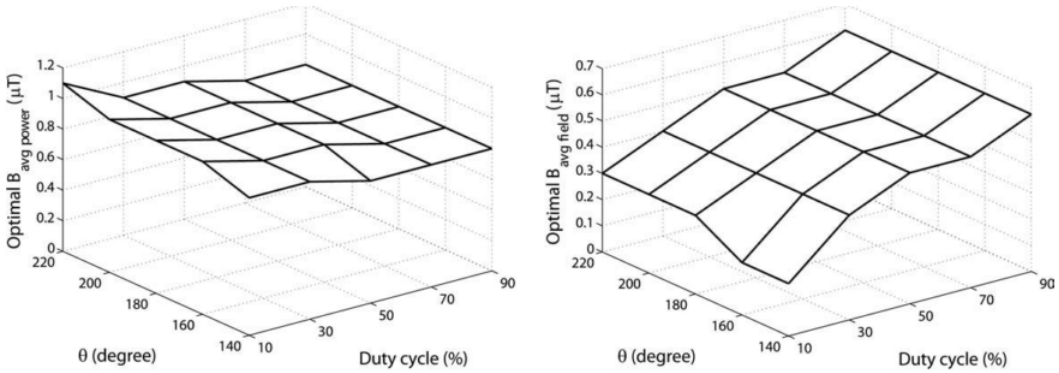


Figure 2.22: Dependence of the $B_{\text{avg power}}$ and $B_{\text{avg field}}$ on the RF flip angle and duty cycle. $B_{\text{avg power}}$ (left), remains relatively constant with varying flip angle and duty cycle. Image taken from [275].

As far as the flip angle is concerned, a value of 180° has been reported in producing the maximal CEST contrast [197] [274] (Figure 2.23). Finally, Schmitt et al showed that the most important parameter of a RF pulse train during pulsed CEST is the pulse repetition time (PRT). PRT, is defined as the sum of the pulse's duration and inter-pulse

delay and its optimal value was shown to be 50%. In other words, a duty cycle of 50% is the best compromise between effective and selective proton saturation with minimal implications from direct water saturation and SAR [170].

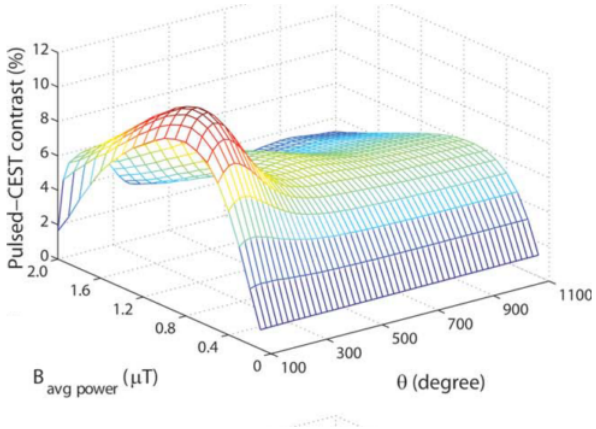


Figure 2.23: Pulsed CEST contrast dependence on $B_{avg\ power}$ and flip angle. The maximum contrast is generated at a 180° flip angle. Image taken from [275].

2.2.4 Sequences for CEST imaging

Clinically, a multi-slice or volumetric CEST scheme would be the most useful implementation in describing the extent of the pathology of interest. One inherent limitation of CEST MRI is the fundamental requirement that the acquisition of a full Z-spectrum is achieved by a frequency sweep, spanning a few hundred Hz, where one image is acquired per irradiation offset. Single slice acquisitions [263] [88] [192], can be performed in clinically relevant times (~10 mins [88]). A six offset acquisition scheme can also be used to reduce the total scanning time while maintaining sufficient SNR on the CEST images in-vivo[266] [223]. Even though single slice CEST maps are adequate for studying the phenomenon in animals [165] [267] and humans [168] a more extensive coverage of the lesions of interest is desirable.

What is challenging in implementing a multi-slice CEST scheme is the fact that, the greater the time between the initial pre-saturation pulse and echo the greater the CEST signal reduction. A post-processing method to correct for the relaxation-induced CEST signal loss when using a classic multi-slice spin echo sequence was reported in

[194]. Dixon et. al. modified a typical multi-slice gradient echo sequence by adding a saturation pulse before each new slice selection. Thus, not only was the CEST signal maintained, but also added to the up-coming slices, increasing the detection sensitivity [31]. Similarly, Sun et al. added a saturation pulse after each slice is acquired in GRE-EPI sequence, compensating this way for the relaxation induced signal drop. The modified sequence was also devoid of signal variation among the slices [195].

The problem of signal variation between slices in multi-slice acquisitions can be overcome by volumetric excitation (3D). As a large number of data is collected during these acquisitions, use of fast readouts (TSE/EPI family) is mandatory. Volumetric CEST acquisitions in-vivo have been reported in [35] (3D-TFE), [164] (3D-GRE), [90] (3D-GRE EPI), [271](3D-TSE EPI), [154] and [153](3D-GRE), [259] (3D-TSE), [145] (3D-TFE). With the exception of the first and last reference, all other studies were performed on brain glioma patients.

Gaussian shaped pulses are the most common type of pulses used for saturation [193], [274], [170], [197], [234]. Other RF shapes that have been reported include Hanning-windowed Gaussian [29], Fermi [31] and single lobe SINC-Gauss [89]. An alternative method of selectively labelling exchangeable proton groups involves the use of excitation instead of saturation pulses. These so called label transfer modules (LBM), are combinations of 90°- 180° pulses, that spatially encode the chemical shift evolution of exchanging spins [238]. This approach allows the time domain removal of the semi-solid magnetisation and direct water saturation contamination of the water signal. Even though the acquired data is acquired in the frequency domain, an inverse Fourier transform allows the fitting of the acquired Z-spectra in the time domain. The individual uncontaminated CEST peaks are indicated by the residuals of the fitting procedure [237].

Fast readouts can enhance the temporal resolution of the CEST experiment. Examples of such readouts include, (RARE) [124], combination of gradient and spin echo (GRASE) [271] and single shot FISP acquisition [172]. To further improve acquisition

times, a reduction of the k space sampling points can be considered. Such under-sampling strategies involve half-Fourier acquisition [136], keyhole sampling [213] and compressed sensing [131]. The trade-off of under-sampling is reduced signal to noise ratio in the acquired images. Therefore, the implementation of the aforementioned strategies will be challenging in characterising small regions of interest, as the latter already suffer from weak signal generation.

2.3 Endogenous CEST

The three types of exchangeable proton groups that have been investigated in endogenous CEST experiments are: amides (-NH), amines (NH_2) and hydroxyl (-OH). The properties of those proton groups are summarised in the following figure (Figure 2.24).

	Amide protons (–NH)	Amine protons (–NH_2)	Hydroxyl protons (–OH)
Chemical shift	3.5 ppm	1.8–3.0 ppm	0.5–1.5 ppm
Exchange rate (k_{sw}) range	10–100 s^{-1}	>500 s^{-1}	500–1,500 s^{-1}
Endogenous metabolites	Multiple unknown	Glutamate (Glu), creatine (Cr)	Glycosaminoglycans (GAG), glycogen, myoinositol (MI), glucose
$CEST^{a}_{asym}$	1–4 %	7–10 %	2–8 %
Sensitivity to pH	Yes	Yes	Yes
CEST applications	Cancer/stroke	Skeletal muscle and myocardial muscle energetics, cancer metabolism (Cr), neuropsychiatric disorders (Glu)	Osteoarthritis (GAG), neurological disorders (MI), cancer metabolism (glucose)

[a] At 7T under physiological conditions

Figure 2.24: Amide (-NH), amine (NH_2) and hydroxyl (-OH) proton group properties. Table taken from [106].

Among these types, amides are of particular interest in charactering cancer and stroke pathology. This is because the amide CEST signal reflects amide concentration and pH changes that accompany tumours and ischaemia. A detailed overview of the applications of the amide proton transfer (APT) CEST in tumours is presented after a brief discussion on the applications of the amine and hydroxyl containing metabolites.

2.3.1 Amines (NH_2)

2.3.1.1 Glutamate

Glutamate (GluCEST) is a major neurotransmitter in the brain resonating at +3 ppm from water. The GluCEST signal is linearly dependent on both concentration and pH. As such, its signal can reflect the pH decrease during ischaemia at 7T [10]. The latter was demonstrated in a rat model, following a middle cerebral artery occlusion. A 100% increase, at the ipsilateral side, of the GluCEST signal was found 4.5 hours after the occlusion. Moreover glutamate injection in a rat brain tumour model showed a gradual increase of the GluCEST signal in the first 2 hours after injection (Figure 2.25). The increased glutamate concentration in the tumour was confirmed using proton spectroscopy. Finally, the regional variation of glutamate in healthy volunteers was confirmed on the measured GluCEST signal. Particularly, it was found that gray matter exhibits a 5% increase in the GluCEST signal, consistent with concentration estimates derived from proton spectroscopy.

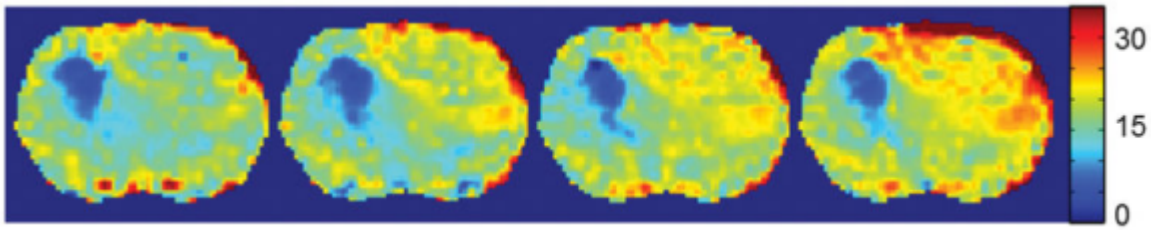


Figure 2.25: GluCEST maps of a rat brain tumour model acquired pre-injection and at 1, 1.5 and 2.0 h following the injection of the glutamate solution. A gradual increase of GluCEST was found within 2 hours of injection. Image taken from [10].

Even though the GluCEST signal can be contaminated by the signals of creatine and GABA, the authors reported that 70% of the measured signal originates from glutamate. The GluCEST signal contamination was further investigated by Kogan et al. [107]. Possible contamination of the measured signal can occur from choline, NAA, myo-inositol, creatine and glycogen. Out of these metabolites, choline does not contain any exchangeable proton groups, while the amides of NAA do not exhibit any

CEST effects at physiological pH. Furthermore, the hydroxyl groups of myo-inositol, resonate at +1 ppm and their contribution to the GluCEST signal is considered minimal. At physiological pH, a similar reasoning also excludes contributions from the creatine amine groups. Finally, since the exchange rate of the amine proton groups in glycogen is higher than that of glutamate, a higher B_1 is required to saturate them. In conclusion, the authors proposed a saturation power of 3.6μT, as ideal in achieving the least contaminated glutamate signal.

An alternative approach in characterising amine signals is reported in [83]. In this study, spin locking (SL) theory was implemented for charactering amine proton exchange (APEX). SL is practically the same experiment as CEST, with the addition of two on resonance flip RF pulses at the start of the acquisition. In addition, SL can be tuned to specific exchange rates (and therefore pH) by adjusting the SL pulse parameters. Previous studies have used low power-long duration RF pulses to characterise the amine signal (GluCEST). Nevertheless, such pulses reduce the detection sensitivity of proton groups with 'intermediate' exchange rates. Amines are such a proton group and are more efficiently saturated using intermediate power and duration pulses. An increase in the saturation pulse power, however, leads to increased semi-solid magnetisation transfer, water saturation and NOE contamination in conventional CEST. SL on the other hand, has been shown to achieve higher selectivity/sensitivity for faster exchange rates, as opposed to CEST. In particular, the measured APEX glutamate signal, in-vitro and in an ischaemic rat model, was found to be 4% higher in SL acquisitions versus CEST and the reported sensitivity gain was 18% [82]. The APEX signal results as a weighted summation of the signals from many amine groups including glutamate, glutamine and taurine. Thus, it resonates around +3 ppm from water, similar to the CEST studies. However, further study is required in order to identify the individual contributions of the various amine groups. The APEX contrast is calculated similarly to MTR_{asym} in CEST. Nevertheless, as shorter pulses are used in APEX, the NOE and conventional magnetisation transfer contamination is greatly reduced as compared to

CEST measurements. Finally, APEX is also sensitive to pH changes during ischaemia, in-vivo. At normal pH, its signal originates mainly from proteins, while at decreased pH, the GABA and glutamate contributions increase. The latter results in ischaemic regions being hyper-intense on APEX images as opposed to hypo-intense APT images due to lower pH [272].

2.3.1.2 Creatine

Creatine (Cr), is another amine proton containing metabolite whose protons resonate at +1.8 ppm from water [193]. Cr, along with (PCr) and adenosine-5-triphosphate (ATP), are the major metabolites of the enzyme creatine kinase (CK). While non-invasive quantification the total Cr (Cr + PCr) is possible using ^{1}H-MRS, there is no available MRI method to quantify free Cr separately from PCr at high resolution. Harris et al. [62] however, showed that Cr, can individually be detected using CEST. The authors reported a broad resonance from creatine amine protons, centred at ~1.8 ppm, in vitro at 3T. Furthermore, no CEST contrast was generated by PCr and ATP owning to their slower exchange rates, as compared to Cr (Figure 2.26). This result demonstrates the importance of the choice of experimental CEST parameters in the detection/suppression of various exchangeable proton groups.

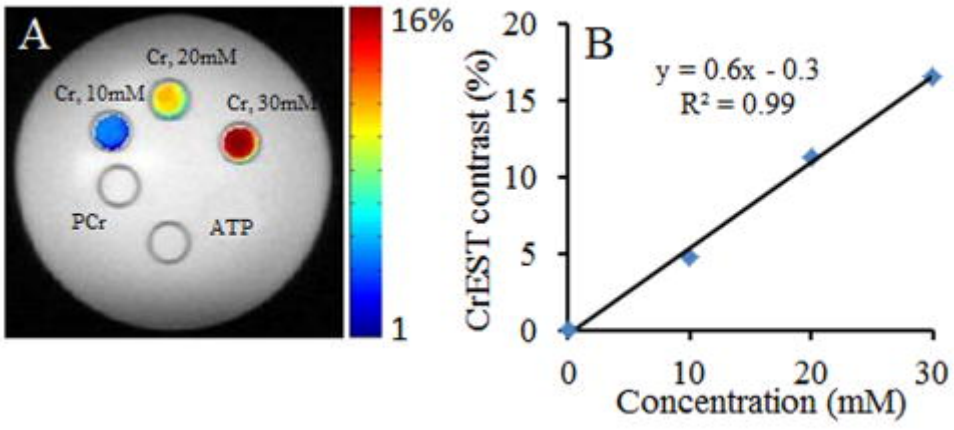


Figure 2.26: **A.** CEST contrast of Cr, PCr and ATP. **B.** CrCEST contrast linear dependence on concentration. Image taken from [62].

Creatine CEST (CrCEST), was successfully implemented in detecting creatine concentration changes, before and after exercise, through the detected CrCEST signal. [140, 108]. In particular, CrCEST was found to immediately increase during exercise with a subsequent return to the baseline ~14 minutes after the exercise ended (Figure 2.27). More importantly, the Cr signal was not only successfully been detected at 7T, but also at the clinically relevant field of 3T.

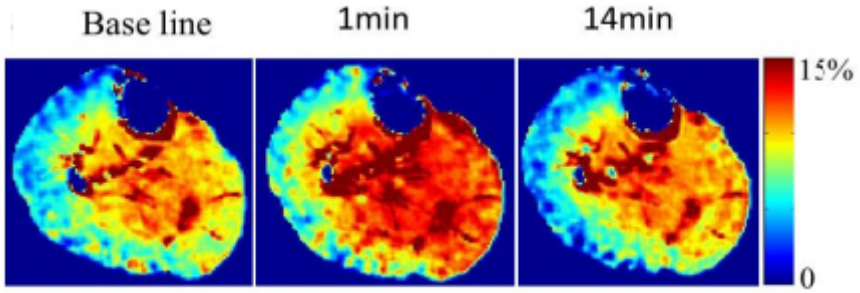


Figure 2.27: CrCEST in human calf muscles at 7T. During exercise, CrCEST signal rapidly increases, before returning to its baseline ~14 minutes after the onset of the exercise. Image taken from [140].

2.3.2 Hydroxyl (-OH)

Metabolites containing hydroxyl protons include: glycogen, glycosaminoglycans (GAG), myo-inositol, glucose and lactate.

2.3.2.1 Glycogen

Glycogen molecules function as energy storage units and can be synthesised in the liver, muscles, brain and stomach. In-vivo monitoring of glycogen would be beneficial in the management of conditions like obesity, type 2 diabetes or insulin-related diseases. One method of non-invasive in-vivo detection of glycogen is by performing ^{13}C-MRS. However, the equipment needed to perform the latter is not usually available in the clinic and an alternative non spectroscopic method would be more preferable. At first glance, detection of glycogen might seem challenging, as its protons have only

a small chemical shift from water (~ +0.5-1.0 ppm at 4.7T). Nevertheless, glycoCEST was successfully been performed in-vitro and in-vivo at 4.7T [212]. As expected, the glycoCEST signal increases linearly with glycogen concentration. Moreover, glycogen depletion is reflected on the measured glycoCEST signal of mouse liver (Figure 2.28).

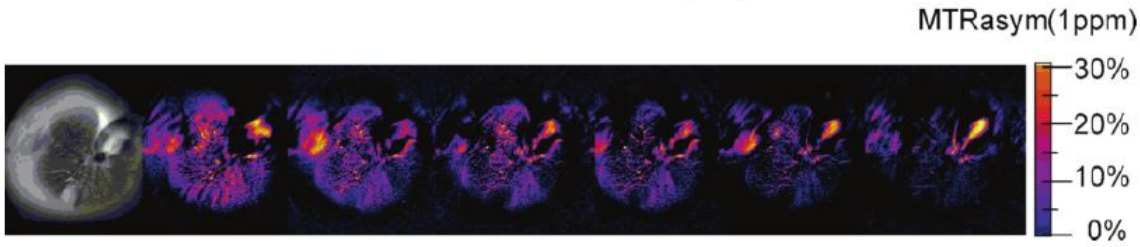


Figure 2.28: Glycogen depletion over time is reflected as decreased glycoCEST signal in perfused mouse liver at 4.7T. Image taken from [212].

Similar results were reported from Chen et al. at 3T [16]. After a 24 hour fasting period, a significant decrease in the measured glycoCEST signal indicated glycogen depletion from the liver of both rats and humans. In addition, CCl4 intoxication, that resembles liver fibrosis, resulted in significant decrease of the detected glycoCEST signal in the rat model.

2.3.2.2 GAGs

Glycosaminoglycans (GAGs) are polysaccharides that take part in spinal, musculoskeletal or cell regulatory functions. Non-invasive in-vivo detection of GAGs would help the characterisation of conditions like osteoarthritis (loss of GAG in cartilage) or vertebral disk degeneration. GAGs contain both amide and hydroxyl proton groups resonating at +3.5 ppm and +1 ppm respectively. According to Ling et al. [122], the hydroxyl groups are a more reliable gagCEST agent. This is because they have higher concentrations (double) and exchange rates than the amide GAG groups. As a result, the latter exbibit only 1-2% gagCEST signal as opposed to almost 20% of the former, in vitro. In addition, NOE signals present in cartilage will severely contaminate the already weak amide signal. On the other hand, the elevated concentration and fast

exchange rates of the hydroxyl groups can outweigh the NOE contamination. Loss of GAG in cartilage was demonstrated both ex-vivo and in-vivo (Figure 2.29).

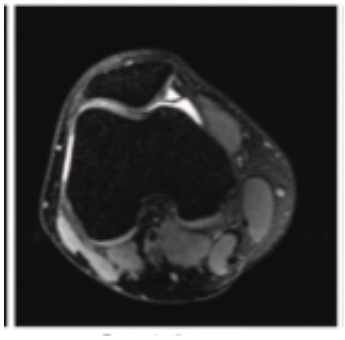


Figure 2.29: gagCEST signal decrease, in the medial side of the patellofemoral human knee joint, indicating loss of GAG, at 3T. Image taken from [122].

Singh et al. [174] have reported insignificant gagCEST signal at 3T and about 6% at 7T (Figure 2.30). The difference with the previous study was attributed to B_0 and B_1 corrections. The latter was emphasised as a necessary condition for acquiring reliable gagCEST signals in-vivo.

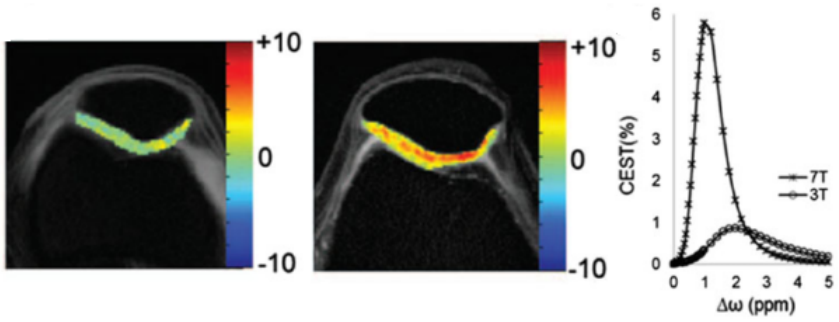


Figure 2.30: **Left to right:** B_0 and B_1 corrected gagCEST maps at 3T, 7T and the corresponding asymmetry plot. Image taken from [174].

GAG content of intervertebral discs (IVDs) was studied by Schleich et al. [169]. The authors demonstrated the feasibility of a gagCEST analysis in characterising the topological GAG distribution of the cervical spine at 3T. Higher gagCEST effects were found in lower IVDs and negative a correlation was demonstrated between gagCEST values and cervical disc degeneration. The latter result was also reported by Krishnamoorthy et al. [109] (Figure 2.31).

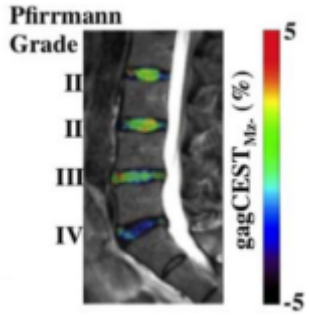


Figure 2.31: Higher grade of intervertebral discs degeneration results in decreased gagCEST contrast. Image taken from [109].

2.3.2.3 Myo-inositol

Myo-inositol (mIns) is one of the most abundant brain metabolites. It is mostly located in glial cells and its increase indicates glial cell proliferation. mIns contains 6 exchangeable hydroxyl proton groups and exhibits a resonant peak at + 0.6 ppm from water. Its exchange rate was determined to be 600 s^{-1}, in-vitro at 7T [61]. MICEST signal has a linear dependence on mIns concentration and was also found to slightly increase with temperature. Contamination of the MICEST signal from other major brain metabolites, at physiological concentrations and pH, is negligible. In healthy human brain, increased MICEST signals were observed in white matter as opposed to gray matter (Figure 2.32), a result which is consistent with MRS measures of myo-inositol concentration.

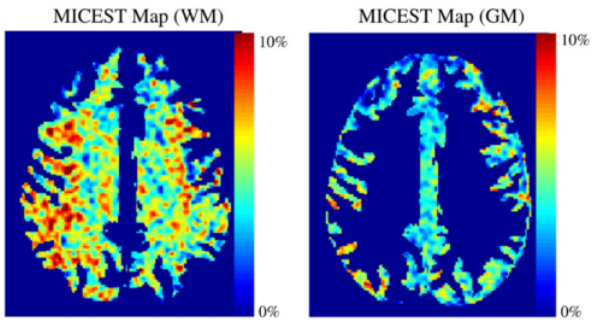


Figure 2.32: MICEST map of white and gray matter. White matter shows elevated MICEST signal, indicating a higher concentration of myo-inositol. Image taken from [61].

Harris et al. [63], hypothesised that MICEST could monitor glial cell proliferation in Alzheimer's disease. As such, the authors compared the MICEST signals of an Alzheimer's disease mouse model (APP-PS1) with wild type. It was found that, the higher MICEST contrast in APP-PS1 mice (Figure 2.33) correlated with higher glial cell proliferation, as validated from MRS and immunohistochemistry. These findings suggest that the in-vivo detection of changes in mIns concentration in Alzheimer's disease, is feasible, using the MICEST.

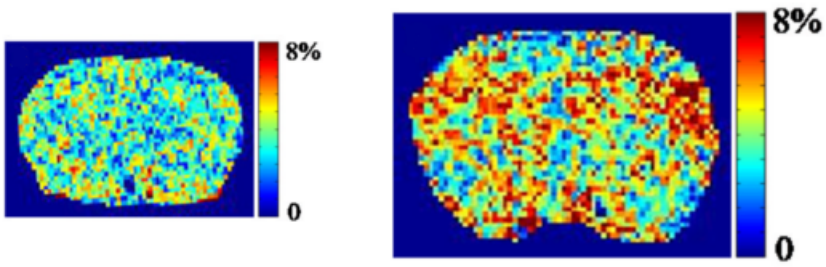


Figure 2.33: **Left:** MICEST signal in wild type mouse. **Right:** Elevated MICEST signal in the Alzheimer's disease mouse model, indicating glial cell proliferation. Image taken from [63].

2.3.2.4 Glucose

Glucose breakdown and uptake serves as an energy source in most organisms. Usually, any impairment or altered glucose consumption is indicative of an underlying disease. Tumours in particular, exhibit increased glucose metabolism as opposed to healthy tissue. This increase in uptake is most effectively being assessed with positron emission tomography (PET). Imaging takes place after the injection of a positron-emitting radionuclide, namely, [^{18}F]FDG, that serves as an imaging tracer. FDG-PET provides valuable functional information based on the increased glucose uptake and glycolysis of cancer cells and can reflect metabolic changes before the occurrence of any morphological alterations. Despite its high sensitivity and specificity, an FDG-PET scan comes at the cost of harmful ionising radiation being absorbed by healthy tissues. The following paragraphs describe several attempts using CEST (glucoCEST), as an alternative, non-invasive, imaging method of glucose uptake in-vivo.

Chan et al. [12] investigated the uptake efficacy of the naturally occurring sugar, D-glucose, in a tumour bearing mouse model at 11.7T. Similarly to what was previously shown [212], the authors reported a D-glucose exchanging CEST peak at +1.3 ppm from water, in-vitro. The glucoCEST signal was found to linearly depend on D-glucose concentration for up to ~50mM, where proton back exchange is minimal. An inverse relationship, between pH and glucoCEST signal, was also reported. Furthermore, the authors hypothesised that, the slightly acidic extracellular pH of solid tumours [177], creates favourable conditions for glucoCEST. This is because low pH, decreases the glucose proton exchange rate, which in turn allows for more efficient proton saturation. To that end, D-glucose infusion in mice, bearing two different tumour cell-lines, was imaged (Figure 2.34).

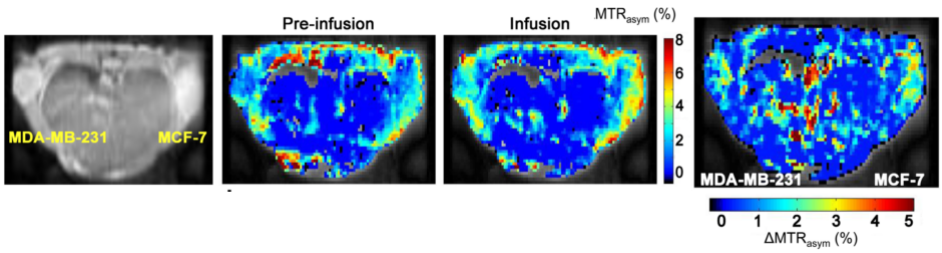


Figure 2.34: **Left to right:** Anatomical image showing the location of the tumours, pre D-glucose infusion CEST, post D-glucose infusion CEST and post infusion FDG-PET. Image taken from [12].

Both glucoCEST and FDG-PET images showed signal increase in the tumour locations, post infusion. However, the measured glucoCEST signal was 1-4% more than the FDG-PET signal. In addition, the former showed a significant signal difference between the two tumour types, while the latter did not. Interestingly, the more acidic tumour generated lower CEST signal than the less acidic one. This was expected considering that acidosis lowers the proton exchange rate. Even though glucoCEST contrast is altered after D-glucose infusion, the authors concluded that, in its current state, glucoCEST signal does not provide metabolic information. Instead, it reflects extracellular localisation of the infused glucose.

A significant correlation between the median tumour glucoCEST and FDG uptake was reported by Walker-Samuel et al. [218]. Even though, the weight of contribution of glucose and its metabolic by-products, to the glucoCEST signal, is not clear, glucose infusion resulted in significant signal differences between two colorectal tumour mouse models. Again, the less hypoxic tumour generated higher glucoCEST signal. The possibility of glucoCEST reflecting vascular permeability was rejected, as there was no correlation between Gd uptake and glucoCEST hyper-intensity.

(2DG) is yet another molecular glucose analogue. 2DG is phosphorylated into 2DG-6-phosphate (2DG6P) in-vivo and can serve as an effective glucoCEST agent. Its CEST effect was studied in-vitro and in-vivo by Nasrallah et al. [147]. At 7T, the 2DG CEST signal exhibits a linear dependence on concentration and is centred at ~ +1ppm from water. ^{31}P-MRS, after 2DG infusion in healthy rats, confirmed the origin of the glucoCEST signal, as being from 2DG and 2DG6P. The time course variation of the 2DG glucoCEST signal is shown in Figure 2.35.

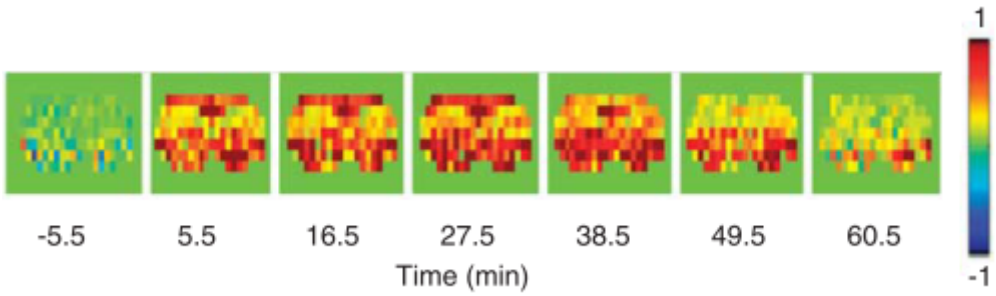


Figure 2.35: Uptake of 2DG in healthy rat brain. The first image serves as a baseline. Image taken from [147].

In healthy rat brain, glucoCEST signal reaches its peak, at about 40 mins after infusion, before eventually returning to the baseline. During the same time-frame, blood glucose level was found to be constant, following a rapid initial increase immediately after infusion. This suggests that blood glucose does not contribute to glucoCEST. In a separate experiment, the maximum D-glucose glucoCEST signal was found to be 40% less than that of 2DG, even though its temporal variation showed similar trend. More

importantly, when the BBB impermeable L-glucose was scanned, no CEST signal increase was seen, further suggesting that plasma and extracellular glucose do not affect glucoCEST. In any case, the intravascular and extracellular spaces are about 5% and <15% respectively, of the total rat brain tissue volume. Thus, plasma and extracellular contributions should be small and the glucoCEST signal is dominated by intracellular glucose. Imaging glucose uptake with CEST is characterised by poor temporal resolution, since the acquisition of a full Z-spectrum is time consuming. To increase detection sensitivity, use of fast imaging readouts and modified Z-spectrum acquisition is necessary. Alternatively, measuring glucose uptake with spin locking allows for robust detection of 2D-glucose, for doses as low as 0.25 g/kg [86]. It was previously shown [83] that the intermediate hydroxyl proton exchange rates, as the ones found in glucose, are more efficiently saturated with high power-short duration RF pulses. The latter, along with the vast increase in temporal resolution of spin locking, allow for more precise characterisation of the glucose uptake. Moreover, spin locking glucoCEST (glucoCESL) is independent from T_1 and T_2 variations and less sensitive to B_0 inhomogeneities when compared to glucoCEST. In spite of its increased sensitivity, the uptake dynamics of D-glucose and 2DG, at 9.4T in rat brain, were found similar with the ones described by glucoCEST. However, glucoCESL has the advantage of providing a quantitative index for determining changes in glucose concentration in-vivo, namely the differences in the longitudinal relaxation rates of water with time. The latter is important, as quantifying glucose uptake by integrating areas under the Z-spectrum, spanning a few ppm [147], does not provide frequency specific information on signal contributions.

The first translation of using D-glucose as an uptake marker in humans was reported by Wu et al. [236]. After D-glucose injection, uniform and strong signal enhancement was seen in both healthy and glioma patients, in blood vessels, while spatially varying signal enhancements were seen in tumours. In addition, different tumour locations were enhanced at different times, suggesting glucoCEST sensitivity to perfusion

related properties. These enhancements were observed even in non Gd-enhancing tumours. What is more, they appeared to regionally match T_{2w} hyper-intense regions (Figure 2.36). The red and yellow arrows in Figure 2.36, indicate an enhancing tumour rim and contralateral vasculature. Both these regions appear to enhance in the early stages of glucose uptake, with the enhancement at the rim indicating potential BBB disruption.

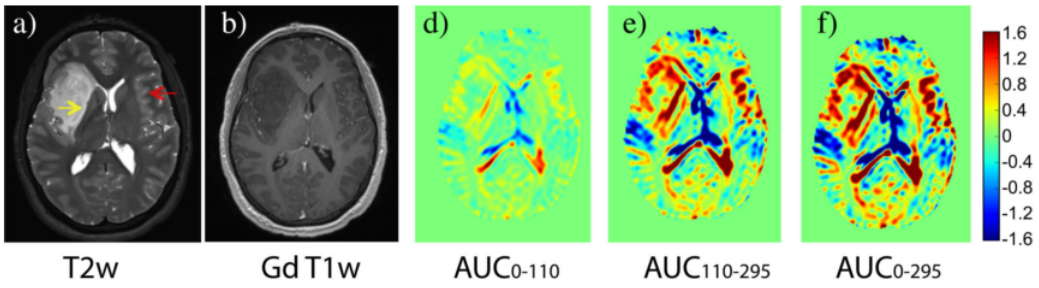


Figure 2.36: T_{2w}, Gd-T_{1w} and glucoCEST images of patient with anaplastic astrocytoma acquired at 7T. The subscripts in the glucoCEST images denote time in seconds. Image taken from [236].

Wang et al. [219] demonstrated the feasibility of imaging glucose uptake with glucoCEST, in patients with head and neck cancer, at 3T. A consistent contrast increase was found in all patients, post glucose injection (Figure 2.37).

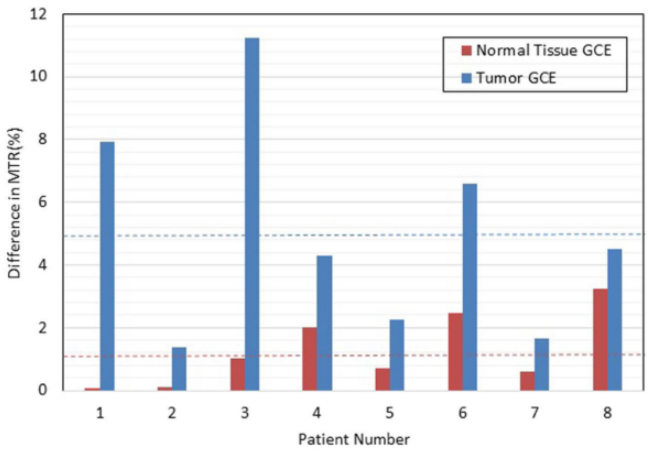


Figure 2.37: Comparison of the difference between pre and post glucose injection CEST signal in tumour and normal tissue. Image taken from [219].

The challenge in calculating glucoCEST maps at 3T lies in the fact that, the glucose resonance lies within +1 ppm from water. As such, the CEST effect might be dampened by the dominant water peak. A higher acquisition field would increase the separation between the proton pools and benefit glucoCEST quantification. The results presented in Figure 2.37, have been derived from calculating the total CEST signal from +1 to +5 ppm. This region contains a plethora of other metabolite exchange peaks but it is assumed that their contributions cancel out after calculating the asymmetry. The spatial distribution of glucose, in PET and glucoCEST maps, did not match exactly and only a general correlation between them was seen Figure 2.38. The latter suggests that glucoCEST does not measure glucose distribution. Instead it measures the metabolic products and by-products of glucose uptake.

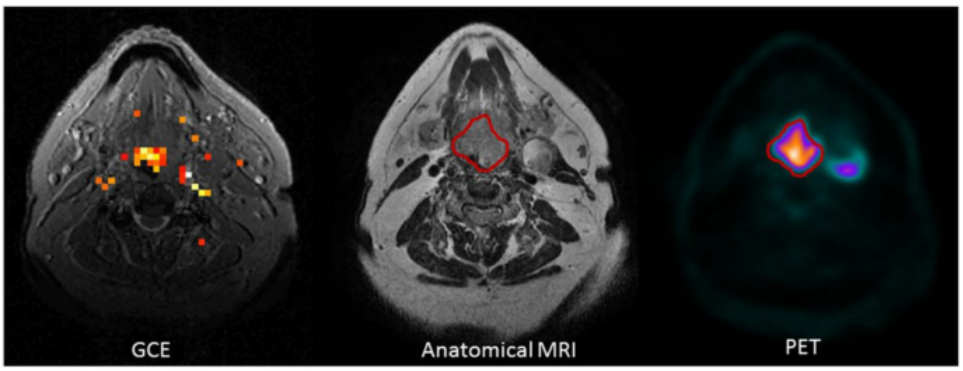


Figure 2.38: Glucose Contrast Enhanced MRI, Anatomical MRI and FDG-PET images of a tumour patient. Image taken from [219].

2.3.2.5 Lactate

Lactate CEST (LATEST), was recently added to the list of the CEST detected metabolites [24]. Non-invasive imaging of lactate is important in metabolic disorders, where glycolysis is prevalent. Tumours in particular exhibit up-regulated (LDH) and thus, increased lactate concentrations. As lactate was found to correlate with tumour recurrence, metastasis and treatment outcome [9, 217], non-invasive imaging of lactate is important. Its changes can be measured in-vivo with ^{1}H and ^{13}C-MRS [23]. However, as with all spectroscopic methods the latter suffer from low spatial resolution.

DeBrosse et al. [24], have measured lactate in-vitro and in-vivo using CEST. At 7T and 9.4T, the Z-spectra of phantoms of sodium lactate, show a lactate CEST peak centred between ~ +0.3 to +0.5 ppm (Figure 2.39).

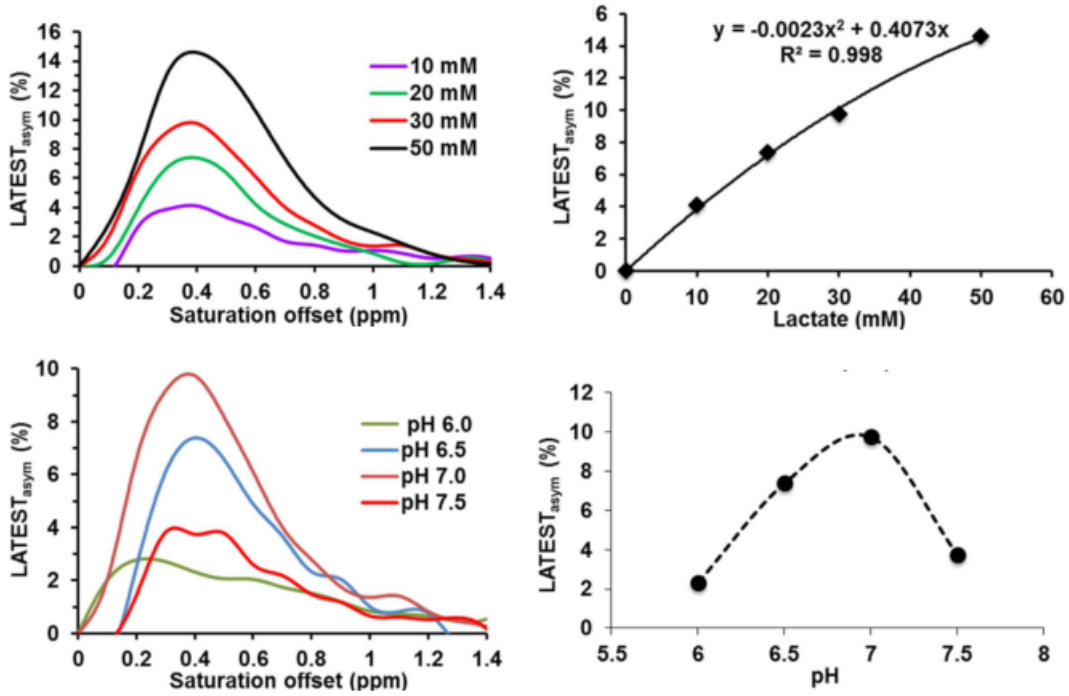


Figure 2.39: **Top row:** Lactate asymmetry spectrum and concentration dependence. **Bottom row:** Lactate asymmetry spectrum and pH dependence. Image taken from [24].

LATEST depends linearly on lactate concentration and exhibits a maximum effect at pH 7. The exchange rate (k_{sw}), estimated from phantoms at pH 7, is ~350 ± 50 s^{-1} at 25 °C and ~550 ± 50 s^{-1} at 37 °C. This suggests that LATEST increases with temperature. Furthermore, infusion of 300 mM of pyruvate in a lymphoma flank tumour mouse model showed an increase in LATEST contrast pre and post infusion (Figure 2.40). In particular, LATEST data from three animals showed a ~60% increase in LATEST asymmetry, after ~40 minutes post-infusion of pyruvate. Endogenous tumour lactate is also indicated by the signal increase, pre infusion. The concentration of the latter has be shown to range between 2-10 mM [114].

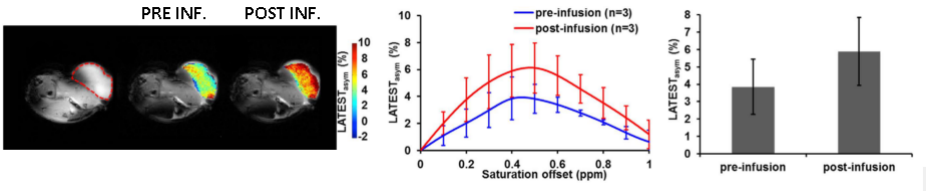


Figure 2.40: **Left:** Anatomical, pre and post pyruvate LATEST images. **Middle:** pre and post infusion LATEST asymmetry curves **Right:** pre and post infusion LATEST contrast comparison. Image taken from [24].

Confirmation that LATEST signal indeed arises from infused pyruvate was provided by correlating its magnitude with endogenous lactate concentration, measured by multiple quantum filtered proton magnetic resonance spectroscopy (SEL-MQC ^{1}H-MRS). LATEST signal increase pre and post exercise, was further observed in healthy human calf muscle. Figure 2.41 shows ten LATEST images acquired three minutes after the exercise stopped. The last image closely resembles the baseline, suggesting a resting state LATEST magnitude of 1.5%. Hydroxyl groups from other endogenous metabolites (e.g glucose, glycogen, GAGs, creatine) will also contribute to the baseline LATEST. However, the authors argued that their contribution is small. Moreover, LATEST contrast increase, due to T_2 changes, post exercise were also dismissed.

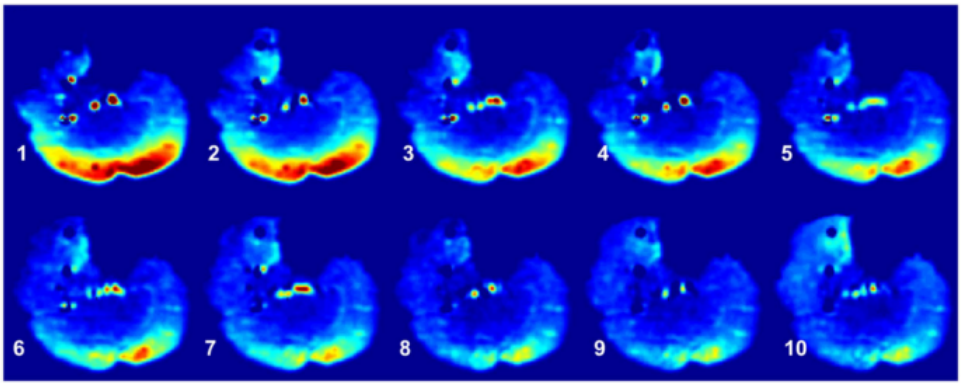


Figure 2.41: LATEST images of human calf muscle 3 minutes post exercise. The signal falls back to the baseline in about 18 minutes after exercise cessation. Image taken from [24].

The in-vivo results presented here were acquired at 7T. LATEST Z-spectra and asymmetry curves indicate an exchange peak centred at +0.4 ppm or 160 Hz from

water. This separation becomes only 50 Hz, at 3T. Thus, it is unlikely that such a detection is possible at lower fields, unless the lactate resonance is shifted further away from water. Lanthanide complexes are capable of binding to lactate [203] and as such, Zhang et al. [253] imaged the lactate-EuDO3A complex molecule, in-vitro at 9.4T and in-vivo at 4.7T. This hybrid molecule exhibits a CEST resonance peak at +47 ppm from water, in-vitro (Figure 2.42). Its chemical exchange rate is ~ 2000 s^{-1}, at physiological pH, indicating that a high B_1 saturation power is required for saturation (14.1μT).

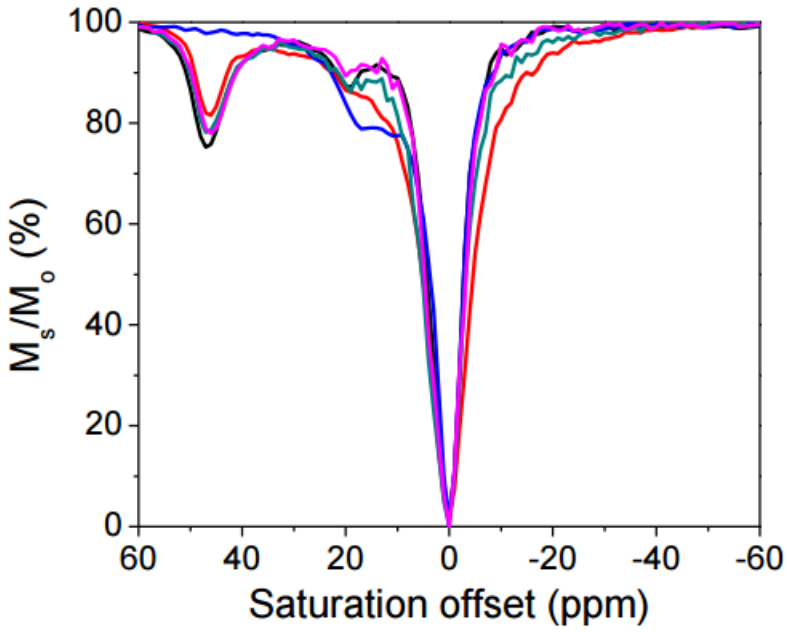


Figure 2.42: Z-spectra of various EuDO3A complexes measured at 9.4T, in-vitro. **Black line**:50 mM EuDO3A+50 mM lactate, **Red line**:50 mM EuDO3A+ 50 mM (NaH2PO4+ Citric acid+ NaHCO3+Lactate) **Blue line**: 50 mM EuDO3A+50 mM Citric acid. **Green line**: 50 mM EuDO3A in 4% HSA. **Purple line**: 50 mM EuDO3A +50 mM lactate in cell culture medium. Image taken from [253].

Figure 2.43, shows lactate-EuDO3A detection in the bladder of healthy mice, at 4.7T. Even though there was no CEST signal detected in tissues, a strong signal enhancement was seen in the mouse bladder, with no further evidence of toxicity for a dose of 0.105 mmol kg^{-1}. This dose might not be sufficient for imaging lactate production by tumours in-vivo. Nevertheless, administering lactate-EuDO3A, in the form

of a nanoparticle, might achieve sufficient agent delivery to the extracellular tumour space, as it was reported that 100-200 nm sized nanoparticles achieve a 24-fold higher accumulation of therapeutic drugs in tumours [166].

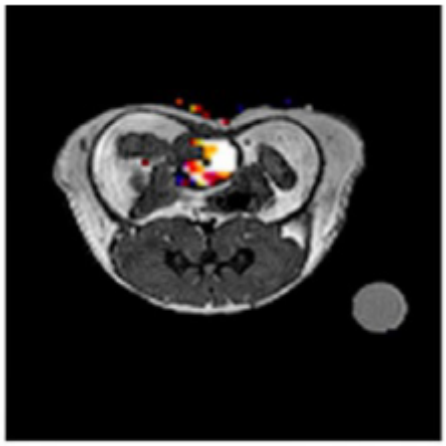


Figure 2.43: CEST image of a mouse bladder showing the presence of the intact lactate·EuDO3A complex at 45 min post injection. Image taken from [253].

2.3.3 Amides (NH)

2.3.3.1 Absolute pH mapping

In-vivo measurement of endogenous amide proton transfer (APT) signals, was first demonstrated on an ischaemic rat model at 4.7T [264]. Amides were found to have exchange rates in the order 10-100 $s^{-1}$and in most tissues their concentration is between 5 to 8 mM [263, 165]. APT exchange rate was also found to be base catalysed. Furthermore, the relationship between measured APT signal and pH was reported as: APT $=5.73 * 10^{pH-9.4}$ [264].

The calculation of the latter is not at all straightforward. First, the amide proton exchange rate needs to be known via either water exchange spectroscopy (WEX) [264, 246], model fitting to experimental data [116, 137, 185], omega plot [32, 199, 233] or multi-angle ratiometric approach [276]. If the amide concentration can be estimated, then the exchange rate can be found with a search algorithm [187]. Otherwise, both the concentration and exchange rate can be calculated using the optimal

B_1 power, yielding the maximum APT signal [184]. Second, the relationship between the exchange rate/measured signal and pH needs to be known. Despite being trivial in-vitro, finding the relationship in-vivo, requires measurement of pH with ^{31}P-MRS [198], [138]. This can be done by either measuring lactate concentration (pH = -0.0593 * [La] + 7.2) or the chemical shift difference, δ, between creatine and phosphocreatine (pH = 6.75 + log[(δ-3.26)/(5.7-δ)]). If the pH is known, then the exchange rate is given by: k_{sw}= 5.57 * $10^{pH-6.4}$ [264]. Next, a calibration curve can be calculated by fitting the measured CEST signal and pH values, as found by ^{31}P-MRS [198]. The latter fitting procedure can also estimate the endogenous amide concentration. Finally, if the water longitudinal relation time, T_1, is known, then an absolute pH map can be calculated (Figure 2.44).

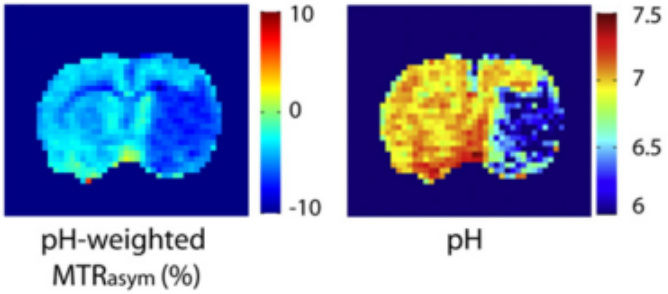


Figure 2.44: **Left:** pH weighted MTR_{asym} map. **Right:** absolute pH map of ischaemic rat model at 4.7T. Image taken from [198].

Absolute pH mapping is also possible using a ratiometric method. McVicar et al. [138] utilised the ratio of two endogenous peaks (amines and amides) to produce absolute pH maps of an ischaemic rat model at 9.4T. This method resembles ratiometric pH mapping using exogenous contrast agents, having at least two proton exchange peaks [129] and has the advantage of being concentration independent. This approach, termed, (AACID) [138], was able to detect pH changes during ischaemia, in rat brain. Endogenous pH was measured with ^{31}P-MRS by finding the chemical shift difference, δ, between creatine and phosphocreatine. The calibration curve, both in-vitro and in-vivo, was linear. Specifically, for endogenous pH calibration: pH = -4 * AACID +12.8.

Low pH during ischaemia was therefore seen as hyper-intense region on CEST images (Figure 2.45).

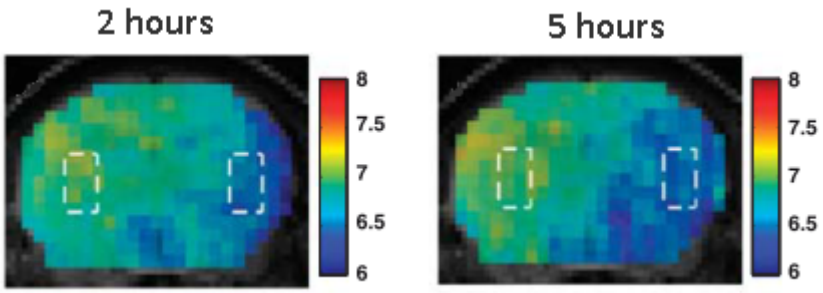


Figure 2.45: Endogenous ratiometric absolute pH maps (AACID), in rat brain at 9.4T, 2 and 5 hours after middle cerebral artery occlusion. Image taken from [138].

Any effect on the measured AACID, due to T_1, T_2 changes was dismissed by numerical simulations. In order to accommodate for the fast exchange rates of amines at 3T, a high B_1 power has to be used. For example, Harris et al. [64] used a B_1 power of $6\mu T$ to produce amine proton weighted images, in brain glioma patients, at 3T. However, such high RF power is unsuitable for saturating the slow exchanging amides. Since both peaks are needed for the concentration independent method, the implementation of the AACID, at 3T is challenging.

Finally, for a system that is driven in steady state ($t_{sat} > T_{1w}$ or at the very least $t_{sat} \approx T_{1w}$), the spillover, MT and T_1 corrected AREX contrast can be used to attain an absolute pH map [246]:

$$pH(in-vivo) = 6.4 + \log(\frac{AREX/DC}{f_b * 5.57})$$

with DC, the duty cycle of the pulsed acquisition and f_b the endogenous amide proton concentration. In this approach, the water T_1 and amide exchange rate, must be also known.

2.3.3.2 Cerebrovascular stroke

APT is positively correlated with intracellular pH [198, 87]. Increased ATP hydrolysis, during stroke, causes intracellular pH to decrease. The latter, lowers the proton exchange rate, resulting in decreased APT effects [196]. Acute ischaemia can be characterised, in-vivo, at 3T, using low B_1 saturation powers (~0.55 μT) [65] and the pH weighted CEST signal was found to be associated with tissue outcome. However, the interpretation of the results is still under debate.

Data acquired in stroke patients, showed reduced APT values in ischaemic core, infarct growth and oligaemia regions, with the core having the lowest of the three. This suggests increased core acidosis, as opposed to surrounding tissue, that ultimately survives [65]. Similarly, Tietze at al. [205] found that, on average ischaemic regions show decreased APT signal, when compared to healthy white matter. However, rather surprisingly, no significant CEST signal difference was found between ischaemic core and penumbra. Mixed results were also reported on the association of the APT signal, of the infarct core and final infarct volume, as the latter did not show a consistent APT signal reduction. A more sophisticated fitting model is perhaps necessary to account for the cascade of events following stroke. For example, conventional magnetisation transfer (MT) remains constant, within a few hours after stroke [191]. In this case, MTR_{asym} analysis is valid, as the constant MT component is removed. At later times, a Lorentzian fitting can be implemented for quantification of endogenous APT signals. More insight is however required, on the endogenous species present in ischaemic tissues, so as to appropriately define the Lorentzian line-shape characteristics.

2.3.3.3 Brain Tumours

Jones et al. [88] reported the first APT CEST study in low grade human brain tumours. APT was compared with commonly used techniques, such as T_{1w}, T_{2w}, Gd-T_1, FLAIR and diffusion and was found to consistently differentiate tumour regions from oed-

ema. More specifically, a 4% APT signal change was reported for tumour regions, as compared to normal appearing white mater and oedema (Figure 2.46).

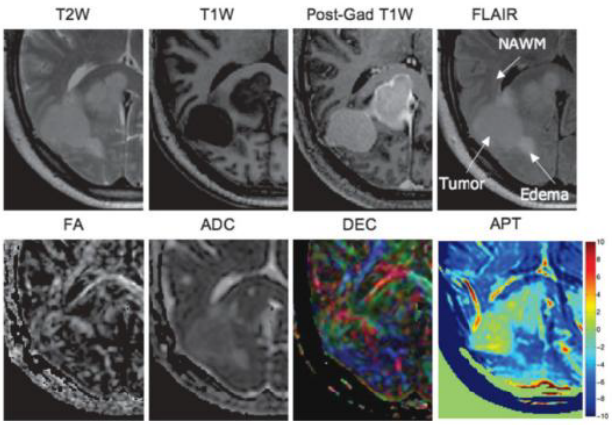


Figure 2.46: Various MR images for a patient with meningioma. For the APT image the mean and the standard error of the APT values were -0.1 ± 0.04 (tumour), -3.3 ± 0.2 (CNAWM), -2.8 ± 0.04 (INAWM), and -2.0 ± 0.08 (oedema). Image taken from [88].

It is known from CEST theory, that the proton transfer ratio (PTR, equation 2.2.4) is influenced by a few factors, including amide concentration, water content, proton exchange rate and water longitudinal relaxation. If APT imaging is to be successful, then the effects of increased amide concentration must outweigh that, of water content. The effect of the latter can be assessed through T_{1w} images, as they generally reflect brain water content. In this study, increased intensity on T_{1w} images was not necessarily related to hyper-intense APT regions. Moreover, the tumour microenvironment is characterised by slightly acidic extracellular space and slightly alkaline intracellular space [52, 161]. Considering that APT is base catalysed [264], then its exchange rate increases with pH which in turn increases APT contrast. This study also provided a benchmark, regarding the APT saturation scheme. A long continuous pulse (3 seconds, 3 μT) was implemented, while energy deposition remained within SAR limits. It was shown later [193], that pulsed saturation can achieve about 95% of the continuous wave contrast, with the optimal RF irradiation power, between the two approaches, being equal. Furthermore, the relationship, between continuous-pulsed wave saturation power, is given by the analytical solution for continuous wave CEST,

as shown by Zu et al. [274].

As shown by magnetic resonance spectroscopy amide proton concentration is increased in tumours, as compared to healthy white matter [73, 268]. More recently, proteomic analysis of various tumour markers, showed that the total protein concentration in tumour and healthy tissue, is the same. However, tumours had an increased cytosolic mobile protein concentration over healthy tissue [239]. Since APT signal reflects the increased mobile tumour protein content, it is expected to be correlated with tumour grade. Indeed, Zhou et al [266] found a clear correlation of the APT signal with tumour grade ($r^2 = 0.92$), with the low grades having almost the same APT contrast as white matter (Figure 2.47). Furthermore, Togao et al [206] have reported the mean APT values of grade II, III and IV tumours, at 3T, as being, $2.1 \pm 0.4\%$, $3.2 \pm 0.9\%$ and $4.1 \pm 1\%$ respectively. These values were significantly different in the pairs, II-III, III-IV and II-IV. Relevant to grading glial tumours, Sakata et al. [164], showed that both single slice and volumetric ROIs, as defined on Gd-enhancing images or FLAIR, provide the same MTR_{asym} values and as such, both approaches correctly correlate the APT signal with its corresponding grade. Adding the APT signal to the apparent diffusion coefficient (ADC) also significantly improves grading than APT or ADC alone [17].

The ability to distinguish between radiation necrosis and tumour recurrence is very important in predicting tumour response to therapy and can have immediate clinical implications.

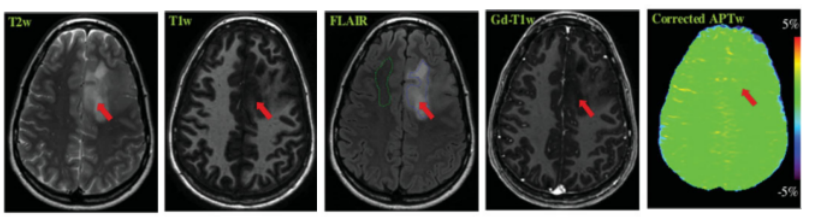


Figure 2.47: Multimodal MRI of a low grade glioma. In the APT image, the tumour is indistinguishable from healthy tissue. Image take from [266].

Zhou et al. [267] have demonstrated that, due to the lack of cytosolic proteins and peptides, necrotic regions, appear hypo-intense on APT images. On the contrary, necrosis can be mistaken as a recurrent tumour due to its hyper-intensity on T_{2w} or Gd-T_{1w} imaging (Figure 2.48). Such low, necrotic APT signals, were also seen in high grade human gliomas, at 3T [259, 223, 270]. As expected, tumour cores showed significantly higher APT signal than necrosis and oedema, but had similar intensities with cystic components, probably due to the presence of mobile proteins in the latter. Moreover, even in high grade tumours, showing no Gd enhancement, APT contrast was increased, in tumour core. (Figure 2.49).

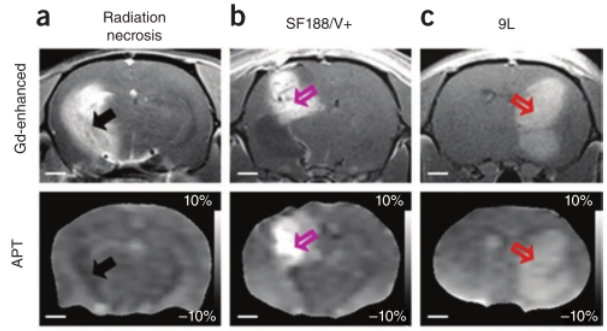


Figure 2.48: Comparison between radiation necrosis and glioma in two brain tumour rat models. Necrosis is hypo-intense on APT images. Image taken from [267].

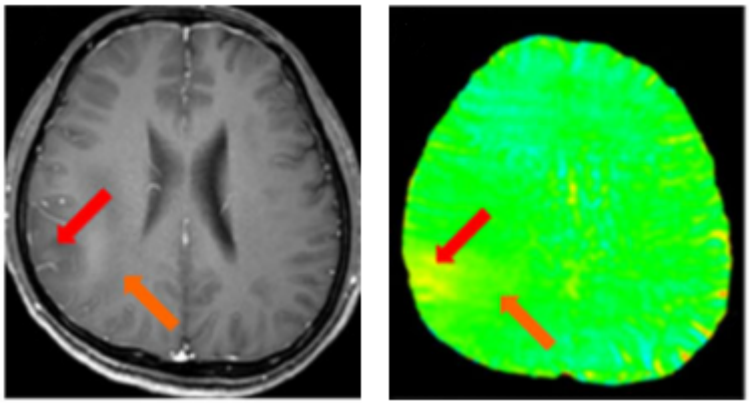


Figure 2.49: Grade III astrocytoma at 3T. **Left:** non enhancing Gd-T_1 image **Right:** APT image, showing high signal intensity in tumour (red arrow) and low signal intensity in oedema (orange arrow). Image taken from [259].

In a preclinical study, Sagiyama et al. [162] found that, successful glioma treat-

ment, with temozolomide (TMZ), results in decreased APT signals. More importantly, this decrease, is detected before any morphological alterations occur. In view of these results, Ma et al. [132], hypothesised that treatment changes, related to pseudo-progression, would exhibit an iso-intense, to normal tissues, APT-weighted signal. On the other hand, true progression, should be reflected as high APT signal. In their study, a total of 32 patients with possible tumour progression, after chemoradiation, were examined. Figure 2.50, shows a typical case of the true-progression patient group and Figure 2.51, shows a case of pseudo-progression.

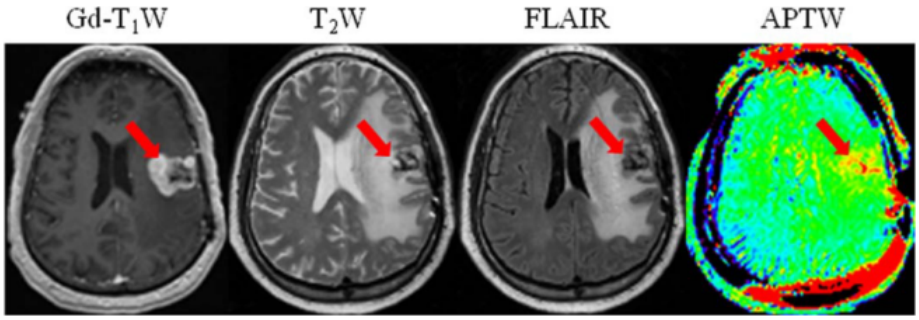


Figure 2.50: Conventional MRI and APT CEST images from a 49-year-old man with tumour progression. The patient had a new contrast-enhancing lesion, 1 month after completion of chemoradiation. Image taken from [132].

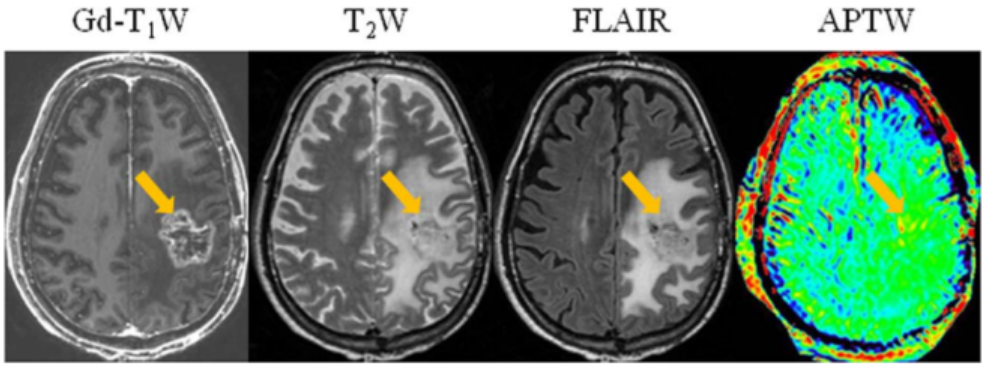


Figure 2.51: Conventional MRI and APT CEST images from a 65-year-old man with pseudo-progression. Indications of new lesion can be seen on conventional MRI images. On the other hand, the lesion appears iso-intense to contralateral healthy brain, on the APT image. Image taken from [132].

The cut-off APT intensity values, to distinguish between true and pseudo-progression were 2.42% and 2.54% with [85% sensitivity - 100% specificity] and [95% sensitivity -

91.7% specificity], respectively. In a larger glioma patient group, (n=65), the addition of APT CEST to contrast-enhanced T_1 weighted imaging significantly improved the cross-validated AUC, from 0.58–0.74 to 0.89–0.91, for differentiating true-progression from pseudo-progression [155]. Both these studies were performed at 3T, with the APT CEST scan being only ~ 10 minutes. APT weighed imaging, can thus provide, a rapid and non-invasive method, for diagnosing true tumour progression in the clinic.

One scenario that complicates the interpretation of the measured APT signal, is the presence of haemorrhagic regions around active tumours. APT values in arteries and highly vascular glioma xenografts were found to exhibit a high MTR_{asym} ($\simeq$ 12%), at room temperature and for B_1 powers between 1-3μT [53, 241, 261]. Thus, haemorrhagic regions, will also appear hyper-intense on APT images, similar to active tumour components. Perhaps a combination of APT and susceptibility weighted imaging can differentiate between blood and solid tumour regions.

We note here that, using $B_1 = 2\mu T$, has been shown to nullify the MTR_{asym}, in healthy tissue, as APT and semi-solid MT cancel out [258]. This allows to better identify hyper-intense tumour regions, with minimal MT contributions. APT signal contamination from other exchangeable protons, of proteins and peptides is also small, as the latter species, do not in general fulfil the slow to intermediate requirement, at 3T. Nevertheless, nuclear overhauser effects from aliphatic protons might still be present in the measured signal, reducing its magnitude and compromising the APT contrast.

Coincidentally, nuclear overhauser effects (NOE), from aliphatic protons, are centred at the exact opposite frequency from APT, i.e -3.5 ppm from water [88], with their range being from -2 ppm to -5 ppm. The NOE effect increases with macromolecular concentration and B_1 power, and was found to be, pH insensitive by Jin et al. [85], using asymmetry analysis, and linearly dependent on pH, by Jones et al. [90], using Lorentzian fitting. White matter exhibits larger NOEs than grey matter, at a ratio 2:1. For NOE-mediated CEST signal, in-vivo, an optimal B_1= 1μT, has been reported [153, 123]. The most possible interaction, between mobile lipids (long T_2) and meas-

ured water signal, is through intermolecular NOEs [30]. The latter proceeds either via dipolar or chemical exchange mechanism, similar to APT. However, as NOE is pH dependent [90], it is believed that NOE effects proceed via chemical exchange, just like APT does.

To account for the presence of NOE, the MTR_{asym} relationship is expressed as follows:

$$\begin{aligned} MTR_{asym}(offset) &= MTR(+offset) - MTR(-offset) \\ &= [S_{sat}(-offset) - S_{sat}(+offset)]/S_0 \end{aligned} \tag{2.3.1}$$

and specifically for APT imaging, equation 2.3.1 is written as:

$$\begin{aligned} MTR_{asym}(3.5ppm) &= APTR + MTR'_{asym}(3.5ppm) \\ &\simeq APTR - NOER(-3.5ppm) \end{aligned}$$

MTR'$_{asym}$ was previously thought to represent the inherent solid macromolecular MT [76], which causes a negative background for the measured MTR_{asym} [88, 165]. However, Zhou et al. suggested that, this term might arise from intermolecular/intramolecular NOEs, of mobile aliphatic protons [269]. Further, in-vitro experiments, showed that, presence of lipids, results in negative MTR_{asym} values, for low B_1 values (0.6-1μT). This negative asymmetry tends to zero, as the pulse power is increased, with 2μT, being the power, that APT contrast dominates over NOE, at 4.7T. Lipid suppression, using a Gaussian-shaped chemical shift selective pulse, was also found to minimise the NOEs, in high lipid brain regions [130].

Figure 2.52, shows the Z-spectra and asymmetry curves, for tumour and contralateral tissue, at two irradiation powers, at 4.7T, in-vivo. It can be seen that, the tumour

exhibits lower NOEs than healthy tissue. In addition, the measured MTR_{asym} in tumour, is negative, owning to the presence of NOEs. As B_1 power increases, MTR_{asym}, becomes positive, as the NOE contribution is lessened. Even though the presence of NOEs does indeed decrease the magnitude of APT, the contrast (ΔMTR_{asym}) between tumour-healthy tissue, is increased. Therefore, the NOE signal is a positive confounding factor, in tumour APT imaging.

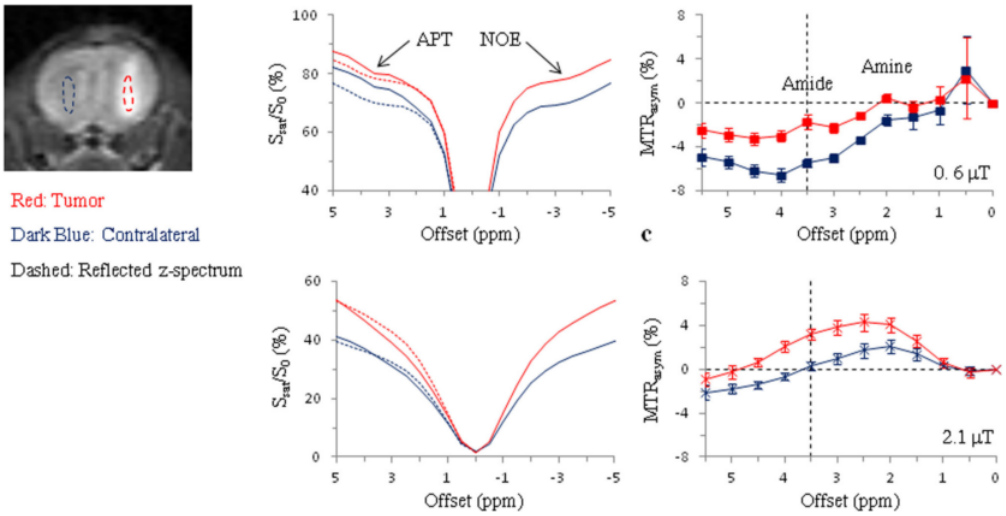


Figure 2.52: APT CEST, of a rat tumour model at 4.7T. **Top:** Z-spectra and asymmetry curves for $B_1 = 0.6\mu T$. **Bottom:** Z-spectra and asymmetry curves for $B_1 = 2.1\mu T$. Image taken from [269].

In a clinical study of glioblastoma (GBM) patients, at 7T, Paech et al. [153] observed that, NOE effects in GBM contrast-enhanced T_1 tumours and necrotic regions, were decreased as compared to healthy white matter. Their acquisition was termed, NOE-mediated CEST, as a low B_1 power ($0.7\mu T$) yields NOE-dominated contrast. As expected, the measured MTR_{asym} values were negative, due to the presence of the NOE effects. Healthy white matter showed even more negative MTR_{asym} values. Figure 2.53, shows that because tumours are characterised by reduced NOE effects, their corresponding MTR_{asym} is increased, as compared to normal white matter.

NOE changes minimally with pH (~ 1%) [90]. In addition, intracellular tumour pH (as opposed to extracellular), slightly increases (0.1 pH) [52, 214] in tumours. Thus, the NOE reduction in tumours, cannot be attributed to pH changes. Due to its dipolar

and/or chemical exchange nature, NOE is thought to be dependent on protein mobility, with high mobile species having lower NOE effects. The latter, along with the fact that water content is increased in tumours [148, 8], could explain the drop in NOE effects. Finally, protein denaturation has been linked with decreased NOE effects [245]. NOE was also shown, to not be correlated with ADC values, but there is an indication of a negative correlation with tumour cellularity, in GBMs [154].

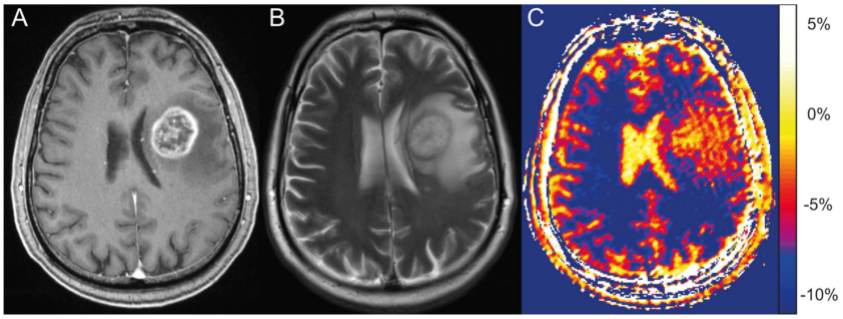


Figure 2.53: Left frontal glioblastoma of a 59 year old patient at 3 Tesla. **A:** Gd-T_1 **B:** T_2 weighted and **C:** NOE-mediated CEST images. As NOE effects drop in tumours, MTR_{asym} is increased. Image taken from [153].

Questions, on whether the APT signal really reflects endogenous mobile proteins, were raised, after compensating the measured signal for the water relaxation T_1 time [235, 247]. This is a reasonable correction, as the APT signal does depend on water relaxation rate [235, 194], along with concomitant MT effects [168, 187]. Data from a pre-clinical study, Figure 2.54, show that MTR_{asym} is inversely correlated with macromolecular content (PSR - pool size ratio of macromolecular protons and water), whereas the relaxation compensated metric, AREX [246], for both APT (AREX-APT) and NOE (AREX-NOE), is not. Similarly, MTR_{asym} is inversely correlated with R_1, while no correlation exists, between AREX-APT and AREX-NOE with R_1. Furthermore, only AREX-NOE was found to be correlated with R_2, while both MTR_{asym} and AREX-NOE correlate with chemical exchange rate (k_{mf}).

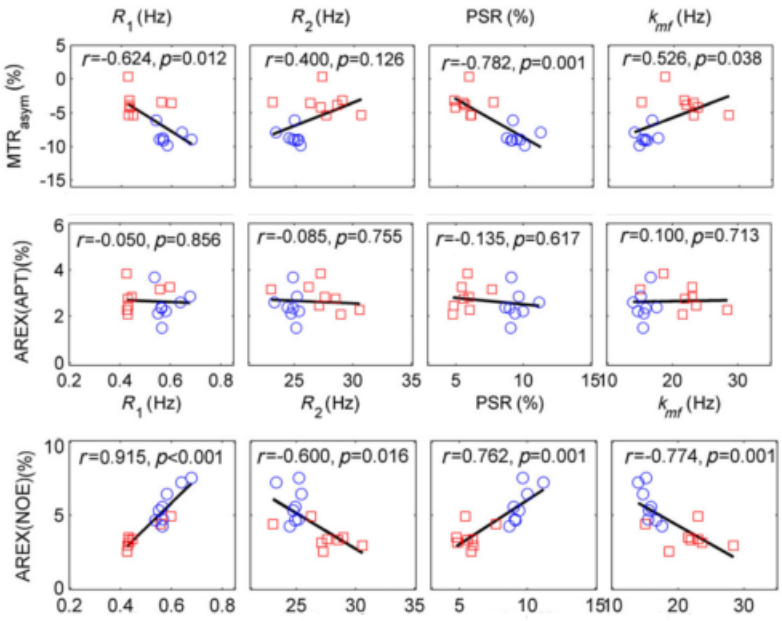


Figure 2.54: Correlations of MTR_{asym}, AREX(APT) and AREX(NOE), with water relation rates R_1 and R_2, pool size ratio (PSR) and chemical exchange rate (k_{mf}). Red squares represent the mean values of each tumour, and the blue circles are the mean values of each region of interest (ROI) of contralateral normal tissue. The Spearman's rank correlation coefficient (r) and p value of each correlation, along with the linear regression line, are also shown. Image taken from [235].

In a clinical study, at 7T [247], AREX was compared with classic MTR_{asym} [264] and Lorentzian difference [90], in characterising high grade gliomas. An example presented in Figure 2.55. This is a glioblastoma patient showing a tumour enhancing ring and central necrosis (Figure 2.55 **A**). MTR_{asym}, shows elevated signal, in a region similar to Gd-T_1 image. Some hyper-intensity is also seen in the necrotic area (Figure 2.55 **B**). Isolated APT and NOE effects, from Lorentzian fitting of the data, show the hyper-intense ring and iso-intense necrosis (Figure 2.55 **C**) and a hypo-intense whole tumour region (Figure 2.55 **D**). Further T_1 corrected data show an iso-intense tumour (Figure 2.55 **E**) and an even higher contrast hypo-intense tumour (Figure 2.55 **F**). In summary, Lorentzian fitting provides a result, similar to Gd-T_1 image, as far as APT contrast is concerned, without the need for contrast injection. In addition, the relaxation compensated AREX-NOE shows a higher contrast between the tumour and normal white matter, than the contrast given by Lorentzian fitting of the NOE effect

alone.

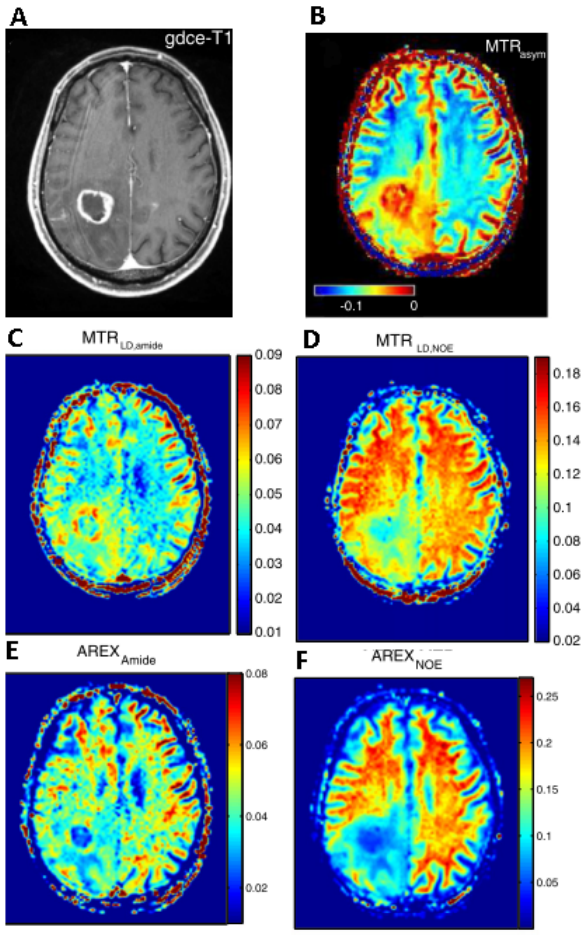


Figure 2.55: Various MRI images of a glioblastoma patient, acquired at 7T. **A:** Gd-T_1 **B:** MTR_{asym} **C:** Amide Lorentzian difference **D:** NOE Lorentzian difference **E:** AREX-APT **F:** AREX-NOE. Image taken from [247].

We note here that, the relaxation-compensated AREX metric, is valid for long saturation times, where the system has acquired its steady state. For shorter saturation times, the Lorentzian difference already provides the apparent exchange dependent relaxation [247]. The fact that AREX-APT shows the same contrast between tumour and healthy tissue is somewhat surprising. Perhaps, there are NOE contributions in the tumour that actually don't decrease, but on the contrary, increase. This would eliminate any AREX-APT signal. In fact, these downfield NOE effects at +3.5 ppm, have been observed in pre-clinical studies [120, 81] and are though to arise from aromatic proton groups. A method for suppressing these aromatic NOE effects is described in

reference [249]. This method assumes a constant ratio between the downfield and upfield NOE effects and evaluates the former based on the more accessible aliphatic protons (upfield NOE at -3.5 ppm). As a result, the downfield NOE suppressed contrast was found to be remarkably similar to the Gd enhancing tumour area , glioblastoma patients (Figure 2.56).

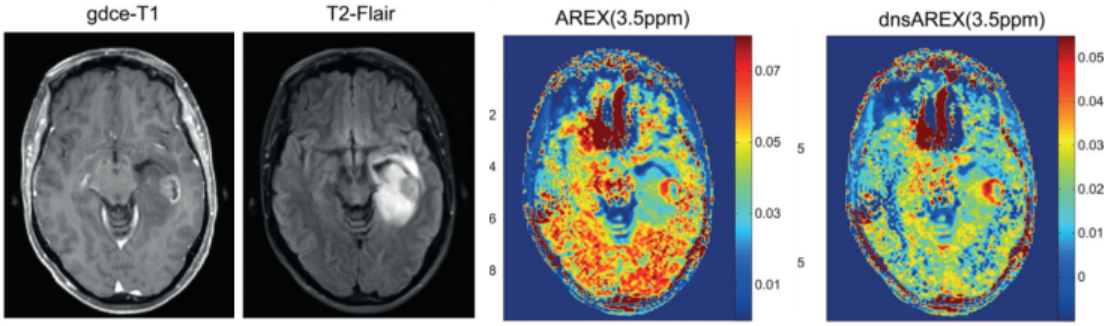


Figure 2.56: Gd-T_1, T_2-FLAIR, AREX and AREX (dnsAREX) images of a glioblastoma patient at 7T. Even though the tumour enhancing ring is identified on the AREX image, the signal size is also similar to the contralateral region. On the contrary, the contrast on the dnsAREX image shows a significantly higher intensity in the enhancement region compared with contralateral white matter. Image taken from [249].

Even though amide proton transfer CEST is of special interest in brain tumour imaging, the technique has also been used in characterising a variety of conditions such as, Parkinson's disease [117, 118, 119], breast cancer [37, 36, 101, 33], prostate cancer [79], lymphomas [80], ischaemia and haemorrhage [178], HIFU treatment evaluation [66] and paediatric brain development [252].

Chapter 3

CEST: In-silico optimisation

3.1 Introduction

Chemical Exchange Saturation Transfer (CEST) is a novel and non-invasive molecular MR technique [222], that under certain physico-chemical and experimental conditions allows the detection of compounds containing amide, amine and hydroxyl proton groups, that are in chemical exchange with free water molecules. The signal arises from macromolecular protons, that are highly restricted ('bound') and are therefore characterised by very short T_2 relaxation times (μsec). Moreover, their concentrations are in the milli-molar range. The practical implication of the very low transverse relaxation times and concentrations is that these protons cannot be directly detected by an MRI experiment. Their detection is nevertheless feasible, indirectly, and this is facilitated via the natural mechanisms of magnetisation transfer and chemical exchange [229].

CEST has been utilised as a contrast enhancement mechanism in a variety of pathologies including: skeletal muscle damage [140], diabetes or insulin-related diseases [212], osteoarthritis and vertebral disk degeneration [169], Parkinson's disease [119], Alzheimer's disease [63], stroke [191, 205, 65] and brain tumours [88, 266, 263, 210, 165, 223, 172, 271].

As a frequency specific application, CEST is extremely susceptible to B_0 and B_1 inhomogeneities and an accurate contrast measurement heavily relies on correcting for the latter influences [100, 190, 226]. In addition, when the saturation time $\simeq T_{1,water}$, then the CEST effects are scaled by the longitudinal relaxation of water and should be corrected accordingly [246].

Optimising a CEST experiment involves identifying the optimal values of the experimental variables for which the CEST signal is reliably being detected. For continuous wave irradiation, the parameters include the irradiation B_1 power, the pool size and the saturation time [193], whereas for pulsed CEST there are a couple more parameters to consider, namely, the number of pre-pulses, duration and inter-pulse delay (RF duty cycle) [170].

The optimisation can either be done by directly and explicitly setting the values of the experimental parameters and measuring the signal, directly from the scanner, or by a simulating the response of the physical system under various conditions. The latter approach was used here to describe the response of a 2-pool model [228], under continuous wave irradiation and variable B_1, pool size and saturation time. Furthermore, the response of the 2-pool model was also investigated under different levels of SNR. The relationship between the measured APT signal and SNR was derived, along with the error and relative accuracy in quantifying the CEST effect in the presence of noise. This study is useful in outlining the steps taken in order to identify the impact of experimental parameters, including the SNR, in optimising CEST studies.

3.2 Materials and Methods

A two pool model was implemented, as described in reference [228]. The time dependent Bloch equations for such a model are:

$$\begin{aligned}
\frac{dM_x^a}{dt} &= \Delta\omega_a M_y^a(t) - R_2^a M_x^a(t) - k_a M_x^a(t) + k_b M_x^b(t) \\
\frac{dM_x^b}{dt} &= \Delta\omega_b M_y^b(t) - R_2^b M_x^b(t) - k_b M_x^b(t) + k_a M_x^a(t) \\
\frac{dM_y^a}{dt} &= -\Delta\omega_a M_x^a(t) - R_2^a M_y^a(t) - k_a M_y^a(t) + k_b M_y^b(t) + \omega_1 M_z^a(t) \\
\frac{dM_y^b}{dt} &= -\Delta\omega_b M_x^b(t) - R_2^b M_y^b(t) - k_b M_y^b(t) + k_a M_y^a(t) + \omega_1 M_z^b(t) \\
\frac{dM_z^a}{dt} &= -\omega_1 M_y^a(t) - R_1^a [M_z^a(t) - M_0^a] - k_a M_z^a(t) + k_b M_z^b(t) \\
\frac{dM_z^b}{dt} &= -\omega_1 M_y^b(t) - R_1^b [M_z^b(t) - M_0^b] - k_b M_z^b(t) + k_a M_z^a(t)
\end{aligned} \tag{3.2.1}$$

The subscripts a and b, refer to the two exchanging proton pools. In this case, bulk water (a) and APT (b). For example, $M_x^a(t)$ denotes the x component of the magnetisation in bulk water at time t. k_a and k_b refer to the exchange rates from pool a to b and from b to a respectively. These rates are measured in s^{-1}. M_0^a and M_0^b denote the thermal equilibrium magnetisation of each pool. $\Delta\omega_a$ and $\Delta\omega_b$ are calculated as ω_a- ω and ω_b- ω respectively, where ω_a and ω_b are the resonant frequencies of pools a and b respectively. The frequency of the RF irradiation is denoted by ω, and the RF pulse power is denoted by ω_1. Finally, $R_{1,2}^{a,b}$ describe the longitudinal and transverse relaxation rates of each pool. Z-spectra were simulated by numerically solving the equations above, using the matrix exponential (*expm* in Matlab) method from reference [146], where the system of 6 differential equations is first reduced to a single, homogeneous linear differential equation (vector equation), and then solved using a matrix operation like so (we work in the rotating frame and it is assumed that the RF pulse is applied along the x-axis of the frame):

$$\frac{dM}{dt} = A \cdot M^{T}$$

with

$$M = (M_x^a(t)\ \ M_y^a(t)\ \ M_z^a(t)\ \ M_x^b(t)\ \ M_y^b(t)\ \ M_z^b(t)\ \ 1)$$

and

$$\mathcal{A} = \begin{pmatrix} -(R2a + ka) & kb & da(i) & 0 & 0 & 0 & 0 \\ ka & -(R2b + kb) & 0 & db(i) & 0 & 0 & 0 \\ -(da(i)) & 0 & -(R2a + ka) & kb & w1 & 0 & 0 \\ 0 & -(db(i)) & ka & -(R2b + kb) & 0 & w1 & 0 \\ 0 & 0 & -w1 & 0 & -(R1a + ka) & kb & R1a * M0a \\ 0 & 0 & 0 & -w1 & ka & -(R1b + kb) & R1b * M0b \\ 0 & 0 & 0 & 0 & 0 & 0 & 0 \end{pmatrix}$$

The major parameter values of each pool are described in the following table (Table 3.1):

	water	APT
T_1 [s]	1.4	1
T_2 [s]	0.5	0.033
offset [ppm]	0	3.5
equilibrium magnetisation (pool size)	1	0.001
exchange rate [s^{-1}]	-	50

Table 3.1: Simulation parameters of the 2-pool model.

Other parameters were set as follows: $B_0 = 3T$, $t_{sat} = 2s$, frequency sweep$\rightarrow -10$ to $+10$ ppm, $B_1 = 1\mu T$, single pulse.

As a first step, the detection dependence of an 'ideal', noise-free, APT signal on experimental parameters was investigated. As such, three experimental parameters, namely, the saturation power, pool size and saturation time were individually varied. Subsequently, the 'true' APT signal was calculated after each experimental parameter change. The exchange rate was not considered in this analysis as it is an inherent property of a proton pool and thus cannot be explicitly determined in real experiments.

Even though SNR is an outcome of real MRI experiments, in a simulation study, it can be one of the parameters that can be varied explicitly. To determine therefore whether SNR affects the detection sensitivity of the APT signal, a noise-free Z-spectrum of ~4% APT was simulated. This spectrum served as the benchmark, against which noisy Z-spectra were compared to. To generate the noisy spectra, the 'ideal' spectrum of ~4% APT was superimposed with random noise (*rand* function in Matlab - Note: the histogram of the values returned by *rand,* suggests a roughly normal distribution with a mean close, but not exactly, 0). The standard deviation of the noise was used to calculate the SNR, defined as $\frac{M_0}{\sigma}$, where σ is the standard deviation and M_0 the equilibrium magnetisation. The APT signal in the noisy spectra was quantified by fitting the 2-pool model (equation 3.2.1) in the spectra (*fit* function in Matlab) using the Levenberg-Marquardt algorithm. The starting values and bounds of the model parameters that were allowed to vary during the fit are shown in the next table:

	water [ppm]	$R_{2,water}[s^{-1}]$	APT [ppm]	k_{APT} $[s^{-1}]$	f_{APT}	$R_{2,APT}[s^{-1}]$
starting	0.3	2	3.5	50	0.001	1
lower bound	0	1	3	30	0	0.5
upper bound	1	4	4	70	0.005	2

Table 3.2: 2-pool model parameter variation for fitting the noisy Z-spectra. k_{APT} and f_{APT} denote the exchange rate and pool size of the APT pool respectively.

APT values at +3.5ppm were calculated for the following SNR values: 100, 90, 80, 70, 60, 50, 40, 30, 20 and 10, using asymmetry analysis and thus by subtracting the downfield values, of the normalised Z-spectra, from the corresponding upfield ones according to the following equation:

$$MTR_{asym}(\Delta\Omega) = \frac{MT(-\Delta\Omega) - MT(+\Delta\Omega)}{M_0} \tag{3.2.2}$$

The effects of the SNR on the sensitivity detection of the APT peak are first described graphically and then through two measures:

1) percentage error, which was defined as:

$$\frac{APT_{true} - APT_{noise}}{APT_{true}} \times 100 \tag{3.2.3}$$

and

2) relative accuracy, which was defined as:

$$\frac{APT_{noise}}{APT_{true}} \tag{3.2.4}$$

All analysis was performed in Matlab (The MathWorks, Natick, 2018a).

3.3 Results

We first examine the feasibility of detecting the APT peak at, +3.5ppm, in noiseless spectra for different values of B_1 power, pool size and saturation time. These parameters were varied individually, one by one, while keeping the other parameters fixed.

Figure 3.1 shows the effect of various B_1 powers on the magnitude of the CEST peak. For the model under investigation, the optimal power is 1μT, as it corresponds to the largest peak. Although peak magnitude is the most important outcome in a CEST experiment, the width of the measured peaks and of the water line-shape must also be considered while optimising an experiment. The reason for this is that in more complex systems, and especially in-vivo, there may be proton groups resonating in neighbouring frequencies, to that of interest, and line broadening will result in erroneous quantification of the desired peak because of peak overlaps.

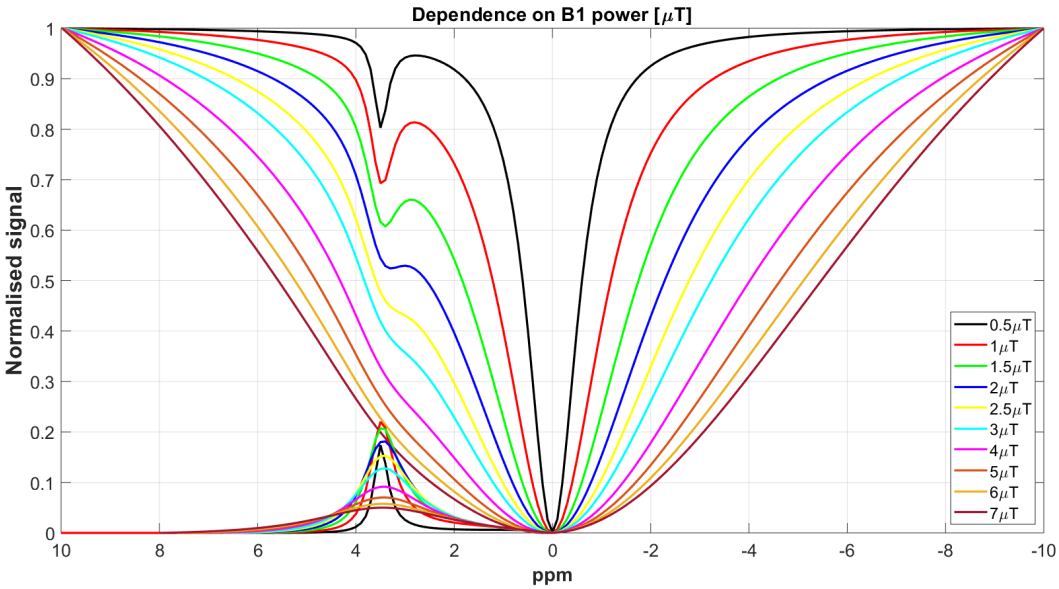


Figure 3.1: Dependence of the APT CEST signal on B_1 power.

It is clear from Figure 3.1, that the higher the pulse power (1.5μT and above) the broader the Z-spectrum becomes. This width increase is detrimental for the peak's magnitude for B_1 powers exceeding 2.5μT and further increases gradually obliviate the APT peak because of large spill-over effects.

The relationship between the CEST signal and B_1 power is demonstrated in Figure 3.2. Generally, low pulse power leads to lower CEST effects and high pulse power leads to higher CEST effects. The lowest B_1 power simulated here was 0.5μT and the contrast generation increase is evident once the power becomes 1μT. However, peak amplification does stop at that exact pulse power, as further increases, result in non-negligible spill-over effects and subsequent and gradual 'masking' of the desired peak for greater B_1 powers.

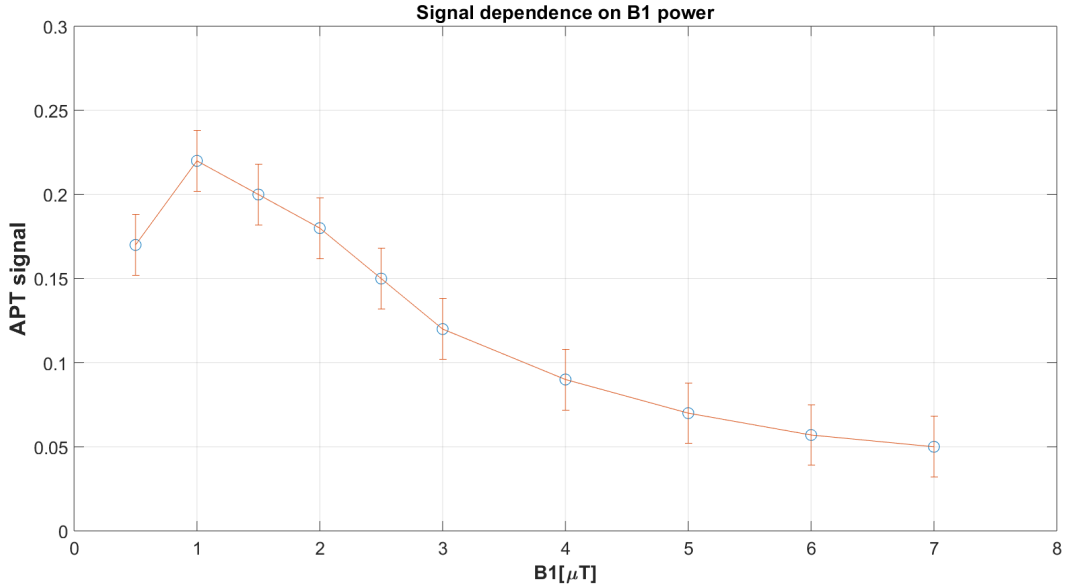


Figure 3.2: Relationship between the measured APT signal and B_1 power.

Figure 3.3 shows the effect of various APT pool sizes on the magnitude of the CEST peak. The interpretation of the result is straightforward: CEST signal grows proportionally to the size of the proton exchange pool. The reason for this is that when modelling CEST systems, the equilibrium magnetisations are set to be proportional to the size of their corresponding pools. For example, bulk water equilibrium magnetisation is always set to 1 (maximum value in the simulation), while the equilibrium magnetisations of any other proton exchange groups are set equal to values shown in the legend of Figure 3.3. In fact, CEST signal is linearly proportional to pool size as demonstrated in Figure 3.4. Despite the fact that pool sizes ~0.01 are unrealistic,

especially in-vivo, the curves do reflect an accurate response of the measured signal as a function of pool size.

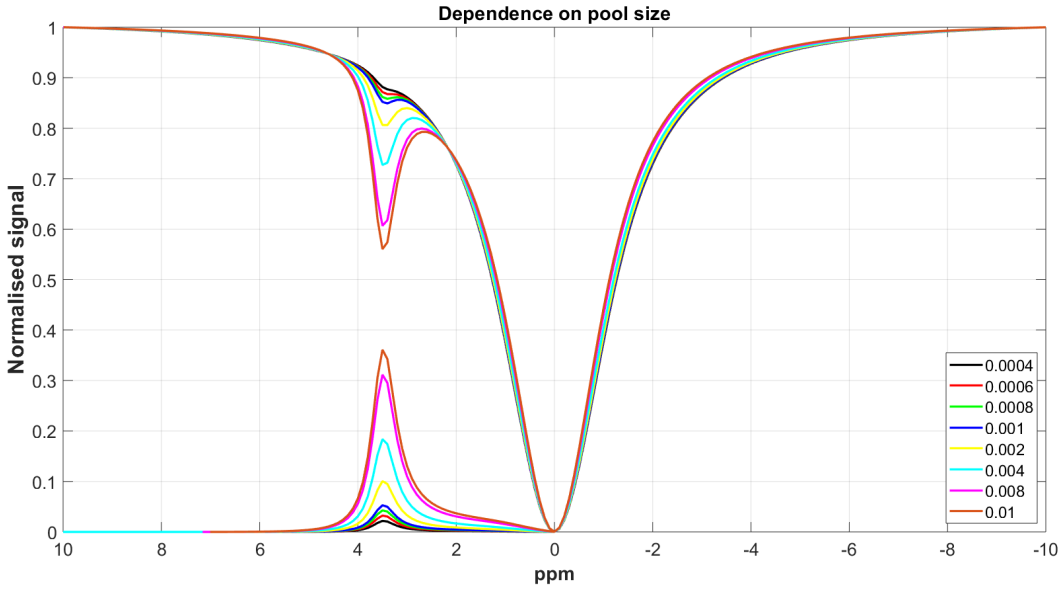


Figure 3.3: Dependence of the APT CEST signal on APT pool size.

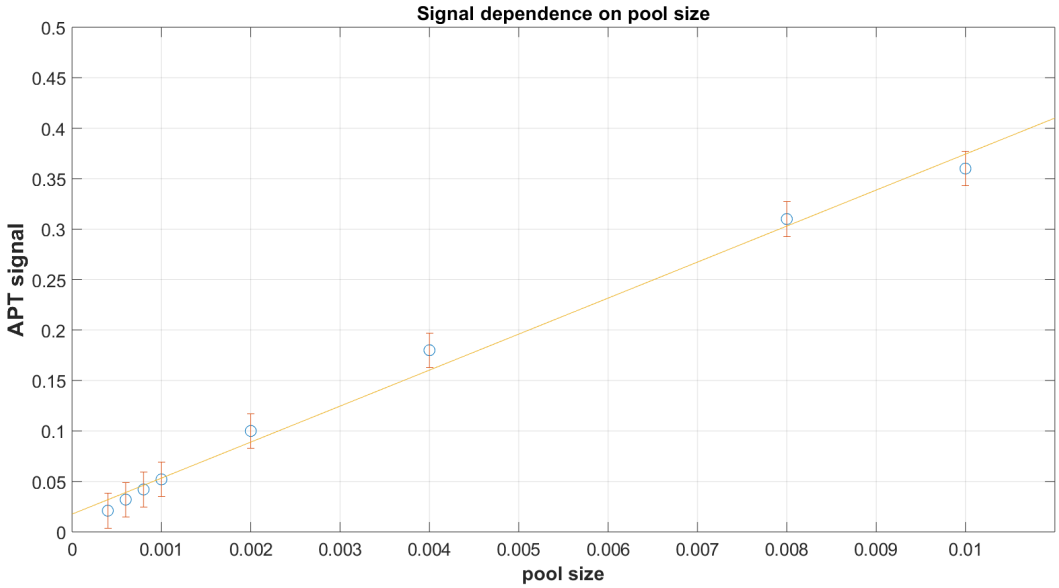


Figure 3.4: Linear relationship between the measured APT signal and APT pool size.

Finally, we look at the effect of various saturation times on the magnitude of the APT CEST peak. The response of the 2-pool model for various such saturation times is shown in Figure 3.5. The benefit of longer saturation is seen up until ~2 seconds, as the APT signal keeps growing and the pool is fully saturated. Nevertheless, saturating for longer times does not result in greater CEST effects. We can conclude therefore that the CEST effect keeps accumulating as long as the saturation time is increasing. Nevertheless, eventually, the effect reaches its steady state and further increase of saturation time has no impact on the magnitude of the measured signal.

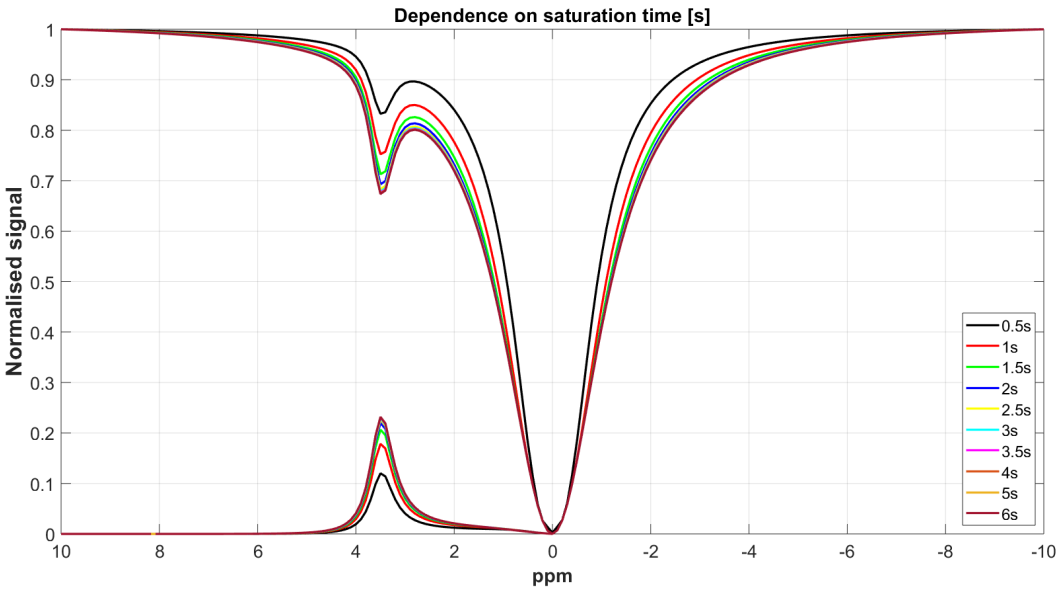


Figure 3.5: Dependence of the APT CEST signal on saturation time.

This conclusion is more accurately illustrated in Figure 3.6. CEST contrast keeps growing up until ~3 seconds of saturation time and then reaches a plateau. This is the steady state for the model under investigation. No matter how long the pool is saturated after this limit, the magnitude of detectable APT peak at +3.5ppm will not increase. This is an important point to consider as it informs on the optimal saturation time, given the MRI application, while at the same time preventing the usage of unnecessarily long acquisition schemes that have no real benefit in a CEST experiment and only prolong the overall scan time. The latter should be avoided, particularly in

multi-slice/volumetric acquisitions, where greater sample coverage already implies a longer scan time. Additionally, for in-vivo applications, longer saturation times result in more power deposition in tissues and thus there is always the risk of exceeding the SAR safety limits.

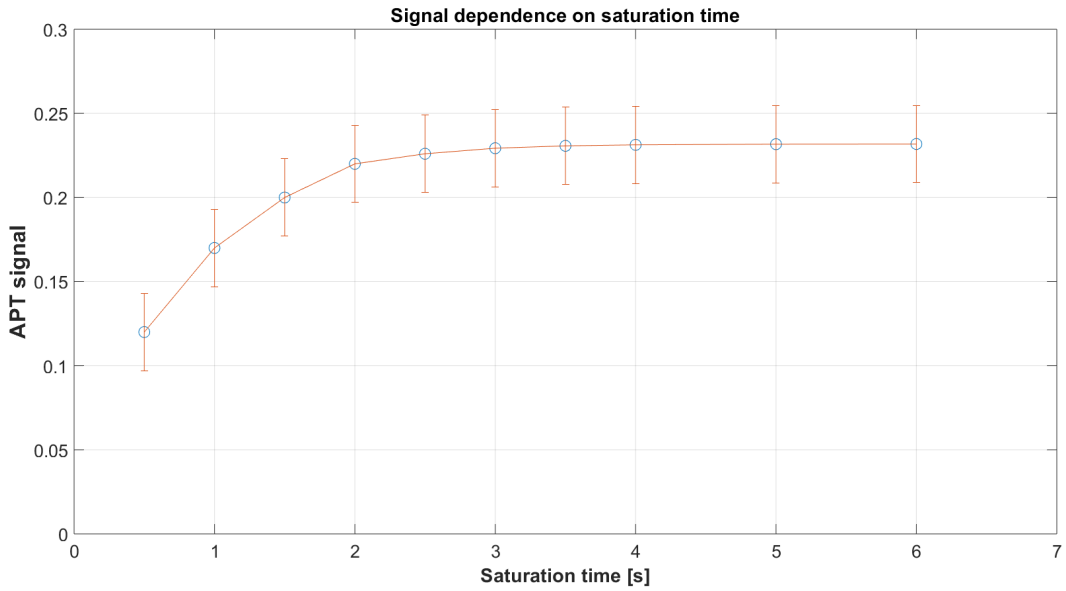


Figure 3.6: Relationship between the measured APT signal and saturation time. The CEST effect plateaus at 3s and beyond.

So far the analysis was focused on 'ideal', noise-free Z-spectra. However, it would be useful to also investigate the impact of SNR on the ability to detect CEST effects, as the presence of noise is an unavoidable reality in every MRI experiment. As such, the following paragraphs describe the detection of an APT peak, of ~4% in magnitude, under the effect of various noise levels, superimposed on the 'ideal' ~4% APT model. The quantification of the APT signal was facilitated by fitting a 2-pool model (equations 3.2.1) on the noisy, simulated data, as described in the Materials and Methods section and by using equation 3.2.2 and further investigation and interpretation of the results was facilitated by using equations 3.2.3 and 3.2.4.

Figure 3.7 shows the starting spectrum for analysing the SNR effects on the detectability of the APT peak at +3.5ppm. This benchmark spectrum was generated with the following model parameters: $T_{1,water} = 1.4s$, $T_{2,water} = 0.5s$, $T_{1,APT} = 1s$,

$T_{2,APT} = 0.033s$, APT pool size of 0.001, exchange rate of $50s^{-1}$, $B_1 = 1\mu T$, $B_0 = 3T$ and saturation time of 2s.

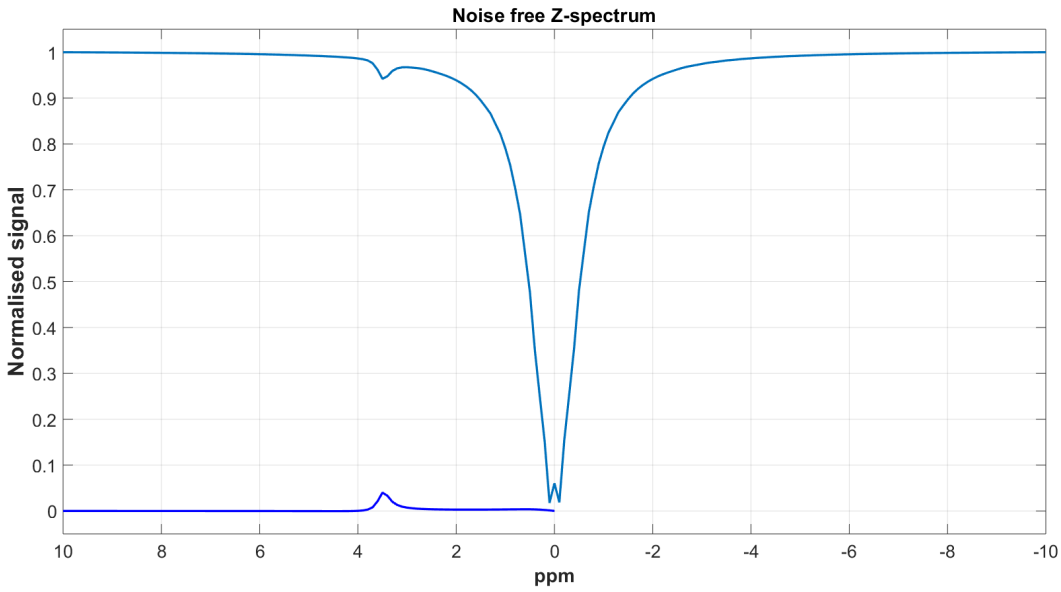


Figure 3.7: Noise-free spectrum. The benchmark for analysing the effects of SNR on the APT peak.

The spectrum in Figure 3.7 is exactly the same as the first noisy spectrum considered in this analysis, namely the spectrum for SNR = 100. The said spectrum is illustrated in the next figure (Figure 3.8). The figure contains 3 sets of data: the benchmark Z-spectrum (solid blue line), the data after the addition of random noise (red dots) and a yellow dashed line indicating the fitting of the 2-pool model on the noisy data. The magnitude of the CEST effect is illustrated at the bottom of the spectrum for both the noise-free spectrum (solid blue line) and the fitted spectrum (dashed yellow line). Obviously, for SNR = 100, no difference between the ideal and fitted peaks exists. However, that is not the case for the remaining values of SNR tested here.

The convention of representing the 3 sets of data was carried through every generated noisy Z-spectrum for the remaining SNR values of 90, 80, 70, 60, 50, 40, 30, 20 and 10. For demonstration purposes, the fitted Z-spectrum for an intermediate SNR = 50 and for the lowest SNR value of 10 are also shown in Figures 3.9 and 3.10.

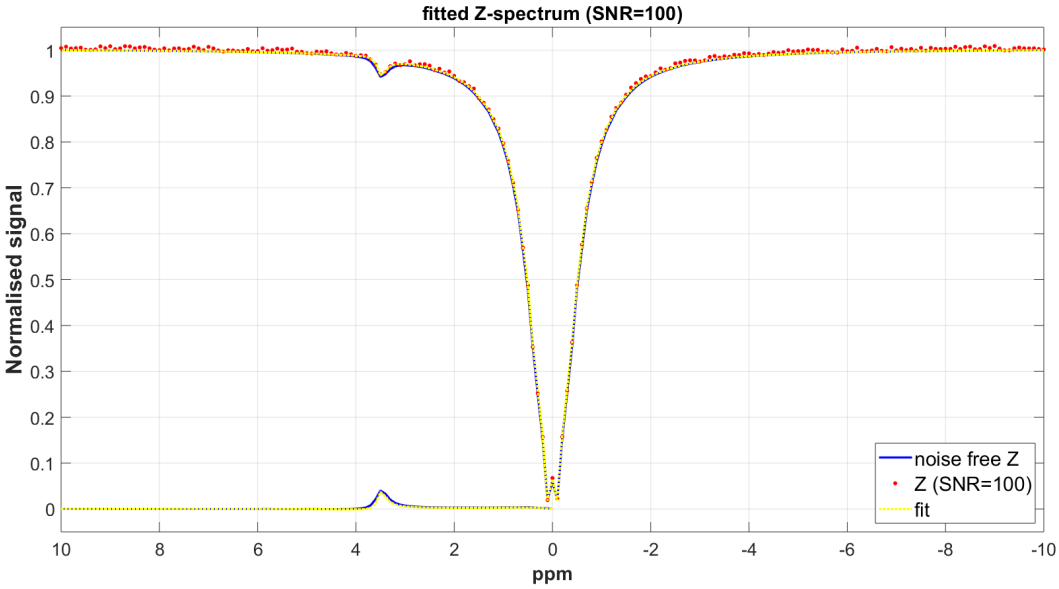


Figure 3.8: Fitting the benchmark Z-spectrum with the 2-pool model equations while SNR = 100. The noise-free and fitted spectra match one another.

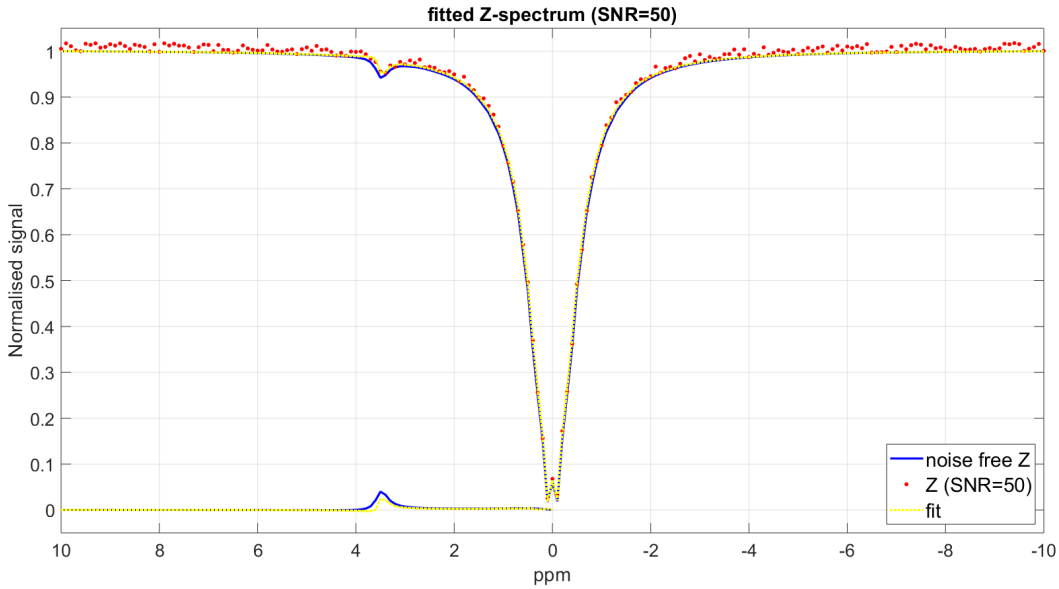


Figure 3.9: Fitting the benchmark Z-spectrum with the 2-pool model equations for an intermediate SNR = 50. Evidently, the fitted APT peak differs from the ideal one.

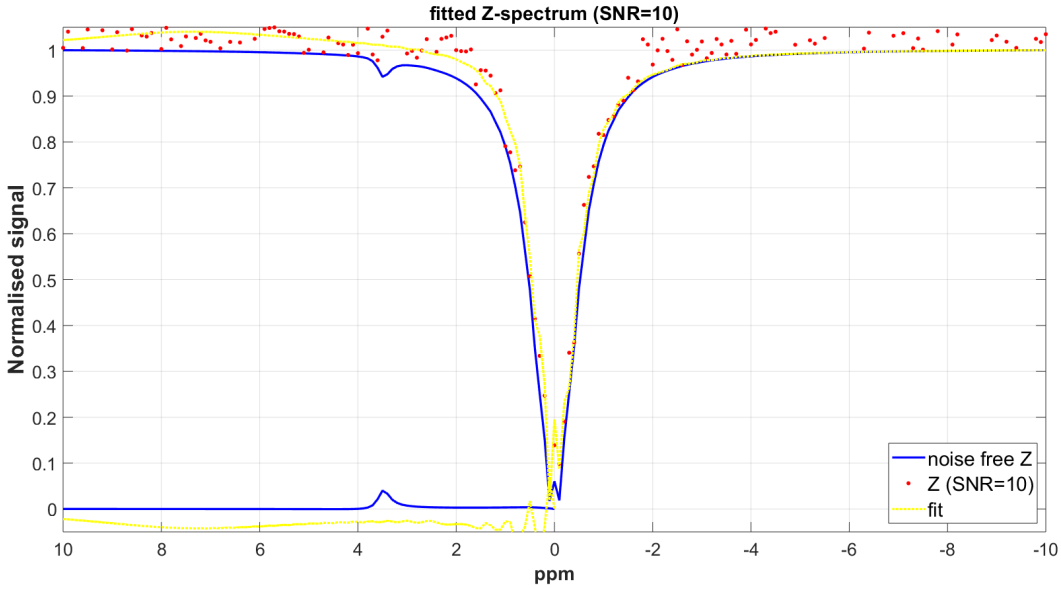


Figure 3.10: Fitting the benchmark Z-spectrum with the 2-pool model equations for SNR = 10. The fitted APT peak can no longer be quantified.

Figure 3.9 is indicative of the impact of increasing noise in CEST experiments in the sense that it diminishes the effectiveness of fitting an experimental Z-spectrum in order to quantify the desired CEST effects. This trend, of sequentially diminishing quantification effectiveness in the presence of increasing noise levels, was consistently observed until the lowest investigated SNR = 10. In fact, for such a low SNR, the fitting severely underperforms and that in turn results in a total inability to quantify any CEST effects, as indicated in Figure 3.10.

The fitted APT peaks for all SNR values are jointly plotted in Figure 3.11 along with a magnified version of the result. We note here that the result for SNR =10 is excluded from the magnified image as it doesn't carry any peak quantification potential. Furthermore, the reader's attention should be drawn to the correct numerical values of the peaks in the magnified image and particularly at where 0 resides in each image. The mismatch was unavoidable, for illustration purposes, and the correct scale of the magnified image is indicated with light grey at the right side of the magnified image.

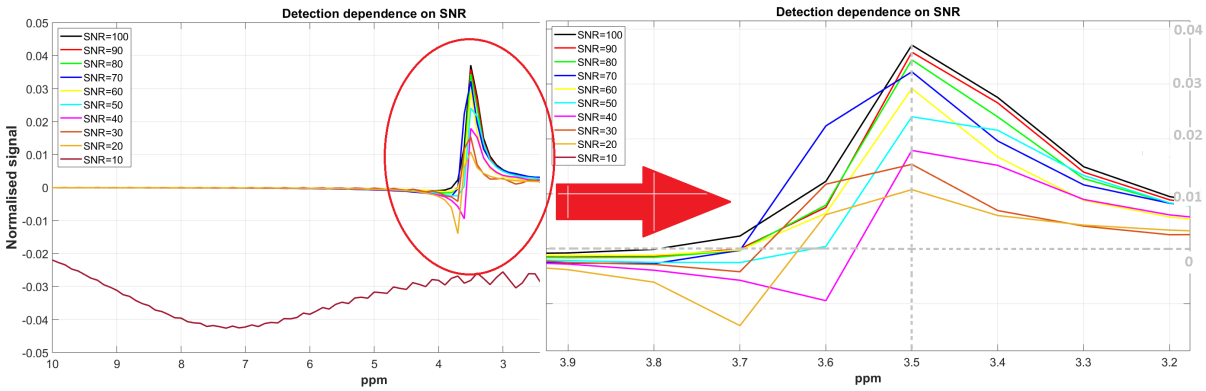


Figure 3.11: Fitted APT magnitude at +3.5ppm for each one of the SNR values tested in this study. To the aid visual interpretation of the result, a magnified version of the circled area is also shown.

Figure 3.11 shows that each time the SNR is dropped by 10, the magnitude of the measured APT peak also diminishes in a linear fashion by a good approximation. This result is illustrated in the figure below, where the value of each APT effect, as quantified by fitting the 2-pool model on the noisy data, is plotted against SNR.

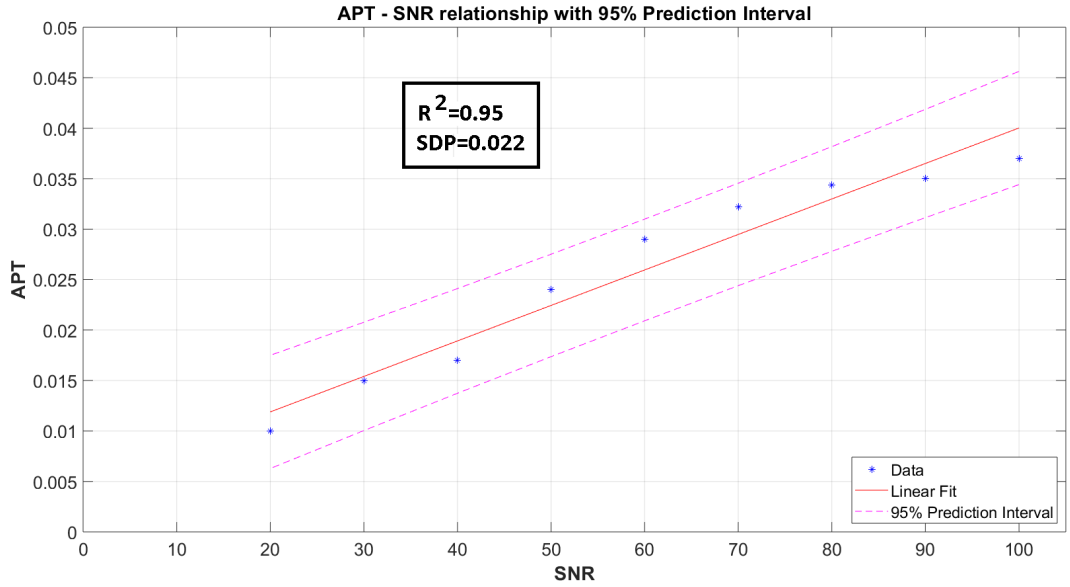


Figure 3.12: The relationship between the CEST effect and SNR for the 2-pool model studied here is linear.

A linear fit (red line in Figure 3.12) seems to describe the data well ($R^2 = 0.95$) and can serve as a guide in predicting the impact of a certain level of SNR on the ability

to quantify the CEST effect of interest. A 95% prediction interval (dashed lines) is also indicated on each side of the fitted line, in Figure 3.12, indicating the range within which any new observation should fall. Finally, the standard deviation of prediction (SDP) has also been calculated (SDP=0.022). This measure describes standard deviation of the differences between the data points and the fit and in this case is 0.022 or 2.2% APT units.

By using equation 3.2.3 we can now examine the percentage error in quantifying the APT peak in the presence of noise. The relationship between this error and SNR is described in Figure 3.13.

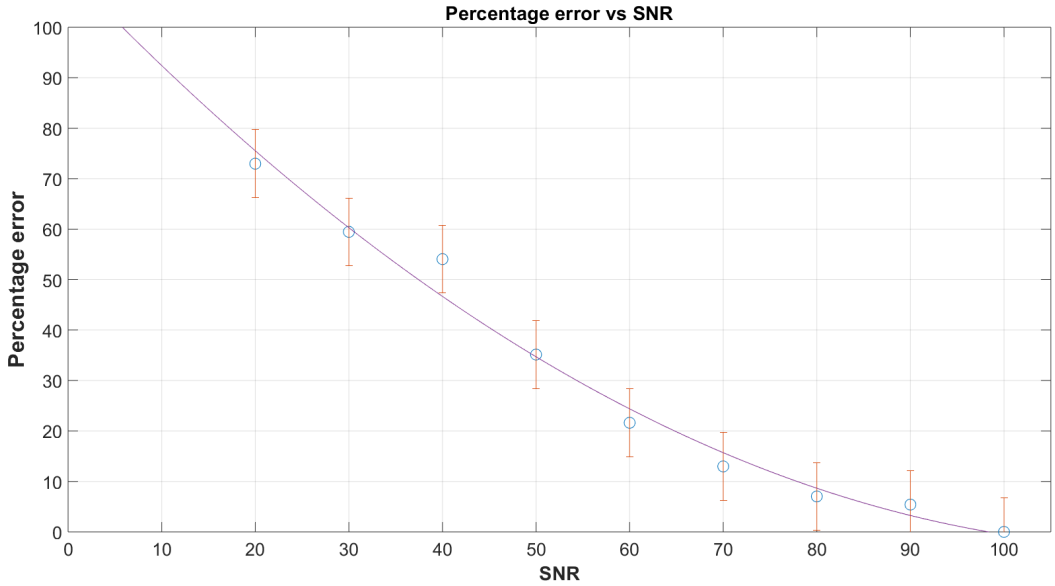


Figure 3.13: Relationship between percentage error and SNR.

It is evident from the figure above that the percentage error decreases exponentially as SNR is increased and is eventually nullified in the ideal scenario of SNR = 100. Even at an intermediate SNR of 50, the error in measurement is ~40%. On the other hand, for the smallest possible errors in quantification (~10%) the SNR should be ~70, at minimum. We note here once again that there was no data point used for SNR = 10 due to the inability to quantify the APT peak at such a low SNR.

Finally, by using equation 3.2.4 we can derive the relationship between the relative accuracy in measurement and SNR (Figure 3.14). The derived curve was found to asymptotically approach the ideal case, where the 'true' and measured signals are equal.

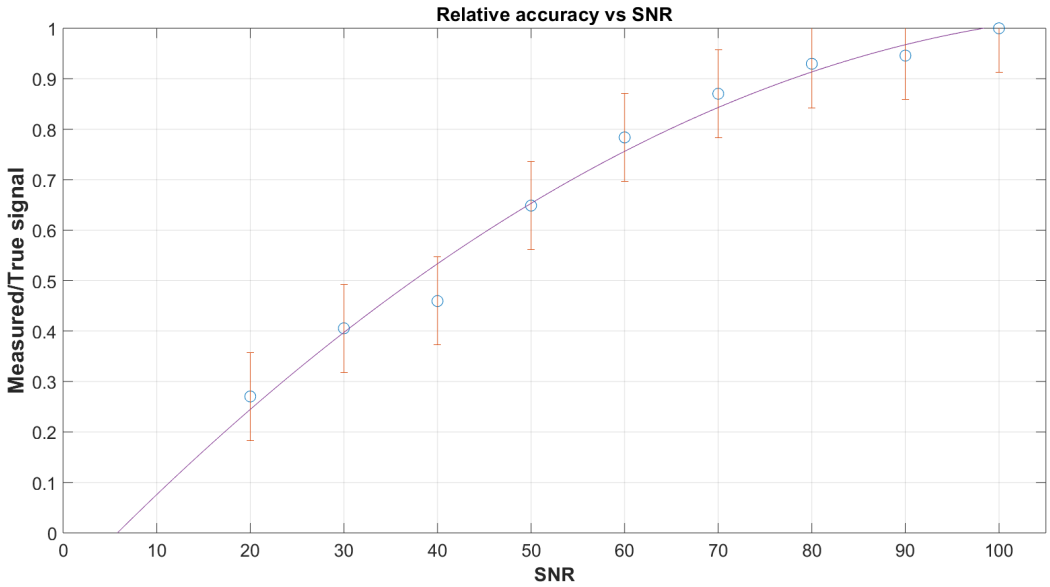


Figure 3.14: Relationship between relative accuracy and SNR.

At the highest SNR, the relative accuracy and percentage error take their largest and smallest value, respectively (Figures 3.14 and 3.13) and in a way mirror one another while changing in opposite directions. The lowest value (~0.27) of the relative accuracy occurs at SNR = 20. For an accuracy of ~0.8 and above, the CEST experiment should be performed with an SNR = 70 at the very least, as shown in Figure 3.14.

3.4 Discussion

The optimisation of an experiment can either be performed directly, by changing the experimental variables in real time and measuring the response, or, when possible, through a simulation. For the latter, a model, that accurately describes the physical system should be implemented and its temporal evolution, under various experimental conditions, should be recorded. The modified, time dependent, Bloch equations (including exchange terms [134]) facilitate the simulation of CEST systems. Numerous such models have been described in the CEST literature with a complexity that is directly proportional to the number of proton pools being modelled. For example, 2 and 3-pool models [228], 4-pool model [116] and models including both CEST and MT pools [29, 244]. To mitigate the complexity of modelling multi-pool systems a simplified and scalable solution was reported by Zhou et al. [268].

The aim of simulating a CEST system is to simultaneously solve a system of differential equations, where each equation describes the temporal evolution of the 'x', 'y' and 'z' component of magnetisation of each pool. This can either be done numerically (using the Runge-Kutta method or a matrix exponential operation [146]) or analytically [248]. The latter approach offers a more straightforward insight into the interactions of the various exchange pools when compared to numerical methods. Ultimately, a simulation yields the 'z' component of the water magnetisation, which is exactly what is measured in a real experiment.

This simulation study was not designed with a particular CEST application in mind. It's aim was however to demonstrate the steps that can be taken in order to investigate the impact of various experimental parameters, in the measured CEST effects of a 2-pool model under a continuous wave irradiation. The time dependent Bloch equations were numerically solved, using the matrix exponential operation [146], and the magnitude of the APT peak was calculated after varying 4 experimental parameters: irradiation power (B_1), APT pool size, saturation time and SNR. The latter para-

meter, can be explicitly set in a simulation, even though in a real experiment it is an actual outcome of the MRI experiment. The quantification of the APT peak, in the presence of noise, was facilitated by fitting the 2-pool model (equation 3.2.1) on the noisy Z-spectra, using the Levenberg-Marquardt algorithm. We note here two things: first, the proton exchange rate (from solute to bulk water) was excluded in this analysis as it is an inherent property of the CEST system and cannot be explicitly set in a real experiment and second, the optimisation of a pulsed CEST experiment can be performed in a similar manner, with the only difference being the discretization of the RF pulse shape (of any type: Gaussian, SINC, Fermi or otherwise), as demonstrated in section 2.2.1.6 of this thesis and in references [197] and [274].

We first investigated the effects of irradiation power (B_1), APT pool size and saturation time, in 'ideal', noise-free Z-spectra. As far as the B_1 power is concerned, Figures 3.1 and 3.2 show that $1\mu T$ is the ideal power for the model under investigation, as it results in the largest CEST effect and smallest spill-over. Spill-over effects refer to directly saturating bulk water which results in an overall broadening of the Z-spectrum. This broadening can be seen here, as B_1 power is progressively increased and the CEST effect is being diluted. An optimal B_1 power of $1\mu T$ for amides has also been reported in the literature, while for amines, the optimal power was shown to be $7\mu T$ [188]. The latter observation reflects that the higher the exchange rate, the higher the B_1 power that is required for sufficient labelling. In fact, the optimal saturation is achieved when the exchange rate ($k_{solute \rightarrow water}$) equals the RF power (expressed in Hz) [228].

The effect of the solute pool size was investigated next. The result is presented in Figures 3.3 and 3.4 and its interpretation is straightforward: the bigger the solute pool, the bigger the effect, with the relationship between the two, being linear. In a simulation, this is a direct result of modelling the equilibrium magnetisations to be directly proportional to their corresponding pool sizes. Nevertheless, the linearity of the relationship was also shown to be valid in-vitro. In the latter case, phantoms of increasing solute concentration (representing the solute pool size) correspond to

linearly increasing CEST signal [24, 61, 62]. This demonstration confirms the validity of modelling the equilibrium magnetisations as described in this study.

Lastly, the impact of the saturation time on noise-free spectra is described in Figures 3.5 and 3.6. It was found that a saturation time longer than 3 seconds does not offer any benefit in generating more APT contrast, as the signal plateaus at $t_{sat} = 3s$ and beyond. In other words, at a saturation time of 3 seconds, the CEST signal reaches its steady state. Considering the equivalency between a continuous and pulsed acquisition of the same average power, a steady state CEST signal, after 3 seconds, is also to be expected for a pulsed acquisition of the same average power [19]. The result reported here is in line with the analytical solution of the 2-pool model [265] (and equation 2.2.4), that describe the dependence of the CEST metric, termed Proton Transfer Ratio (PTR), on saturation time, among other variables. Knowing the optimal saturation time prevents unnecessary long acquisition schemes and usually saturation times in the order of seconds are adequate to saturate exchangeable protons, with residence times in the order of milliseconds [208]. As a rule of thumb, saturation must be applied for a time, at least equal to that of $T_{1,water}$ and ideally longer than the latter [31]. Otherwise, the longitudinal relaxation time of bulk water dilutes/scales the CEST effects and all measurements should be corrected for $T_{1,water,}$ relaxation effects as shown in references [194, 246].

Being able to simulate the response of a physical system enables one to control a plethora of variables. Three of these variables were discussed in the paragraphs above. Even though such an analysis is useful in providing a comprehensive picture of the response of a physical model under various conditions, it ignores the presence of noise.

Signal to noise ratio (SNR) is the standard used to characterise the performance of an MRI system. All MRI images contain both useful information (signal) and noise. In MRI, noise arises from two sources: from the sample itself (e.g. molecular movements of charged particles) and from the electronic components of the system (e.g. resistance in coils and cables). As a result, noise causes unwanted disturbances of the measured

signal and in extreme cases severely compromises the quality of images and the ability to accurately extract useful information from them. As such, in this study the impact of various levels of SNR on the measured APT signal was analysed, making SNR the fourth relevant parameter, in CEST experiments, that was investigated.

A benchmark Z-spectrum (Figure 3.7) of ~4% APT was simulated as a starting point. The magnitude of the initial APT signal was intentionally chosen to be small, as it was assumed that smaller signals are more susceptible to the presence of noise. After the simulation of the 'ideal' Z-spectrum, additional spectra were simulated with the addition of different levels of random noise, for a total of 10 noisy spectra (SNR values of: 100, 90, 80, 70, 60, 50, 40, 30, 20 and 10). Three examples of noisy spectra were shown in Figures 3.8, 3.9 and 3.10.

The quantification of the APT peak in the noisy spectra was facilitated by fitting a 2-pool model to the simulated and noisy data and by using equation 3.2.1. This method of quantification was preferred over high-order polynomial and Lorentzian fitting because the former was shown to underestimate the APT effect (regardless of the polynomial order [240]) and the latter is primarily used to isolate the simultaneous CEST effects in multi-pool systems [243, 262]. Besides, being able to fit a CEST model in experimental (real) data has the advantage of fully describing the physical system, as the fit allows for determining unknown system parameters like relaxation times, pool sizes and exchange rates. Nevertheless, an accurate determination of such parameters requires repeated Z-spectrum measurements (and hence fits) which is not always feasible due to time restrictions [137, 159, 250].

Figure 3.12 shows the change in the fitted APT peak magnitude as the SNR changes. The relationship is linear with a good approximation ($R^2 = 0.95$) and for the lowest SNR (= 10) the fit cannot be used for quantifying the CEST effect. From this result we can conclude that the presence of noise deteriorates the ability to reliably fit noisy data and thus accurately describe the CEST effect. The fitted line, along with the 95% prediction bounds in Figure 3.12 can be used to estimate the expected APT magnitude

as a function of SNR in any 2-pool system of interest.

It is further shown in Figures 3.13 and 3.14 that the percentage error and relative accuracy are both affected by the change in SNR. For example, Figure 3.13 shows that, for the present system, an SNR = 50 results in an error of ~40% and when a small APT effect (like the ~4% used here) is concerned, one has to wonder whether, under such conditions, a CEST effect or noise, is really being measured. In any case, for errors within ~10% (from the 'ideal', noise-free signal) and relative accuracy of ~0.8, a CEST experiment should be performed with an SNR = 70, at the very least.

We conclude this discussion by mentioning the possible ways of increasing the SNR in a CEST experiment. First, the most simple way in doing so is by using a higher main magnetic field (e.g. 7T) [99], even though this approach can lead to increased SAR levels. Second, increasing the signal averages results in higher SNR. This approach however is time consuming and a workaround, of a six point method, was proposed in [266]. In this study, the SNR is increased by repeating the acquisition at only a few offsets ($\pm$3ppm,$\pm$3.5ppm,$\pm$4ppm), around the offset of interest (+3.5 ppm for amides) in conjunction with the acquisition of a full Z-spectrum. Third, using larger voxels, reducing acceleration, and implementing higher flip angle does enhance SNR. Additionally, more signal can be gained by increasing the slice thickness or reducing the readout bandwidth [28]. Moreover, since the centre of k-space determines the signal to noise ratio and image intensity, a CEST sequence that allows initial central k-space sampling can be used [19]. Finally, a post-processing method, termed 'Downsampling Expedited Adaptive Least-squares fitting' was shown to improve the CEST SNR, in-vivo. According to this method, a globally averaged and hence high SNR, Z-spectrum serves as the starting point of sequentially fitting images, of progressively increasing resolution. This fitting approach resulted in an increased fitting reliability of noisy data when compared to the conventional multi-Lorentzian fit, for suboptimal SNR values [262].

3.5 Conclusion

This study investigated the impact of four experimental parameters in the ability to quantify the APT CEST effect in a 2-pool system, under continuous wave irradiation. A comprehensive response of the system was described for various irradiation powers, pool sizes and saturation times, under noise-free conditions. It was found that the optimal experimental parameters for the system under investigation were: $B_1 = 1\mu T$, pool size of 0.01 and saturation time of 3 seconds, at most.

It was further shown that the presence of noise degrades the ability to quantify the APT effect, by the use of a 2-pool model fit on noisy data, in a linear fashion. Ideally, the present model should be imaged with an SNR of ~70 so that the percentage error and relative accuracy in the measurements is ~10% and 0.8, respectively.

Chapter 4

pH mapping using exogenous CEST contrast agents: in vitro feasibility assessment

CEST signal depends on the concentration of the exchangeable protons and also the pH, as the latter affects the proton exchange rate. An increased proton concentration gives higher CEST signals due to the large number of protons cycled through the proton carrying compounds and water. pH reflects the concentration of hydronium (H_3O^+) ions. These ions are the result of the protonation (addition of a proton to a water molecule) of water. The existence of such ions affects the available water molecules that can receive an exchangeable proton and therefore the measured CEST signal.

Many iodinated X-ray contrast media contain hydroxyl, amide and amine proton groups that have been shown to generate CEST contrast. In the experiments described here we aim to 1) investigate the pH dependence of three exogenous clinically approved CT contrast agents with CEST 2) derive a calibration curve between the measured CEST signal and extracellular pH. When the calibration curve is known then pH can be determined from the measured CEST signal.

4.1 Introduction

Tumour microenvironment differs significantly from that of healthy tissue. For example, the complex vascular networks found in solid tumours result in unbalanced or heterogeneous blood supply and poor perfusion compared to normal tissues. Consequently, lower oxygen levels are expected in tumours. In addition, the increased glucose metabolism in tumours leads to increased H^+ production lowering the pH levels.

As described in the following figure, (Figure 4.1), blood transfers oxygen and glucose that are diffused in the cells. There, glucose is converted to pyruvate and in the absence of oxygen, is reduced to lactate which is exported from the cell. In the presence of oxygen, pyruvate is oxidized to HCO_3^- and then exported from the cell. Both processes create H^+ ions that are transferred outside of the cell lower the extracellular pH [52].

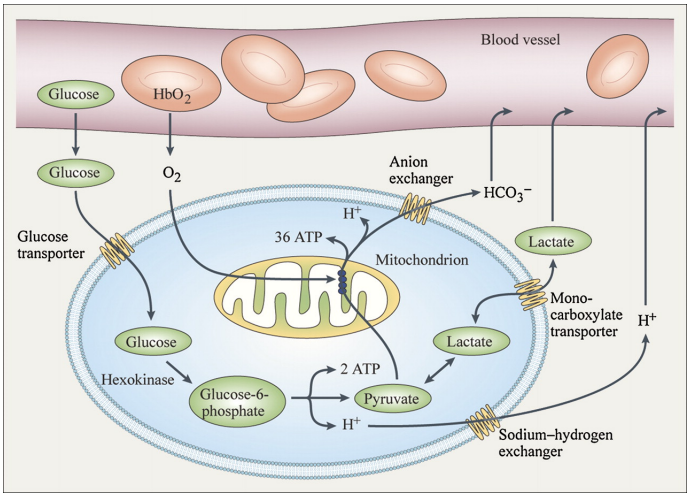


Figure 4.1: Glucose metabolism in mammalian cells [255].

Being able to measure pH is important because pH levels (along with oxygen levels) determine some tumour characteristics. More specifically, low (acidic) pH levels have been associated with increased radio/chemo-resistance, increased metastatic behaviour and invasion and also with inhibition of DNA repair mechanisms that can lead to the onset of cancer [48]. As for the pH range that is relevant to human brain tumours

it lies between 5.5-7.5 [52], [44].

The current MR methods that can be used to measure pH include both spectroscopic and imaging methods and are summarised in the following table.

Method	Probe	Drawbacks
^{31}P-MRS	endogenous ^{31}P, exogenous 3-aminopropylphosphonate	low spatial resolution
^{1}H-MRS	exogenous marker (imidazole)	
^{19}F-MRS	exogenous marker (fluoroscein)	
Hyperpolarisation	^{13}C	short acquisition window
Relaxometry	Dedicated Gd agents	concentration dependent
CEST	endogenous proteins, exogenous agents	concentration, pH and T_1 dependent

Table 4.1: Spectroscopic and imaging methods of measuring pH.

Measuring pH using ^{31}P, ^{1}H and ^{19}F spectroscopy is based on the chemical shift pH dependence and its difference from the physiological state [133, 41]. However, the inherent limitation of spectroscopy is the larger pixel size compared to MR imaging that leads to lower spatial resolution.

pH measurements using hyperpolarised ^{13}C, are based on the ratio of bicarbonate over carbon dioxide. The disadvantage of hyperpolarisation is that a measurement should be completed within 1-2 mins, because the hyperpolarised signal decays fast with time [75].

Relaxometry is based on the pH dependence of the relaxation times of special Gd agents (gadolinium-DOTA-4AmP5-, mixed with dysprosium). This method is a concentration dependent method as it relies on the concentration measurement of

dysprosium, after which, the concentration of the Gd agent can be extrapolated [256, 1].

Finally, CEST, can be used for pH measurements utilising both endogenous (amides) [193, 198, 138] and exogenous agents [129]. In either case, the difficulty lies in rendering the CEST signal depend only on pH, while eliminating the concentration and T_1 influences. In other words, in order to work out the pH from a measured CEST signal one has to measure the concentration of the amides first. Moreover, the relaxation times of water should be measured along with the proton exchange rates [264, 137, 184]. This would require a separate set of experiments that render the process rather complicated.

A workaround involves using the signal ratio of two or more CEST signals [221]. This ratiometric approach allows for concentration and T_1 independent pH measurements, as the ratio of the two signals will only reflect the influence of the pH, through the respective ratio of the exchange rates of each signal:

$$\frac{Signal_1}{Signal_2} = \frac{k_1[agent]T_1}{k_2[agent]T_1} \tag{4.1.1}$$

where

k_1, k_2 : the exchange rates of the respective proton groups.

It is obvious from equation 4.1.1, that both CEST signals must arise from the same agent. Otherwise, the concentration terms cannot be eliminated and should therefore be determined by a separate method. This limits the application of the ratiometric method to those agents having two or more detectable exchangeable proton groups.

As opposed to pH sensitive CEST contrast agents based on gadolinium (Gd-III) [1], lanthanide (Ln-III) [203] and dendritic (Yb-III) [156] complexes, the agents studied in this work are already approved for clinical use which ensures an immediate in-vivo translation. At the time of the study, this was the first feasibility assessment of three such agents in measuring pH, in-vitro, with CEST MRI.

4.2 Materials and Methods

The three iodine based contrast agents used were, Iodixanol (brand name - Visipaque, GE Healthcare), Iopamidol (brand name - Niopam, Bracco UK Ltd) and Iopromide (brand name - Ultravist, Bayer Healthcare). These agents are routinely used in diagnostic CT examinations (arteriography, ventriculography) as they enhance the visualisation of vascular lesions. They are usually administered intravascularly or intravenously, at doses between 5 - 15 ml in adults. The agents are distributed in the extracellular space through the blood vessels and are almost cleared within 24 hours after administration.

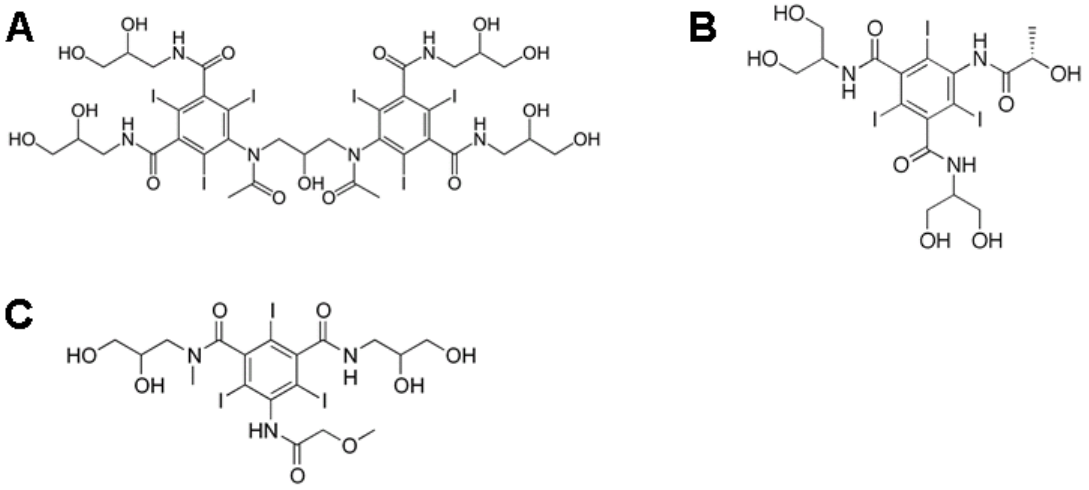


Figure 4.2: Chemical formulas of Visipaque (A), Niopam (B) and Ultravist (C).

As it can be seen in the above figure, all agents contain multiple amide and hydroxyl groups. These groups could potentially have measurable CEST effects if their respective resonant frequency offset from water is a lot greater than their proton exchange rate.

Solutions of the three contrast agents at a concentration of 200 mM were prepared in phosphate buffer (PBS) in 15ml centrifuge tubes. The pH range was varied between 5 - 9.3 for Visipaque, 6.1 - 7.5 for Niopam and 4.7 - 7.5 for Ultravist. For pH measurements a digital pH meter with a glass electrode was first calibrated at 3 pH values: 4, 7 and 10

pH units, using buffer solutions of deionised water/Potassium hydrogen phthalate (pH =4), deionised water/Disodium hydrogen phosphate dihydrate/Potassium dihydrogen-orthophosphate (pH =7) and deionised water/Sodium carbonate/Sodium bicarbonate (pH =10). Due to the small size of the phantoms, the pH was adjusted by adding 0.1mM of HCl (for lowering the pH) or NaOH (for increasing the pH) by using a micropipette, while constantly reading the pH until the desired value was achieved. All scanning was performed on a Bruker Biospin 7T small bore imaging system, using a transmit-receive volume coil. Field homogeneity was optimised using the Fastmap protocol. To avoid ADC overflow, the gain was adjusted so that the digital echoes on the x, y and z projections, did not overlap with the ADC range. After a reference scan at -20ppm offset irradiation, a Z-spectrum was acquired for each solution, using two Gaussian pulses (bandwidth 100 Hz, 1.5 μT, duration 52 ms) and a gradient echo readout (TR = 200 ms, TE = 5.2 ms, FOV = 2 mm, slice thickness = 2 mm, matrix size = 128 x 128). The acquisition of a full Z-spectrum, for a single slice, required 33 min (65 scans, with the pre-saturation offset irradiation varied between -8 ppm and +8 ppm at 75 Hz intervals). All images were normalised by the reference image. Z-spectra were derived by plotting the normalised signal against the irradiation frequency offset and asymmetry curves were calculated as the normalised signal difference between the positive and negative irradiation offsets around the resonance frequency of water (set at 0 ppm). Pixel by pixel asymmetry maps were produced to illustrate the variation of the signal with pH. Finally, calibration curves for two of the agents were derived by fitting the signal peak ratio against pH. All analysis was performed in Matlab (The Mathworks, 2010).

4.3 Results

4.3.1 Visipaque

Figure 4.3 shows the Z-spectrum and asymmetry curves for Visipaque for eight different pH values. The agent showed one pH dependent peak at 4.2 ppm from water.

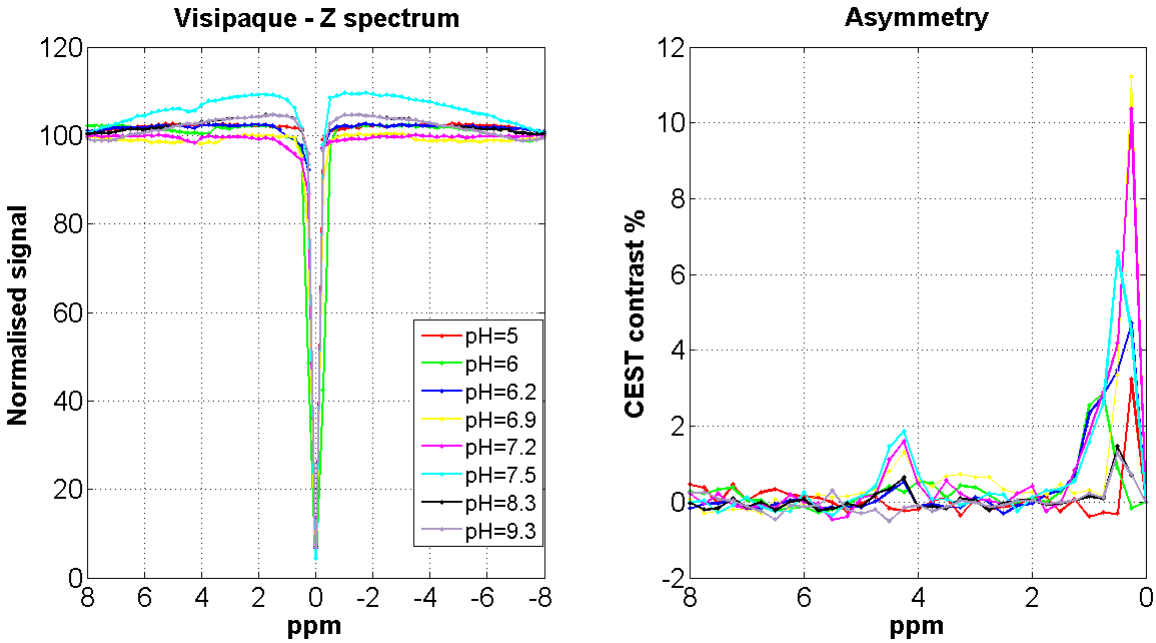


Figure 4.3: Z-spectrum and asymmetry curves for Visipaque.

As mentioned in the Materials and Methods section, the reference image (M_0) was acquired at -20ppm from water (centred at 0ppm). At this frequency no saturation is expected and the normalised images ($\frac{M_z}{M_0}$) should be at most 1 (or 100% in the scale used to display the intensities). Ideally, the reference image is acquired with the saturation pulse turned off completely. In this case however, the saturation pulse was still on while the signal was measured at -20ppm. As a result, the ratio $\frac{M_z}{M_0}$ could be > 1. This is because M_0 reflects, an even though distant from water, saturated nevertheless, signal. This would make $M_z > M_0$, leading to normalised spectra greater than 100%. This is most obvious in the case of $pH = 7.5$. The result is not consistent because each sample was scanned individually.

Despite this oversight, the Z-spectra in Figure 4.3 show a CEST peak at +4.2 ppm.

As demonstrated in reference [209], water exchange (WEX) experiments have shown that the resonance peak at +4.2ppm corresponds to mobile proteins and specifically amides. This is for two reasons: first, the acquired peaks were narrow and that means that the measured signal comes from mobile proteins ($FWHM = \frac{1}{T_2}$) and second, the measured exchange rates in the WEX experiments were ~10-40 Hz. These rates correspond to amides, as indicated in reference [121]. The narrow width of the Z-spectra at 0ppm, reflects the bandwidth of the Gaussian pulse (100Hz). Spectral distortions upon direct water saturation were reported previously in CEST experiment simulations [170]. Pulse bandwidths greater than the water line-width result in inconsistent measurements of signal intensities. The Z-spectra reported here indicate no such problem. In any case, a short pulse bandwidth is preferable for frequency specific applications, such as CEST. The trade off however, is longer pulse durations (because of the time-bandwidth product) which essentially reflects a property of the Fourier transform. The spectra are centred around 0ppm, symmetrically, and this indicates no presence of magnetisation transfer (MT) or other exchange peaks on the up-field frequencies (negative side of the Z-spectra) or otherwise. The asymmetry analysis is then expected to isolate the amide CEST effect at +4.2ppm. The large peak within 0.5ppm from water, in the asymmetry spectrum does not indicate a proton exchange peak. The peak is due to minimally asymmetric direct water saturation and is aggravated by non-properly centred Z-spectra and broadening of direct water saturation line-shapes. This effect, even though irrelevant in this experiment, can obliviate the detection of proton groups resonating in close proximity to water (e.g OH^- myo-inositol protons [61, 100]). To complicate things, partial volume effects can shift the centre of the exchange peaks, while low field strengths and very short pulse durations can broaden both the direct water saturation and exchange peak line-shapes. In this case, asymmetry analysis is inadequate to quantify CEST effects at such close proximities and a Lorentzian fitting analysis should be used instead [244].

The pH dependence of the CEST effect of Visipaque is more clearly seen in Figure 4.4. A small positive asymmetry of less than 2% was found for all the pH values except at the two extremes of pH = 5 and pH = 9.3. Furthermore, the asymmetry grows linearly as the pH changes from acidic to neutral, in the pH range between 6 - 7.5, before starting to drop again at the basic pH of 8.3.

This transition is further reflected in the asymmetry maps shown in Figure 4.5. The map signal intensity increases between pH = 6 and pH =7.5 with pH =6.2 and pH =8.3 having almost the same value. The slightly negative asymmetry for pH = 5 and pH = 9.3 is also reflected in the maps.

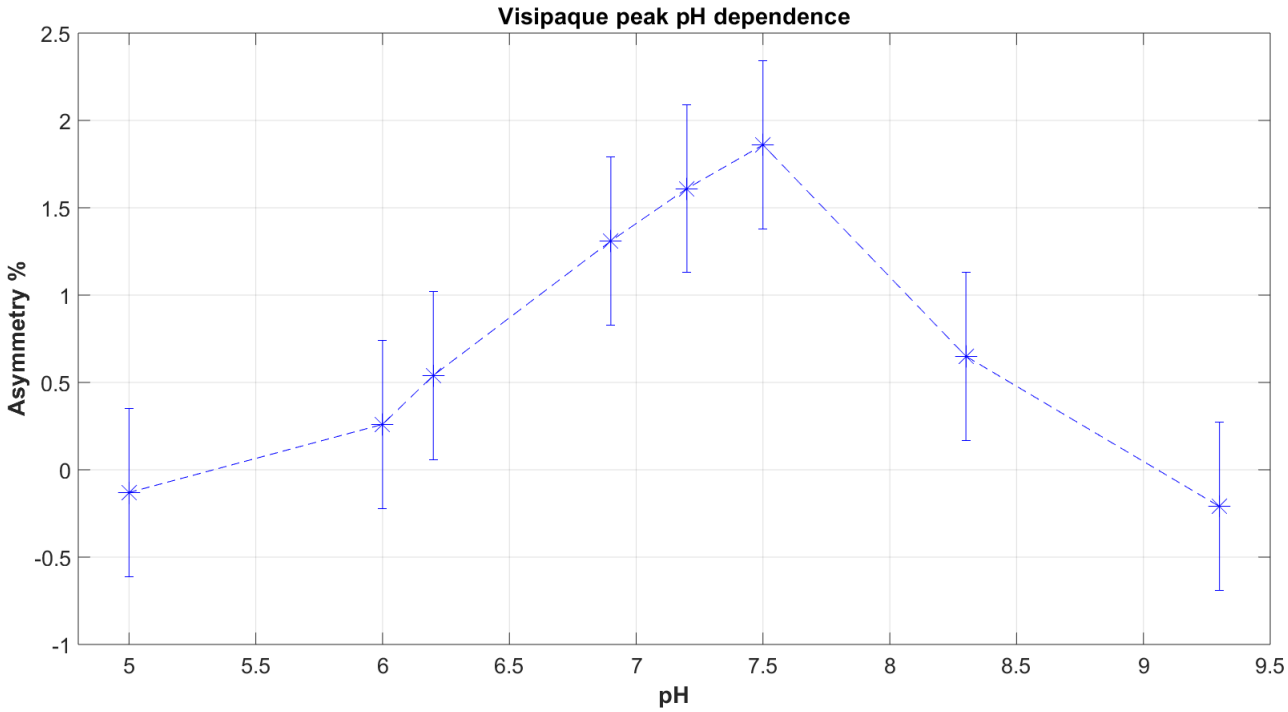


Figure 4.4: Visipaque CEST peak pH dependence. The bars indicate standard deviation..

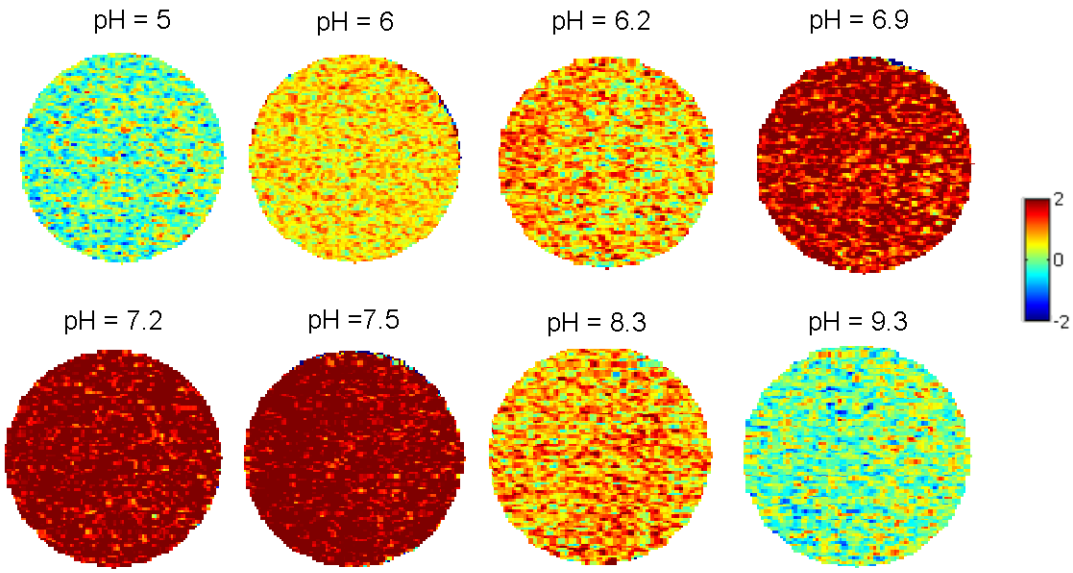


Figure 4.5: Pixel by pixel asymmetry maps for Visipaque. The images were cropped using an elliptical mask during post-processing.

4.3.2 Niopam

The second contrast agent, Niopam, showed four CEST peaks. One at -3 ppm from water and three at the positive offsets of 1.9 ppm, 4.2 ppm and 5.4 ppm (Figure 4.6). Further analysis focused on the two most prominent peaks at 4.2 ppm and 5.4 ppm. The peaks show pH dependence and a maximum CEST contrast of about 15%, which is 7.5 times more than in Visipaque.

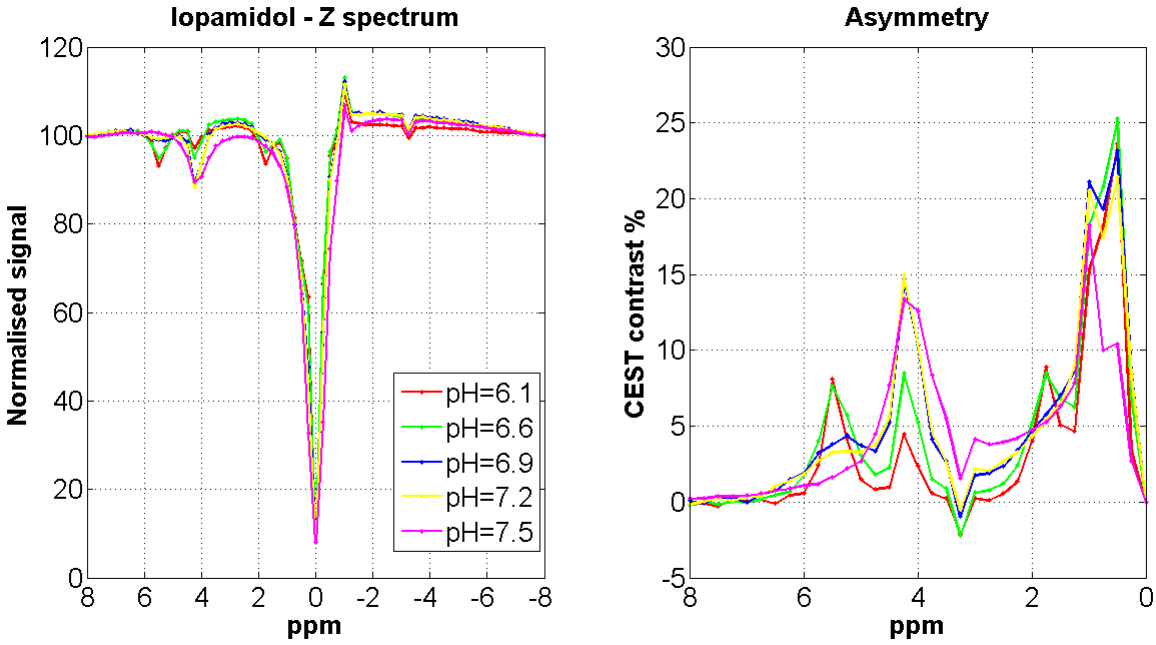


Figure 4.6: Z-spectrum and asymmetry curves for Niopam.

It is evident from the asymmetry curves in Figure 4.6, that the CEST effect at 4.2 ppm and at 5.4 ppm change in opposite directions, as the pH is varied. Therefore, their ratio is also expected to be sensitive to pH.

The variation of the CEST signal of each peak with pH is more clearly described in the following pixel by pixel asymmetry maps (Figures 4.7 and 4.8).

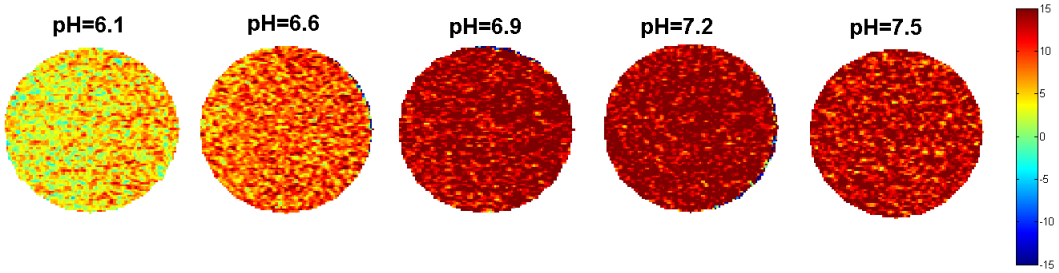


Figure 4.7: Pixel by pixel asymmetry maps for the 4.2 ppm peak of Niopam. The images were cropped using an elliptical mask during post-processing.

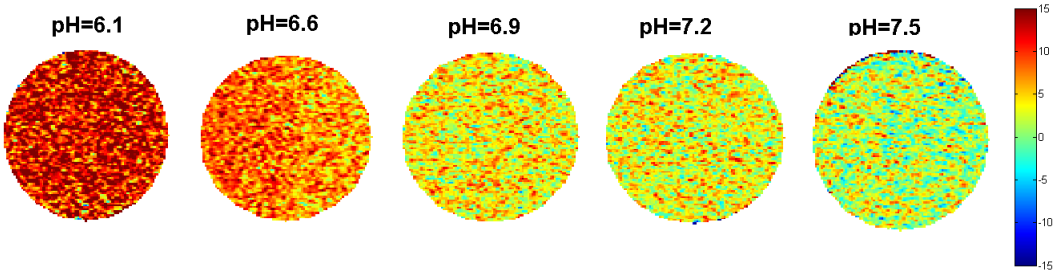


Figure 4.8: Pixel by pixel asymmetry maps for the 5.4 ppm peak of Niopam. The images were cropped using an elliptical mask during post-processing.

Figure 4.7 clearly shows how the CEST effect is increased as the pH changes towards more neutral values. The maximum CEST contrast for the 4.2 ppm peak occurs at pH = 7.2, having a value of ~ 15%. This is also the maximum measurable contrast among all the Niopam peaks. Additionally, asymmetry analysis correctly reflects the small intensity drop at pH = 7.5 for the same peak.

The maximum contrast of the 5.4 ppm peak occurs at the lowest and most acidic pH of 6.1, as is demonstrated in the maps of Figure 4.8. Interestingly, the CEST signal of the 4.2 and 5.4 ppm peaks, at pH = 6.6, was found to be, almost, identical in magnitude with the asymmetry values being ~ 8.5% and 7.6% respectively (Figure 4.6). This 0.9% difference is again reflected by the pixelwise asymmetry analysis by comparing the asymmetry maps at pH = 6.6 in Figures 4.7 and 4.8.

The ratiometric method is applicable for this contrast agent as it demonstrates at least two pH dependent CEST peaks. As such, the ratio of the CEST signal of the 4.2 over the 5.4 ppm peak was plotted against pH and a calibration curve was derived by

fitting the data. As it can be seen in the following figure, the relationship between the signal ratio and pH is linear, with R^2 = 0.88.

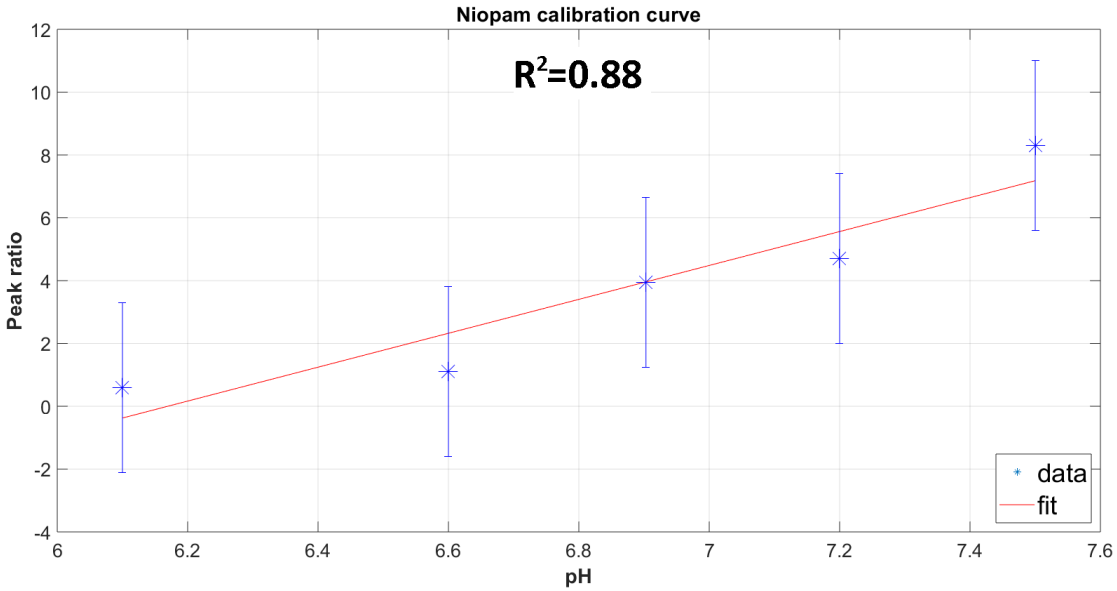


Figure 4.9: Signal ratio of the 4.2 ppm over the 5.4 ppm peak against pH for Niopam. The bars indicate the standard deviation.

In order to to provide an estimate of the uncertainty in the calibration curve, the 95% prediction bounds and the standard deviation of precision (SDP) were calculated and presented in Figure 4.10. The standard deviation of precision describes the standard deviation of the differences between the data points and the fit. In the case of Niopam, the SDP is 0.2 pH units.

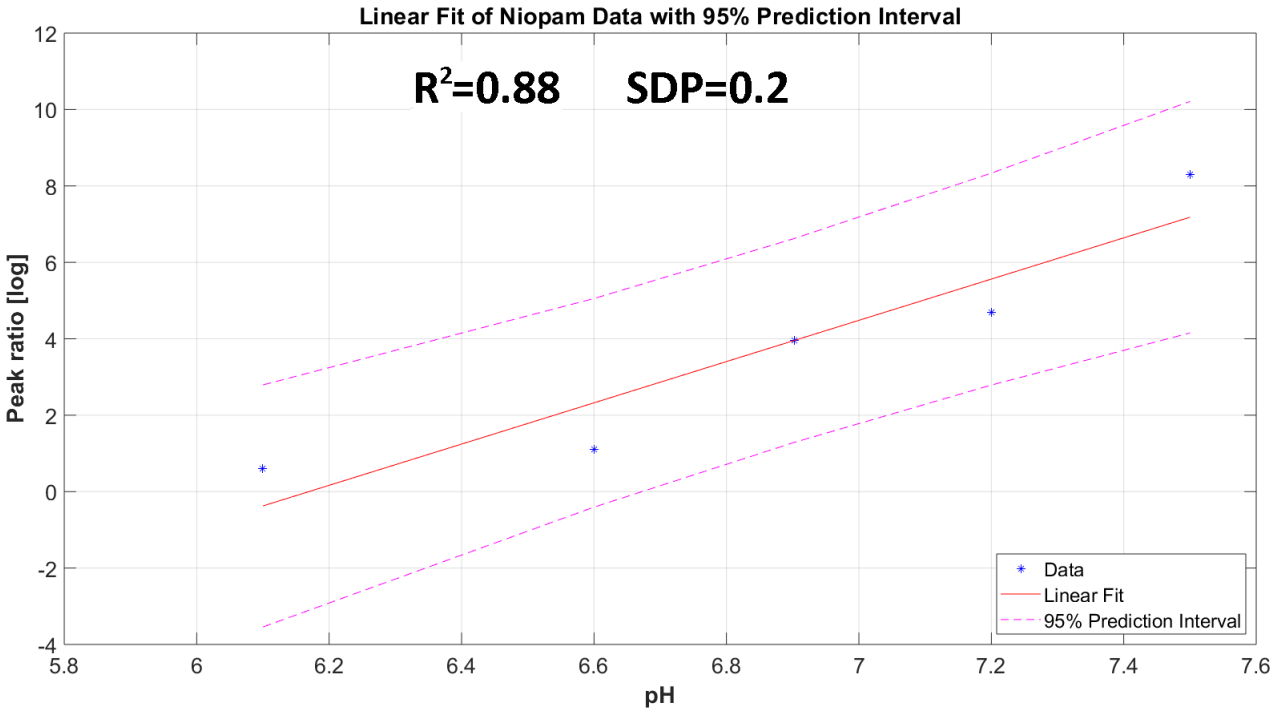


Figure 4.10: 95% prediction bounds in the calibration curve for Niopam.

4.3.3 Ultravist

The last contrast agent, Ultravist, showed three pH dependent CEST peaks. One at the negative offset of -1 ppm from water and two at the positive offsets of 4.2 ppm and 5.6 ppm. The analysis was focused at the latter two peaks, as they occur away from the water resonance and represent clear and isolated CEST effects. Figure 4.11 illustrates the Z-spectrum and asymmetry curves for Ultravist for five pH values ranging between 4.7 - 7.5.

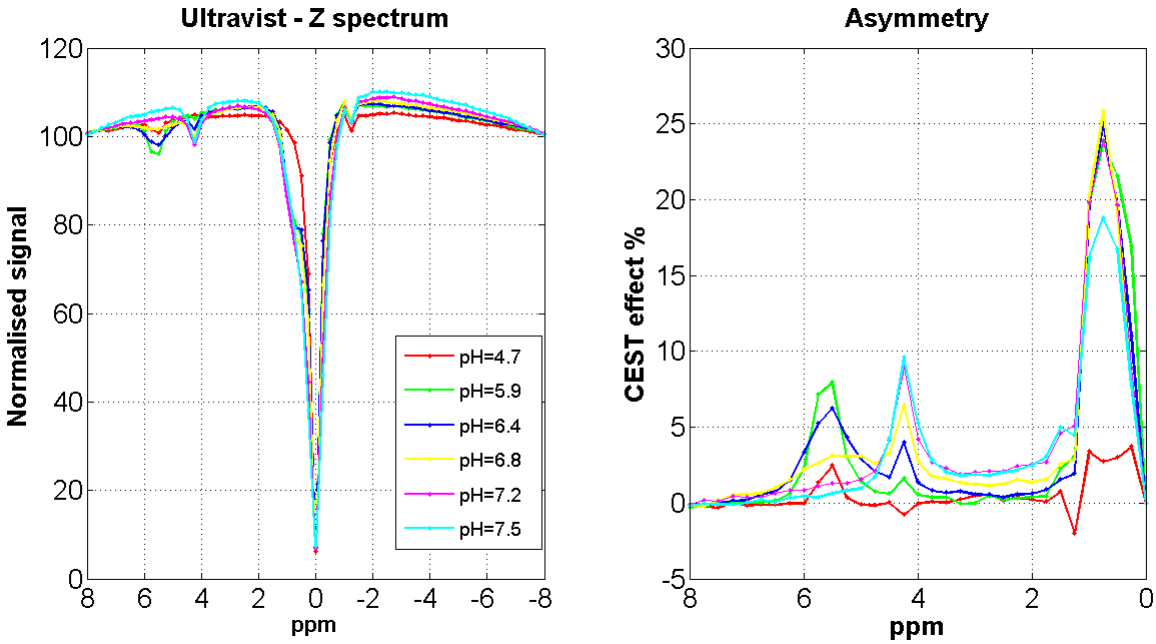


Figure 4.11: Z-spectrum and asymmetry curves for Ultravist.

As indicated by the asymmetry curves in Figure 4.11, the maximum CEST effect occurs for pH = 7.5 at 4.2 ppm, having a magnitude of ~ 10%. Again, the effect at this offset is base catalysed, as it is reduced when the pH is decreased. Furthermore, for all pH values the asymmetry at this frequency was found to be positive, except at the extreme value of pH = 4.7. Similarly to Niopam, the peak at 5.6 ppm exhibits a stronger signal for acidic pH values. Nevertheless, the effect of this peak was found to decrease to less than 2.5% at pH = 4.7 and even more for the neutral pH values of 7.2 and 7.5.

The pH dependence of each peak is more readily described by the following pixel

by pixel asymmetry maps.

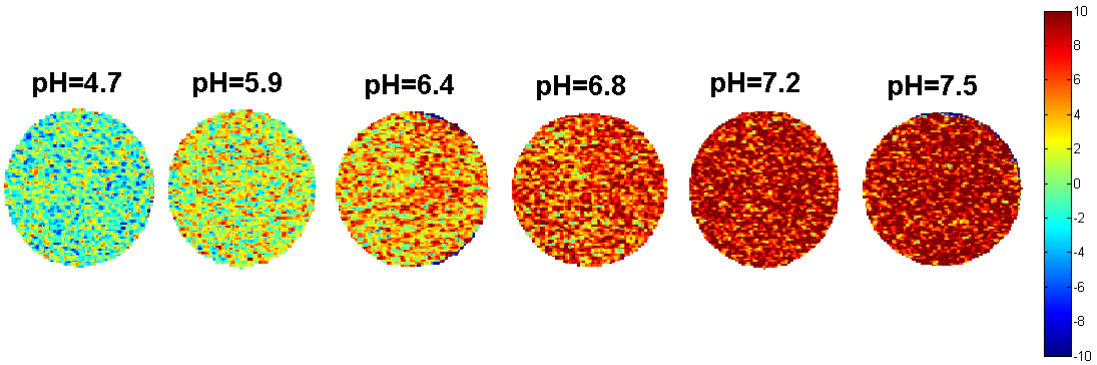


Figure 4.12: Pixel by pixel asymmetry maps for the 4.2 ppm peak of Ultravist. The images were cropped using an elliptical mask during post-processing.

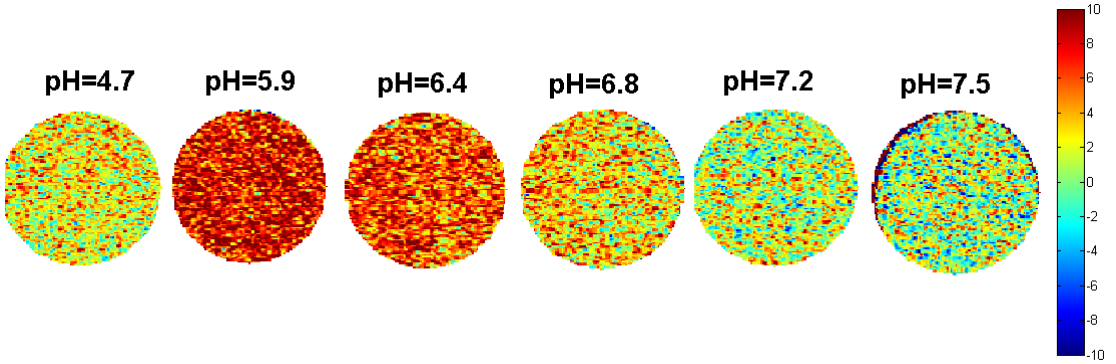


Figure 4.13: Pixel by pixel asymmetry maps for the 5.6 ppm peak of Ultravist. The images were cropped using an elliptical mask during post-processing.

As it can be seen in Figure 4.12, the CEST effect of the 4.2 ppm clearly increases as the pH becomes neutral, with the highest effect of ~ 10% occurring at pH = 7.5. The negative asymmetry at pH = 4.7 is also evident in the corresponding map. As far as the second peak, at 5.6 ppm, is concerned, the CEST effect is maximised at pH = 5.9. The effect at this pH is 2% less than the maximum of the 4.2 ppm peak. This small difference is again illustrated by the asymmetry maps. Further pH decrease does not lead to a stronger CEST signal at this offset. Instead, the effect is decreased by 5.6% as compared to the one at pH = 5.9. At neutral pH, the effect is almost non-existent at this offset as it drops below 1%.

Similarly to Niopam, the ratiometric method is also applicable here. Again the

signal ratio of the 4.2 ppm peak over the 5.6 ppm peak was calculated and plotted against pH. A log-linear relationship was found just like for the previous contrast agent. However, in this case the fitting was more reliable with R^2 = 0.99 (Figure 4.14).

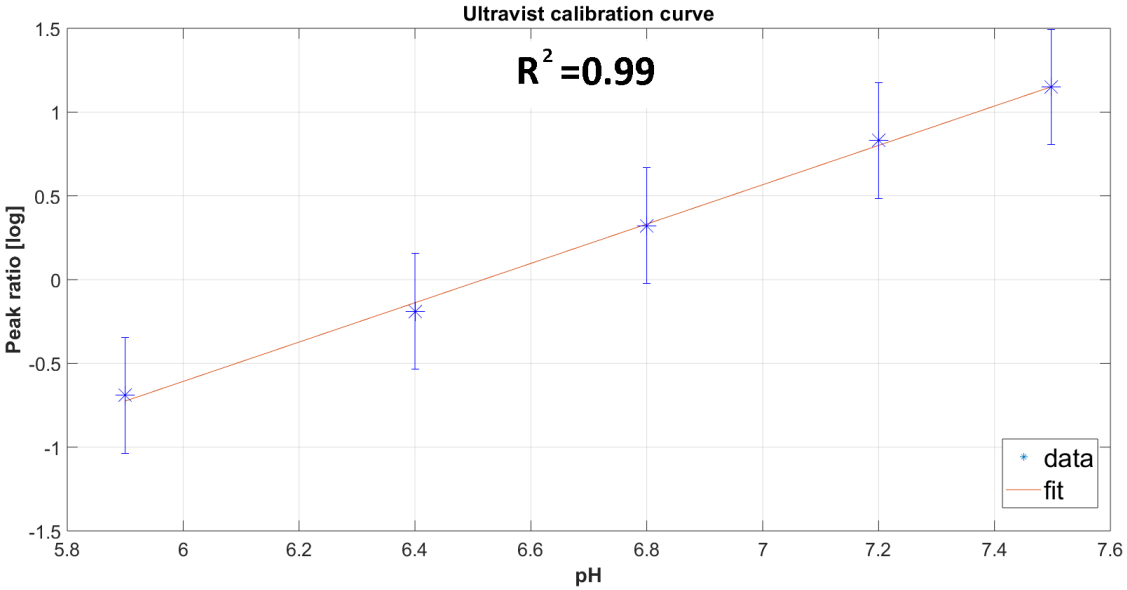


Figure 4.14: Signal log ratio of the 4.2 ppm over the 5.6 ppm peak against pH for Ultravist. The bars indicate the standard deviation.

In order to to provide an estimate of the uncertainty in the calibration curve, the 95% prediction bounds and the standard deviation of precision (SDP) were calculated and presented in Figure 4.15. The standard deviation of precision describes the standard deviation of the differences between the data points and the fit. In the case of Ultravist, the SDP is 0.024 pH units.

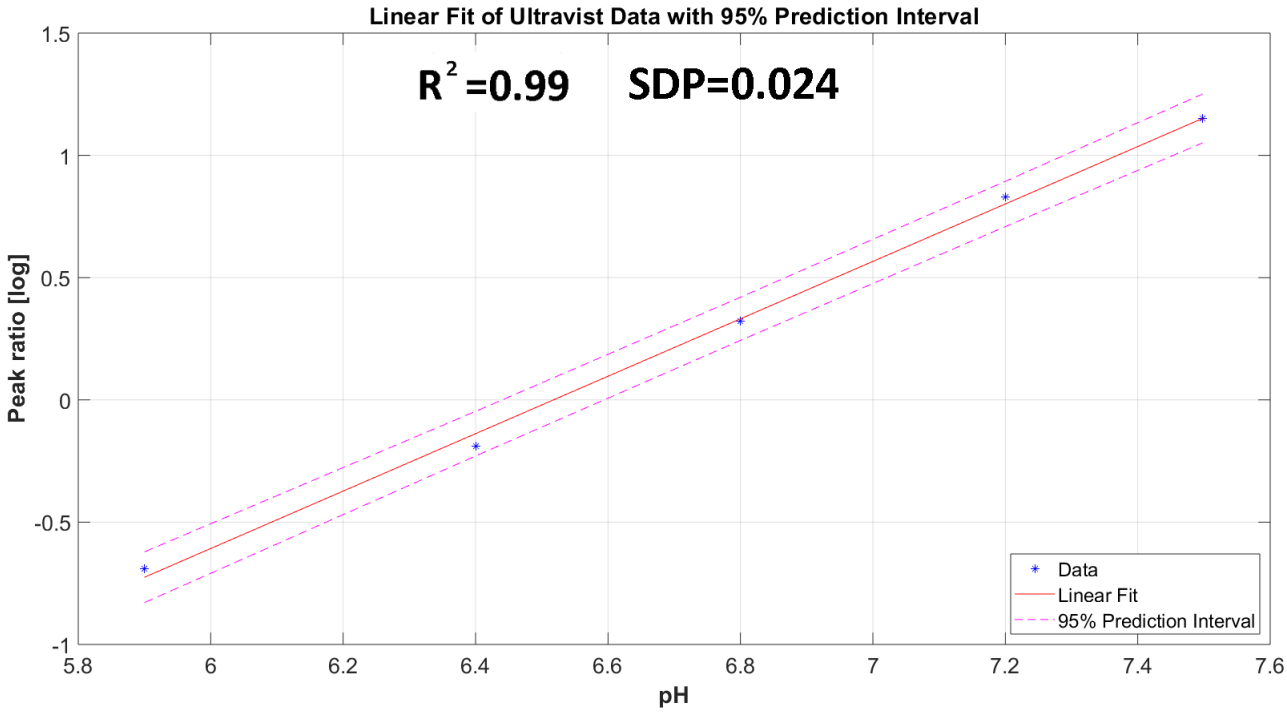


Figure 4.15: 95% prediction bounds in the calibration curve for Ultravist.

4.4 Discussion

All three contrast agents showed pH dependent CEST effects. However, the ratiometric approach was only applicable to Niopam and Ultravist, as these agents showed at least two CEST peaks. On the other hand, Visipaque, even though containing multiple proton exchange groups, showed only one exchange peak at 4.2 ppm. The latter indicates that under intermediate saturation B_1 power (~1.5 μT) the conventional ratiometric approach is not applicable to this contrast agent. Nevertheless, it is known that the saturation efficiency, depends on both the radiofrequency B_1 power and exchange rate, k_{ex}, ($\alpha = \omega_1^2/(\omega_1^2 + k_{ex}^2)$) . Higher exchange rates require stronger RF pulses in order for an effective saturation to occur. It is possible that, under higher B_1 irradiation power, fast proton exchange groups in Visipaque can effectively be saturated, leading to more than one measurable CEST effects for this agent. By surveying the literature, one report was found, where for a pulse power of B_1= 3μT, Visipaque shows an additional CEST peak at ~ 1.9 ppm, from water [4].

The conventional ratiometric approach for concentration independent pH measurements requires agents having multiple non-equivalent proton exchange groups. This limits the selection of the suitable contrast agents. An extension to the conventional approach is the RF power-based ratiometric method for pH mapping [127]. The latter approach allows for concentration independent pH mapping by using agents having only one pH dependent exchange peak. The difference with the conventional approach is that instead of measuring the ratio of two separate exchange peaks, the ratio of the signals, from the same peak, for two B_1 powers, is measured. The feasibility of the method was demonstrated at 7T using Iobitridol (brand name - Xenix, Guerbert), which is again an iodine based X-ray contrast agent. The agent showed one pH dependent amide peak at 5.6 ppm and a linear calibration curve between the pH range 5.5 - 7.5. The approach is concentration independent and was used to measure the extracellular pH in a xenograft breast tumour mouse model [127]. As compared

to the conventional approach, the RF power-based method requires the acquisition of two Z-spectra, one for each RF power. Consequently, it is important to implement fast acquisition sequences so that the concentration of the agent is not significantly different between the acquisitions. The RF power-based ratiometric method was further developed by correcting the measured signal ratio for RF spillover effect and water relaxation T_1 influences. The new metric, termed PRICEST, shows little dependence on labile concentration and substantially reduced T_{1w} and T_{2w} dependence. Even though the results were only demonstrated in-vitro, at 4.7T, PRICEST signal successfully indicated the pH values of creatine solutions. The accuracy in determining pH after the corrections was increased from 0.12 ± 0.13 to 0.04 ± 0.03 [232, 186].

In-vitro and in-vivo pH mapping using Niopam has been reported in the literature at both 3T and 7T [129], [2], [139]. High resolution ^{1}H-MRS spectra of Niopam in water solution have been used to assign the resonant frequencies at 4.2 ppm to amide groups and at 5.4 ppm to 2-hydroxypropanamido groups [129]. Both peaks are detectable, even at 3T. However, this was shown to be feasible for very low B_1 powers (< 0.6 μT), as the peaks merge, when stronger RF pulses are used [139]. Similar to our results, linear calibration curves in the pH range between 5.5 -7.5 were reported in vitro, at both 3T and 7T. These curves were further used for in in-vivo pH mapping in mouse kidney [129] and in determining the pH in the bladder of a patient, at 3T, one hour after he had undergone a CT scan. The study at 3T [139] also illustrates the complications in detecting CEST signals at lower fields, as the smaller the magnitude of the main magnetic field the lower the frequency separation between the proton exchange groups. The latter, leads to peak overlap and, especially in-vivo, could cause contamination of the signal of interest by a neighbouring group. We note here that, the CEST signal - pH calibration curve has to be determined in-vitro, before any in-vivo pH mapping can be performed. A different pH determination method was reported Randtke at al. [158] and Jones et al. [91]. In this approach, the Bloch equations are modified to contain pH as a parameter. This is done by replacing the contrast agent's exchange

rate k_{sw}, with its equivalent based catalysed relation: $k_{sw} = k_0 + k_b * 10^{pH-pk_w}$ [264]. The three constants of the previous relationship can be determined in-vitro, by fitting the equation to Z-spectra of phantoms, at different pH levels. Subsequently, the modified Bloch equations are fitted to in-vitro or in-vivo Z-spectra and the pH along with the agent's concentration is determined by the fitting parameters. This method is also valid for agents having only one exchange peak.

An in-vitro study of Ultravist at 7T [15] has reported similar results to the ones presented here. The log peak ratio of the two exchange peaks produced a linear calibration curve with $R^2 = 0.95$. The reported CEST effects were higher than the ones measured in our experiments, as a stronger pulse power and a much longer (5 sec) saturation time were used. In contrast to our asymmetry analysis, a Lorentzian line fitting was used for CEST effect quantification. Nevertheless, at least for in-vitro conditions, the asymmetry analysis is adequate in describing the signals arising from the two peaks, as indicated by the pixel by pixel asymmetry maps in Figures 4.12 and 4.13. In a further in-vivo study by the same author, Ultravist was used to quantify extracellular tumour pH in a mammary carcinoma mouse model [15]. MicroCT scans validated the delivery of the agent in the tumour, regardless of the route of administration (subcutaneous or IV-infusion). This could also be true in the case of brain tumours, as the blood-brain-barrier disruption might allow for the contrast agent to be accumulated in the tumour. The same study also suggests that the required dose in order for a measurable CEST effect to be detected in humans is ~ 0.27-0.39 $\frac{gI}{Kg}$, which is 4 to 5.5 times less than the maximum recommended dose. However, implementation of the method at a lower field will be challenging, considering the significant drop in signal to noise ratio and possible overlap of the two peaks at 4.2 and 5.6 ppm. Further considerations for in-vivo application of the ratiometric method involve correcting for B_0 inhomogeneities using spline fitting [88], B_0 maps [190] or WASSR [100] and identifying a quantification method that will correctly measure the effect of each peak without any contamination from other CEST peaks or conventional MT effects.

It is clear that using contrast agents for absolute pH measurements, by nature, provides a means of quantifying extracellular pH. Nevertheless, the ratiometric approach has further been extended to measuring intracellular pH. The feasibility of the method was demonstrated in-vitro and in a mouse model of cerebral ischaemia [138]. As this approach is still ratiometric, two measurable, in in-vivo, CEST effects are required. The reported study utilised the ratio of the widely described amide peak at 3.5 ppm and an amine peak at 2.75 ppm. Both CEST signals are thought to arise from intracellular proteins and peptides and therefore their ratio is expected to reflect intracellular pH. The method is valid under the assumptions that the amide and amine populations are constant throughout healthy tissues and pathology and that the relationship between the measured CEST signal and pH is linear, in-vivo. For the latter, ^{31}P-MRS is required in order for a calibration curve to be derived in-vivo. Unfortunately, the study has been conducted at 9.4T and even though the amide peak at 3.5 ppm has previously been detected, in-vivo, at lower fields, detection of the amine peak remains questionable.

Being able to reliably and non-invasively measure pH is an attractive diagnostic feature, as pH is related to tumour characteristics such as, radio/chemo resistance, metastatic behaviour and invasion and inhibition of DNA repair mechanisms [48]. The current most common MR method for such measurements is ^{31}P-MRS and as a spectroscopic method, suffers from low spatial resolution, as compared to imaging methods. The measurement relies on the difference between inorganic phosphate (Pi) and an endogenous reference (usually PCr). ^{31}P-MRS measures intracellular pH, as the Pi signal arises from intracellular phosphates [182]. According to data from reference [214] the mean intracellular pH for human brain tumours is 7.10. In addition, healthy tissue pH is either similar to the latter or slightly lower (~7.01). Understandably, intracellular pH is maintained alkaline or neutral by pH regulatory mechanisms as an acidic environment will lead to an eventual cell death. Furthermore, hypoxic anaerobic glycolysis in tumour cells renders the extracellular pH in tumours acidic due to

the accumulation of lactic acid and other acidic metabolites. As reported in [214], most human tumours exhibit extracellular pH values between 6.15 - 7.40, whereas normal tissues usually have pH between 7.0 - 7.4.

As our results indicate both Niopam and Ultravist exhibit a linear and concentration independent relationship between the ratio of the measured CEST signals and pH within a range that is relevant to human brain tumours (6.0 - 7.5). Selective accumulation of the agents in the tumour after blood brain barrier disruption and non-toxic dosage are essential prerequisites for the application of the ratiometric method in-vivo. As the signals arise from amide groups exchanging with slow to intermediate rates, low B_1 power (< 3 μT and within SAR limits) will be sufficient for effectively saturating these protons. The 360 Hz separation of the two peaks at 7T is adequate for uniquely detecting each effect. However, this difference is halved at 3T and might cause the peaks to overlap. Direct water saturation is not expected to be a problem with either Niopam or Ultravist as both agents resonate far from the water resonance. It is possible that signal contamination from conventional MT or upfield NOE effects will compromise the accuracy of the asymmetry analysis. In this case alternative quantification methods such as Lorentzian fitting [90] or time domain analysis [237] can be implemented to isolate the CEST effect from each peak. Many other pharmaceutical excipients, possessing exchangeable protons, can also be used for CEST imaging. These finished drug products exhibit high safety profiles and can be administered in adequately enough doses, for in-vivo detection. What is more, some of these agents have two exchangeable proton peaks and are therefore suitable for ratio-metric analysis [128].

4.5 Conclusion

Under the irradiation of two Gaussian pulses at a power of 1.5 μT and 100 ms total duration, the clinically approved X-ray contrast agent Visipaque was found to exhibit one pH dependent CEST peak. It cannot therefore be used for concentration independent absolute pH mapping using the conventional ratiometric approach. On the contrary, Niopam and Ultravist were found to have at least two pH dependent CEST peaks within a pH range relevant to human brain tumours. The derived calibration curve for both agents was linear, with the linearity being higher for Ultravist (R^2 = 0.88 vs R^2 = 0.99). The asymmetry analysis correctly described the variation of CEST signal ratio with pH as indicated by pixel by pixel asymmetry maps.

Chapter 5

Pulsed CEST at 3T. Comparison between single slice and 3D acquisitions.

This chapter describes a comparison between a 2D product and a 3D research gradient echo sequence in generating CEST signals from a series of phantoms. Both sequences have been modified in order to allow for CEST acquisitions. The 2D sequence has been adapted by myself, whereas the modifications on the 3D version were performed by a team from Institute of Psychiatry, Psychology and Neuroscience in King's College London.

As a first step, both sequences were tried on a water phantom. Sequentially, their efficacy was tested on the X-ray contrast agent, Ultravist and then on creatine and creatine plus glutamate phantoms. Shimming has been a major problem resulting and many 2D datasets to be disregarded. A comparison between high order shimming the default linear shimming is presented at the end of the chapter.

5.1 Introduction

Chemical exchange saturation transfer (CEST) is a variation of the magnetisation transfer (MT) contrast mechanism involving the physical proton exchange between various proton containing compounds and water. Signals arising from endogenous amides, amines and hydroxyl have been described in literature, both in-vivo and in-vitro [122, 88, 266, 267, 260, 168, 211]. CEST benefits from higher magnetic fields as the resonant frequency separation between the signals of interest increases. Moreover, the T_1 increase at high field also contributes to higher CEST effect [265].

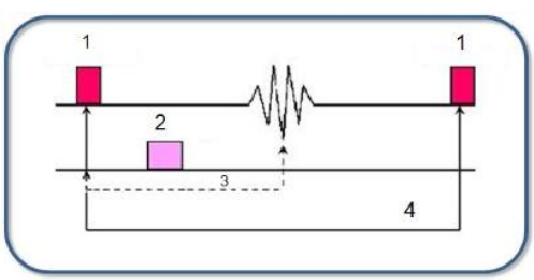
Despite the challenges of lower signal to noise ratio and possible contamination of the CEST signal by neighbouring exchange sites, CEST contrast has successfully been detected at 3T [88, 223, 168, 270]. This includes CEST signals, not only from endogenous proteins (amides), but also from exogenous contrast agents [129, 127, 139, 158, 15]. To quantify the CEST contrast, the conventional asymmetry analysis and a modified variation of it, have both been used, even in-vivo [260].

In this work, a single slice gradient recalled sequence was adapted for CEST scanning. To test the efficacy of the sequence, the duration, power and number of prepulses was varied. The sequence was tried on water, Ultravist and creatine phantoms, using linear shimming to correct for B_0 inhomogeneities. As a comparison, the scans were repeated using a multi-slice 3D gradient echo sequence. Linear shimming was compared to high order shimming using the multi-slice 3D sequence on a creatine plus glutamate phantom. The CEST contrast was quantified using the conventional asymmetry analysis, in all cases.

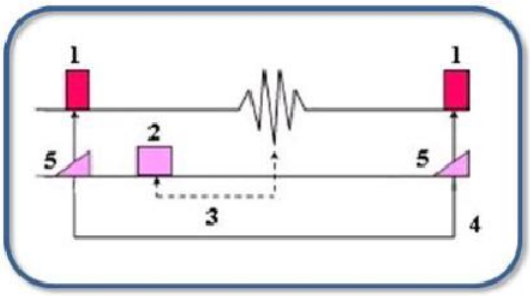
5.2 Materials and methods

5.2.1 Sequences

Both sequences that were used are gradient echo based sequences. More precisely, they are modified versions of the product sequences under the names '2dfast' and 'efgre3D' (GE, Healthcare). The former is a typical gradient recalled sequence, where the echo is formed by the frequency encoding gradient reversal. The latter belongs to the spoiled gradient echo sequences, where a continuous phase shifting of the excitation RF is used to spoil any residual transverse magnetisation (Figure 5.1).



#	Description
1	Variable pulse
2	Gradient rephasing pulse
3	TE
4	TR



#	Description
1	Variable pulse
2	Gradient pulse
3	TE
4	TR
5	Phase shift

Figure 5.1: The 2D gradient echo (left) and the 3D spoiled gradient echo (right) sequences that were modified for CEST imaging.

The sequences described above were modified by adding a pre-saturation module before the main sequence. This consisted of a Fermi pulse and a Gauss pulse for the single and multi-slice case respectively. As it can be seen in the following figure (Figure 5.2) the Fermi pulse is characterised by a plateau of a constant amplitude and exponential decay at its sides, whereas the Gauss pulse is shaped like the Gaussian function. Mathematically the pulses are described by the following equations:

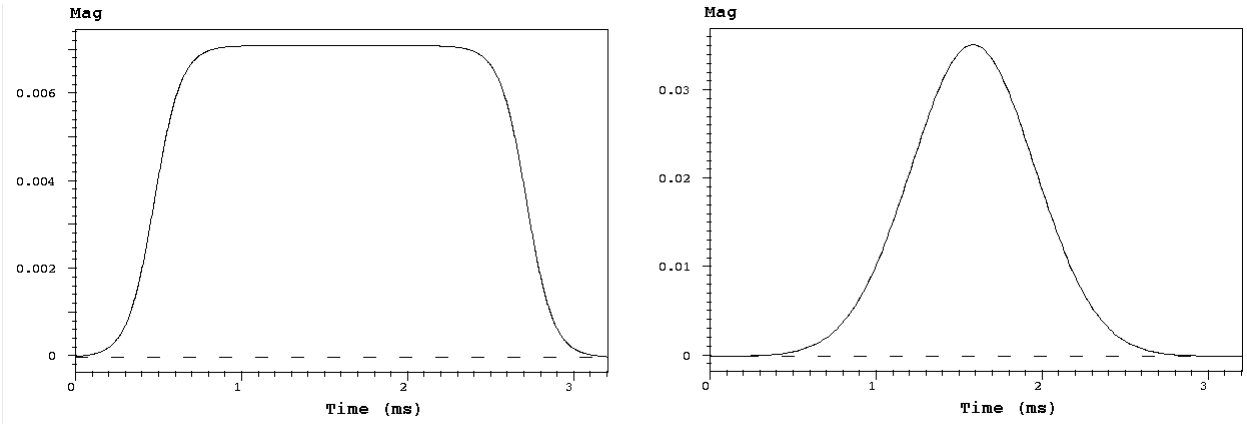


Figure 5.2: Time domain graphs of the Fermi (left) and Gauss (right) RF pulses used for CEST imaging.

$$B_1(t) = \frac{A_F e^{i\Delta\omega_{RF}t}}{1 + exp(\frac{|t|-t_0}{a})}$$

where

A_F: the B_1- field peak amplitude

t_0: a measure of the pulse width

α: a measure of the pulse's transition width

for the Fermi pulse and

$$B_1(t) = A_G e^{-\frac{t^2}{2\sigma^2}} e^{i\Delta\omega_{RF}t}$$

where

A_G: the B_1- field peak amplitude

σ: the standard deviation of the pulse, in units of time

for the Gauss pulse.

The width (duration) of the Fermi pulse is given by:

$$T_F = 2t_0 + 13.8a$$

and the time-bandwidth product for the Gaussian pulse is given by [7]:

$$T_G \Delta f_G \simeq 2.8$$

An illustration of the added pre-pulse module, including the Fermi pulse, in the 2D sequence is presented below. The graph is a simulation of the sequence using GE's WTools software. The software simulates the programmed/modified sequences to a good approximation and provides a first step at debugging the code defining the sequence.

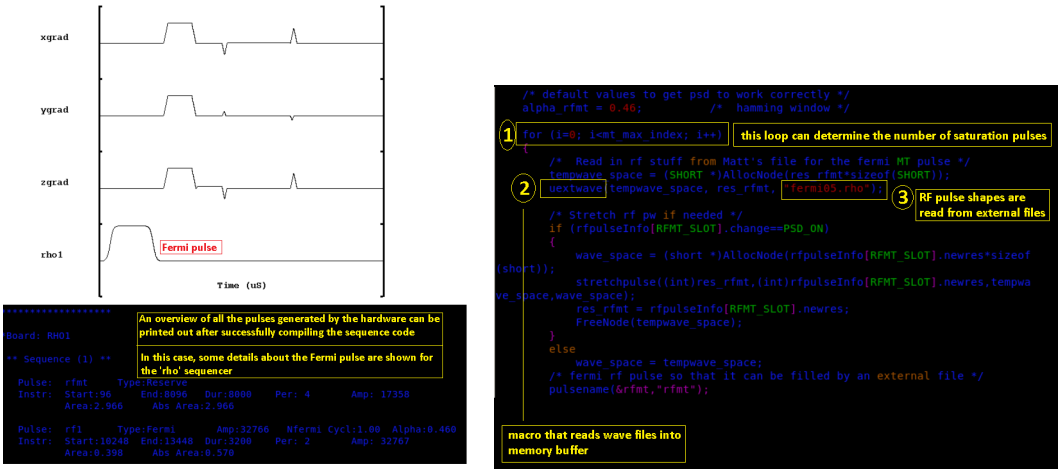


Figure 5.3: Fermi pulse addition to the 2D gradient echo sequence. The pulse is generated on the 'rho' sequencer of the scanner (**left**). Code example of incorporating the Fermi pulse in the pulse sequence (**right**).

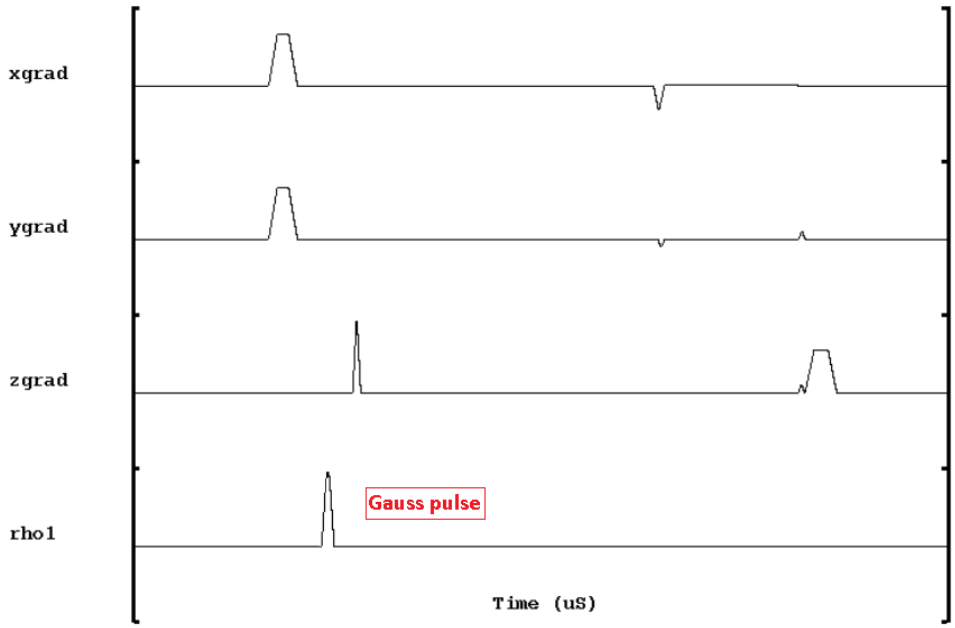


Figure 5.4: Gauss pulse addition to the 3D gradient echo sequence. The pulse is generated on the 'rho' sequencer of the scanner.

The 2D sequence was modified for CEST imaging as follows: first the variable controlling the frequency of the RF pulse was changed, to allow for a frequency sweep between -1020 Hz to1020 Hz or -8 to +8 ppm at 3T. For more efficiency the variable was also set as one of the scanner interface displayed adjustable variables. Second, the pulse width was hardcoded as either 20 ms, 40 ms or 80 ms, with the default width of the pulse being either 8 or 16 ms. Even though a width of 100 ms would also successfully work on the scanner, a maximum of 80 ms was eventually used. This allows for some flexibility in manipulating the flip angle (RF power) as the sequence must be operated within SAR limits. All attempts in increasing the pulse duration over 100 ms would result in overlapping waveforms between the pre-saturation pulse and the excitation pulse, that is also generated on the same hardware. Similar code changes were then performed to the variable controlling the flip angle of the pre-saturation pulse, and hence it's power. Finally, in order to add more pre-pulses into the sequence, a loop was added in the code allowing for repetitive creation of the Fermi RF pulse. Up to four pulses were successfully added in this manner. The majority of the changes

were done on the code defining the MT module, that is then inlined to the code of the main '2dfast' sequence.

As mentioned before, the 3D sequence was programmed elsewhere. The current version available allows setting the B_1 power, the type of the pre-pulse and it's duration. It consists of a single pre-pulse and the maximum duration that can be used is 20 ms. The data presented here have been acquired using a Gaussian pulse and, as opposed to the linear k-space filling of the 2D sequence, a reverse elliptic centric k-space filling is implemented.

5.2.2 Phantoms

Four types of phantoms were used: Distilled water, Ultravist, at a concentration of 370 mgI/ml and physiological pH, creatine at a concentration of 50mM and pH = 7 in distilled water and finally, creatine plus glutamate at a concentration of 50mM each and pH = 7 also in distilled water. Ultravist was transferred in a 50ml plastic test-tube, whereas all the other phantoms were prepared in 500ml plastic containers. The phantoms were prepared at a chemistry lab (5th floor, School of Life Sciences) equipped with a digital pH meter (for checking/controlling pH levels: the same one described in section 4.2 - Materials and Methods of the previous chapter) and a large container of distilled water, among other things. All phantoms were prepared at physiological pH = 7 and this was verified using the pH meter.

5.2.3 Scanning

All scanning was performed on a 3T GE MR750 scanner using a 32 channel head coil. Single slice images were acquired using TR = 120 ms, TE = 30 ms, 128 x 128 matrix size, slice thickness 5 mm, 19 sec per offset. For multi-slice acquisitions, TR = 30 ms, TE =18 ms, 64 x 64 matrix size, slice thickness 3 mm, 4 slices in total.

The frequency sweep was determined from the phantom used. Z-spectra were

acquired symmetrically around the water resonance (set at 0 ppm). More offsets were acquired around the resonant frequencies of the respective samples in an attempt to sample the exchange peaks more accurately. In all experiments with the 3D sequence, one scan was performed without saturation in order to be used for normalisation, while in the 2D sequence a distant offset (-15ppm) image was used for data normalisation. Linear shimming was performed before each acquisition. For comparison, both linear and high order shimming were performed on the creatine plus glutamate phantom.

5.2.4 Data analysis

All images were converted from DICOM to analyse and arranged appropriately into 3D or 4D volumes. The reference image was used to normalise the data. For the multi-slice acquisition, one reference image was acquired per slice. The images were first thresholded and then smoothed. The minimum and maximum signal intensities were used as bounds to interpolate (interp1, in Matlab) in-between the measured offsets resulting in 1000 pairs of intenistiy-ppm. This interpolation was used to facilitate the next step of analysis, namely B_0 correction. To correct for B_0 inhomogeneities, an internal B_0 map was calculated by finding the offset corresponding the minimum intensity on each pixel. Sequentially, a spline was fitted on a pixel by pixel basis, with its minimum being shifted based on the internal B_0 map. Z-spectra were derived by plotting the normalised signal intensity against the frequency offset and asymmetry curves were calculated by subtracting the positive from the negative normalised signals.

5.3 Results

5.3.1 Distilled water

Figure 5.5 illustrates the Z-spectrum acquired from a water phantom for three different pre-saturation durations. This is a single slice acquisition using one Fermi pre-pulse. As the flip angle is the same for all three acquisitions (670°), increasing the duration of the pulse lowers the peak B_1 power, so the area under the RF envelope is constant. In other words, 'stretching' the RF pulse results in lower saturation.

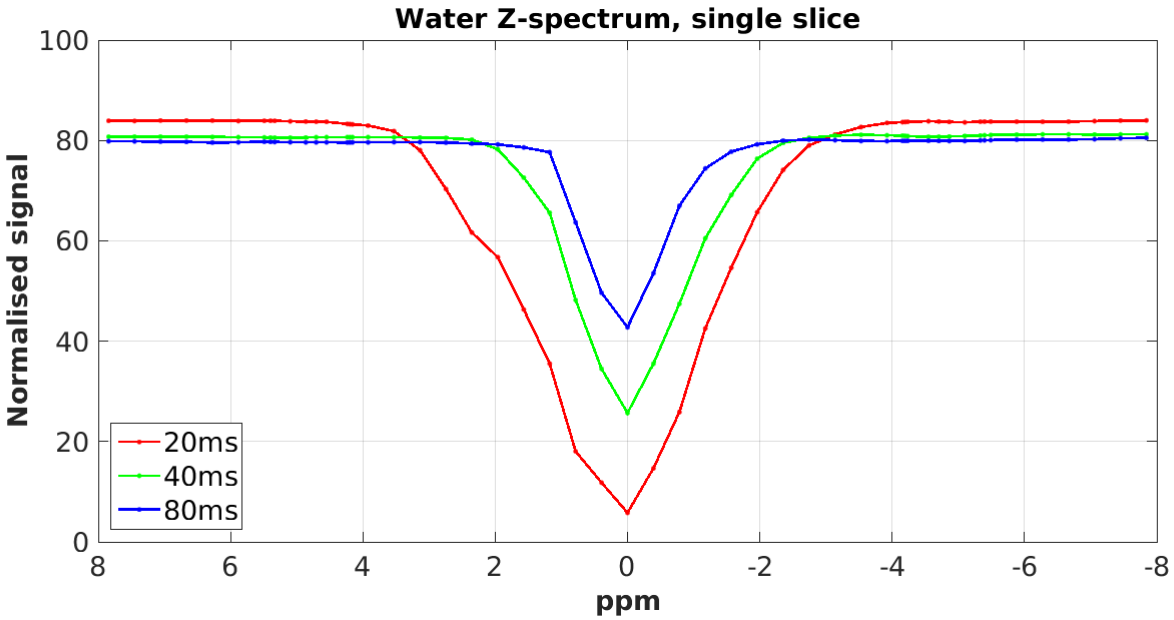


Figure 5.5: Single slice water Z-spectrum for three RF bandwidths.

The same phantom was then scanned using the 3D sequence. Four slices were acquired for two B_1 powers and durations. Figure 5.6 illustrates the Z-spectrum of the second slice as measured after performing linear shimming. Evidently, the short saturation pulses exhibit a broader full width at half maximum (FWHM) as their bandwidth is double the bandwidth of the longer pulses (280 Hz vs 140 Hz).

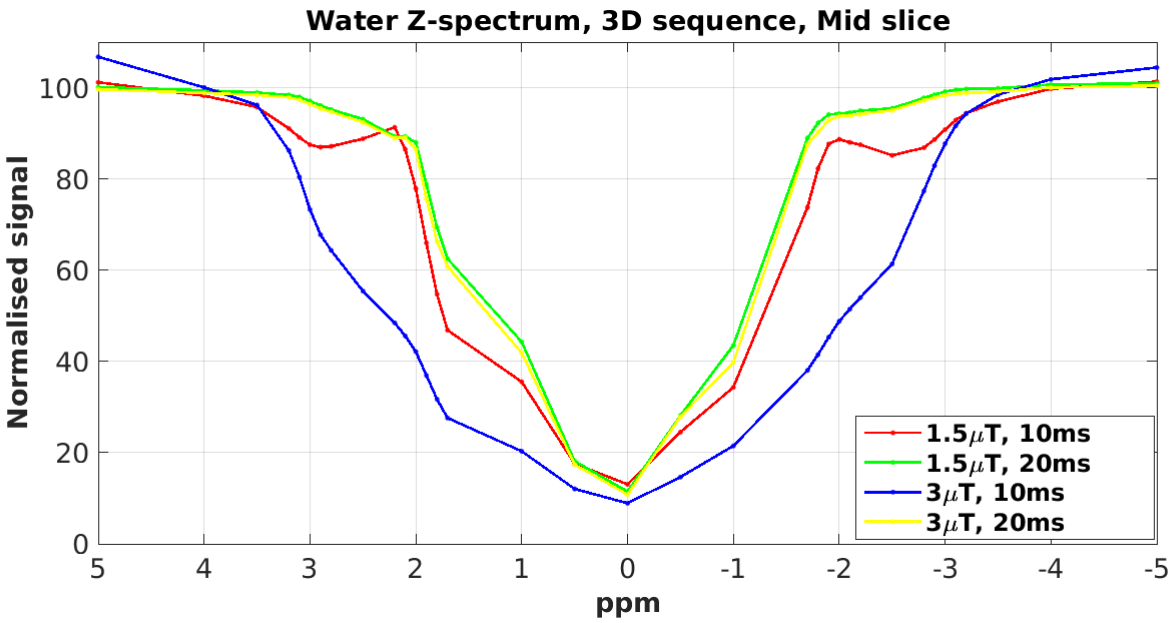


Figure 5.6: Water Z-spectrum of the middle slice using the 3D sequence.

With the exception of the spectrum for 1.5 μT and 10 ms all the other spectra are fairly symmetric, yet a lot broader than the ones acquired using the Fermi pulse. This is because the bandwidth of the latter is at least two times less than the bandwidth of the Gaussian pulse used for the 3D acquisition. Unfortunately, 140 Hz is the minimum allowed bandwidth for the Gaussian pulse. Alternatively, a SINC pulse of the same duration (20 ms) might improve the acquisition, as its bandwidth would be 100 Hz.

The red and blue curves in Figure 5.6 demonstrate that the water resonance is directly saturated by the short duration Gaussian pulse. Such spectral distortions occur when the saturation pulse bandwidth exceeds the water line-width [170]. These distortions are absent from the curves in Figure 5.5 because the Fermi pulse of the 2D sequence has shorter bandwidth than the Gaussian pulse.

5.3.2 Ultravist

The single slice acquisition Z-spectrum of the Ultravist phantom is presented in Figure 5.7. Again three pulse widths were used to investigate effect of pulse bandwidth on the CEST signal. The Z-spectrum is in line with our previous results at 7T, where only the

peak at 4.2 ppm was prominent at physiological pH. However, here the peak appears shifted by 0.2 ppm.

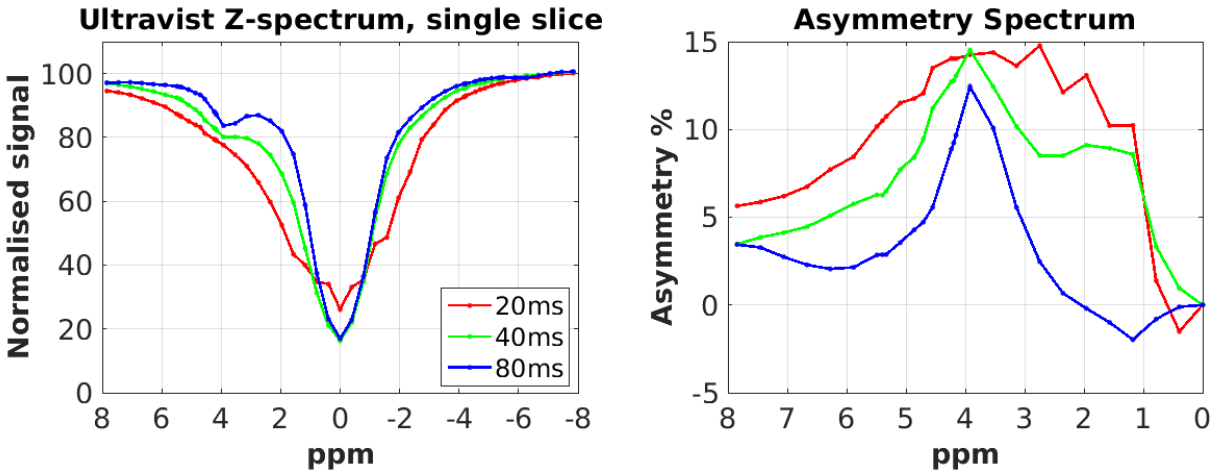


Figure 5.7: Z-spectrum and asymmetry curves for Ultravist for three RF pulse durations.

The red line in the Figure 5.7 illustrates a blurring of the Z-spectrum that sometimes occurs for very short RF pulses. The increased bandwidth of the shorter pulses might sometimes decrease the spectral resolution of the Z-spectra, as neighbouring points in the spectrum are excited repeatedly. This problem is more pronounced when the step size of the frequency sweep is smaller than the bandwidth of the RF pulse. This has consistently been observed in our data when short RF pulses were used (e.g Figure 5.6).

The asymmetry curves in Figure 5.7 show a decrease in the CEST contrast of the peak around 4 ppm when the pulse is stretched, while the flip angle remains constant, as the RF pulse gets weaker. The small dip at 5.6 ppm for the 80 ms corresponds to the second peak that has been detected at 7T. As we have previously demonstrated at 7T, this peak is more pronounced for acidic pH. Consequently, it will be more prominent at lower pH values (unlike the physiological pH used here) and lower saturation powers.

The addition of more Fermi pulses was investigated next. As was mentioned before, there was a limit in how long the pre-saturation module can be, before any overlap with the next generated pulse of the sequence occurs. In our case, that was around

100 ms. Therefore, addition of more pulses meant that their width had to be short in order to comply with this restriction. The Z-spectra after adding three and four pre-pulses of 20 ms are presented in Figure 5.8.

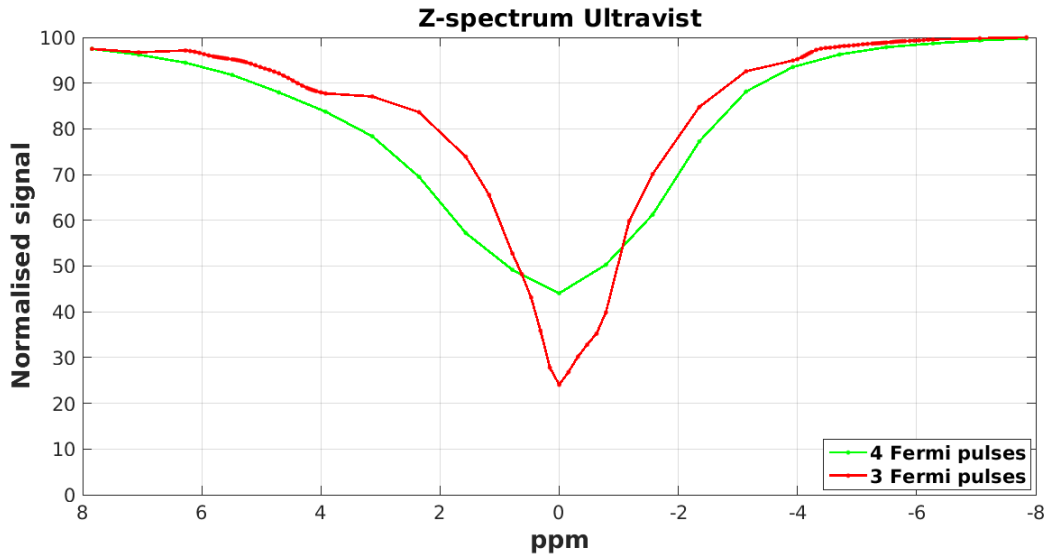


Figure 5.8: Single slice Z-spectrum for Ultravist using three and four 20 ms pre-pulses.

Evidently, the addition of more pre-pulses results in lower saturation, despite an increased RF duty cycle caused by the smaller inter-pulse delay. The measured asymmetry is less than 10% in both cases (Figure 5.9), being 4% less than the minimum asymmetry measured using one pulse (blue line) in Figure 5.7.

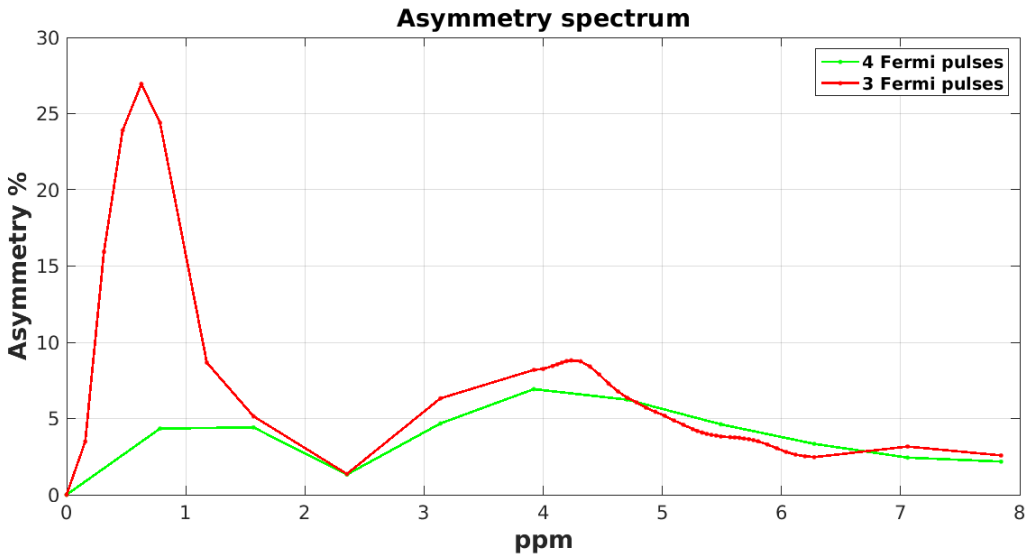


Figure 5.9: Single slice asymmetry curves for Ultravist, using three and four 20 ms pre-pulses.

Being restricted by the maximum time of the pre-pulse module, no further RF duty cycle improvements can be attempted, as the pulse train duration must remain within 100 ms in total. Increasing the number of pre-pules is beneficial in terms of energy deposition simply because the latter can be reduced, when using more, but weaker, RF pulses. In our case, SAR was always within the recommended limits, being less than 1 W/Kg during all experiments. Considering the latter and also that the saturation achieved is less that when using a single RF all further scanning was performed using one Fermi pulse.

The Ultravist phantom was sequentially scanned using the 3D sequence. Again four slices were acquired. For demonstration purposes, the Z-spectra of the second slice were chosen and presented below. The Gaussian pre-pulse was applied at two B_1 powers and pulse widths. Similarly with the single slice acquisition, linear shimming was performed before each acquisition. The results are presented in Figure 5.10.

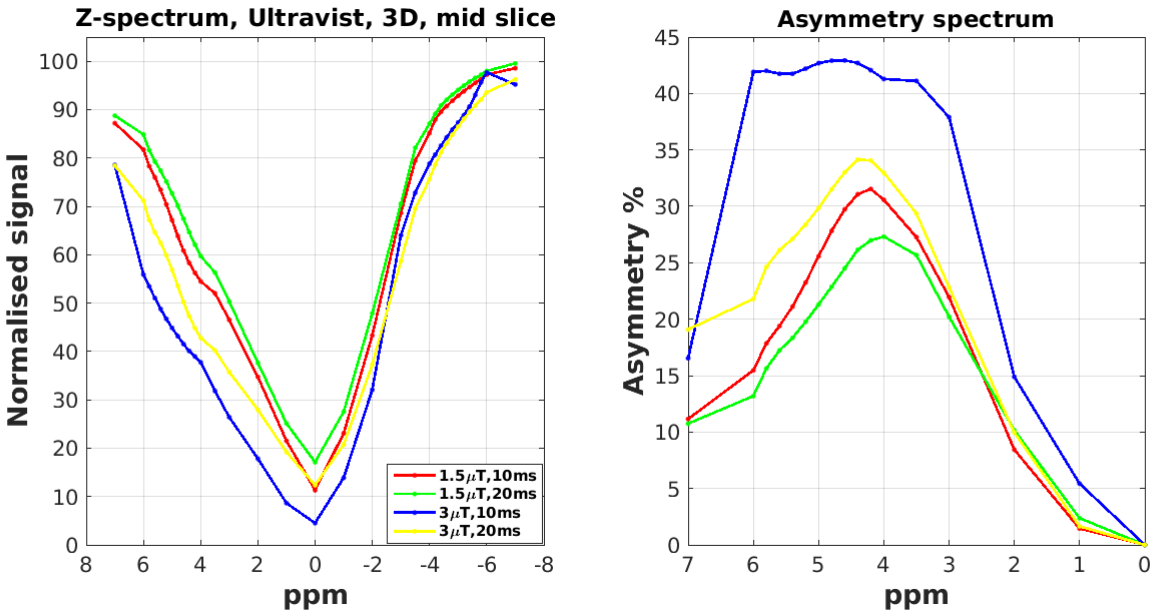


Figure 5.10: Z-spectrum and asymmetry curves of the second slice, for Ultravist.

As it can be seen on the previous figures, using higher B_1 power increases the saturation. Similarly to what was found for the 2D acquisition (Figure 5.7), the acquisitions for shorter saturation times give rise to a larger CEST signal than the ones having longer saturation and same B_1 power, as stretching the area under the RF envelope reduces its amplitude. The maximum CEST effect measured with the 3D sequence is ~42%. However, the large suppression (blue line) leading to this magnitude of asymmetry could be a result of a repeated excitation of neighbouring offsets, considering the large pulse bandwidth (240 Hz). As the phantom was prepared at physiological pH, the prominent peak is the one resonating at 4.2 ppm. The small dips at around 5.6 ppm of the second Ultravist peak are barely visible in the asymmetry curves, just like when using the 2D sequence.

The Z-spectra in Figure 5.10 seem to be more suppressed at the positive frequencies. Since no overall Z-spectrum shift is observed, then this suppression is not due to ineffective B_0 shimming [231]. Instead, the appearance of the spectra could be due to the degradation of the excitation profile of the frequency selective Gaussian pulse. Because of the complexity of the Bloch equations, such RF pulses are rarely designed

while taking account the effects of relaxation. Even though the longitudinal relaxation times are generally longer than the duration of the frequency selective RF pulses and thus their effects can be ignored, the same cannot be said for the transverse relaxation times. The latter are comparable to the time scale of the RF pulse and can lead in compromised excitation profiles [173]. The effects of the relaxation times were found to only be dependent on the ratio of (relaxation time)/(pulse length) for a variety of pulse shapes, including the Gaussian used here [58].

Overall, the asymmetry measured using the Gaussian pulse was found to be larger than the asymmetry measured using the Fermi pulse. For a direct comparison of the 2D and 3D data, Z-spectra and asymmetry curves are jointly plotted in Figure 5.11.

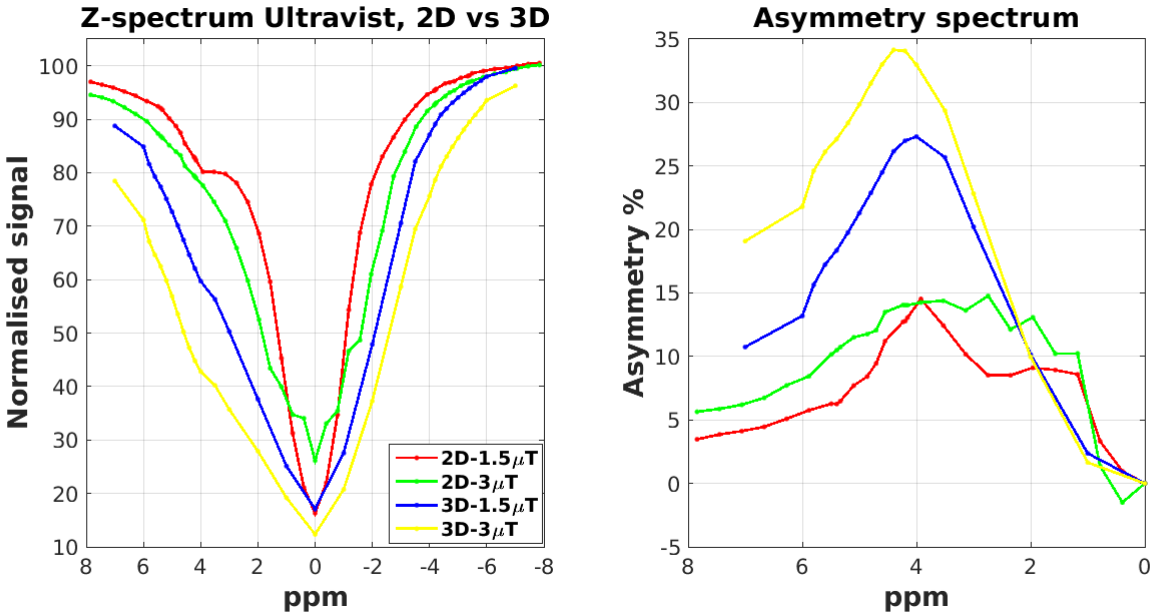


Figure 5.11: Z-spectra and asymmetry curves for Ultravist acquired using the single and multislice sequences.

The direct comparison of the asymmetry values for the Gaussian and Fermi pulses shows that a maximum contrast of 34% is achieved when using a 3 μT Gaussian pulse and a width of 20 ms. On the contrary, the maximum contrast measured using a Fermi pulse is ~15% or more than 50% less than the Gaussian pulse.

5.3.3 Creatine

The efficacy of the sequences in generating CEST contrast is further compared using a 50mM creatine in distilled water phantom. The Z-spectra and asymmetry curves when using the 2D sequence are presented in Figure 5.12. The Z-spectrum of the 20 ms RF pulse (red line) is extremely distorted and therefore it's asymmetry has been suppressed in the asymmetry spectrum, by excluding the negative values. The initial part of the intermediated pulse width (green line) has also been excluded. However, a clear peak is seen at 1.9 ppm, corresponding to creatine. In contrast to Ultravist, a lower B_1 power is more efficient in saturating the creatine peak. This indicates that the creatine proton exchange rate is slower than the Ultravist proton exchange rate. The maximum asymmetry measured in our single slice acquisition is 2.8%

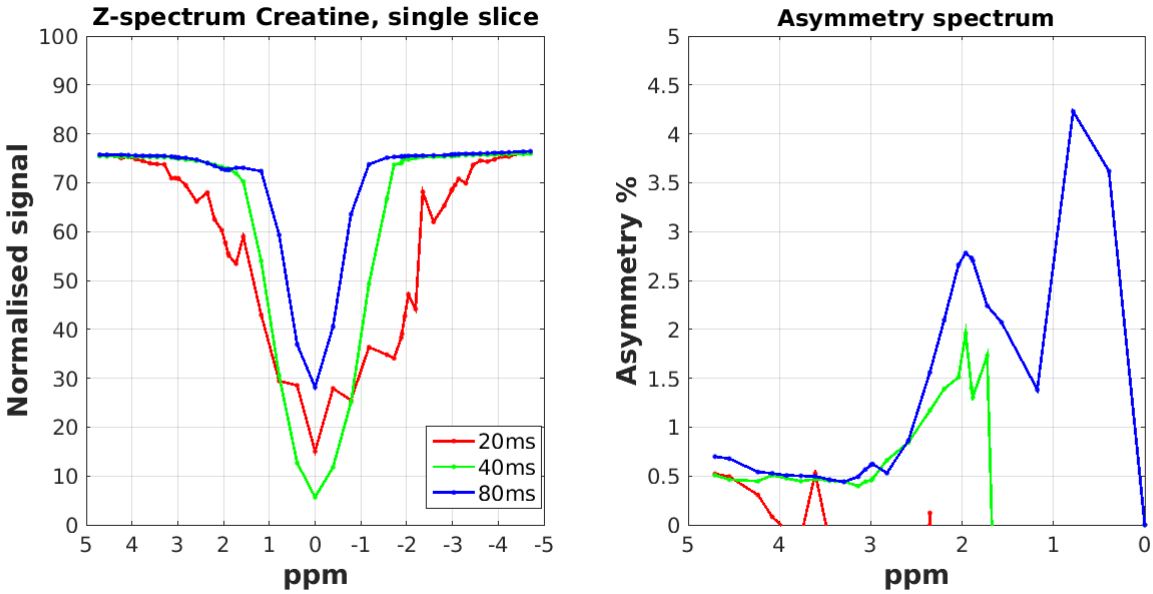


Figure 5.12: Single slice Z-spectra and asymmetry curves for 50mM of creatine and three different pulse widths.

In Figure 5.12 we can see once again that the spectrum for the shortest Fermi pulse (red curve, 20ms) is distorted. Since the effect is apparent all across the spectrum, it can't be due to very dense sampling and repeated excitation of neighbouring points because no such saturation scheme was implemented. The spectra were indeed

sampled more densely around 2ppm (creatine peak) but were at least 1ppm apart at the other frequencies. The distortion can then be attributed to a Fermi pulse bandwidth greater than the water line-shape. The blue curve in Figure 5.12 demonstrates that a longer Fermi pulse reduces the saturation efficiency, as 'stretching' the pulse lowers its peak B_1 amplitude so the area under the pulse shape is maintained.

Figure 5.13 illustrates the Z-spectra and asymmetry curves of the multi-slice acquisition for the same 50 mM creatine phantom. The figure presents data from the second, out of the four, slices that have been acquired.

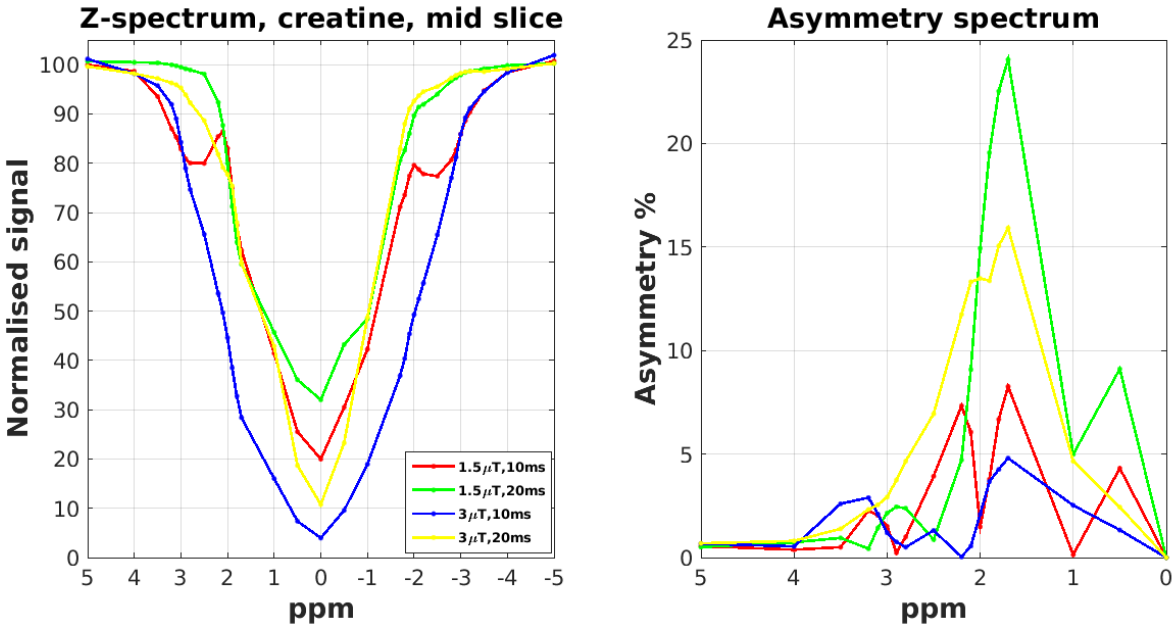


Figure 5.13: Z-spectra and asymmetry curves of the second slice for the 50mM creatine phantom. Data have been acquired at two B_1 powers and durations.

The red and blue curves in Figure 5.13 are similar to the ones of the same colour in Figure 5.6. Even though the samples are different (creatine and distilled water respectively) the Gaussian pulse results in broad Z-spectra, in both cases, because of its bandwidth. At the time of the experiments described in this chapter it was not possible to reduce the pulse's bandwidth below 140 Hz. Similarly to Figure 5.12, the lowest B_1 RF pulse power generates the largest CEST contrast, at the creatine peak, (green line) suggesting a slow exchange rate. Also, in both pulse powers, the RF having a longer

duration generates a higher signal.

Just like in the Ultravist phantom, the Gaussian RF pre-pulse generates a higher saturation than the Fermi pulse used in the single slice sequence. A direct comparison between the Z-spectra and asymmetry curves of the two sequences is presented in Figure 5.14. In this case, there is a clear difference between the normalisation of the two datasets. Even though the asymmetry is calculated from within the same dataset, this normalisation difference affects the measured asymmetry, as the Z-spectra have roughly the same minima, but a ~25% difference in their maxima. The noisy green Z-spectrum does show an asymmetry, surprisingly, but it should be disregarded. The remaining curves indicate that, for creatine, a maximum asymmetry of 24% has been measured using a 1.5 μT Gaussian pulse and 20 ms in duration (blue line).

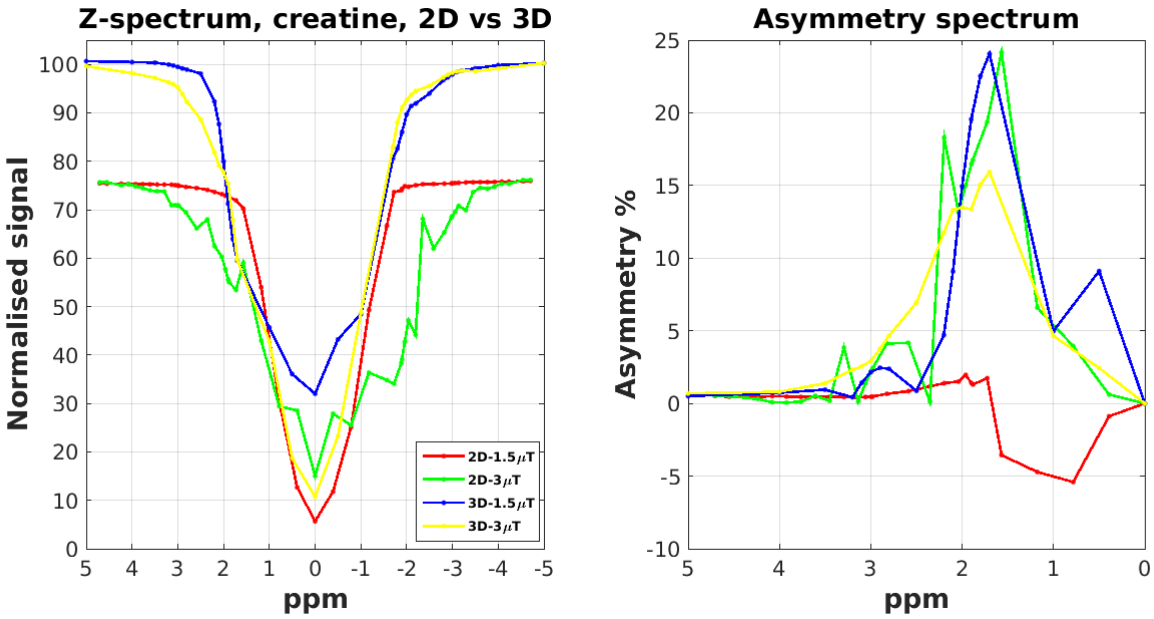


Figure 5.14: Z-spectra and asymmetry curves, for creatine, acquired using the single and multislice sequences.

The green curve in Figure 5.14 is the same as the red curve in Figure 5.12 and the explanation for its distortion is given in the paragraph below Figure 5.12. Finally, it is worth commenting on the following: the reason that the Z-spectra of the 2D sequence in Figure 5.14 have a different normalisation magnitude is because the image used for

normalisation (reference image) was chosen to be part of the saturation scheme, at a large distance from 0ppm nevertheless. The saturation scheme was hardcoded in the sequence code and was subsequently accessed through the scanner's user interface. On the other hand, the 3D sequence was programmed so as the saturation scheme was read from an external text file, with the additional possibility of running the sequence without any saturation. This is illustrated below:

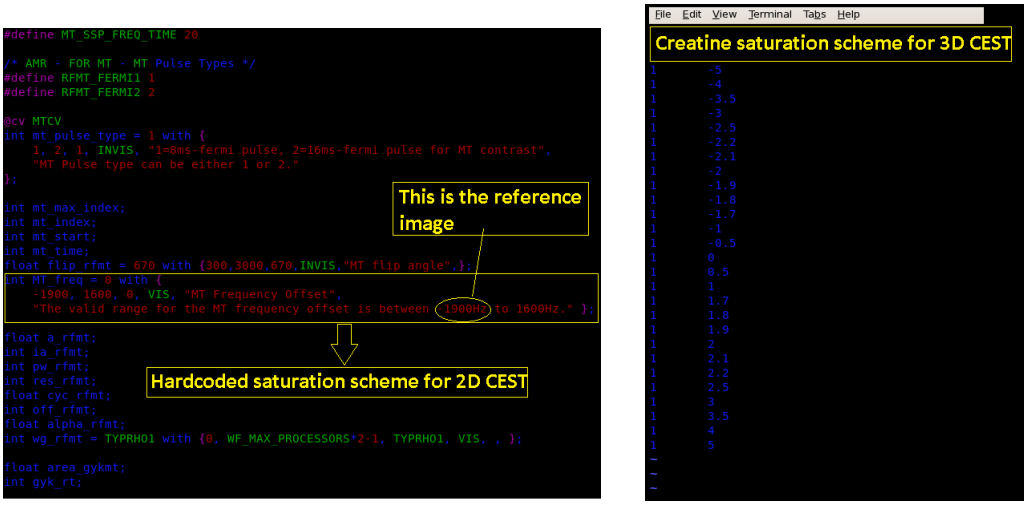


Figure 5.15: Hardcoded saturation scheme for the 2D CEST sequence (**left**). Externally read saturation scheme for the 3D CEST sequence. In this example the scheme for creatine is shown (**right**)

5.3.4 Creatine plus glutamate

A 500ml phantom containing 50 mM creatine and 50 ml glutamate was used to compare two different types of shimming, for CEST imaging. By default, the scanner performs a linear shim, correcting for linear gradients in the field, by adjusting the DC currents in the gradient coils. Sequentially, this correction is propagated on a slice-by-slice basis. However, any residual higher order heterogeneities can lead to blurring and signal loss. For high order shimming a package that was developed at Stanford University and is implemented by GE, was used. The filed map calculation is performed using a spiral sequence and the shim terms optimised are zero (Z_0), first (X, Y, Z_1), all the second order components (XY, X^2-Y^2, ZX, ZY, Z_2), and Z_3 [45].

In order to assess the B_0 homogeneity of the shim, an internal B0 shift map (in ppm) was calculated by finding the frequency of the minimum signal intensity on a pixel by pixel basis after high order (Figure 5.16) and linear (Figure 5.17) shimming. These maps were calculated from the creatine plus glutamate phantom.

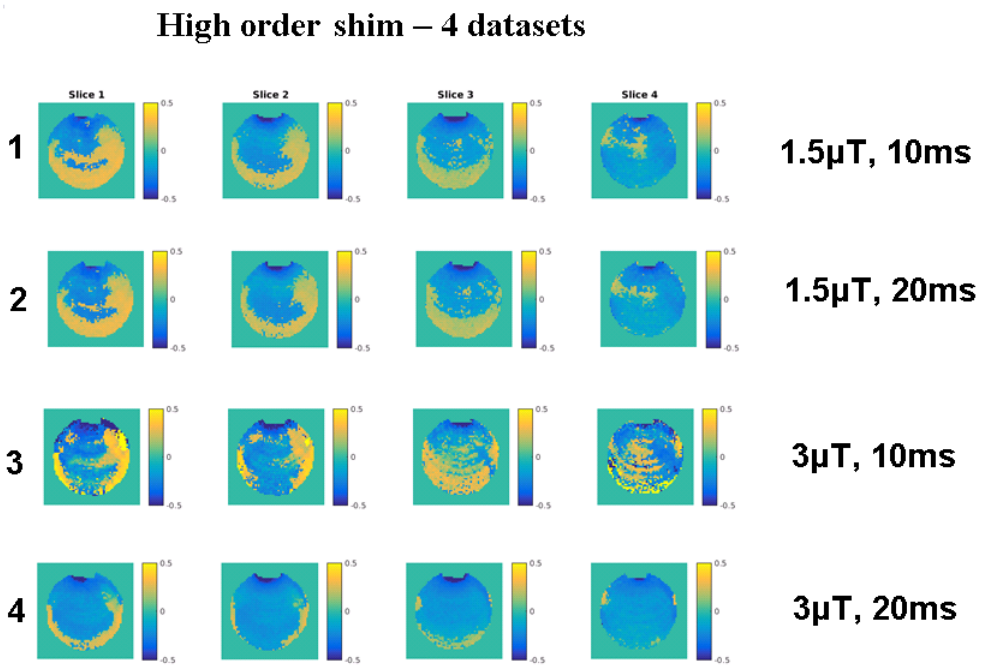


Figure 5.16: Internal B0 shift maps after high order shimming for four datasets.

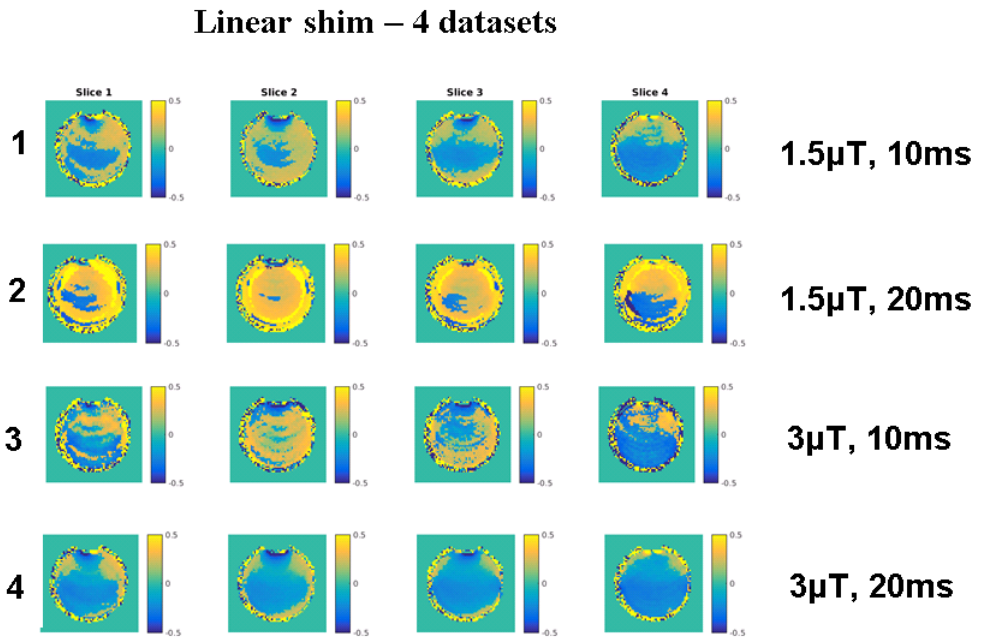


Figure 5.17: Internal B0 shift maps after linear shimming for four datasets.

The maps are displayed between -0.5 - 0.5 ppm in both cases. Overall, linear shimming results in internal B_0 shifts greater than $\pm$0.5 ppm, as compared to high order shimming. For the latter, the calculated internal shifts are within $\pm$0.5 ppm. The most homogeneous shimming achieved corresponds to dataset 4, acquired for a B_1= 3 μT and 20 ms in duration for both high order and linear shim. Internal B0 correction is a more robust method of correcting for B0 inhomogeneities, than an external map, because the measured homogeneity reflects the field during the actual APT measurement. Both creatine and glutamate are most efficiently saturated with B_1= 2.5μT and 3μT, respectively (optimal labelling). The highest B_1 power used here therefore results in the most homogeneous field, as only when the labelling efficiency is suboptimal, the B0 field distribution becomes asymmetrical. The corresponding Z-spectra and asymmetry curves, for dataset 4, after each shimming approach are presented in Figures 5.18 and 5.19.

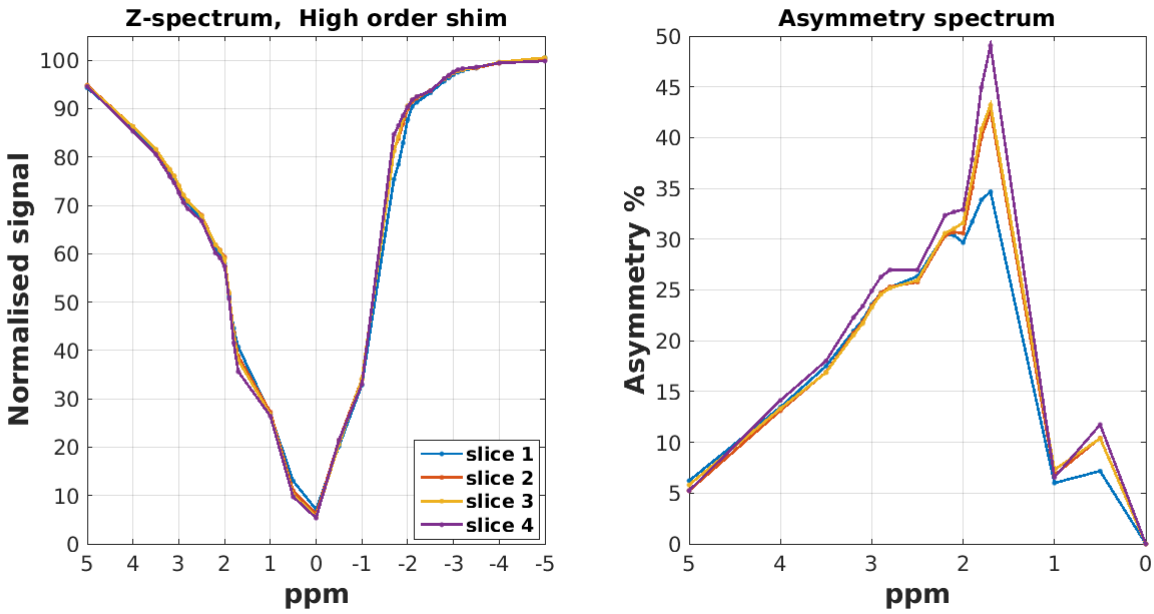


Figure 5.18: Z-spectrum and asymmetry curves, for every slice of dataset 4, after high order shimming.

Both the creatine and glutamate peaks are detected at 1.9 ppm and 3 ppm respectively. The glutamate signal is almost the same in every slice, whereas the creatine shows

an increasing signal with slice number. Linear shimming leads to a similar result, as indicated below.

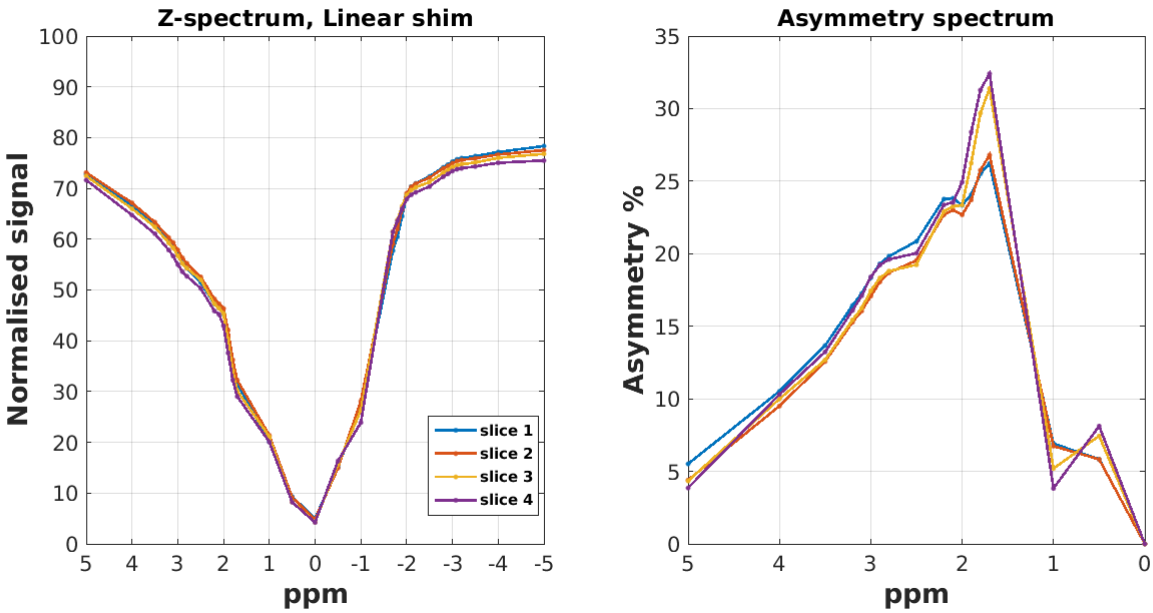


Figure 5.19: Z-spectrum and asymmetry curves, for every slice of dataset 4, after linear shimming.

Both datasets have been normalised by the same reference. Even tough this does not affect the overall shape of the Z-spectrum, the measured asymmetry is slightly higher in Figure 5.18, for high order shimming.

Despite giving similar results for comparable homogeneities, the outcome differs when the internal B0 shifts are increased. As an example, the Z-spectra and asymmetry curves for dataset 2 and each shimming method are presented in Figures 5.20 and 5.21.

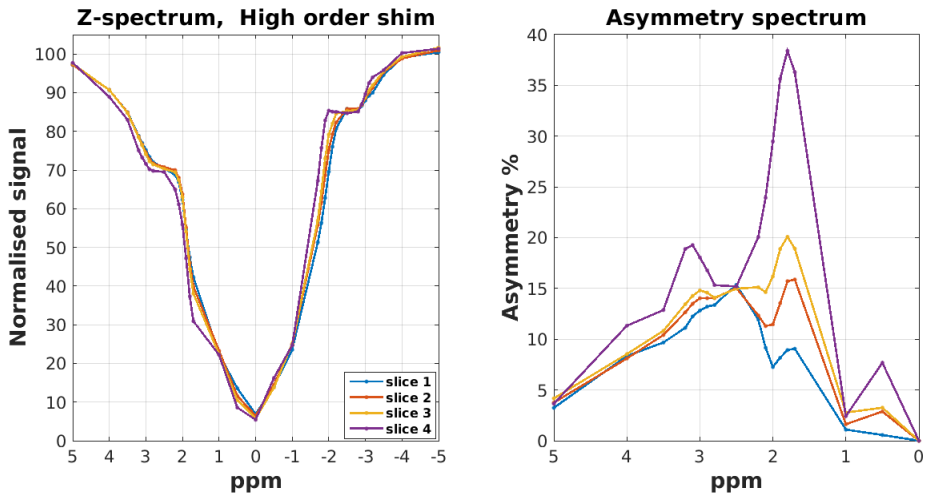


Figure 5.20: Z-spectrum and asymmetry curves, for every slice of dataset 2, after high order shimming.

As illustrated in the above figure, high order shimming performs similarly for dataset 2, as both peaks at 1.9 ppm and 3 ppm are clearly visible. On the contrary, the high B_0 shifts of dataset 2, after the linear shim, result in a larger suppression of the negative side of the Z-spectrum, for offsets close to 0 ppm. As a result, the creatine peak at 1.9 ppm appears inverted in Figure 5.21. The glutamate peak still exhibits a positive asymmetry as the suppression of the Z-spectrum, further away from 2 ppm, is higher on the positive side. Furthermore, the minimum of the Z-spectrum in Figure 5.21 is higher than for high order shimming, indicating a less efficient saturation.

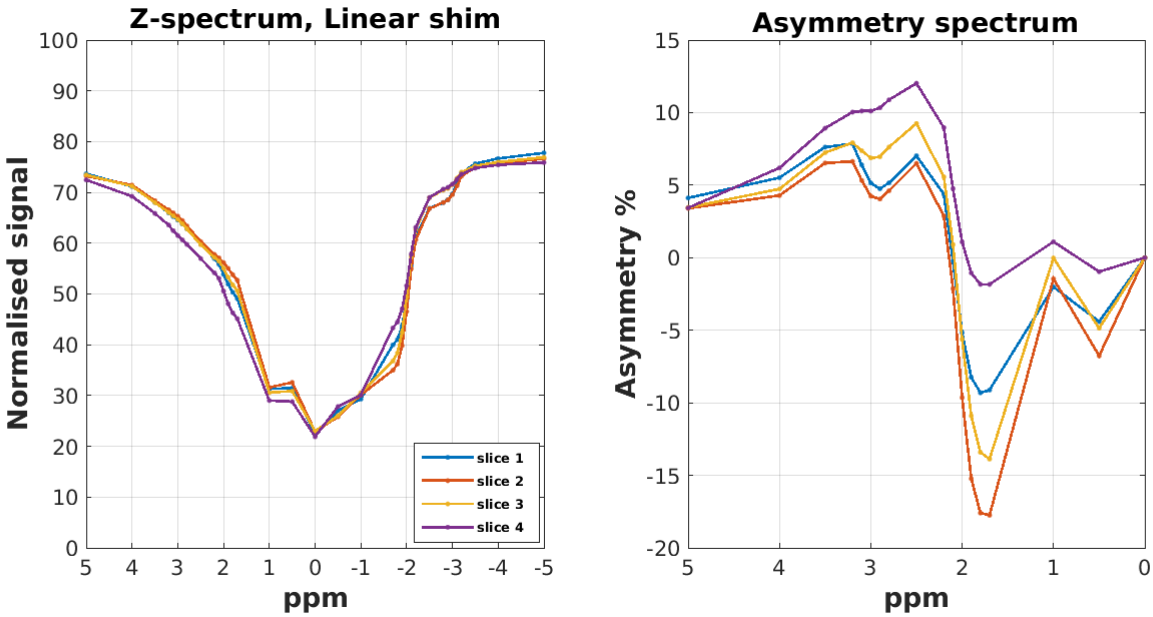


Figure 5.21: Z-spectrum and asymmetry curves, for every slice of dataset 2, after linear shimming.

Both datasets were corrected using the same method of spline fitting. Evidently, the derived Z-spectra and asymmetry curves are strongly affected by B_0 inhomogeneities. A combination of high order shimming and spline fitting B_0 correction seem to give the most reasonable results for the creatine and glutamate phantom. We note here that the slice CEST signal variation in Figures 5.18-5.21 reflects that $t_{sat} < T_1$ and the CEST effects are scaled by T_1 (t_{sat} is only 20ms in this experiment).

5.4 Discussion

The efficacy in generating CEST contrast of a single slice and a 3D gradient echo sequences was tested on a series of phantoms. Using either sequence, CEST signals were detected in Ultravist and creatine phantoms. Furthermore, CEST signals from creatine and glutamate were detected using a multislice acquisition and two different shimming approaches.

As a first step, both sequences were tried on a water phantom (Figures 5.5 and 5.6). The derived Z-spectra of the single slice acquisition are narrower than the ones acquired with the 3D sequence. This is a direct consequence of the larger bandwidth of the Gaussian pulse used in the multislice sequence (minimum 140 Hz), as compared to the bandwidth of the Fermi pulse (minimum 50 Hz) used for a single slice acquisition. In addition, distortion of the Z-spectrum occurred during the application of a 10 ms RF pulse (red line in Figure 5.6). This decrease in spectral resolution sometimes occurs during short RF pulses and is especially pronounced when the step size of the frequency sweep is smaller than the bandwidth of the RF pulse [170]. Even though 33 offsets were used, in order to sample the Z-spectrum in detail, and despite using the same shimming and B_0 correction method, the Z-spectra derived from the 3D acquisitions are not as smooth as the ones using the single slice sequence.

The Ultravist phantom was prepared in a 50ml test-tube. Despite the small size of the phantom, the signal was detectable by the 32 channel head coil. On a separate scanning, using a larger phantom, the Z-spectra appeared sharper, so the size of the phantom is something to be considered. In both the single slice and 3D acquisitions, the prominent detected peak was the one corresponding to the amide group resonating at 4.2 ppm. As the phantom was prepared at pH = 7, this is the only peak expected to be detected, similarly to our previous results at 7T. A very small dip in the asymmetry spectra at ~ 5.6 ppm can be seen in Figure 5.10 acquired using the multi-slice sequence. This frequency corresponds to the second Ultravist peak and is more pronounced for

lower pH values, as was shown by our previous results at 7T. The asymmetry of the 4.2 ppm peak at 3T, was ~15% for the single slice sequence and ~35% for the multi-slice. Both values are higher than the respective value measured at 7T. This is because at 3T the concentration of the of the agent is double the concentration used during the 7T experiments. Furthermore, it was found that the Gaussian pre-saturation pulse generates larger asymmetry than the Fermi RF pulse (Figure 5.11). It is not clear why this is the case. It is possible that there is mismatch between the selected RF pulse properties chosen, in order for the pulses to have the same peak B_1 magnitude. Simulations, at 3T, for both Gauss and Fermi pulse shapes indicate a similar Z-spectrum derivation [43]. In addition, both pulse shapes have successfully been implemented in CEST imaging [197, 31]. Loss of spectral resolution was observed in the single slice acquisition, when a short RF pulse was used, suggesting a repeated excitation of neighbouring offsets (red line in Figure 5.7). This was not observed in the 3D data for Ultravist. Adding more RF pre-pulses in the 2D sequence resulted in a decrease of the calculated asymmetry. As shown in [170], a longer time T = (pulse width + inter-pulse delay) is favourable for CEST contrast, with the optimal durations being 100 ms each. Due to sequence design limitations, in our experiments, these times are 20 ms and 10 ms respectively. Therefore, despite having a 75% duty cycle [274] no advantage was found when adding more pre-saturation pulses (Figure 5.9).

All datasets were normalised by a non-saturated reference scan, acquired before the Z-spectrum frequency sweep. Our data show that there is a distinct difference between the normalised Z-spectra, acquired with the single and multislice sequences, presented in Figure 5.14, for the creatine phantom. This difference is not pronounced for the Ultravist phantom, and is not clear why this is the case for creatine. In any case, this difference of ~ 20% might be the reason for a reduced asymmetry magnitude in the 2D case (Figure 5.14). In spite of having a smaller magnitude (~3% for the single slice) the creatine peak at 1.9 ppm is detected with both sequences. Again, a distortion of the Z-spectrum was seen for short RF pulses with a duration of 10 ms (Figures 5.12

and 5.13).

All the previous phantoms have been scanned after performing the default linear shimming. For comparison a creatine plus glutamate phantom was scanned using both high order and linear shimming under two different B_1 powers and durations (Figures 5.16 and 5.17). Internal B0 shift maps, in ppm, were calculated by finding the frequency of the minimum signal intensity on each pixel. Its deviation from 0 ppm was the assigned B0 shift. The analysis showed that high order shimming results in shifts within $\pm$0.5 ppm, whereas the shifts, after linear shimming, extended beyond that range. The two shimming methods produce similar Z-spectra and asymmetry curves for fairly homogeneous internal B0 fields (dataset 4), where both the creatine and glutamate peaks at 1.9 ppm and 3 ppm, respectively, are clearly seen (Figures 5.18 and 5.19). On the other hand, the homogeneity of dataset 2, acquired with B_1= 1.5μT and 20 ms duration, differs significantly between high order and linear shim (Figures 5.16 and 5.17). Inspection of Figure 5.20 shows that the increased homogeneity of the high order shimming results, in both, creatine and glutamate peaks to be detected. The result for the same dataset, after linear shimming, is slightly different however (Figure 5.21). Greater suppression of the Z-spectrum at the negative offsets, close to 0 ppm, results in the asymmetry calculated for the creatine to be negative. The peak is detected, but appears inverted. The asymmetry for glutamate at 3 ppm remains positive, suggesting a larger suppression of the positive offsets further away from 0. This discrepancy demonstrates that higher order shimming is more beneficial for CEST acquisitions. Furthermore, linear shimming might not be adequate for CEST imaging in-vivo, where the shape of the patient's head will influence the B_0 homogeneity at a larger extend than a phantom does.

In terms of energy deposition, the SAR values for both sequences were a lot lower than the recommended maximum of 3 W/Kg (did not exceed 0.5 W/Kg). Therefore, in theory both sequences can be tested in-vivo. However, the single slice sequence is much slower than the 3D sequence and provides less coverage. Nevertheless, the

acquisition scheme could be modified to contain less offsets, reducing scan time [84]. The latter in combination with repeated scans, at the offsets of interest, will benefit signal to noise ratio at 3T [266].

A limitation of our sequences is the maximum allowed RF pulse duration. For the 3D sequence this is only 20 ms and for the 2D one 80 ms. These values are a lot lower than the duration of the RF pules reported in the literature and is at the order of seconds [247, 206]. For in-vivo applications a pulse-train of short pulses is used in order to maintain a low SAR, but the total saturation adds up to more time than in our experiments. Understandably, a longer saturation time will benefit the CEST labelling efficiency. The low measured SAR in our experiments, allows for an increase in the saturation time and perhaps the B_1 power, but unfortunately the implementation of the latter is complicated by pulse sequence design restrictions.

5.5 Conclusion

CEST signals have been measured in-vitro, in a series of phantoms, using single and multi-slice gradient echo sequences. At physiological pH, the exchange peaks of Ultravist at 4.2 ppm, creatine at 1.9 ppm and glutamate at 3 ppm, have been detected. The Gaussian pre-saturation pulse of the 3D sequence seems to provide a more efficient saturation as compared to the Fermi pulse, used in the single slice acquisitions. High order shimming allows for a better B_0 correction in contrast to the default linear shimming.

Chapter 6

Glioma characterisation with CEST MRI at 7T

The following paragraphs describe the study of human brain gliomas using CEST MRI at high field. This was a joint project between the department of Radiological and Imaging Sciences (Queen's Medical Centre) and the Sir Peter Mansfield Magnetic Resonance Centre (University of Nottingham). The study was approved and sponsored by the University of Nottingham. Favourable ethical approval was also granted by the East Midlands - Nottingham 2 Research Ethics Committee (Study Reference: 09/H0408/7).

6.1 Introduction

MRI is an important medical imaging tool for localising, diagnosing, characterising and assessing the treatment of brain tumours [47, 157]. It is a non-invasive technique capable of utilising a wide range of image contrasts. On the one hand, conventional MRI contrasts are based on different spin relaxation properties of body tissues, under a static magnetic field and varying radiofrequency (RF) irradiation. Examples of such image contrasts include T_{1w}, T_{2w}, proton density (PD) and T^*_2 [150]. On the other hand, advanced MRI contrasts exploit structural tissue properties (diffusion-weighted MRI) [143], functional properties (perfusion MRI [3], resting state fMRI [113], BOLD [126]) and chemical structure (MR spectroscopy [56, 176]).

Recently, a new technique termed, amide proton transfer (APT) Chemical Exchange Saturation Transfer (CEST) was added to the magnetic resonance imaging arsenal [264, 265]. This method enables the non-invasive imaging of endogenous compounds, that are otherwise undetectable via standard MRI and spectroscopy, due to their milli-molar concentrations. In other words, CEST, is an amplification method, capable of detecting milli-molar endogenous protein concentrations, via the dominant water signal. This is possible after the physico-chemical, saturated proton exchange from such proteins, to water and the subsequent reduction of the measured water signal. Studies of brain tumour CEST have demonstrated the feasibility of APT-CEST imaging in differentiating tumour core from oedematous [88] and necrotic regions [267, 259, 269, 223, 270], but not from cystic components. The reported APT signals in tumours, were significantly higher from those in oedema/necrosis. Such an increase was attributed to increased protein synthesis in tumours [73, 268]. More recently, proteomic analysis of tumour markers, has confirmed the latter hypothesis [239]. APT signal was further found to be correlated with tumour grade [206, 17] capable of assessing treatment response [162] and differentiating between tumour recurrence and pseudo-progression [132, 155]. Due to complex endogenous tissue com-

partmentalisation, proton chemical exchange is almost always accompanied by additional magnetisation transfer effects. These effects arise from rather immobile semi-solid proteins (conventional magnetisation transfer, MT) [29, 160, 168] and aliphatic [153, 235, 90, 30, 245, 89, 154] or aromatic [249, 248] proton groups (Nuclear Overhauser Effects, NOE). Even though the latter perplexes the interpretation of the APT signal, it can be exploited as an additional MRI contrast in characterising brain tumours.

In this study, brain glioma patients were recruited and subsequently scanned at high field (7T). Mean APT and NOE signals, of solid tumour regions and normal white matter, were determined, via Lorentzian fitting of the Z-spectra. The correlation of the measured signals with apparent diffusion coefficient (ADC) of tumour and control regions was also investigated.

6.2 Materials and Methods

6.2.1 Recruitment process

The recruitment process for the study was a challenging task. This was because: 1) the study group was one of an aggravated pathology, 2) there was a short time window for a research scan, between the patient's admittance and the subsequent clinical procedures (biopsy, surgery, treatment), 3) the access and up-to-date information regarding new admitted cases was limited.

The ethics documentation was prepared by myself. That included the study protocol under the title, "Imaging anatomical and physiological characteristics of Brain Tumours using Ultra High-Field Magnetic Resonance Imaging", the patient consent form and information leaflet. The latter served as a concise explanation of what the participation entails and was given to each potential participant.

For the first two months of the project I was not responsible for acquiring consent. I was however responsible for meeting the participants in the glioma ward and transferring them to and from the research centre, back to the hospital. After this initial period I started seeking consent, myself. That meant attending the radiological multidisciplinary meetings, on a weekly basis, in an attempt to find potential participants which would then be approached by phone and/or post. On a few occasions I attended the glioma clinic, where patients would come and discuss their scans with their treating physician. If a patient was identified by my supervisor (Prof. Auer), I would then proceed and meet them during their stay in the ward. When successful, I would arrange their transport and accompany them throughout the duration of the research scan. The scanning sequence used was already in place, before the start of my project and the scanner operation was performed by a collaborator (Dr. Mougin).

6.2.2 Patient demographics

Our study has been approved by the University of Nottingham and the local research ethics committee. A total of seven glioma patients (4 male, 3 female; median age 59 [range 42-70 years]; 4 glioblastomas (GBM) and 3 low grades (LGG)) were recruited from the neuro-oncology clinic at Queen's Medical Centre (Nottingham University Hospitals NHS Trust). Written informed consent was acquired from each participant. Clinical diagnosis and histological evaluation was performed before our examination. All patients had also undergone MRI scans, as part of their clinical care, at 3T. The time between the clinical scans, at 3T and research scans, at 7T, were within 2 weeks at most. None of the participants had received any prior treatment, at the time of the research scan. The inclusion and exclusion criteria, in identifying our research participants, are summarised below (Table 6.1).

Inclusion	Exclusion
Over 16 years of age	Patients who have had previous surgery
Patients with primary or secondary brain lesions	Patients with any contradictions to MRI
Pre-treatment low & high grade gliomas	Patients with large tattoos especially in the head neck and shoulder region
Post-treatment low & high grade gliomas	Patients that do not have the capacity to consent

Table 6.1: Inclusion and exclusion criteria for recruiting brain glioma patients

A detailed description of the pathology for every patient is presented in the following table (Table 6.2).

Table 6.2: Pathology of the patients scanned at 7T.

#	**Age (years)**	**Lesion**	**Location**
1	58	Low grade glioma	Left insula

Table 6.2: Pathology of the patients scanned at 7T.

#	**Age (years)**	**Lesion**	**Location**
2	51	Low grade glioma	Occipital region
3	40	Glioblastoma (WHO grade IV)	Left temporal
4	67	Glioblastoma (WHO grade IV)	Left frontal
5	70	Glioblastoma (WHO grade IV)	Right parietal
6	59	Glioblastoma (WHO grade IV)	Right temporal
7	45	Low grade glioma	Left frontal

Figure 6.1 shows the 3T clinical scans, that were used for region of interest definitions.

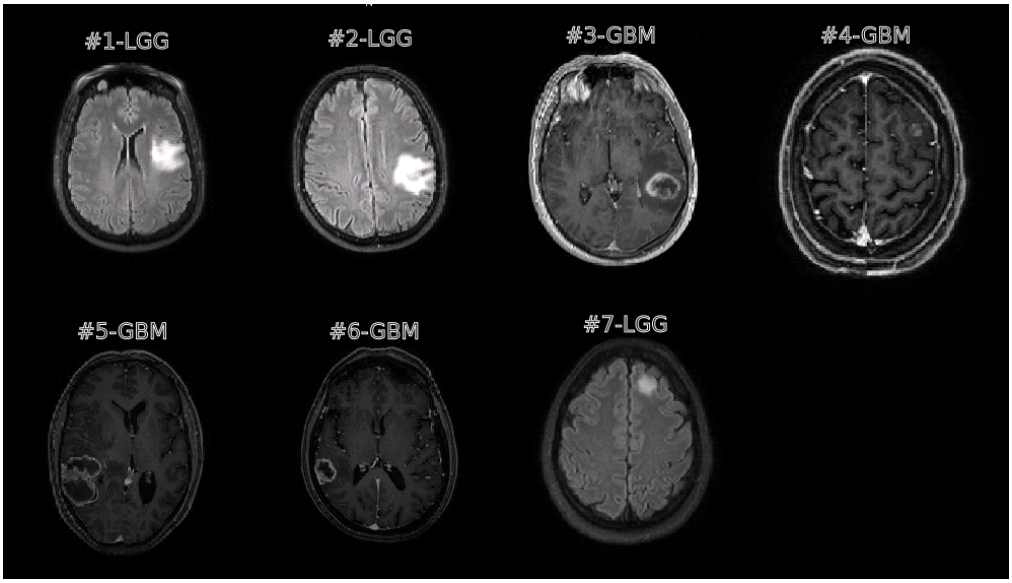


Figure 6.1: Clinical patient scans at 3T. **Top row:** (left to right): T_2-FLAIR image of LGG, T_2- FLAIR image of LGG, Gd-T_1 image of GBM, Gd-T_1 image of an early GBM. **Bottom row:** (left to right): Gd-T_1 image of GBM, Gd-T_1 image of GBM, T_2-FLAIR image of LGG.

6.2.2.1 Histological notes

The histology reports were kindly provided by the Queen's Medical Centre's (Nottingham University Hospitals NHS Trust) neurosurgery team.

Patient 1: Low grade glioma. Surveillance only. No biopsy samples taken.

Patient 2: Low grade glioma. Surveillance only. No biopsy samples taken.

Patient 3: Glioblastoma. Pieces of cerebral tissue including areas of glial tumour. This is characterised by large pleomorphic astroglial cells with glassy cytoplasm. Mitosis, microvascular proliferation and necrosis are all seen. Small cell areas are seen around necrotic foci. No neuronal markers are expressed . IDH1 staining is negative.

Patient 4: Glioblastoma. Paraffin section confirmed the smear report of a diffuse astrocytic neoplasm. Although some areas are bland, much of the tumour shows mitotic activity, vascular proliferation and necrosis.

Patient 5: Glioblastoma. Paraffin section confirmed the smear report of a malignant glioma. This cellular astroglial neoplasm shows mitotic activity, vascular prolif-

eration and necrosis. Wild type IDH1 mutation is also confirmed.

Patient 6: Glioblastoma. Paraffin section confirms the smear report of a malignant glioma. The tumour shows mitotic activity, vascular proliferation and necrosis, but it is also characterised eosinophil granular bodies and giant cells. The possibilities of anaplastic variants of pleomorphic xanthoastrocytoma or ganglioglioma have been considered, but the appearances are judged to be those of a glioblastoma.

Patient 7: Low grade glioma showing oligodendroglial differentiation. There is no mitotic activity, microvascular proliferation or necrosis. The tumour shows patchy expression of GFAP. The MIB1 labelling index is low. There is expression of the common mutation in IDH1.

6.2.3 7T scanning protocol

Research scans were performed on a 7T Philips Achieva system equipped with a 32 channel receiver coil. The sequences and scanning parameters implemented were as follows: 1) 3D-Turbo field echo MT/CEST sequence (Figure 6.2) consisting of a pre-saturation train of 30 Gaussian pulses (total duration = 1.8 sec) and power of B_1= 2μT, TE/TR = 2.8/6 ms, FOV=192x186x50 mm and 1.5 mm isotropic image resolution. For the calculation of the Z-spectra 24 offset frequencies (including a reference image) were acquired in a total scan duration of 8 min (coverage of 30 slices). 2) T^*_2 weighted MPRAGE sequence, TE/TR = 8/15 ms, FOV = 192x180x156 mm, TFE factor = 8 and a total of 156 slices, 3) Diffusion weighted sequence at b = 0 and 1000 s/mm^2, FOV=230x119x230 mm, EPI factor =63 for a total of 24 slices.

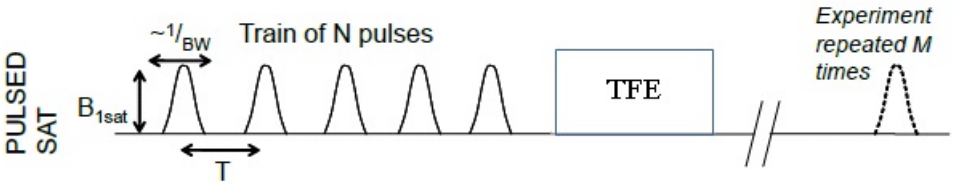


Figure 6.2: Schematic diagram of the CEST sequence (pulsed per-saturation module + TFE readout) [145].

6.2.4 Data analysis

6.2.4.1 3T clinical data and ADC maps

All patients, as part of their clinical management, had undergone routine radiological diagnostic multimodal MRI using a 3T Philips Achieva scanner. The clinical protocol at 3T included: T_2 - FLAIR (TE = 140 ms, TI = 2750 ms, TR = 10000 ms, voxel 0.9x0.9x3 mm), T_{1w} MPRAGE pre and post Gd contrast (TE = 3.684 ms, TI = 960 ms, TR = 8.0486 ms, voxel 1x1x1 mm), T_{2w} (TR = 3000 ms, TE = 80 ms, voxel 0.4x0.4x5 mm), DTI (16 directions, b = 1000 s/mm^2, TE = 56.8 ms, TR = 8000 ms, voxel 2x2x3 mm) and perfusion (TE = 23.796 ms, TR = 15.7 ms, voxel 1.8x1.8x3.5 mm). Subsequently, the 4D diffusion data, were further processed in order to produce mean diffusivity (ADC [mm^2/s]) maps using the FSL diffusion toolbox [6]. An example, of a low and high grade ADC map is presented in Figure 6.3.

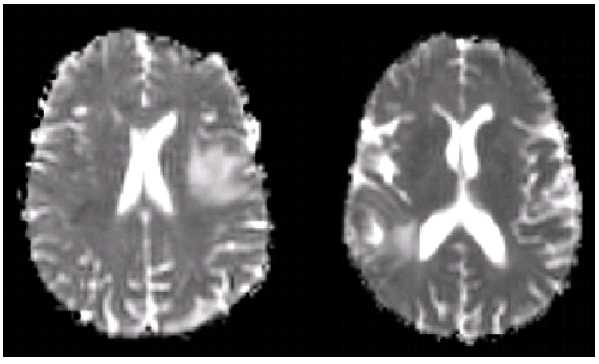


Figure 6.3: ADC maps of a low grade left insular glioma (left) and a right temporal GBM (right).

The diffusion data processing pipeline consisted of: 1) correcting for eddy current distortions induced by the gradients 2) registering all volumes to a reference volume (typically the first volume of the stack where the diffusion gradient is zero) 3) creating a brain mask 4) fitting the diffusion tensors on the corrected data voxelwise, to produce the parametric ADC maps. Diffusion data processing was performed using the FDT algorithm provided in FSL [6].

6.2.4.2 Registrations

In order to analyse data acquired at two different field strengths (3T clinical and 7T research scans) and also reduce motion artefacts, the analysed images were brought to the same space. Since the analysed regions of interest (ROIs) were initially identified on the clinical 3T images, all the 3T and 7T images were registered on the 3T Gd-T_1 data. First, as described in figure 6.4, all the 3T images and the 7T MPRAGE images, were registered on the 3T Gd-T_1images. Second, all the subsequent 7T data were registered on the 7T MPRAGE, in order to bring them to the common registration space of the 3T Gd-T_1.

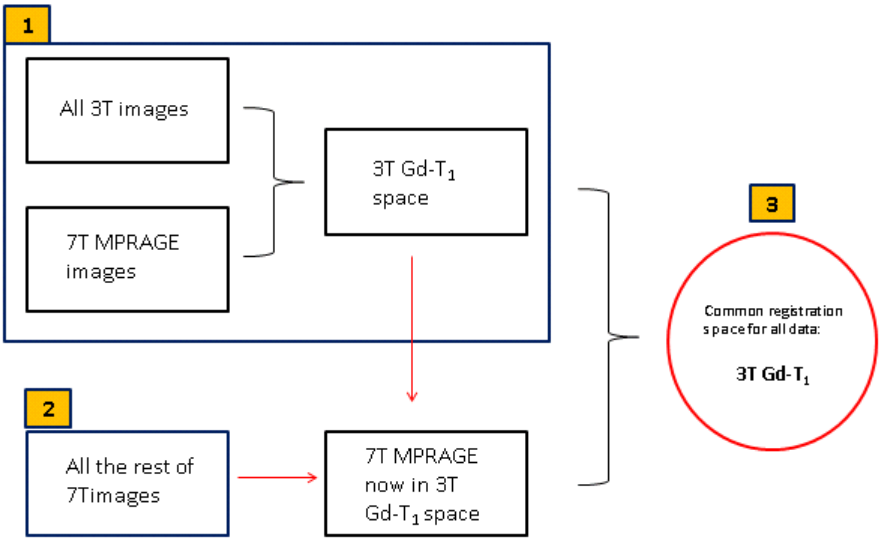


Figure 6.4: Registering 3T - 7T images flowchart.

With the exception of registering the clinical diffusion data on the 3T Gd-T_1 all

other registrations were performed using the linear image registration tool (FLIRT)[77], provided with FSL. The quality of the linear registration algorithm was visually assessed, by examining the location of the lesion between the registered images. Due to distortions on the diffusion data, the linear registration resulted in unacceptable misalignment of the registered modalities. Therefore, a separate non-linear registration (having more than 12 degrees of freedom) was performed using the locally developed image analysis software NeuRoi [201].

Figure 6.5 shows an example of cross-field registration in the case of a GBM (patient #6). The 3T data were acquired using gadolinium, whereas for the research scans no contrast was used. In Figure 6.5, a sequential overlay of the 7T linages onto the 3T images demonstrates the spatial location of the lesion with respect to each modality. The quality of registration was assessed visually and was based on the location of the active tumour margins and brain edges. The guide for the latter was the enhancement observed in the 3T dataset.

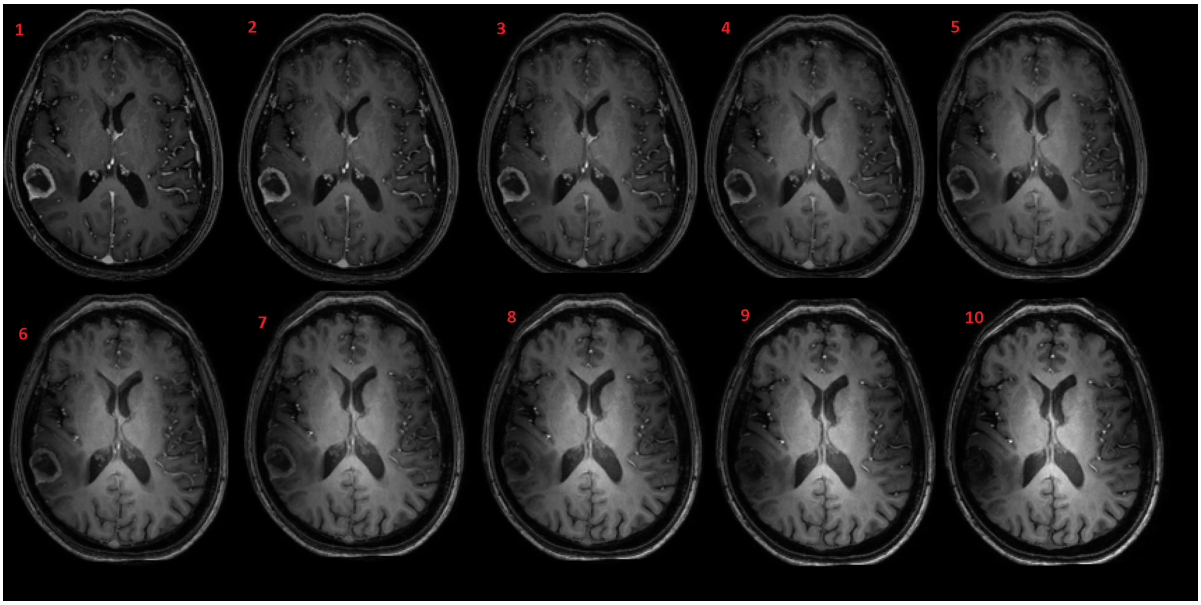


Figure 6.5: Example of assessing the registrations: In this case: 7T MPRAGE to Gd-T_1 3T. Image #1 is the base Gd-$T_1$and the subsequent images sequentially reveal the registered MPRAGE on the base image.

6.2.4.3 ROI definitions

All ROIs were drawn on the clinical 3T images, using NeuRoi [201]. Since none of the low grade gliomas showed any Gd enhancement, the active part of the tumour was defined as hyper-intense regions on the T_2 FLAIR images. For the GBMs, the tumour ROIs were drawn on the Gd-T_1enhancing regions. Any haemorrhagic components were identified on high resolution 7T SWI and were subsequently subtracted from the Gd enhancing ROIs, in order to remove haemorrhagic susceptibility contamination, on the active tumour signal. For all cases, contralateral control regions of healthy white matter, were also acquired.

Figure 6.6 shows an example of two 7T SWI images for a GBM (patient #5) and the ROIs drawn indicate haemorrhage. Even though other conditions, such as multiple sclerosis and stroke, do benefit from a sensitive detection of the amount of iron in the brain (e.g deoxyhemoglobin, hemosiderin and ferritin), the presence of deoxygenated blood in tumours is detrimental for the frequency specific detection of amides in CEST MRI. This is because blood products introduce undesirable susceptibility artefacts and thus magnetic field inhomogeneities due to a reduction in T_2^* and phase differences between the blood products and the tissue of interest. Considering that the concentration of endogenous amides is in the milli-mollar region, signal losses due to susceptibility changes across voxels, reduce the detection sensitivity of CEST. As such, the haemorrhagic components identified on the SWI images were subtracted from the subsequent CEST analysis.

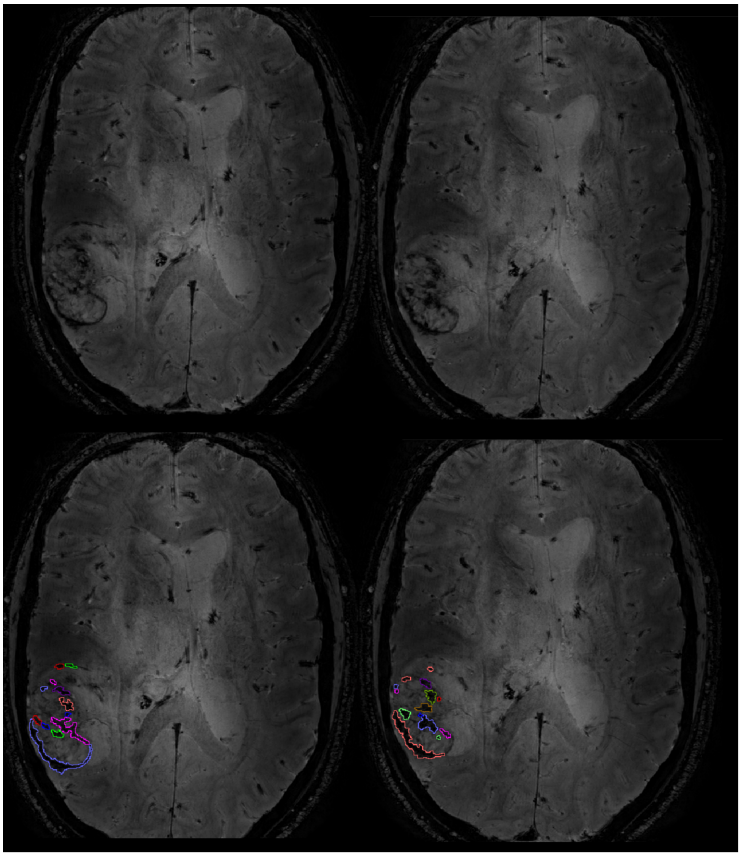


Figure 6.6: Haemorrhagic tumour components on 7T SWI images. **Top row:** Original images. **Bottom row:** ROIs of haemorrhagic components.

6.2.5 Quantitative APT and NOE maps

In order to produce quantitative APT and NOE maps, the data were fitted voxelwise, using a Lorentzian line-shape, representing each endogenous proton pool (bulk water, amide and aliphatic protons). The Lorentzian line-shape is described by the following equation [244]:

$$L(A, \Gamma, \Delta\omega) = \frac{A\Gamma^2/4}{\Gamma^2/4 + \Delta\omega} \tag{6.2.1}$$

where:

A: the amplitude

Γ: the line-width

$\Delta\omega$: the centre frequency of each proton pool.

The area under each Lorentzian curve was calculated using numerical trapezoidal integration. Before the fit, all Z-spectra were interpolated voxelwise in order to correct for B_0 inhomogeneities. After finding the minimum of each interpolated Z-spectrum, the spectra were shifted so as the minimum intensity to correspond to zero offset (water centre frequency). This correction was done by using the Z-spectrum itself (internal correction). The fitting algorithm for localising the minimum of the spectrum was a smoothing spline (part of Matlab library functions). A brain mask was manually drawn on each slice at the start of this analysis.

The B_0 corrected data were then normalised using the unsaturated CEST image. Subsequently, the data was fitted using the Levenguard-Marquard algorithm. Each proton pool was fitted with equation 6.2.1. The amplitude, width, centre frequency and fitting bounds for each pool were chosen as indicated in Appendix D. The number of fit iterations for our acquisition ($B_1 = 2\mu T$) was 40.

6.3 Results

6.3.1 APT and NOE maps in tumours and controls

6.3.1.1 Quality of fitting

The following two figures are indicative of the quality of information obtained by showing the Z-spectra in grey matter (GM), white matter (WM), tumour and control, for 2 patients. The data show Lorentzian fitted Z-spectra and the respective magnitude of the APT and NOE peaks (dotted lines at the bottom of the spectra). The effects were calculated as means of the ROIs shown on the images. The fitting seems to perform well and shows a more pronounced APT and NOE effects in WM. Furthermore, the tumour has an increased APT/decreased NOE when compared to the control. In both cases, the ADC map is also shown. Only greyscale images are presented here for visual clarity of the ROIs. The APT and NOE colour-maps, for all patients, are shown in the next section.

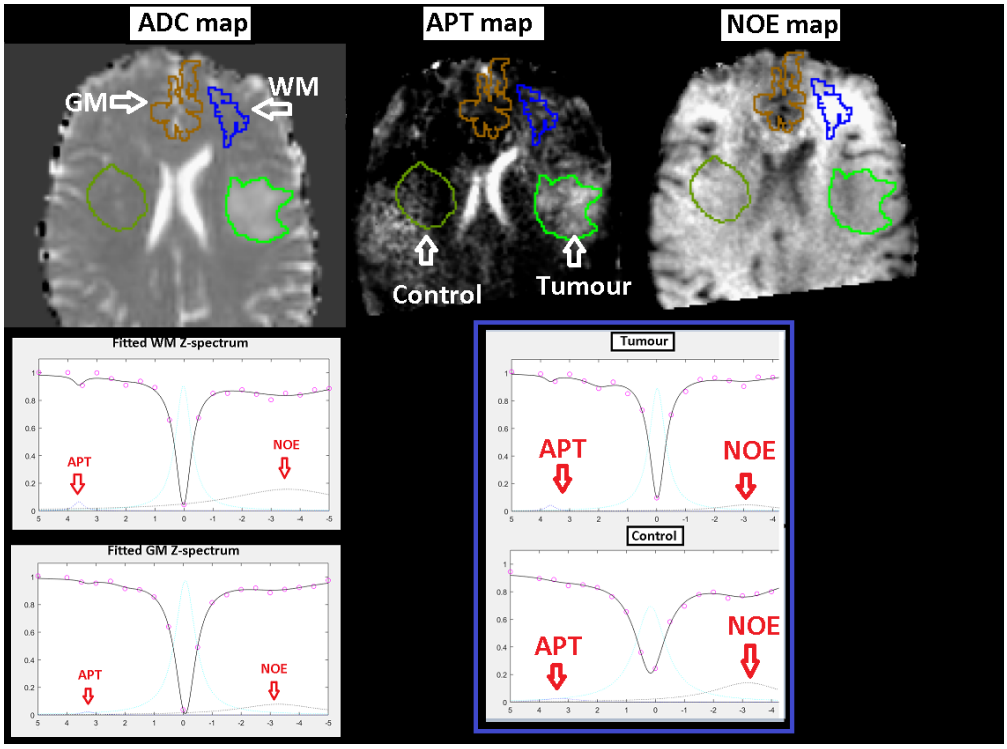


Figure 6.7: Z-spectra in white, grey matter, tumour and control for the ROIs shown on the images.

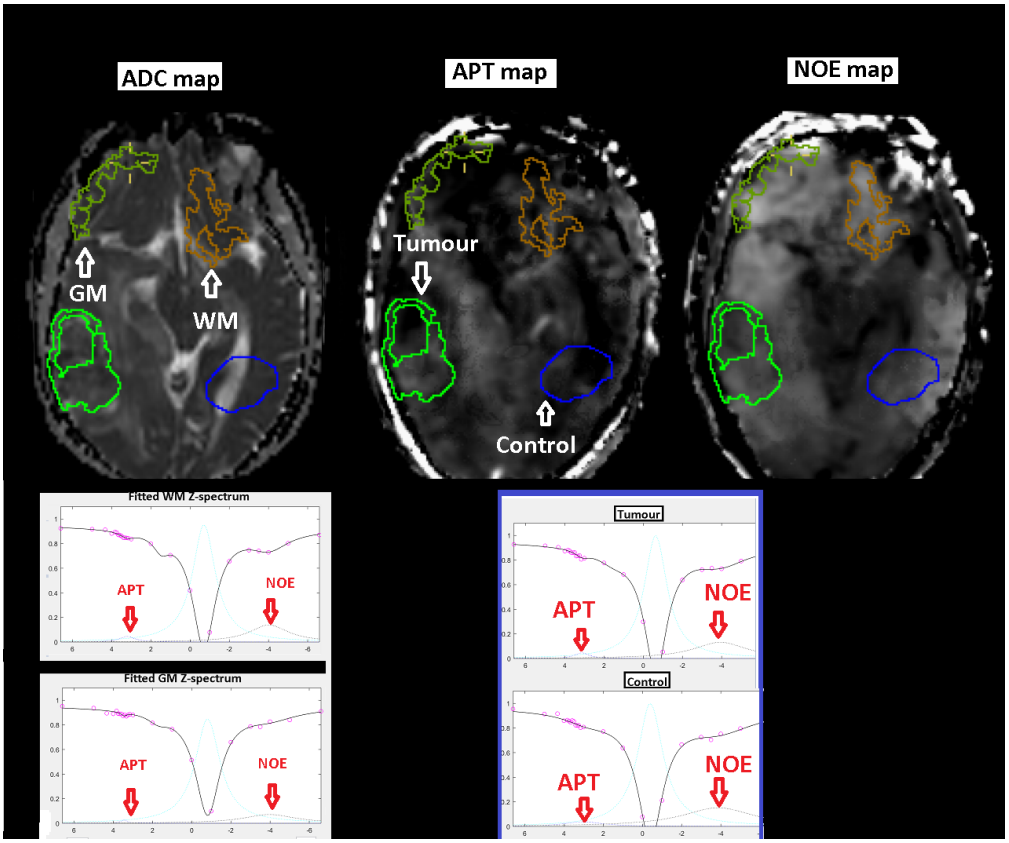


Figure 6.8: Z-spectra in white and grey matter for the ROIs shown on the images.

6.3.1.2 APT and NOE colour-maps for all patients

This section contains the APT and NOE colour-maps for all patients (n=7, Figure 6.9, Figure 6.10, Figure 6.11, Figure 6.12). The results are presented in the same order as indicated in Figure 6.1. The colour-maps demonstrate the magnitude of the respective APT and NOE effects in tumour and control ROIs that are indicated on the corresponding greyscale maps. The statistical analysis (next section) was done in all ROIs of our multi-slice acquisition. For demonstration purposes however, this section contains only single slice maps.

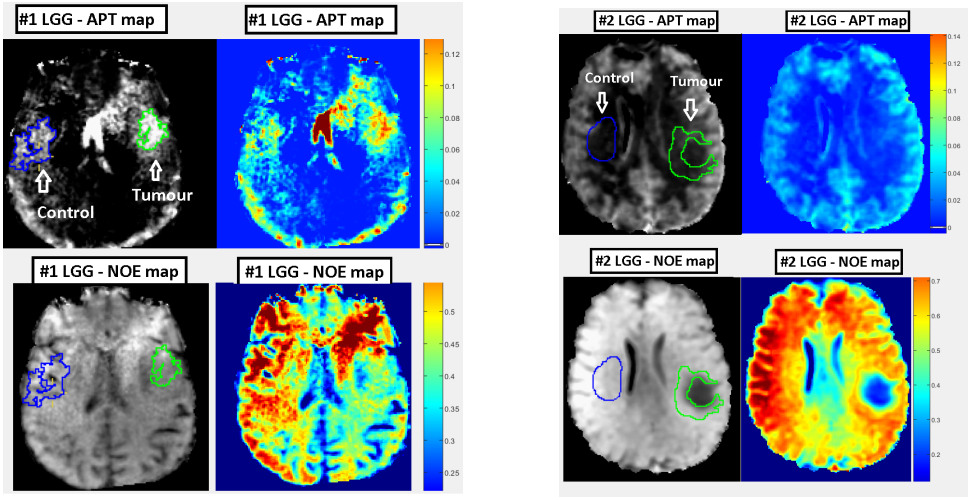


Figure 6.9: APT and NOE maps for #1 (LGG) and #2 (LGG).

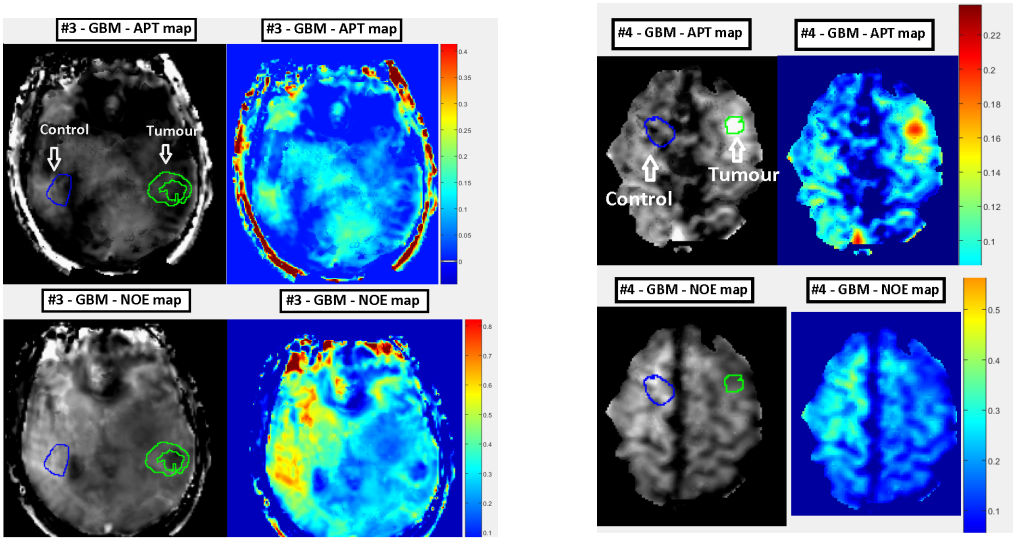


Figure 6.10: APT and NOE maps for #3 (LGG) and #4 (GBM).

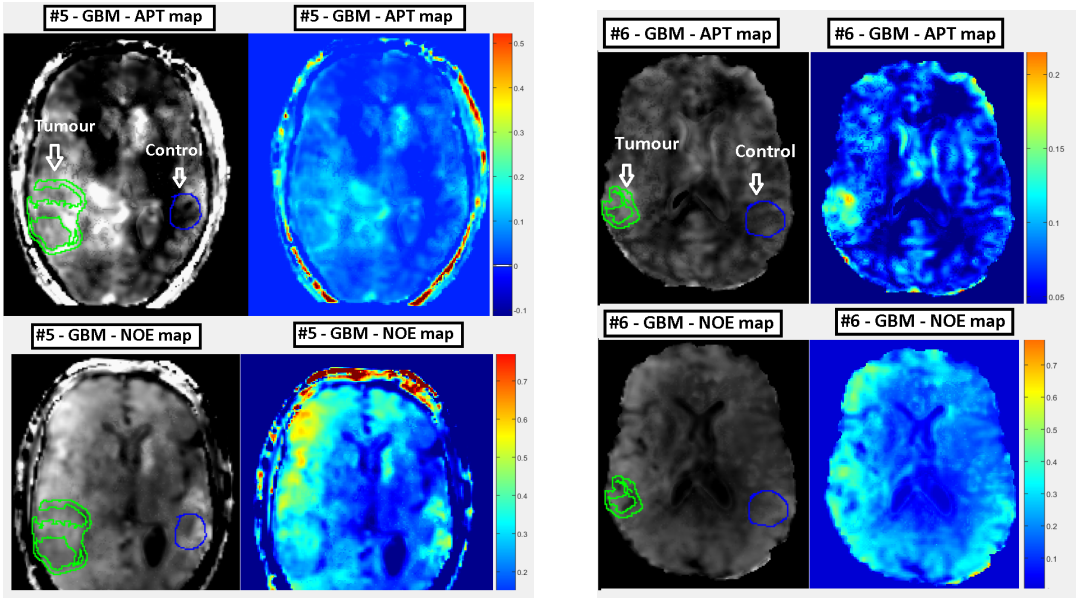


Figure 6.11: APT and NOE maps for #5 (GBM) and #6 (GBM).

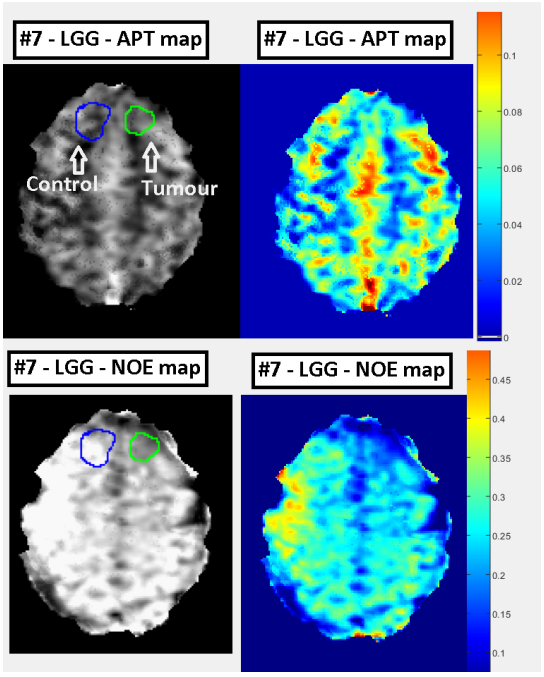


Figure 6.12: APT and NOE maps for #7 (LGG).

6.3.1.3 Statistical analysis of all ROIs

The mean control, tumour APT and tumour NOE values reported here were calculated by averaging the respective values of the ROIs of all controls, all low grades and all GBMs. For example, the mean tumour APT value, in low grade gliomas, was calculated by finding the mean of all tumour ROIs on the APT maps, of all low grades. The mean NOE value was calculated in a similar way.

Note: The mean values were multiplied by 100 and are reported as % in the statistical analysis. For example, the single slice result in Figure 6.12 was used in the calculations as ~5% APT and ~15% NOE signal.

Figure 6.13 summarises the results for tumour and control mean APT values in low grade gliomas and GBMs. The error bars indicate the standard deviation. The results for APT indicate an increased mean APT signal in both low grades and GBMs, as compared to normal appearing white matter. In addition, the APT signal increase is higher for GBMs (~8%) than low grades (~2%). Due to non-normal distribution of the data, a non-parametric test (Wilcoxon rank-sum test) was used to test the significance of the difference between tumour and control APT values. Both differences were found as significant, with $p<0.01$.

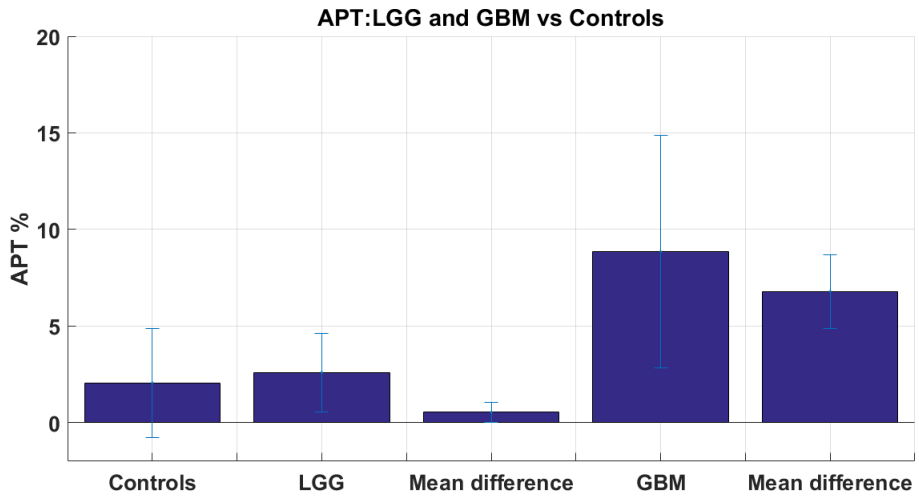


Figure 6.13: Mean APT values and standard deviation of controls, low grade gliomas (LGG) and GBMs. The mean difference and 95% confidence interval is also provided. The non-parametric Wilcoxon test indicated that both mean differences of low grade gliomas and GBMs and controls, were significantly different ($p<0.01$).

Figure 6.14 summarises the results for tumour and control mean NOE values in low grade gliomas and GBMs.

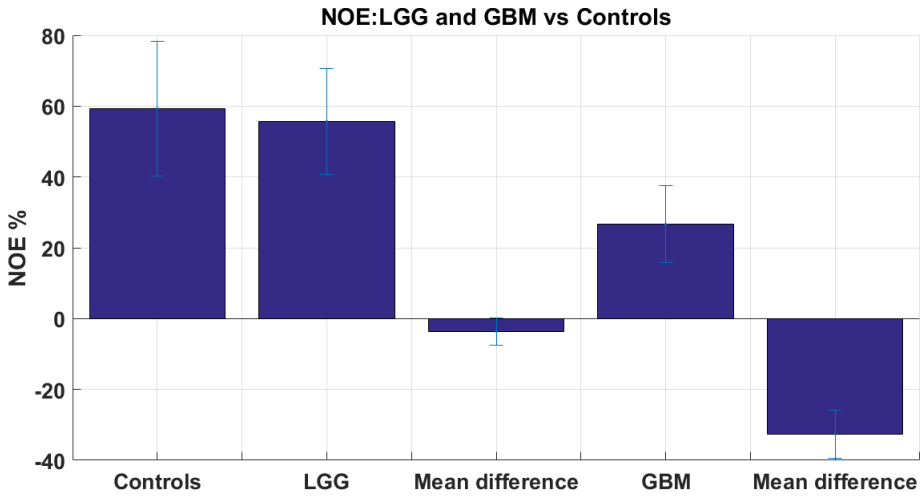


Figure 6.14: Mean NOE values and standard deviation of controls, low grade gliomas (LGG) and GBMs. The mean difference and 95% confidence interval is also provided. The non-parametric Wilcoxon test indicated that both mean differences of low grade gliomas and GBMs and controls, were significantly different ($p<0.01$).

The error bars indicate the standard deviation. The results for NOE indicate a decreased mean NOE signal in both low grades and GBMs, as compared to normal appearing white matter. Furthermore, the NOE signal decrease is higher for GBMs (~35%) than low grades (~5%). These differences were also found to be significant by the Wilcoxon rank-sum test ($p<0.01$).

6.3.2 APT and NOE signal correlation with ADC

Joint scatter-plots of the quantitative APT and NOE maps with the calculated apparent diffusion coefficient maps (ADC) were plotted to investigate the correlation between the measured APT or NOE signal with tissue cellularity. The analysis compares the acquired signal of APT or NOE with the ADC values between tumour and healthy control ROIs pixel by pixel. The scatter-plots and the statistical analysis were performed using the locally developed software ImViw and Matlab. Each result includes

the computed Pearson correlation coefficient r, the p value and also a linear regression line, showing the type of the relationship.

6.3.2.1 APT - ADC correlations in low grades

Figure 6.15 shows the joint scatter-plots of the APT signal (x axis) and ADC (y axis) in tumour (red) and control (blue) regions of interest in three low grade gliomas. The correlation coefficients and their respective p values are presented below the graphs. The results show that in the first two cases there is a negative correlation between the APT - ADC in tumours whereas in the third case the correlation is positive. On the contrary, all three cases show a positive correlation between the APT - ADC in healthy controls regions. All correlations were significant.

The negative correlations in Figure 6.15, in tumours, indicate an inverse relationship between cellularity and APT signal. Even though LGGs are less cellular than GBMs

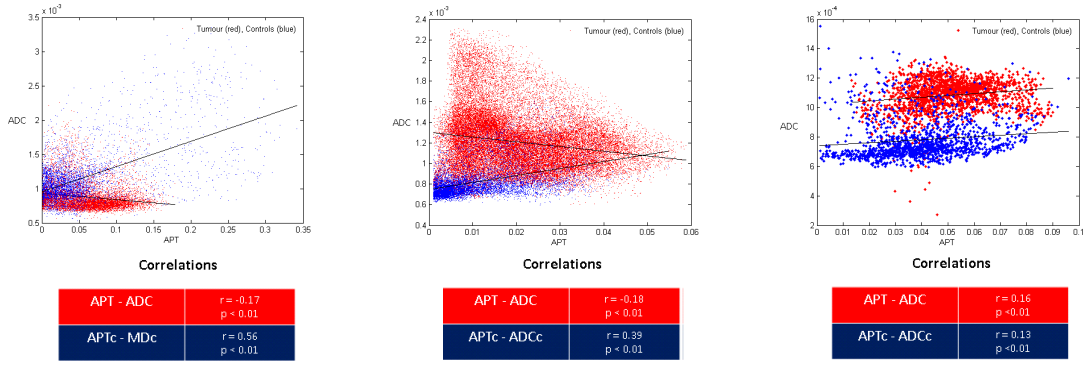


Figure 6.15: Joint scatter-plots of APT - ADC between tumour and healthy control regions in low grade gliomas. Red indicates tumour and blue indicates controls.

6.3.2.2 APT - ADC correlations in high grades

Figure 6.16 shows the joint scatter-plots of the APT signal (x axis) and ADC (y axis) in tumour (red) and control (blue) regions of interest in the four GBM cases.

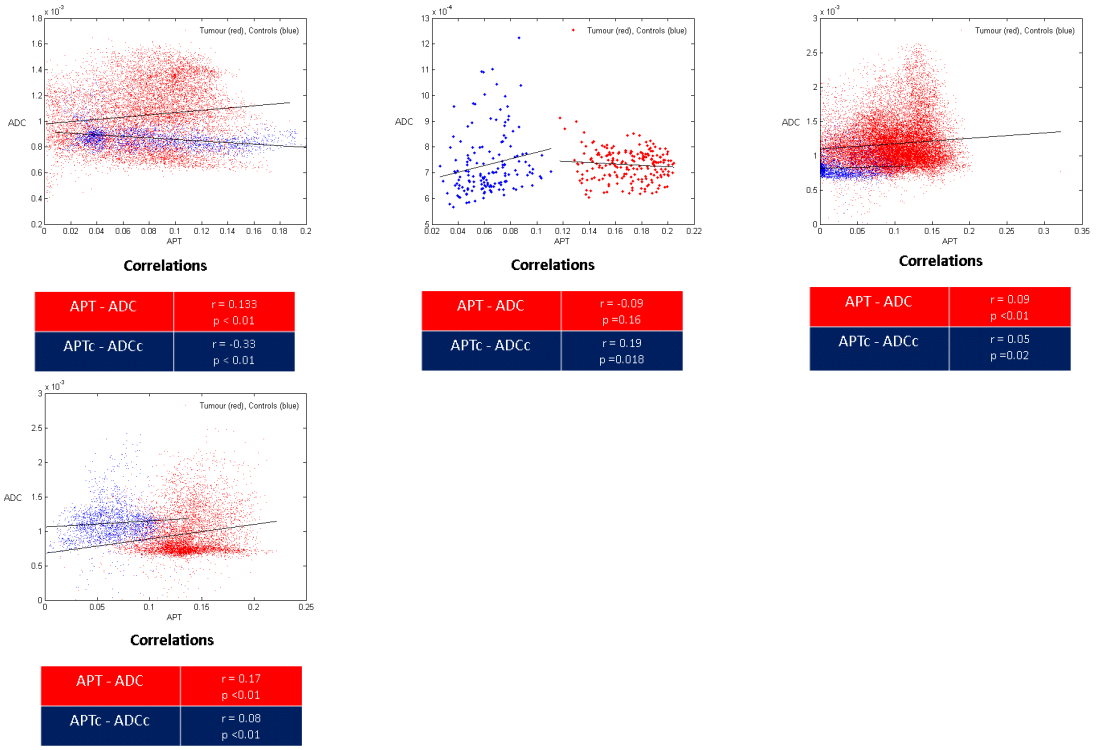


Figure 6.16: Joint scatter-plots of APT - ADC between tumour and healthy control regions in high grade gliomas. Red indicates tumour and blue indicates controls.

Cases one, three and four show a positive correlation between the APT - ADC signals, while the second case shows a negative correlation. For the APT - ADC in controls, all correlations are positive with the exception of the first case. The p values found indicate that all correlations are significant.

6.3.2.3 NOE - ADC correlations in low grades

Similarly with the previous analysis, figure 6.17 summarises the joint scatter-plots of the NOE signal (x axis) and ADC (y axis) in tumour (red) and control (blue) regions of interest in the three low grade gliomas. The correlations between the NOE effect and ADC are negative in both tumour and controls for the first two cases, while in the last case the correlation in tumours is positive and in controls negative.

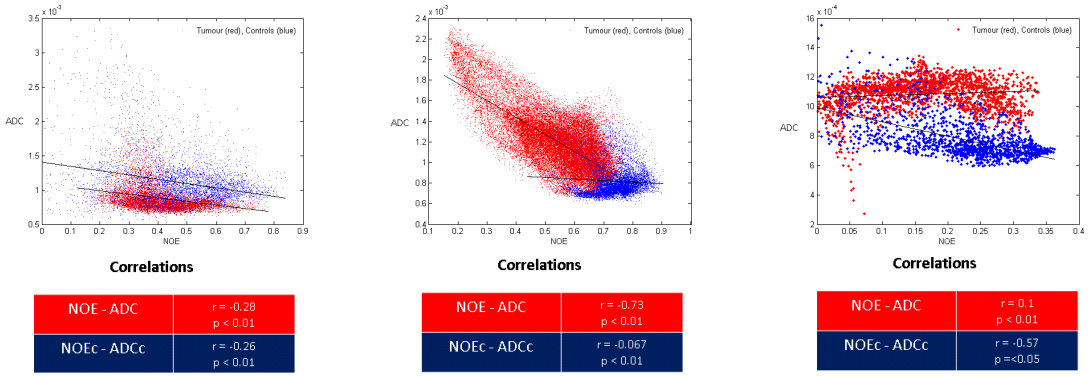


Figure 6.17: Joint scatter-plots of NOE - ADC between tumour and healthy control regions in low grade gliomas. Red indicates tumour and blue indicates controls.

6.3.2.4 NOE - ADC correlations in high grades

Finally, 6.18 presents the results of the correlation analysis between NOE - ADC for the four GBM cases. While all the NOE - ADC correlations where negative for the control ROIs, the tumour ROIs showed three positive and one negative correlation.

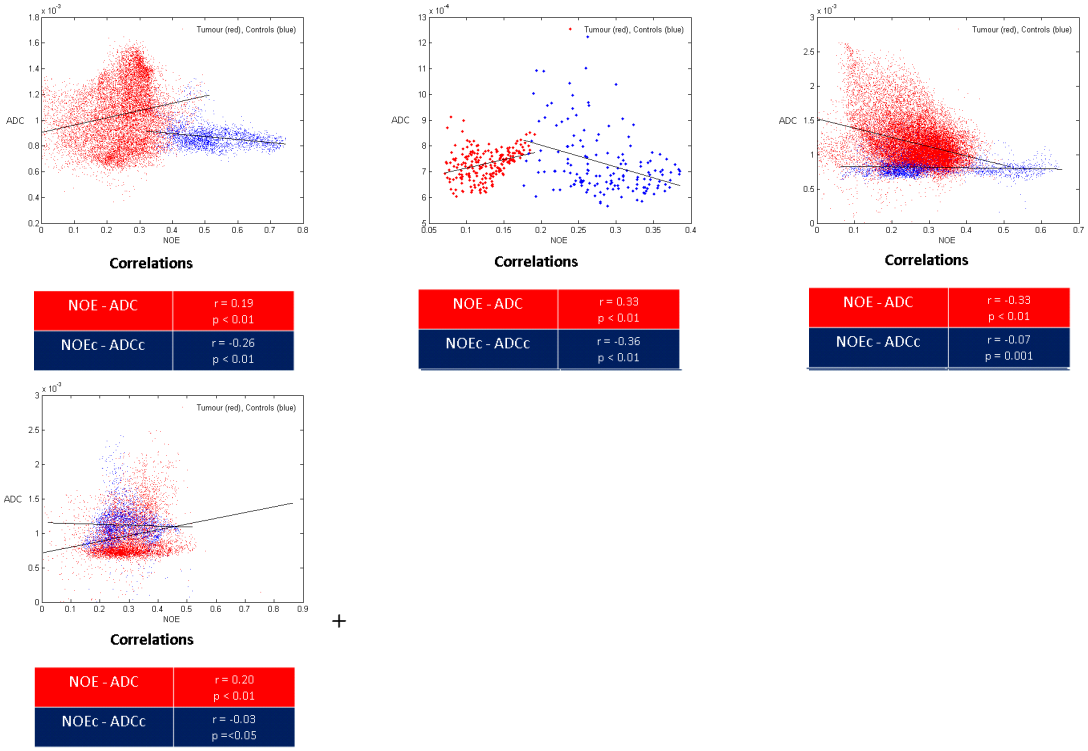


Figure 6.18: Joint scatter-plots of NOE - ADC between tumour and healthy control regions in high grade gliomas. Red indicates tumour and blue indicates controls.

Just like in the low grades, all correlations between NOE - ADC in tumours and controls of GBMs were found to be significant.

6.3.2.5 Summary of correlations

In summary, (Figure 6.19) no particular trend in the relationships between the measured APT-ADC and NOE-ADC in tumours was observed, with the exception of the NOE-ADC and APT-ADC signals in controls, which show a weak negative and positive, correlation, respectively. The large variation of correlations between CEST and diffusion metrics in tumours may be driven by spatial heterogeneity, perhaps even errors in co-registration (7T vs 3T) and individual factors (e.g. age and partial volume effects of free water). It is thus not surprising that no consistent trend was observed. Nevertheless, we would have expected to see an anti-correlation between APT and ADC, at least in HGGs, as more cellularity would lead to lower ADC and higher APT. This is borderline true only in one case shown here (Figure 6.16, middle graph), so this hypothesis cannot be confirmed without further investigation. In any case, the result reported here is limited to the enhancing subtype and not really the tissue subtype.

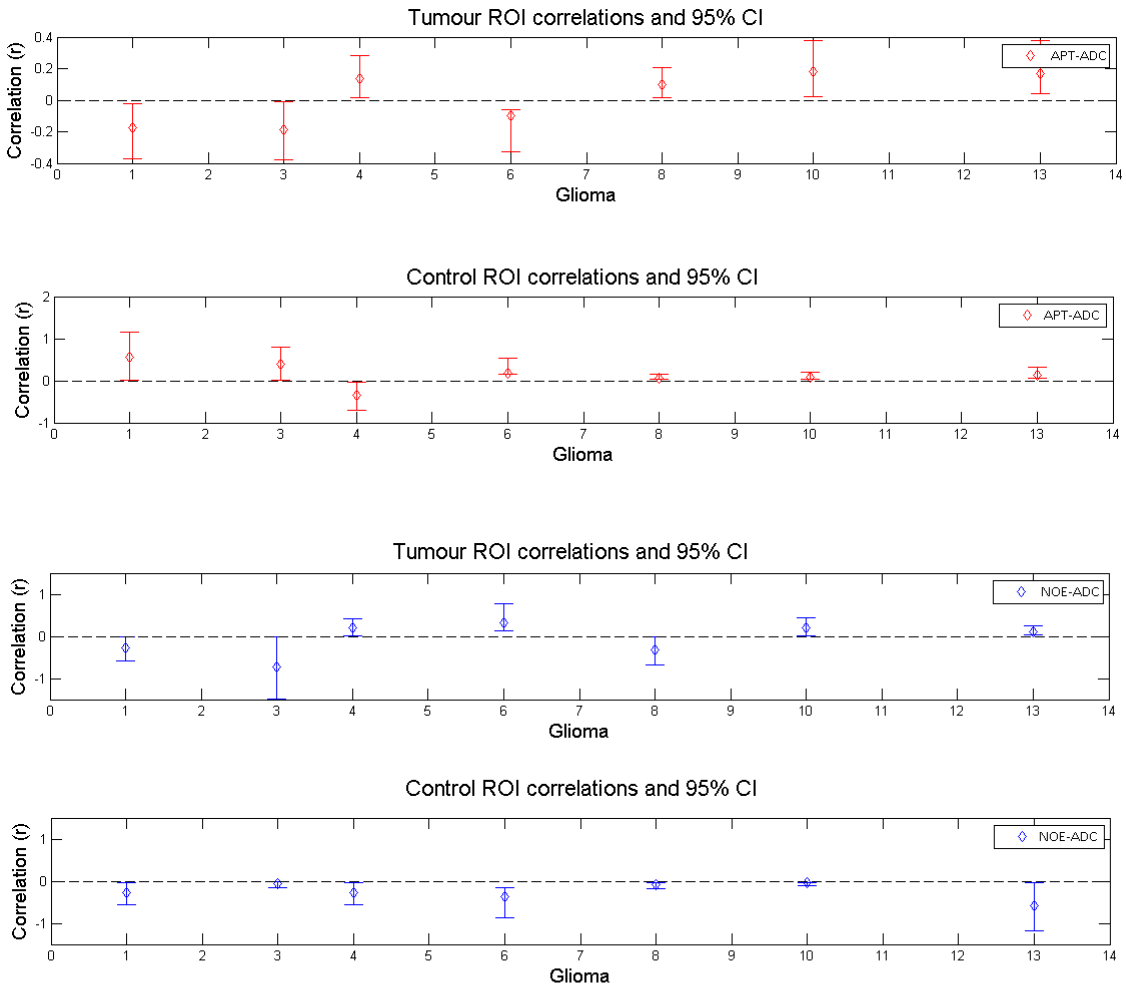


Figure 6.19: Summary of the APT - ADC and NOE - ADC correlations in tumours and controls for all glioma cases.

6.4 Discussion

In this study, we obtained quantitative APT and NOE maps, of low grade glioma (n=3) and glioblastoma (n=4) patients, at 7T. We used a 3D-Turbo field echo sequence, that allowed full brain coverage (30 slices). Due to the small number of patients, mean APT and NOE signals were calculated by averaging the respective APT and NOE intensities over all same grade cases. Regions of interest (ROIs) were identified on the clinical 3T patient scans. Tumour ROIs were defined on the Gd-T_1 images, for GBMs and on the T_2- FLAIR images, for low grades. Any haemorrhage was identified on the 7T susceptibility weighted images and was subsequently subtracted from the tumour ROIs.

The mean APT signal, in both low grades and GBMs, was significantly higher, than in normal appearing white matter (Wilcoxon rank-sum test). Furthermore, there was a 3-4 fold increase of the mean APT signal in GBMs, as compared to low grade gliomas (Figure 6.13), which indicates a correlation of the APT signal with tumour grade. The APT tumour hyper-intensity, spatially agrees, with Gd enhancement, in glioblastoma. In addition, the APT defined tumour regions seem to extend, outside of the Gd enhancement. This shows that, not only APT imaging can provide useful radiological information without contrast injection, but also identify active parts of the tumour, where no blood-brain-barrier has occurred. Roughly 10% of glioblastomas and 30% of anaplastic astrocytomas show no Gd enhancement [171]. The latter is also true in low grades. In our study, none of the low grade glioma cases showed any Gd enhancement. However, the measured APT intensity was capable of identifying the active parts of the tumour, even in the non Gd-enhancing cases. Patient 4, in particular, was suspected of having a glioblastoma (later confirmed from biopsy), at the time of the research scan and his clinical Gd-T_1 images show a small intensity enhancement. However, the presence of an APT enhancement before any significant appearance of the Gd-enhancing region, indicates that, the APT enhancement could be a precursor

to blood-brain-barrier disruption . Thus, APT imaging can provide complementary information, to the widely used Gd-T_1 imaging. Except grading, APT imaging can also provide invaluable information regarding tumour recurrence and pseudo-progression. More importantly, APT intensity changes occur before any morphological alternations [132, 155]. Ultimately, such detection of true tumour recurrence has a significant impact on a patient's effective course of treatment.

Significantly lower tumour NOE signals were found in both low grades and glioblastomas (Figure 6.14). These signals arise from lipid molecules and are coincidentally centred at -3.5 ppm, in the Z-spectrum. Their range however can extend from -2 ppm to - 5 ppm. Lower tumour NOE effects can be attributed to increased tumour water content [148, 8], protein denaturation [245] and reduced mobile lipid content [247]. A comparison with clinical spectroscopy results would confirm or refute the NOE reduction shown here, but such information was not available at the time of this analysis.

Regarding the correlation of the APT and NOE signal with apparent diffusion coefficient (ADC), no particular trend was found in the correlation of the Gd-T_1 defined tumour regions of APT and NOE with ADC. This suggests that, these MRI contrasts provide different information about low grade gliomas and GBMs and that the magnetisation transfer metrics are most likely independent from cell density. In controls, the NOE-ADC and APT-ADC signals showed a weak negative and positive, correlation, respectively. Overall, the extend and direction of correlations is highly variable and the association between the imaging markers used here appears highly complex. A more detailed analysis is required to explore and understand these relationships further, perhaps through machine learning based classification/prediction tasks or tumour fingerprinting. At the time of this study, there was only one report in the literature that has also found no trend between CEST and diffusion metrics [154]. However, the latter study investigated the correlation between, MTR_{asym}, instead of Lorentzian fitting, and ADC, in glioblastomas.

By using a 3D sequence to acquire whole brain volumes, we expect that our data

are minimally influenced by motion artefacts. Moreover, we have corrected for B_0 inhomogeneities. Nevertheless, the effects of T_1 variation and RF inhomogeneity, have not been compensated for. However, it was suggested that, for non-steady state acquisitions, such as ours, Lorentzian fitting yields, T_1 compensated contrast [246]. Furthermore, the chosen RF power was such that, APT and NOE signals are less sensitive to B_1 inhomogeneities [123]. Further analysis of the data could include comparison of the APT, NOE and also MT signals, from necrotic, haemorrhagic and oedematous compartments, with solid tumour signal. Finally, identification of an intensity threshold, capable of distinguishing, between low and high grades. The latter would be useful in cases where low measured signal is inadequate for tumour classification.

6.5 Conclusion

In conclusion, using an advanced ultra-high CEST protocol, in a series of cerebral gliomas, we were able to show that APT, unconfounded by NOE, is several-fold elevated in glioblastoma. Furthermore, no particular trend was observed between magnetisation transfer and diffusion metrics. APT maps show promise in providing added diagnostic value with impact on patient management, as they may support more accurate planning of biopsy targets, surgical excision and radiotherapy.

Chapter 7

Discussion

Imaging biomarkers are essential tools of clinical imaging that, not only guide clinical decision making, but also facilitate further research in oncology and beyond.

An imaging biomarker is defined as a biological characteristic that serves as an indicator of normal or pathological nature and is derived/measured from medical images. All imaging biomarkers must fulfil two needs: the need to answer clinical questions and the need of being easily applicable in clinical practice.

A biomarker is distinct and separate from the modality used to derive it and can either provide qualitative (categorical) or quantitative measurements. For example, a clinical decision can be based upon the relevant biomarker being above or below a certain cut-off point. Even though imaging biomarkers provide cost effective, non-invasive and readily available tools, they must be comprehensively tested before being adopted into the scope of routine healthcare. As such, every new biomarker has to pass through a series of stages before being integrated into clinical practice. These stages include, discovery and data collection, validation (reproducibility, consistency, strength, specificity) and finally qualification (can the biomarker improve diagnosis or predict outcomes?) [151]. Ultimately, new biomarkers should address unmet diagnostic needs and meet their burden of proof against already established ones.

MRI is the gold standard in screening, diagnosing, staging, targetting treatments and monitoring the response of brain gliomas. Gliomas originate from the glial cells of the central nervous system. These cells do not conduct electrical impulses and their main function is to support and protect neurons. Gliomas are the most common primary brain tumours and are classified into circumscribed and diffuse tumours, with the latter category being subdivided into grades II, III and IV, in adults [98]. There is a plethora of already established MRI glioma biomarkers routinely used in the management of this type of cancer.

First, there are the relaxation based biomarkers. These biomarkers utilise the relaxation properties and their differences in tissues and their measurement produces T_{1w}, T_{2w}, T_2-FLAIR and Gd-T_1 images. Each one of these modalities carries a unique diagnostic value. For example, T_{1w} images are useful for viewing blood products, micro-calcifications, fat and melanin levels. T_{2w} images for visualising gliosis, oedema and non-enhancing parts of tumours. Gd-T_1 images report on blood-brain-barrier disruption and are used in assessing treatment response (by measuring the size of enhancement), grading (positive correlation with enhancement [70]) and defining tumour boundaries of high grade gliomas. The pitfalls associated with the relaxation based biomarkers are that these markers only provide structural information and do not consistently report cases of pseudo-responce and pseudo-progression (e.g. necrosis appears hyper-intense on Gd-T_1). Also, not all high grade gliomas enhance after gadolinium injection.

A second category of MRI glioma biomarkers are the diffusion based ones. Diffusion reflects water mobility and is measured as flux through a surface over time ($\frac{\mathrm{mm}^2}{sec}$). Examples of biomarkers related to diffusion include the apparent diffusion coefficient (ADC) and fractional anisotropy (FA). The former measures the magnitude of diffusion and the latter the degree of diffusion asymmetry within a voxel. Typically these measures are used in separating LGG from HGG [20], in assessing infiltration [25] and guiding surgery (using tractography) [11]. Diffusion pulse sequences utilise

strong gradients in order to encode this microscopic phenomenon. This results in unwanted eddy-currents that compromise the homogeneity of the main magnetic field, necessitating the need for distortion corrections [13]. Another issue associated with characterising gliomas with diffusion is the lack of standardisation among centres. Different institutes use different sequence parameters to derive cut-off points separating the various tumour grades and that makes it hard to establish a common reference.

Perfusion reports on blood flow over mass ($\frac{\mathrm{ml}}{\mathrm{g/min}}$) and is typically used to measure angiogenesis (dynamic susceptibility contrast MRI) and vascular permeability/leakiness (dynamic contrast enhanced MRI). The former modality measures susceptibility related signal losses, due to the paramagnetic effects of gadolinium, by quantifying measures such as CBF, CBV and MTT. Being a susceptibility based technique, dynamic susceptibility contrast MRI suffers from drop in SNR in bone/air boundaries and in the presence of blood products. Moreover, an over/underestimation of CBV is possible, when gadolinium leaks into the extracellular space, shortening the longitudinal and transverse relation times of water. Furthermore, the pharmacokinetic models used in dynamic contrast enhanced MRI are highly complex and require a number of assumptions (e.g. defining $\mathrm{k}^{\mathrm{trans}}$ in high vs low permeability situations). Overall, perfusion has been proven effective in glioma grading [39] and treatment response [40] but is unreliable in differentiating radiation necrosis from recurrent a tumour [112] and pseudo-progression from true early progression [14].

Even though not an imaging method, magnetic resonance spectroscopy (MRS), is routinely used for characterising brain gliomas, as it measures the metabolic profiles of tissues. For example, choline is associated with cell membrane turnover, NAA with neuronal viability, creatine with cell metabolism, myo-inositol with astrocytic integrity and lipids/lactate with hypoxia or necrosis. MRS is highly sensitive in detecting brain tumours but it lacks specificity. For example, higher levels of choline have been reported in HGG [46, 72] but the result is not consistent [73] (perhaps because of the presence of necrosis) and so is the reliability of MRS in differentiating neoplastic from

non-neoplastic pathologies [71] or progression from pseudo-progression [200]. Other limitations of spectroscopy include the need for manual input (in selecting the voxel of interest) and its lower spatial resolution as compared to imaging methods (cm^3 vs mm^3).

CEST is a promising, non-invasive molecular MRI technique that amplifies the detection of molecular entities containing exchangeable proton groups, like amides (APT CEST). As a new glioma biomarker, APT CEST has been shown to consistently differentiate tumour regions from normal appearing white matter and oedema [88, 259, 223], to positively correlate with tumour grade [266, 164], and to reliably differentiate between tumour recurrence and pseudo-progression [132, 267]. Finally, successful response to TMZ treatment was also associated with reduction in APT intensities [162]. Proteomic analysis of tumour biomarkers has confirmed that the APT signal arises from mobile tumour proteins [239] which are also found, at high concentrations, in tumours [73, 268]. Initially, APT signals where quantified via asymmetry analysis [263], but this simplistic treatment was soon replaced by more sophisticated methods such as model [116, 137] and Lorentzian [244, 242, 30] fitting. This change was necessary as it was realised that the CEST contrast is a complex mix, arising from multiple species (especially in-vivo), that except from mobile proteins (amides), include, semi-solid macromolecules (responsible for the broad conventional magnetisation transfer, MT [29]), aliphatic protons (responsible for the downfield NOE effects [247, 249]) and a plethora of other metabolites (e.g. glutamate [10, 107], creatine [62], glycogen [212], myo-inositol [63], glucose [12] and lactate [24]). That is not to say that the APT asymmetry analysis is erroneous, for in-vivo applications. It must however be stated that the quantified APT contrast possibly contains contributions from other sources and that the derived images/maps are APT-weighted [195, 196, 269].

In chapter 3, the aspects of optimising a CEST experiment, were discussed. Typically, the experimental parameters under consideration are those that can be explicitly determined/tested. Here, an in-silico optimisation procedure was presented and the

effects of B_1 power, APT pool size, saturation time and SNR were investigated. The latter parameter is a result of an actual MRI experiment, but in the scope of a simulation it can be included among the parameters that we can be explicitly set. The results shown in Figures 3.1 - 3.6, inform on the optimal parameters for the model under investigation. The effects of saturation power, length and pool size on the APT CEST signal have been well documented in the literature, mostly in-silico and in-vitro [188, 170, 242, 185]. In-vivo, it was also shown that the saturation power can be used to suppress/enhance APT and NOE contributions. For example, an irradiation power less than $1\mu T$ results in the suppression of the APT contribution and to a NOE-dominated signal [90, 153]. Unfortunately, so far there is a lack of consensus when it comes to optimal irradiation power and duration and before a standardisation, across centres, is possible, issues like hardware limitations and B_1 inhomogeneity should be addressed. Another important point to consider here is also the lack of a standard method of quantifying CEST effects. Asymmetry analysis, model fitting and Lorentzian methods have all been used throughout the literature. Even though asymmetry analysis is preferred for simpler pool systems, quantification of the CEST effects in-vivo relies on either model or Lorentzian fitting. Fitting a multi-pool model on experimental data is tedious (e.g. a 4-pool model contains twelve differential equations [116]) and the fitting of 4D CEST images (x, y, slices, offsets) pixel-wise, is extremely time consuming on conventional workstations. Nevertheless, model fitting allows for the determination of unknown system parameters and it could be preferred in certain studies. On the other hand, Lorentzian fitting, is faster, straightforward and also allows for entangling the complex CEST signal. The study described in chapter 3 also investigated the effects of SNR on the accuracy of quantification of the APT peak by using a 2-pool model fitting. An SNR of ~70 was shown to result in about 10% error in measuring the CEST effect. In order to determine which method of quantification is more robust, Lorentzian fitting should also be tested under different SNR conditions, against an ideal spectrum and its accuracy should be compared to that of model fitting. Perhaps, once such a

comparison is performed then CEST effects would be consistently quantified with a single approach.

The APT signal is pH dependent (in fact it is base catalysed [264]) and could potentially be used for in-vivo pH mapping. Such mapping is important in gliomas as acidic pH levels have been associated with increased radio/chemo-resistance, increased metastatic behaviour and invasion and inhibition of DNA repair mechanisms [48]. The challenges of in-vivo pH mapping with CEST revolve around the knowledge of the amide exchange rate and concentration, in-vivo. Even though both of these parameters can be worked out through various methods [32, 116, 276], an additional derivation is required and that is, knowing the relationship between the exchange rate (pH is reflected though it) and the measured APT CEST signal. To achieve the latter, separate experiments (^{1}H [264] or ^{31}P MRS [198]) must be performed before the actual CEST study. A somewhat more simple approach for pH mapping is based on a ratiometric method [129, 221]. This method requires an exogenous agent, that either exhibits two CEST effects, or a single effect, which has to be measured twice (at different B_1 powers) [127]. Chapter 4 discusses the feasibility of three such agents in measuring pH, in-vitro, at 7T, for the first time. All agents are clinically approved for CT scanning (iodinated agents), but contain exchangeable proton groups and are thus suitable for CEST imaging. The agents were scanned at various pH levels and calibration curves along with prediction intervals were derived. One agent, namely, Iodixanol (Visipaque) was found unsuitable for ratiometric CEST pH mapping, while Iopamidol (Niopam) and Iopromide (Ultravist) were found to exhibit a log-linear dependence of their peak ratio on pH. Considering the optimisation procedure described in chapter 3, an in-silico optimisation for ratiometric pH mapping would require a minimum modification on the existing code. This modification simply replaces the exchange rates of the model with their equivalent expression, containing pH as a variable, like so: $k_{sw} = k_0 + k_b * 10^{pH-pk_w}$ [264]. An optimised acquisition scheme would allow for accurate derivation of calibration curves in-vitro. To test this method further, patients

could be scanned with CEST MRI directly after their contrast enhanced CT brain scans. One of the agents tested here, (Niopam), was detected in the bladder of patient [139], before. In the case of gliomas however, it is unclear if such an approach would succeed, mainly because of the agent's half-life properties and also its uncertain penetration of the blood-brain-barrier and accumulation in the tumour.

Translating a CEST study at a lower field is challenging not only because the shortening of the longitudinal relaxation of water is detrimental for the CEST contrast (equation 2.2.4 and [99]) but also because the chemical shifts between the CEST pools are reduced. One of the iodinated contrast agents that was scanned at 7T (Ultravist, chapter 4) was also studied at 3T, among other compounds. Two sequences were compared for their ability to measure CEST effects at 3T: a 2D sequence that was programmed locally and a 3D sequence that was programmed at King's College. Both sequences were gradient echo based sequences. Besides the apparent difference in the allowed coverage of each sequence, the 3D sequence offers another advantage, namely, centric elliptical k-space filling. Since the centre of k-space determines the signal to noise ratio, the 3D sequence should generate images of higher signal. Chapter 5 describes the performance of each sequence and even though stronger CEST signals were measured with the 3D vs 2D sequence, Ultravist did not show the second CEST peak that was detected at 7T (chapter 4). This is attributed to the fact that the phantom was prepared at physiological pH, at which the CEST peak in question has its minimum magnitude (this peak is pronounced for acidic pH). Furthermore, based on the results described in chapter 3, the 3D sequence is expected to allow for a more robust quantification of CEST effects, in the presence of noise, even though this hypothesis cannot be confirmed at this point. The biggest drawback of the 3D sequence was the maximum allowed pulse duration that could be used at the time of the study. 20ms is simply not an adequate time for efficient saturation and also results in large RF bandwidths. The latter bandwidths cause distortions in the Z-spectra and this was something that was consistently observed in the results presented in chapter 5. Although

most CEST studies are performed at 7T (for the obvious gains in SNR), a few in-vivo glioma studies have been successfully performed at 3T [88, 258, 259, 266]. Despite obvious shortcomings in the length of saturation, the 3D sequence showed potential for translating CEST studies at 3T. As an extension to the work done at 7T (chapter 4) the pH dependence of the iodinated agents could have been investigated at 3T. In any case, an optimised CEST sequence on a research scanner is a great opportunity to investigate the APT contrast at a clinically relevant field, on healthy volunteers, at first, and in glioma patients next. For example, it would be interesting to know whether the novel exchange peak at -1.6 ppm, detected at high field [273, 254], can also be detected at 3T. This peak has been attributed to phospho-cholines and is associated with increased tumour perfusion. Perhaps, then CEST allows for accessing tumour perfusion characteristics [251].

In the final study on this thesis (chapter 6), a series of cerebral gliomas were characterised using an advanced ultra-high field CEST protocol, allowing for full brain coverage. At the time of this study there was only one report in the literature, where a 3D sequence was used to characterise gliomas, in-vivo [270]. Lorentzian fitting, as opposed to asymmetry analysis, was used to produce APT maps, unconfounded by NOE, and the other way around and CEST metrics were correlated with diffusion metrics. Because of the small number of patients, the ROI analysis was performed on all tumour ROIs, on the APT maps, of all low and high grades, respectively. A similar procedure was followed for calculating the NOE signals. It was known from the literature that the APT signal correlates with tumour grade [266, 164] and here we reported a similar trend: the APT signal was several-fold elevated in glioblastoma, when compared to low grades and controls. This possibly reflects a higher mobile protein content in GBMs (and in Gd-enhancing regions), a result which agrees with proton spectroscopy [73]. On the other hand, the opposite was observed for NOE (in the same Gd-enhancing regions): NOE signals decreased in both LGGs and GBMs and more so in GBMs. It is believed that the NOE signals arise from mobile aliphatic protons [30]

and that they build up slower than the APT effects [90]. Therefore, a pulsed acquisition, with increased inter-pulse delay allows for their expression. NOE signals have also been correlated with the structural state of proteins and particularly with protein folding [245]. The reduced NOE signals reported here perhaps then reflect the loss of protein folding mechanisms in tumours and particularly in GBMs. Large variations were observed in the correlation of CEST with diffusion metrics and overall no particular trend was found. Thus, diffusion and CEST biomarkers report on different aspects in gliomas. A similar result was reported in [154] even when the CEST effects were quantified by asymmetry analysis. From a clinical perspective, what would be useful to do further, is to identify an intensity threshold (cut-off), capable of distinguishing low and high grades. This would beneficial in cases where low measured signal is inadequate for tumour classification. Finally, a study could be designed where patients are scanned before and after treatment and their progress is monitored. Cases of pseudoprogression can then be compared with true progression with the hypothesis being that the former exhibit low (if any) APT signal when compared to the latter.

CEST is an emerging molecular MRI technique that shows promise in characterising gliomas. APT signal correlates with tumour grade, differentiates tumour recurrence from radiation necrosis and can possibly monitor treatment effects. CEST can be performed without the use of additional hardware and does not require administration of contrast agents. Its added value is still under investigation and this work tried to illustrate of few of its advantages and pitfalls.

Appendix A

Matrix exponential solution to Bloch equations

From reference [146] the matrix A for a two pool system is:

$$\mathcal{A} = \begin{pmatrix} -(R2a + ka) & kb & da(i) & 0 & 0 & 0 & 0 \\ ka & -(R2b + kb) & 0 & db(i) & 0 & 0 & 0 \\ -(da(i)) & 0 & -(R2a + ka) & kb & w1 & 0 & 0 \\ 0 & -(db(i)) & ka & -(R2b + kb) & 0 & w1 & 0 \\ 0 & 0 & -w1 & 0 & -(R1a + ka) & kb & R1a * M0a \\ 0 & 0 & 0 & -w1 & ka & -(R1b + kb) & R1b * M0b \\ 0 & 0 & 0 & 0 & 0 & 0 & 0 \end{pmatrix}$$

For the three pool system A is defined as:

$$\mathcal{A} = \begin{pmatrix} -k2a & cb & cc & -(da(i)) & 0 & 0 & 0 & 0 & 0 & 0 \\ cab & -k2b & 0 & 0 & -(db(i)) & 0 & 0 & 0 & 0 & 0 \\ cac & 0 & -k2c & 0 & 0 & -(dc(i)) & 0 & 0 & 0 & 0 \\ (da(i)) & 0 & 0 & -k2a & cb & cc & -w1 & 0 & 0 & 0 \\ 0 & (db(i)) & 0 & cab & -k2b & 0 & 0 & -w1 & 0 & 0 \\ 0 & 0 & (dc(i)) & cac & 0 & -k2c & 0 & 0 & -w1 & 0 \\ 0 & 0 & 0 & w1 & 0 & 0 & -k1a & cb & cc & M0a/T1a \\ 0 & 0 & 0 & 0 & w1 & 0 & cab & -k1b & 0 & M0b/T1b \\ 0 & 0 & 0 & 0 & 0 & w1 & cac & 0 & -k1c & M0c/T1c \\ 0 & 0 & 0 & 0 & 0 & 0 & 0 & 0 & 0 & 0 \end{pmatrix}$$

Appendix B

Simulation parameters

The simulation parameters for the two-pool system described in Figures 2.11, 2.12 and 2.13 were as follows:

T1a = 1.1; % water T1, T2a = 0.07; % water T2, R1a = 1/T1a; R2a = 1/T2a; T1b = 1.1; % cest T1, T2b = 0.015; % cest T2, R1b = 1/T1b; R2b = 1/T2b; kb = 50; % cest −> exchange rate, ka =(M0b/M0a)*kb; % water −> cest exchange rate, M0a =1, Field −>3T.

The simulation parameters for the three-pool system described in Figures 2.14 and 2.15 were as follows:

T1a = 1.1; % T1 water relaxation time [s], T2a = 0.07; % T2 water relaxation time [s], R1a = 1/T1a; R2a = 1/T2a; T1b = 1.1; % T1 of labile protons [s], T2b = 0.015; % T2 of labile protons [s], R1b = 1/T1b; R2b = 1/T2b; T1c = 1; % sec, T2c = 0.015; % sec, R1c = 1/T1c; R2c = 1/T2c; cc = 6*cb; % exchange rate 3rd pool−>bulk water [1/sec], M0a = 1; % thermal equilibrium Mag of water, M0b = 0.005; % thermal equilibrium Mag labile, M0c = M0b; Field −>3T.

The simulation parameters for the three-pool system described in Figure 2.16 were as follows:

T1a = 1.7; T2a = 0.048; R1a = 1/T1a; R2a = 1/T2a; T1b = 1.7; T2b = 0.033; R1b = 1/T1b; R2b = 1/T2b; T1c = 1.7; % sec for MT, T2c = 0.01*(10^-6); % sec for MT, R1c = 1/T1c; R2c = 1/T2c;

M0a = 1; M0b = 0.0006; M0c = 0.06; kba = 100; %CEST−>water, kca = 4.6; %MT−>water, kab =(M0b/M0a)*kba; % water −> cest, kac =(M0c/M0a)*kca; % water −> cest, MT line-shape −>superLorentzian, Field −>3T.

The simulation parameters for the two-pool system described in Figure 2.17 were as follows:

T1a = 3; % water T1, T2a = 0.1; % water T2, R1a = 1/T1a; R2a = 1/T2a; T1b = 1; % cest T1, T2b = 0.015; % cest T2, R1b = 1/T1b; R2b = 1/T2b; M0a = 1; % water equilibrium magnetisation, M0b = 0.002; % cest equilibrium magnetisation, kb = 50; % cest −> water exchange rate, ka =(M0b/M0a)*kb; % water −> cest exchange rate, f = 200; % 4.7T, tg = 15*10^(-3); % gauss pulse duration in [s], td = tg; % equal to tau_g for 50% dc, N = 64; % steps, c = tg/(2*(sqrt(-log10(tl)))); theta = pi; % flip angle, B1 = (theta/g)*((exp((-(((i*tg/N) - tg/2).^2)/c.^2)))/(sum(exp((-(((i*tg/N) - tg/2).^2)/c.^2))*tg/N)));

Appendix C

Patient recruitment documents

Study Number:

Patient Identification Number for this study:

CONSENT FORM

Title of Project: "Imaging anatomical and physiological characteristics of Brain Tumours using Ultra High-Field Magnetic Resonance Imaging."

Name of Researchers: Prof. Dorothee Auer; Dr Tilak Das

		Please tick
1.	I confirm that I have read and understood the information sheet dated 23 Mar 2009 (version 1.5) for the above study.	☐
2.	I have had the opportunity to consider the information, ask questions and have had these answered satisfactorily.	☐
3.	I understand that my participation is voluntary and that I am free to withdraw at any time, without giving any reason, without my medical care or legal rights being affected.	☐
4.	I understand that sections of any of my medical notes and clinical diagnostic images may be looked at by investigators and responsible individuals from regulatory authorities or from Nottingham University Hospitals NHS Trust where it is relevant to my taking part in research. I give permission for these individuals to have access to my records.	☐
5.	I agree to the consultant clinician (Neurosurgeon / Neurologist / Oncologist) looking after me being informed of my participation in this study and of the result of my brain scan, should they wish to see this.	☐
6.	I agree that samples of my brain tissue, if taken during a biopsy or operation at any stage, may be stored and used in ethically approved future biological research studies.	☐
7.	I agree to take part in the above study.	☐

_____ Name of	_____ Patient
Signature	Signature
Date	
Date	

Study Ref:

Patient Information Leaflet

The University of Nottingham

Imaging of Focal Brain Pathology using Ultra High-Field Magnetic Resonance Imaging (MRI)

You are being invited to take part in a research study. Before you decide, it is important for you to understand why the research is being done and what it will involve. Please take time to read the following information carefully. Talk to others about the study if you wish. Please ask us if there is anything that is not clear or if you would like more information. Take time to decide whether or not you wish to take part.

The Study

What is the purpose of the study?

The purpose of the study is to find out whether Ultra High-Field MRI, an MRI scanner that uses a stronger magnetic field (7 Tesla) than used in hospitals routinely (1.5 or 3 Tesla), can help us to better define the characteristics of brain lesions that have already been detected using a regular MRI scanner.

Taking Part

Why have I been invited to take part?

Your consultant has referred you to us because an MRI scan that was organised for you previously has shown that you may have a brain lesion.

Do I have to take part?

This study is entirely voluntary. It is up to you to decide whether or not to take part. If you do decide to take part you will be given this information sheet to keep and be asked to sign a consent form, a copy of which you will get to keep. If you decide to take part you are still free to withdraw at any time and without giving a reason. This will not affect the standard of care you receive.

What will happen to me if I take part?

If you consent to take part, we will ask you to answer some questions to ensure it is safe for you to have an MRI scan. You will then undergo an MRI scan very similar to MRI scans that you may have already had. This scan will take place at the Sir Peter Mansfield Magnetic Resonance Centre within the University of Nottingham. If you are an outpatient, we will organise a date and time for you to attend the scan. If you are an inpatient, we will organise a date and time and transport to the MRI scanner, ensuring that you do not miss any of the tests or meetings that your doctors may have organised on the ward. With your consent, the MRI scan may involve the use of intravenous contrast (‘dye’) that is injected into your veins in exactly the same way as your previous MRI scans.

Study Ref:

Patient Information Leaflet

The University of Nottingham

MRI Scanning

What is an MRI scan?

You will likely already have experienced an MRI scan. MRI stands for Magnetic Resonance Imaging. An MRI scan uses a magnetic field rather than x-rays to take pictures of your body. The MRI Scanner is a hollow machine with a tube running horizontally through its middle. You will lie on a bed that slides into the tube. The scan lasts from 30 to 60 minutes and will provide detailed pictures of your brain. It can be noisy and some people find it claustrophobic, but it is completely painless.

What am I expected to do in the scanner?

You will be required to lie still during the scan, and move your head as little as you can.

What are the possible disadvantages and risks of taking part?

Disadvantages can include temporary dizziness or a strange taste in your mouth and minor bruising from the insertion of a 'venflon' or line for the injection of the contrast ('dye'). The main risk from MRI is if you have any metallic foreign objects in your body, but you will not have had the regular hospital MRI scan if this were the case.

What are the possible benefits of taking part?

There will not likely be a direct benefit to you. The benefit will be in improving the care of patients like yourself in the future. It is possible, but unlikely, that we find something that we should tell your consultant about in case he or she feels this may change how you are currently managed, and we ask for permission to do this on the consent form.

Confidentiality

Will my taking part in this study be kept confidential?

Yes, all information which is collected about you during the course of the research will be kept **strictly confidential**. Any information about you which leaves the hospital will have your name and address removed so that you cannot be recognised from it. With your permission the consultant looking after your case will be informed of your participation. These points are included on the consent form you will be asked to sign.

What will happen to any tissue samples that are taken?

If you have had or may have a biopsy or an operation for the brain lesion, we would like to be able to access the records and the tissue sample from the procedure in the future, so that we can relate what we see on the scans to the tissue that is obtained. We will ask for your permission to access your medical records as well as the tissue samples for future research studies.

What will happen to the results of the research study?

The results of the study will hopefully be published in specialist medical journals and related conferences. They may also be sent to health authorities. Of course, you will not be identified in any report or publication arising from this research.

Study Ref:

Patient Information Leaflet

The University of Nottingham

Questions or Problems

What if something goes wrong?

A qualified medical doctor from the project team will always accompany you. If you experience feelings of panic or distress at any time during the study, the examination will be stopped immediately. In a medical emergency, the research team are competent to provide prompt first aid treatment and will call an ambulance team if necessary.

If taking part in this project harms you, there are no special compensation arrangements. As mentioned above, we do not anticipate significant risks to you by participation in this study, but in the unlikely event that you are harmed you can take legal action but may have to pay for it. Regardless of this, if you wish to complain about any aspect of the way you have been approached or treated during the course of this study, you may contact anyone on the research team (contact details below). In addition, you may contact the NHS Patient Advice and Liaison Service (PALS) for further assistance by calling 0800 1830204.

Who has reviewed the study?

This study is being conducted by the Academic Radiology Department of the University of Nottingham, and is being sponsored by the University of Nottingham. This study has been approved by the Nottingham Research Ethics Committee and by the Research and Development Department of the Queen's Medical Centre, Nottingham.

Contact for further information

For more information or if you have any concerns, questions about this study or complaints, please contact the Chief investigator, Prof. D. Auer via Ms. Sharon Forman (Research Administrator) - Tel. 01158 231179.

If you have any complaints about the way the investigator has carried out the study, you may contact the Patient Advice and Liaison Service (PALS) at Nottingham - Tel. 0800 1830204.

Appendix D

Lorentzian pool fitting parameters

	Water	APT	NOE
A	0.9 (bounds: 0.02-1)	0.025 (bounds: 0-0.4)	0.02 (bounds: 0-0.5)
Γ	1.4 (bounds: 0.3-10)	0.5 (bounds:0.2-3)	3 (bounds: 1-5)
Offset (ppm)	0	+3.5	-3.5

Bibliography

[1] Silvio Aime. "a macromolecular gd (iii) complex as ph-responsive relaxometric probe for mri applications.". *Chemical Communications 16 : 1577-1578.*, 1999.

[2] Silvio Aime, Luisella Calabi, Luca Biondi, Mario De Miranda, Stefano Ghelli, Lino Paleari, Cristina Rebaudengo, and Enzo Terreno. Iopamidol: Exploring the potential use of a well-established x-ray contrast agent for mri. *Magn Reson Med*, 53(4):830–834, Apr 2005. doi: 10.1002/mrm.20441. URL `http://dx.doi.org/10.1002/mrm.20441`.

[3] David C Alsop and John A Detre. Multisection cerebral blood flow mr imaging with continuous arterial spin labeling. *Radiology*, 208(2):410–416, 1998.

[4] Lorena Consolino Dario Livio Longo Anemone Annasofia. . "mri-cest assessment of tumour perfusion using x-ray iodinated agents: comparison with a conventional gd-based agent.". *European radiology 27.5 : 2170-2179.*, 2017.

[5] M. E. Arnold, J. T.; Packard. Variations in absolute chemical shift of nuclear induction signals of hydroxyl groups of methyl and ethyl alcohol. *The Journal of Chemical Physics*, 19:1608–1609, 1951.

[6] T E J. Behrens, M. W. Woolrich, M. Jenkinson, H. Johansen-Berg, R. G. Nunes, S. Clare, P. M. Matthews, J. M. Brady, and S. M. Smith. Characterization and propagation of uncertainty in diffusion-weighted mr imaging. *Magn Reson Med*,

50(5):1077–1088, Nov 2003. doi: 10.1002/mrm.10609. URL http://dx.doi.org/10.1002/mrm.10609.

[7] M A Bernstein, K F King, and X J Zhou. *Handbook of MRI pulse sequences*. Elsevier, 2004.

[8] Wolfram Bodsch, Thomas Rommel, Bernd Grosse Ophoff, and Jürgen Menzel. Factors responsible for the retention of fluid in human tumor edema and the effect of dexamethasone. *Journal of neurosurgery*, 67(2):250–257, 1987.

[9] DM Brizel, RL Scher, S Walenta, MW Dewhirst, and W Mueller-Kleiser. Elevated tumor lactate concentrations predict for an increased risk of metastases in head and neck cancer. *International Journal of Radiation Oncology* Biology* Physics*, 48(3):177, 2000.

[10] Kejia Cai, Mohammad Haris, Anup Singh, Feliks Kogan, Joel H Greenberg, Hari Hariharan, John A Detre, and Ravinder Reddy. Magnetic resonance imaging of glutamate. *Nature medicine*, 18:302–306, January 2012. ISSN 1546-170X. doi: 10.1038/nm.2615.

[11] Antonella Castellano, Lorenzo Bello, Caterina Michelozzi, Marcello Gallucci, Enrica Fava, Antonella Iadanza, Marco Riva, Giuseppe Casaceli, and Andrea Falini. Role of diffusion tensor magnetic resonance tractography in predicting the extent of resection in glioma surgery. *Neuro-oncology*, 14:192–202, February 2012. ISSN 1523-5866. doi: 10.1093/neuonc/nor188.

[12] Kannie W Y Chan, Michael T McMahon, Yoshinori Kato, Guanshu Liu, Jeff W M Bulte, Zaver M Bhujwalla, Dmitri Artemov, and Peter C M van Zijl. Natural d-glucose as a biodegradable mri contrast agent for detecting cancer. *Magnetic resonance in medicine*, 68:1764–1773, December 2012. ISSN 1522-2594. doi: 10.1002/mrm.24520.

[13] Rachel W Chan, Constantin von Deuster, Daniel Giese, Christian T Stoeck, Jack Harmer, Andrew P Aitken, David Atkinson, and Sebastian Kozerke. Characterization and correction of eddy-current artifacts in unipolar and bipolar diffusion sequences using magnetic field monitoring. *Journal of magnetic resonance (San Diego, Calif. : 1997)*, 244:74–84, July 2014. ISSN 1096-0856. doi: 10.1016/j.jmr.2014.04.018.

[14] Cristo Chaskis, Bart Neyns, Alex Michotte, Mark De Ridder, and Hendrik Everaert. Pseudoprogression after radiotherapy with concurrent temozolomide for high-grade glioma: clinical observations and working recommendations. *Surgical neurology*, 72(4):423–428, 2009.

[15] Liu Qi Chen, Christine M. Howison, Justin J. Jeffery, Ian F. Robey, Phillip H. Kuo, and Mark D. Pagel. Evaluations of extracellular ph within in vivo tumors using acidocest mri. *Magn Reson Med*, 72(5):1408–1417, Nov 2014. doi: 10.1002/mrm.25053. URL `http://dx.doi.org/10.1002/mrm.25053`.

[16] Shu-Zhong Chen, Jing Yuan, Min Deng, Juan Wei, Jinyuan Zhou, and Yì-Xiáng J Wáng. Chemical exchange saturation transfer (cest) mr technique for in-vivo liver imaging at 3.0 tesla. *European radiology*, 26(6):1792–1800, 2016.

[17] Yoon Seong Choi, Sung Soo Ahn, Seung-Koo Lee, Jong Hee Chang, Seok-Gu Kang, Se Hoon Kim, and Jinyuan Zhou. Amide proton transfer imaging to discriminate between low-and high-grade gliomas: added value to apparent diffusion coefficient and relative cerebral blood volume. *European radiology*, pages 1–9, 2017.

[18] Rhodri Cusack, Benedict Russell, Sylvia ML Cox, Claudia De Panfilis, Christian Schwarzbauer, and Richard Ansorge. An evaluation of the use of passive shimming to improve frontal sensitivity in fmri. *Neuroimage*, 24(1):82–91, 2005.

[19] Zhuozhi Dai, Jim Ji, Gang Xiao, Gen Yan, Shengkai Li, Guishan Zhang, Yan Lin, Zhiwei Shen, and Renhua Wu. Magnetization transfer prepared gradient echo mri for cest imaging. *PloS one*, 9(11):e112219, 2014.

[20] Aneela Darbar, Muhammad Waqas, Syed Faaiz Enam, and Shaikh D Mahmood. Use of preoperative apparent diffusion coefficients to predict brain tumor grade. *Cureus*, 10:e2284, March 2018. ISSN 2168-8184. doi: 10.7759/cureus.2284.

[21] de Boer RW. Magnetization transfer contrast. part 1: Mr physics. *Philips Medical Systems MedicaMundi*, 40:64–73., 1995.

[22] Robin A De Graaf, Peter B Brown, Scott McIntyre, Douglas L Rothman, and Terence W Nixon. Dynamic shim updating (dsu) for multislice signal acquisition. *Magnetic Resonance in Medicine: An Official Journal of the International Society for Magnetic Resonance in Medicine*, 49(3):409–416, 2003.

[23] Ralph J DeBerardinis, Anthony Mancuso, Evgueni Daikhin, Ilana Nissim, Marc Yudkoff, Suzanne Wehrli, and Craig B Thompson. Beyond aerobic glycolysis: transformed cells can engage in glutamine metabolism that exceeds the requirement for protein and nucleotide synthesis. *Proceedings of the National Academy of Sciences*, 104(49):19345–19350, 2007.

[24] Catherine DeBrosse, Ravi Prakash Reddy Nanga, Puneet Bagga, Kavindra Nath, Mohammad Haris, Francesco Marincola, Mitchell D Schnall, Hari Hariharan, and Ravinder Reddy. Lactate chemical exchange saturation transfer (latest) imaging in vivo: a biomarker for ldh activity. *Scientific reports*, 6:19517, 2016.

[25] Anna F Delgado, Markus Nilsson, Francesco Latini, Johanna MÃ¥rtensson, Maria Zetterling, Shala G Berntsson, Irina Alafuzoff, Jimmy LÃ€tt, and Elna-Marie Larsson. Preoperative quantitative mr tractography compared with visual tract evaluation in patients with neuropathologically confirmed gliomas grades

ii and iii: A prospective cohort study. *Radiology research and practice*, 2016: 7671854, 2016. ISSN 2090-1941. doi: 10.1155/2016/7671854.

[26] B. Denisov, V.P. & Halle. Hydrogen exchange and protein hydration: the deuteron spin relaxation dispersions of bovine pancreatic trypsin inhibitor and ubiquitin. *Journal of molecular biology 245, 698-709*, 1995.

[27] V.P. Denisov. Using buried water molecules to explore the energy landscape of the proteins. *Nature Struc. Biolol. 3, 505-509*, 1996.

[28] Anagha Deshmane, Moritz Zaiss, Tobias Lindig, Kai Herz, Mark Schuppert, Chirayu Gandhi, Benjamin Bender, Ulrike Ernemann, and Klaus Scheffler. 3d gradient echo snapshot cest mri with low power saturation for human studies at 3t. *Magnetic resonance in medicine*, 81:2412–2423, April 2019. ISSN 1522-2594. doi: 10.1002/mrm.27569.

[29] Kimberly L Desmond and Greg J Stanisz. Understanding quantitative pulsed cest in the presence of mt. *Magnetic resonance in medicine*, 67:979–990, April 2012. ISSN 1522-2594. doi: 10.1002/mrm.23074.

[30] Kimberly L Desmond, Firas Moosvi, and Greg J Stanisz. Mapping of amide, amine, and aliphatic peaks in the cest spectra of murine xenografts at 7 t. *Magnetic resonance in medicine*, 71(5):1841–1853, 2014.

[31] W Thomas Dixon, Ileana Hancu, S James Ratnakar, A Dean Sherry, Robert E. Lenkinski, and David C. Alsop. A multislice gradient echo pulse sequence for cest imaging. *Magn Reson Med*, 63(1):253–256, Jan 2010. doi: 10.1002/mrm.22193. URL `http://dx.doi.org/10.1002/mrm.22193`.

[32] W Thomas Dixon, Jimin Ren, Angelo JM Lubag, James Ratnakar, Elena Vinogradov, Ileana Hancu, Robert E Lenkinski, and A Dean Sherry. A concentration-

independent method to measure exchange rates in paracest agents. *Magnetic resonance in medicine*, 63(3):625–632, 2010.

[33] Manus J Donahue, Paula C M Donahue, Swati Rane, Christopher R Thompson, Megan K Strother, Allison O Scott, and Seth A Smith. Assessment of lymphatic impairment and interstitial protein accumulation in patients with breast cancer treatment-related lymphedema using cest mri. *Magnetic resonance in medicine*, 75:345–355, January 2016. ISSN 1522-2594. doi: 10.1002/mrm.25649.

[34] Dick J. Drost, William R. Riddle, Geoffrey D. Clarke, and A. A. P. M M. R Task Group 9 . Proton magnetic resonance spectroscopy in the brain: report of aapm mr task group 9. *Med Phys*, 29(9):2177–2197, Sep 2002.

[35] Adrienne N Dula, Elizabeth M Asche, Bennett A Landman, E Brian Welch, Siddharama Pawate, Subramaniam Sriram, John C Gore, and Seth A Smith. Development of chemical exchange saturation transfer at 7t. *Magnetic resonance in medicine*, 66(3):831–838, 2011.

[36] Adrienne N Dula, Blake E Dewey, Lori R Arlinghaus, Jason M Williams, Dennis Klomp, Thomas E Yankeelov, and Seth Smith. Optimization of 7-t chemical exchange saturation transfer parameters for validation of glycosaminoglycan and amide proton transfer of fibroglandular breast tissue. *Radiology*, 275:255–261, April 2015. ISSN 1527-1315. doi: 10.1148/radiol.14140762.

[37] Seth Smith Dula Adrienne Lori R. Arlinghaus Richard Dortch Blake Dewey Jennifer Whisenant Gregory Ayers Thomas Yankeelov. Amide proton transfer imaging of the breast at 3 t: establishing reproducibility and possible feasibility assessing chemotherapy response. *Magn Reson Med. Jul;70(1):216-24*, 2013.

[38] Allan D. Ellster. http://mriquestions.com/active-shimming.html.

[39] M Essig, F Giesel, M Le-Huu, B Stieltjes, H von Tengg, and M-A Weber. Perfusion

mri in cns disease: current concepts. *Neuroradiology*, 46 Suppl 2:s201–s207, December 2004. ISSN 1432-1920. doi: 10.1007/s00234-004-1331-y.

[40] Girish M Fatterpekar, Diogo Galheigo, Ashwatha Narayana, Glyn Johnson, and Edmond Knopp. Treatment-related change versus tumor recurrence in high-grade gliomas: a diagnostic conundrum–use of dynamic susceptibility contrast-enhanced (dsc) perfusion mri. *AJR. American journal of roentgenology*, 198:19–26, January 2012. ISSN 1546-3141. doi: 10.2214/AJR.11.7417.

[41] C. L Florian. "regional and developmental variations in metabolite concentration in the rat brain and eye: a study using 1 h nmr spectroscopy and high performance liquid chromatography.". *Neurochemical research 21.9 : 1065-1074.*, 1996.

[42] Sture ForsÃ©n and Ragnar A. Hoffman. Study of moderately rapid chemical exchange reactions by means of nuclear magnetic double resonance. *The Journal of Chemical Physics*, 39:2892, (1963).

[43] Elena Vinogradov G. Varma David Alsop Robert E. Lenkinski. Optimization of pulsed-gagcest at 3.0t. *Proc. Intl. Soc. Mag. Reson. Med. 19*, 2011.

[44] L. E. Gerweck and K. Seetharaman. Cellular ph gradient in tumor versus normal tissue: potential exploitation for the treatment of cancer. *Cancer Res*, 56(6):1194–1198, Mar 1996.

[45] Glover GH. High order shimming, 2002.

[46] Steven S Gill, David GT Thomas, Nicholas Van Bruggen, David G Gadian, Carol J Peden, Jimmy D Bell, I Jane Cox, David K Menon, Richard A Iles, David J Bryant, et al. Proton mr spectroscopy of intracranial tumours: in vivo and in vitro studies. *Journal of computer assisted tomography*, 14(4):497–502, 1990.

[47] Robert J Gillies, Zaver M Bhujwalla, Jeffrey Evelhoch, Michael Garwood, Michal Neema, Simon P Robinson, Christopher H Sotak, and Boudewijn Van Der Sanden. Applications of magnetic resonance in model systems: tumor biology and physiology. *Neoplasia*, 2(1-2):139–151, 2000.

[48] Robert J. Gillies, Natarajan Raghunand, Gregory S. Karczmar, and Zaver M. Bhujwalla. Mri of the tumor microenvironment. *J Magn Reson Imaging*, 16 (4):430–450, Oct 2002. doi: 10.1002/jmri.10181. URL `http://dx.doi.org/10.1002/jmri.10181`.

[49] Daniel F Gochberg, Richard P Kennan, Matthew D Robson, and John C Gore. Quantitative imaging of magnetization transfer using multiple selective pulses. *Magnetic resonance in medicine*, 41(5):1065–1072, 1999.

[50] N. Goffeney, J. W. Bulte, J. Duyn, LH Bryant, Jr, and P. C. van Zijl. Sensitive nmr detection of cationic-polymer-based gene delivery systems using saturation transfer via proton exchange. *J Am Chem Soc*, 123(35):8628–8629, Sep 2001.

[51] Josef Granwehr and Paul Glover. *MPAGS Lectures on Magnetic Resonance*. 2010.

[52] J.R Griffiths. Are cancer cells acidic? *British journal of cancer*, 64:425–7, 1991.

[53] Rachel Grossman, Betty Tyler, Henry Brem, Charles G Eberhart, Silun Wang, De-Xue Fu, Zhibo Wen, and Jinyuan Zhou. Growth properties of sf188/v+ human glioma in rats in vivo observed by magnetic resonance imaging. *Journal of neuro-oncology*, 110(3):315–323, 2012.

[54] V. Guivel-Scharen, T. Sinnwell, S. D. Wolff, and R. S. Balaban. Detection of proton chemical exchange between metabolites and water in biological tissues. *J Magn Reson*, 133(1):36–45, Jul 1998. doi: 10.1006/jmre.1998.1440. URL `http://dx.doi.org/10.1006/jmre.1998.1440`.

[55] V Guivel-Scharen, T Sinnwell, SD Wolff, and RS Balaban. Detection of proton chemical exchange between metabolites and water in biological tissues. *Journal of Magnetic Resonance*, 133(1):36–45, 1998.

[56] Sachin K Gujar, Sharad Maheshwari, Isabella Björkman-Burtscher, and Pia C Sundgren. Magnetic resonance spectroscopy. *Journal of neuro-ophthalmology*, 25(3):217–226, 2005.

[57] H. S. Gutowsky and A. Saika. Dissociation, chemical exchange, and the proton magnetic resonance in some aqueous electrolytes. *J. Chem. Phys*, 21:1688, 1953.

[58] PHILIP J Hajduk, DAVID A Horita, and LAURA E Lerner. Theoretical analysis of relaxation during shaped pulses. i. the effects of short t1 and t2. *Journal of Magnetic Resonance, Series A*, 103(1):40–52, 1993.

[59] Hui Han, Allen W Song, and Trong-Kha Truong. Integrated parallel reception, excitation, and shimming (ipres). *Magnetic resonance in medicine*, 70:241–247, July 2013. ISSN 1522-2594. doi: 10.1002/mrm.24766.

[60] Stefan Haneder, Sebastian R Apprich, Benjamin Schmitt, Henrik J Michaely, Stefan O Schoenberg, Klaus M Friedrich, and Siegfried Trattnig. Assessment of glycosaminoglycan content in intervertebral discs using chemical exchange saturation transfer at 3.0 tesla: preliminary results in patients with low-back pain. *European radiology*, 23:861–868, March 2013. ISSN 1432-1084. doi: 10.1007/s00330-012-2660-6.

[61] Mohammad Haris, Kejia Cai, Anup Singh, Hari Hariharan, and Ravinder Reddy. In vivo mapping of brain myo-inositol. *NeuroImage*, 54:2079–2085, February 2011. ISSN 1095-9572. doi: 10.1016/j.neuroimage.2010.10.017.

[62] Mohammad Haris, Ravi Prakash Reddy Nanga, Anup Singh, Kejia Cai, Feliks Kogan, Hari Hariharan, and Ravinder Reddy. Exchange rates of creatine kinase

metabolites: feasibility of imaging creatine by chemical exchange saturation transfer mri. *NMR in biomedicine*, 25(11):1305–1309, 2012.

[63] Mohammad Haris, Anup Singh, Kejia Cai, Kavindra Nath, Rachelle Crescenzi, Feliks Kogan, Hari Hariharan, and Ravinder Reddy. Micest: a potential tool for non-invasive detection of molecular changes in alzheimer's disease. *Journal of neuroscience methods*, 212(1):87–93, 2013.

[64] Robert J Harris, Timothy F Cloughesy, Linda M Liau, Robert M Prins, Joseph P Antonios, Debiao Li, William H Yong, Whitney B Pope, Albert Lai, Phioanh L Nghiemphu, et al. ph-weighted molecular imaging of gliomas using amine chemical exchange saturation transfer mri. *Neuro-oncology*, 17(11):1514–1524, 2015.

[65] George WJ Harston, Yee Kai Tee, Nicholas Blockley, Thomas W Okell, Sivarajan Thandeswaran, Gabriel Shaya, Fintan Sheerin, Martino Cellerini, Stephen Payne, Peter Jezzard, et al. Identifying the ischaemic penumbra using ph-weighted magnetic resonance imaging. *Brain*, 138(1):36–42, 2014.

[66] Stefanie J C G Hectors, Igor Jacobs, Gustav J Strijkers, and Klaas Nicolay. Amide proton transfer imaging of high intensity focused ultrasound-treated tumor tissue. *Magnetic resonance in medicine*, 72:1113–1122, October 2014. ISSN 1522-2594. doi: 10.1002/mrm.25000.

[67] Hye-Young Heo, Craig K Jones, Jun Hua, Nirbhay Yadav, Shruti Agarwal, Jinyuan Zhou, Peter van Zijl, and Jay J Pillai. Whole-brain amide proton transfer (apt) and nuclear overhauser enhancement (noe) imaging in glioma patients using low-power steady-state pulsed chemical exchange saturation transfer (cest) imaging at 7t. *Journal of Magnetic Resonance Imaging*, 44(1):41–50, 2016.

[68] Hye-Young Heo, Yi Zhang, Shanshan Jiang, Dong-Hoon Lee, and Jinyuan Zhou. Quantitative assessment of amide proton transfer (apt) and nuclear overhauser

enhancement (noe) imaging with extrapolated semisolid magnetization transfer reference (emr) signals: Ii. comparison of three emr models and application to human brain glioma at 3 tesla. *Magnetic resonance in medicine*, 75(4):1630–1639, 2016.

[69] Hye-Young Heo, Yi Zhang, Dong-Hoon Lee, Xiaohua Hong, and Jinyuan Zhou. Quantitative assessment of amide proton transfer (apt) and nuclear overhauser enhancement (noe) imaging with extrapolated semi-solid magnetization transfer reference (emr) signals: Application to a rat glioma model at 4.7 tesla. *Magnetic resonance in medicine*, 75(1):137–149, 2016.

[70] A I Holodny, A O Nusbaum, S Festa, I N Pronin, H J Lee, and A J Kalnin. Correlation between the degree of contrast enhancement and the volume of peritumoral edema in meningiomas and malignant gliomas. *Neuroradiology*, 41: 820–825, November 1999. ISSN 0028-3940. doi: 10.1007/s002340050848.

[71] R Hourani, LJ Brant, T Rizk, Jon David Weingart, Peter B Barker, and Alena Horská. Can proton mr spectroscopic and perfusion imaging differentiate between neoplastic and nonneoplastic brain lesions in adults? *American Journal of Neuroradiology*, 29(2):366–372, 2008.

[72] Roula Hourani, Alena Horská, Sait Albayram, Larry J Brant, Elias Melhem, Kenneth J Cohen, Peter C Burger, John D Weingart, Benjamin Carson, Moody D Wharam, et al. Proton magnetic resonance spectroscopic imaging to differentiate between nonneoplastic lesions and brain tumors in children. *Journal of Magnetic Resonance Imaging: An Official Journal of the International Society for Magnetic Resonance in Medicine*, 23(2):99–107, 2006.

[73] FA Howe, SJ Barton, SA Cudlip, M Stubbs, DE Saunders, M Murphy, P Wilkins, KS Opstad, VL Doyle, MA McLean, et al. Metabolic profiles of human brain tu-

mors using quantitative in vivo 1h magnetic resonance spectroscopy. *Magnetic resonance in medicine*, 49(2):223–232, 2003.

[74] https://www.nottingham.ac.uk/magres/research/magnetic-resonance spectroscopy.aspx.

[75] Simon Hu. "compressed sensing for resolution enhancement of hyperpolarized 13 c flyback 3d-mrsi.". *Journal of magnetic resonance 192.2 : 258-264.*, 2008.

[76] Jun Hua, Craig K Jones, Jaishri Blakeley, Seth A Smith, Peter C M van Zijl, and Jinyuan Zhou. Quantitative description of the asymmetry in magnetization transfer effects around the water resonance in the human brain. *Magnetic resonance in medicine*, 58:786–793, October 2007. ISSN 0740-3194. doi: 10.1002/mrm.21387.

[77] Mark Jenkinson, Peter Bannister, Michael Brady, and Stephen Smith. Improved optimization for the robust and accurate linear registration and motion correction of brain images. *Neuroimage*, 17(2):825–841, Oct 2002.

[78] Peter Jezzard. Shim coil design, limitations and implications. *ISMRM*, 2006.

[79] Guang Jia, Ronney Abaza, JoAnna D Williams, Debra L Zynger, Jinyuan Zhou, Zarine K Shah, Mitva Patel, Steffen Sammet, Lai Wei, Robert R Bahnson, and Michael V Knopp. Amide proton transfer mr imaging of prostate cancer: a preliminary study. *Journal of magnetic resonance imaging : JMRI*, 33:647–654, March 2011. ISSN 1522-2586. doi: 10.1002/jmri.22480.

[80] Shanshan Jiang, Hao Yu, Xianlong Wang, Shilong Lu, Yufa Li, Lyujin Feng, Yi Zhang, Hye-Young Heo, Dong-Hoon Lee, Jinyuan Zhou, and Zhibo Wen. Molecular mri differentiation between primary central nervous system lymphomas and high-grade gliomas using endogenous protein-based amide proton transfer

mr imaging at 3 tesla. *European radiology*, 26:64–71, January 2016. ISSN 1432-1084. doi: 10.1007/s00330-015-3805-1.

[81] Tao Jin and Seong-Gi Kim. In vivo saturation transfer imaging of nuclear overhauser effect from aromatic and aliphatic protons: implication to apt quantification. In *Proceedings of the 21st Annual Meeting ISMRM*, 2013.

[82] Tao Jin and Seong-Gi Kim. Advantages of chemical exchange-sensitive spin-lock (cesl) over chemical exchange saturation transfer (cest) for hydroxyl–and amine–water proton exchange studies. *NMR in biomedicine*, 27(11):1313–1324, 2014.

[83] Tao Jin, Ping Wang, Xiaopeng Zong, and Seong-Gi Kim. Magnetic resonance imaging of the amine–proton exchange (apex) dependent contrast. *Neuroimage*, 59(2):1218–1227, 2012.

[84] Tao Jin, Ping Wang, Xiaopeng Zong, and Seong-Gi Kim. Mr imaging of the amide-proton transfer effect and the ph-insensitive nuclear overhauser effect at 9.4 t. *Magn Reson Med*, 69(3):760–770, Mar 2013. doi: 10.1002/mrm.24315. URL `http://dx.doi.org/10.1002/mrm.24315`.

[85] Tao Jin, Ping Wang, Xiaopeng Zong, and Seong-Gi Kim. Mr imaging of the amide-proton transfer effect and the ph-insensitive nuclear overhauser effect at 9.4 t. *Magnetic resonance in medicine*, 69:760–770, March 2013. ISSN 1522-2594. doi: 10.1002/mrm.24315.

[86] Tao Jin, Hunter Mehrens, Kristy S Hendrich, and Seong-Gi Kim. Mapping brain glucose uptake with chemical exchange-sensitive spin-lock magnetic resonance imaging. *Journal of Cerebral Blood Flow & Metabolism*, 34(8):1402–1410, 2014.

[87] Kimmo T Jokivarsi, Heidi I Gröhn, Olli H Gröhn, and Risto A Kauppinen. Proton

transfer ratio, lactate, and intracellular ph in acute cerebral ischemia. *Magnetic resonance in medicine*, 57(4):647–653, 2007.

[88] Craig K. Jones, Michael J. Schlosser, Peter C M. van Zijl, Martin G. Pomper, Xavier Golay, and Jinyuan Zhou. Amide proton transfer imaging of human brain tumors at 3t. *Magn Reson Med*, 56(3):585–592, Sep 2006. doi: 10.1002/mrm.20989. URL `http://dx.doi.org/10.1002/mrm.20989`.

[89] Craig K Jones, Daniel Polders, Jun Hua, He Zhu, Hans J Hoogduin, Jinyuan Zhou, Peter Luijten, and Peter van Zijl. In vivo three-dimensional whole-brain pulsed steady-state chemical exchange saturation transfer at 7 t. *Magnetic resonance in medicine*, 67(6):1579–1589, 2012.

[90] Craig K Jones, Alan Huang, Jiadi Xu, Richard AE Edden, Michael Schär, Jun Hua, Nikita Oskolkov, Domenico Zacà, Jinyuan Zhou, Michael T McMahon, et al. Nuclear overhauser enhancement (noe) imaging in the human brain at 7t. *Neuroimage*, 77:114–124, 2013.

[91] Kyle M. Jones. "clinical translation of tumor acidosis measurements with acidocest mri.". *Molecular Imaging and Biology 19.4: 617-625.*, 2017.

[92] Christoph Juchem, Bernd Muller-Bierl, Fritz Schick, Nikos K Logothetis, and Josef Pfeuffer. Combined passive and active shimming for in vivo mr spectroscopy at high magnetic fields. *Journal of magnetic resonance*, 183(2):278–289, 2006.

[93] Christoph Juchem, Terence W Nixon, Scott McIntyre, Douglas L Rothman, and Robin A de Graaf. Magnetic field homogenization of the human prefrontal cortex with a set of localized electrical coils. *Magnetic Resonance in Medicine: An Official Journal of the International Society for Magnetic Resonance in Medicine*, 63(1):171–180, 2010.

[94] Christoph Juchem, Terence W Nixon, Scott McIntyre, Vincent O Boer, Douglas L Rothman, and Robin A de Graaf. Dynamic multi-coil shimming of the human brain at 7 t. *Journal of magnetic resonance (San Diego, Calif. : 1997)*, 212:280–288, October 2011. ISSN 1096-0856. doi: 10.1016/j.jmr.2011.07.005.

[95] Christoph Juchem, S Umesh Rudrapatna, Terence W Nixon, and Robin A de Graaf. Dynamic multi-coil technique (dynamite) shimming for echo-planar imaging of the human brain at 7 tesla. *Neuroimage*, 105:462–472, 2015.

[96] Cristoph Juchem. Shimming: Fields, coils and control. *ISMRM*, 2013.

[97] Murase K. Numerical analysis of the magnetization behavior in magnetic resonance imaging in the presence of multiple chemical exchange pools. *Open Journal of Applied Sciences , 7, 1-14.*, 2017.

[98] Hung-Wen Kao, Shih-Wei Chiang, Hsiao-Wen Chung, Fong Y Tsai, and Cheng-Yu Chen. Advanced mr imaging of gliomas: an update. *BioMed research international*, 2013:970586, 2013. ISSN 2314-6141. doi: 10.1155/2013/970586.

[99] Jinsuh Kim, Yin Wu, Yingkun Guo, Hairong Zheng, and Phillip Zhe Sun. A review of optimization and quantification techniques for chemical exchange saturation transfer mri toward sensitive in vivo imaging. *Contrast media & molecular imaging*, 10(3):163–178, 2015.

[100] Mina Kim, Joseph Gillen, Bennett A. Landman, Jinyuan Zhou, and Peter C M. van Zijl. Water saturation shift referencing (wassr) for chemical exchange saturation transfer (cest) experiments. *Magn Reson Med*, 61(6):1441–1450, Jun 2009. doi: 10.1002/mrm.21873. URL `http://dx.doi.org/10.1002/mrm.21873`.

[101] Dennis W J Klomp, Adrienne N Dula, Lori R Arlinghaus, Michel Italiaander, Richard D Dortch, Zhongliang Zu, Jason M Williams, Daniel F Gochberg, Peter R Luijten, John C Gore, Thomas E Yankeelov, and Seth A Smith. Amide proton

transfer imaging of the human breast at 7t: development and reproducibility. *NMR in biomedicine*, 26:1271–1277, October 2013. ISSN 1099-1492. doi: 10.1002/nbm.2947.

[102] KM Koch, Brown PB, Rothman DL, and RA de Graaf. Dynamically shimmed multivoxel 1h magnetic resonance spectroscopy and multislice magnetic resonance spectroscopic imaging of the human brain. *J Magn Reson 182*, 66-74 2006.

[103] R.D. Koenig, S.H. & Brown. A molecular theory of relaxation and magnetization transfer: application to cross-linked bsa, a model for tissue. *Magnetic Resonance in Medicine 30, 685-95*, 1993.

[104] S.H Koenig. Classes of hydration sites at protein-water interfaces: the source of contrast in magnetic resonance imaging. *Biophysical journal 69, 593-603*, 1995.

[105] R. Koenig S.H. Brown, R.D. & Ugolini. A unified view of relaxation in protein solutions and tissue, including hydration and magnetization transfer. *Magnetic Resonance in Medicine 29, 77-83*, 1993.

[106] Feliks Kogan, Hari Hariharan, and Ravinder Reddy. Chemical exchange saturation transfer (cest) imaging: description of technique and potential clinical applications. *Current radiology reports*, 1(2):102–114, 2013.

[107] Feliks Kogan, Anup Singh, Catherine Debrosse, Mohammad Haris, Kejia Cai, Ravi Prakash Nanga, Mark Elliott, Hari Hariharan, and Ravinder Reddy. Imaging of glutamate in the spinal cord using glucest. *Neuroimage*, 77:262–267, 2013.

[108] Feliks Kogan, Mohammad Haris, Anup Singh, Kejia Cai, Catherine Debrosse, Ravi Prakash Reddy Nanga, Hari Hariharan, and Ravinder Reddy. Method for high-resolution imaging of creatine in vivo using chemical exchange saturation transfer. *Magnetic resonance in medicine*, 71(1):164–172, 2014.

[109] Guruprasad Krishnamoorthy, Ravi Prakash Reddy Nanga, Puneet Bagga, Hari Hariharan, and Ravinder Reddy. High quality three-dimensional gagcest imaging of in vivo human knee cartilage at 7 tesla. *Magnetic resonance in medicine*, 77(5):1866–1873, 2017.

[110] Stefan Kroboth, Kelvin J Layton, Feng Jia, Sebastian Littin, Huijun Yu, Jurgen Hennig, and Maxim Zaitsev. Optimization of coil element configurations for a matrix gradient coil. *IEEE transactions on medical imaging*, 37:284–292, January 2018. ISSN 1558-254X. doi: 10.1109/TMI.2017.2743463.

[111] Stefan Kroboth, Kelvin J Layton, Feng Jia, Sebastian Littin, Huijun Yu, JÃŒrgen Hennig, and Maxim Zaitsev. Switching circuit optimization for matrix gradient coils. *Tomography (Ann Arbor, Mich.)*, 5:248–259, June 2019. ISSN 2379-139X. doi: 10.18383/j.tom.2018.00056.

[112] A J Kumar, N E Leeds, G N Fuller, P Van Tassel, M H Maor, R E Sawaya, and V A Levin. Malignant gliomas: Mr imaging spectrum of radiation therapy- and chemotherapy-induced necrosis of the brain after treatment. *Radiology*, 217:377–384, November 2000. ISSN 0033-8419. doi: 10.1148/radiology.217.2.r00nv36377.

[113] Stefan Lang, Niall Duncan, and Georg Northoff. Resting-state functional magnetic resonance imaging: review of neurosurgical applications. *Neurosurgery*, 74(5):453–465, 2014.

[114] Seung-Cheol Lee, Ming Q Huang, David S Nelson, Stephen Pickup, Suzanne Wehrli, Onikepe Adegbola, Harish Poptani, Edward J Delikatny, and Jerry D Glickson. In vivo mrs markers of response to chop chemotherapy in the wsu-dlcl2 human diffuse large b-cell lymphoma xenograft. *NMR in biomedicine*, 21 (7):723–733, 2008.

[115] Alex X Li, Robert H E Hudson, John W Barrett, Craig K Jones, Stephen H Pasternak, and Robert Bartha. Four-pool modeling of proton exchange processes in biological systems in the presence of mri-paramagnetic chemical exchange saturation transfer (paracest) agents. *Magnetic resonance in medicine*, 60:1197–1206, November 2008. ISSN 1522-2594. doi: 10.1002/mrm.21752.

[116] Alex X Li, Robert HE Hudson, John W Barrett, Craig K Jones, Stephen H Pasternak, and Robert Bartha. Four-pool modeling of proton exchange processes in biological systems in the presence of mri–paramagnetic chemical exchange saturation transfer (paracest) agents. *Magnetic resonance in medicine*, 60(5):1197–1206, 2008.

[117] Chunmei Li, Shuai Peng, Rui Wang, Haibo Chen, Wen Su, Xuna Zhao, Jinyuan Zhou, and Min Chen. Chemical exchange saturation transfer mr imaging of parkinson's disease at 3 tesla. *European radiology*, 24:2631–2639, October 2014. ISSN 1432-1084. doi: 10.1007/s00330-014-3241-7.

[118] Chunmei Li, Rui Wang, Haibo Chen, Wen Su, Shuhua Li, Xuna Zhao, Jinyuan Zhou, Jian Qiao, Baohui Lou, Guodong Song, and Min Chen. Chemical exchange saturation transfer mr imaging is superior to diffusion-tensor imaging in the diagnosis and severity evaluation of parkinson's disease: A study on substantia nigra and striatum. *Frontiers in aging neuroscience*, 7:198, 2015. ISSN 1663-4365. doi: 10.3389/fnagi.2015.00198.

[119] Chunmei Li, Min Chen, Xuna Zhao, Rui Wang, Haibo Chen, Wen Su, Shuhua Li, Baohui Lou, Guodong Song, Shuai Zhang, Jintao Zhang, and Jinyuan Zhou. Chemical exchange saturation transfer mri signal loss of the substantia nigra as an imaging biomarker to evaluate the diagnosis and severity of parkinson's disease. *Frontiers in neuroscience*, 11:489, 2017. ISSN 1662-4548. doi: 10.3389/fnins.2017.00489.

[120] Hua Li, Zhongliang Zu, Moritz Zaiss, Imad S Khan, Robert J Singer, Daniel F Gochberg, Peter Bachert, John C Gore, and Junzhong Xu. Imaging of amide proton transfer and nuclear overhauser enhancement in ischemic stroke with corrections for competing effects. *NMR in biomedicine*, 28:200–209, February 2015. ISSN 1099-1492. doi: 10.1002/nbm.3243.

[121] E Liepinsh and G Otting. Proton exchange rates from amino acid side chains–implications for image contrast. *Magnetic resonance in medicine*, 35:30–42, January 1996. ISSN 0740-3194.

[122] Wen Ling, Ravinder R. Regatte, Gil Navon, and Alexej Jerschow. Assessment of glycosaminoglycan concentration in vivo by chemical exchange-dependent saturation transfer (gagcest). *Proc Natl Acad Sci U S A*, 105(7):2266–2270, Feb 2008. doi: 10.1073/pnas.0707666105. URL `http://dx.doi.org/10.1073/pnas.0707666105`.

[123] Dapeng Liu, Jinyuan Zhou, Rong Xue, Zhentao Zuo, Jing An, and Danny JJ Wang. Quantitative characterization of nuclear overhauser enhancement and amide proton transfer effects in the human brain at 7 tesla. *Magnetic resonance in medicine*, 70(4):1070–1081, 2013.

[124] Guanshu Liu, M Meser Ali, Byunghee Yoo, Mark A Griswold, Jean A Tkach, and Mark D Pagel. Paracest mri with improved temporal resolution. *Magnetic resonance in medicine*, 61(2):399–408, 2009.

[125] Guanshu Liu, Matthew Moake, Yah-el Har-el, Chris M Long, Kannie W Y Chan, Amanda Cardona, Muksit Jamil, Piotr Walczak, Assaf A Gilad, George Sgouros, Peter C M van Zijl, Jeff W M Bulte, and Michael T McMahon. In vivo multicolor molecular mr imaging using diamagnetic chemical exchange saturation transfer liposomes. *Magnetic resonance in medicine*, 67:1106–1113, April 2012. ISSN 1522-2594. doi: 10.1002/mrm.23100.

[126] Nikos K Logothetis and Josef Pfeuffer. On the nature of the bold fmri contrast mechanism. *Magnetic resonance imaging*, 22(10):1517–1531, 2004.

[127] Dario L. Longo, Phillip Zhe Sun, Lorena Consolino, Filippo C. Michelotti, Fulvio Uggeri, and Silvio Aime. A general mri-cest ratiometric approach for ph imaging: demonstration of in vivo ph mapping with iobitridol. *J Am Chem Soc*, 136 (41):14333–14336, Oct 2014. doi: 10.1021/ja5059313. URL `http://dx.doi.org/10.1021/ja5059313`.

[128] Dario Livio Longo. "exci-cest: Exploiting pharmaceutical excipients as mri-cest contrast agents for tumor imaging.". *International Journal of Pharmaceutics 525.1 275-281.*, 2017.

[129] Dario Livio Longo, Walter Dastru, Giuseppe Digilio, Jochen Keupp, Sander Langereis, Stefania Lanzardo, Simone Prestigio, Oliver Steinbach, Enzo Terreno, Fulvio Uggeri, and Silvio Aime. Iopamidol as a responsive mri-chemical exchange saturation transfer contrast agent for ph mapping of kidneys: In vivo studies in mice at 7 t. *Magn Reson Med*, 65(1):202–211, Jan 2011. doi: 10.1002/mrm.22608. URL `http://dx.doi.org/10.1002/mrm.22608`.

[130] Jianhua Lu, Jinyuan Zhou, Congbo Cai, Shuhui Cai, and Zhong Chen. Observation of true and pseudo noe signals using cest-mri and cest-mrs sequences with and without lipid suppression. *Magnetic resonance in medicine*, 73(4):1615–1622, 2015.

[131] Michael Lustig, David Donoho, and John M Pauly. Sparse mri: The application of compressed sensing for rapid mr imaging. *Magnetic resonance in medicine*, 58 (6):1182–1195, 2007.

[132] Bo Ma, Jaishri O Blakeley, Xiaohua Hong, Hongyan Zhang, Shanshan Jiang, Lindsay Blair, Yi Zhang, Hye-Young Heo, Mingzhi Zhang, Peter van Zijl, et al. Applying amide proton transfer-weighted mri to distinguish pseudoprogression

from true progression in malignant gliomas. *Journal of Magnetic Resonance Imaging*, 44(2):456–462, 2016.

[133] M. A. Macri. "regional changes in the metabolite profile after long-term hypoxia-ischemia in brains of young and aged rats: a quantitative proton mrs study." . *Neurobiology of aging,27, 98-104*, 2006.

[134] Harden M McConnell. Reaction rates by nuclear magnetic resonance. *The Journal of chemical physics*, 28(3):430–431, 1958.

[135] Harden M. McConnell and Don D. Thompson. Molecular transfer of non equilibrium nuclear spin magnetization. *J. Chem. Phys*, 31:85, 1959.

[136] G McGibney, MR Smith, ST Nichols, and A Crawley. Quantitative evaluation of several partial fourier reconstruction algorithms used in mri. *Magnetic resonance in medicine*, 30(1):51–59, 1993.

[137] Michael T McMahon, Assaf A Gilad, Jinyuan Zhou, Phillip Z Sun, Jeff WM Bulte, and Peter van Zijl. Quantifying exchange rates in chemical exchange saturation transfer agents using the saturation time and saturation power dependencies of the magnetization transfer effect on the magnetic resonance imaging signal (quest and quesp): ph calibration for poly-l-lysine and a starburst dendrimer. *Magnetic resonance in medicine*, 55(4):836–847, 2006.

[138] Nevin McVicar, Alex X. Li, Daniela F. GonÃ§alves, Miranda Bellyou, Susan O. Meakin, Marco Am Prado, and Robert Bartha. Quantitative tissue ph measurement during cerebral ischemia using amine and amide concentration-independent detection (aacid) with mri. *J Cereb Blood Flow Metab*, 34(4):690–698, Apr 2014. doi: 10.1038/jcbfm.2014.12. URL `http://dx.doi.org/10.1038/jcbfm.2014.12`.

[139] Anja MÃŒller-Lutz, Nadia Khalil, Benjamin Schmitt, Vladimir Jellus, Gael

Pentang, Georg Oeltzschner, Gerald Antoch, Rotem S. Lanzman, and Hans-JÃ¶rg Wittsack. Pilot study of iopamidol-based quantitative ph imaging on a clinical 3t mr scanner. *MAGMA*, 27(6):477–485, Dec 2014. doi: 10.1007/s10334-014-0433-8. URL http://dx.doi.org/10.1007/s10334-014-0433-8.

[140] Ravinder Reddy Mohammad Haris Kejia Cai Anup Singh Ravi Prakash Reddy Nanga Damodar Reddy Hari Hariharan. Detection of exercised induced changes in creatine level in human calf muscles through cest: A preliminary study. *Proc. Intl. Soc. Mag. Reson. Med. 20*, 2012.

[141] Glen Morrell and Daniel Spielman. Dynamic shimming for multi-slice magnetic resonance imaging. *Magnetic Resonance in Medicine*, 38:477-483:1997.

[142] Clare Morrison and R Mark Henkelman. A model for magnetization transfer in tissues. *Magnetic resonance in medicine*, 33(4):475–482, 1995.

[143] ME Moseley, Y Cohen, J Mintorovitch, L Chileuitt, H Shimizu, J Kucharczyk, MF Wendland, and PR Weinstein. Early detection of regional cerebral ischemia in cats: comparison of diffusion-and t2-weighted mri and spectroscopy. *Magnetic resonance in medicine*, 14(2):330–346, 1990.

[144] O. Mougin. Quantitative methods in high field mri, 2010.

[145] O. E. Mougin, R. C. Coxon, A. Pitiot, and P. A. Gowland. Magnetization transfer phenomenon in the human brain at 7 t. *Neuroimage*, 49(1):272–281, Jan 2010. doi: 10.1016/j.neuroimage.2009.08.022. URL http://dx.doi.org/10.1016/j.neuroimage.2009.08.022.

[146] Tanki N Murase K. Numerical solutions to the time-dependent bloch equations revisited. *Magn Reson Imaging.29(1):126-31*, 2011.

[147] Fatima A Nasrallah, Guilhem Pagès, Philip W Kuchel, Xavier Golay, and Kai-Hsiang Chuang. Imaging brain deoxyglucose uptake and metabolism by glucocest mri. *Journal of Cerebral Blood Flow & Metabolism*, 33(8):1270–1278, 2013.

[148] Sarah J Nelson. Assessment of therapeutic response and treatment planning for brain tumors using metabolic and physiological mri. *NMR in biomedicine*, 24(6): 734–749, 2011.

[149] Moriel NessAiver. *All you need to know about MRI physics*. Simply Physics, 1997.

[150] Dwight George Nishimura. *Principles of magnetic resonance imaging*. Stanford University, 1996.

[151] James P B O'Connor, Eric O Aboagye, Judith E Adams, Hugo J W L Aerts, Sally F Barrington, Ambros J Beer, Ronald Boellaard, Sarah E Bohndiek, Michael Brady, Gina Brown, David L Buckley, Thomas L Chenevert, Laurence P Clarke, Sandra Collette, Gary J Cook, Nandita M deSouza, John C Dickson, Caroline Dive, Jeffrey L Evelhoch, Corinne Faivre-Finn, Ferdia A Gallagher, Fiona J Gilbert, Robert J Gillies, Vicky Goh, John R Griffiths, Ashley M Groves, Steve Halligan, Adrian L Harris, David J Hawkes, Otto S Hoekstra, Erich P Huang, Brian F Hutton, Edward F Jackson, Gordon C Jayson, Andrew Jones, Dow-Mu Koh, Denis Lacombe, Philippe Lambin, Nathalie Lassau, Martin O Leach, Ting-Yim Lee, Edward L Leen, Jason S Lewis, Yan Liu, Mark F Lythgoe, Prakash Manoharan, Ross J Maxwell, Kenneth A Miles, Bruno Morgan, Steve Morris, Tony Ng, Anwar R Padhani, Geoff J M Parker, Mike Partridge, Arvind P Pathak, Andrew C Peet, Shonit Punwani, Andrew R Reynolds, Simon P Robinson, Lalitha K Shankar, Ricky A Sharma, Dmitry Soloviev, Sigrid Stroobants, Daniel C Sullivan, Stuart A Taylor, Paul S Tofts, Gillian M Tozer, Marcel van Herk, Simon Walker-Samuel, James Wason, Kaye J Williams, Paul Workman, Thomas E Yankeelov, Kevin M Brindle, Lisa M McShane, Alan Jackson, and John C Waterton. Ima-

ging biomarker roadmap for cancer studies. *Nature reviews. Clinical oncology*, 14:169–186, March 2017. ISSN 1759-4782. doi: 10.1038/nrclinonc.2016.162.

[152] G. Otting. Protein hydration viewed by high-resolution nmr spectroscopy: Implications for magnetic resonance image contrast. *Acc. Chem. Res,28, 171-177*, 1995.

[153] Daniel Paech, Moritz Zaiss, Jan-Eric Meissner, Johannes Windschuh, Benedikt Wiestler, Peter Bachert, Jan Oliver Neumann, Philipp Kickingereder, Heinz-Peter Schlemmer, Wolfgang Wick, et al. Nuclear overhauser enhancement mediated chemical exchange saturation transfer imaging at 7 tesla in glioblastoma patients. *PLoS One*, 9(8):e104181, 2014.

[154] Daniel Paech, Sina Burth, Johannes Windschuh, Jan-Eric Meissner, Moritz Zaiss, Oliver Eidel, Philipp Kickingereder, Martha Nowosielski, Benedikt Wiestler, Felix Sahm, et al. Nuclear overhauser enhancement imaging of glioblastoma at 7 tesla: region specific correlation with apparent diffusion coefficient and histology. *PloS one*, 10(3):e0121220, 2015.

[155] Kye Jin Park, Ho Sung Kim, Ji Eun Park, Woo Hyun Shim, Sang Joon Kim, and Seth A Smith. Added value of amide proton transfer imaging to conventional and perfusion mr imaging for evaluating the treatment response of newly diagnosed glioblastoma. *European radiology*, 26(12):4390–4403, 2016.

[156] JA Pikkemaat, RT Wegh, R Lamerichs, RA Van de Molengraaf, S Langereis, D Burdinski, AYF Raymond, HM Janssen, BFM De Waal, NP Willard, et al. Dendritic paracest contrast agents for magnetic resonance imaging. *Contrast media & molecular imaging*, 2(5):229–239, 2007.

[157] Martin G Pomper and John D Port. New techniques in mr imaging of brain tumors. *Magnetic resonance imaging clinics of North America*, 8(4):691–713, 2000.

[158] Edward A. Randtke. "multislice cest mri improves the spatial assessment of tumor ph.". *Magnetic resonance in medicine 78.1 : 97-106.*, 2017.

[159] Edward A Randtke, Liu Qi Chen, L Rene Corrales, and Mark D Pagel. The hanes-woolf linear quesp method improves the measurements of fast chemical exchange rates with cest mri. *Magnetic resonance in medicine*, 71:1603–1612, April 2014. ISSN 1522-2594. doi: 10.1002/mrm.24792.

[160] Henkelman RM, Huang X, Xiang QS, Stanisz GJ, Swanson SD, and Bronskill MJ. Quantitative interpretation of magnetization transfer. *Magn. Reson. Med. 29: 759-766.*, 1993.

[161] Brian D Ross, Robert J Higgins, James E Boggan, Brian Knitteln, and Michael Garwood. 31p nmr spectroscopy of the in vivo metabolism of an intracerebral glioma in the rat. *Magnetic resonance in medicine*, 6(4):403–417, 1988.

[162] Koji Sagiyama, Tomoyuki Mashimo, Osamu Togao, Vamsidhara Vemireddy, Kimmo J Hatanpaa, Elizabeth A Maher, Bruce E Mickey, Edward Pan, A Dean Sherry, Robert M Bachoo, et al. In vivo chemical exchange saturation transfer imaging allows early detection of a therapeutic response in glioblastoma. *Proceedings of the National Academy of Sciences*, 111(12):4542–4547, 2014.

[163] Sengupta Saikat, Welch E. Brian, Zhao Yansong, Foxall David, Starewicz Piotr, Anderson Adam, Gorea John, and Malcolm J Avison. Dynamic b0 shimming at 7 tesla. *Magn Reson Imaging.*, 29(4): 483, 2011.

[164] Akihiko Sakata, Tomohisa Okada, Akira Yamamoto, Mitsunori Kanagaki, Yasutaka Fushimi, Tsutomu Okada, Toshiki Dodo, Yoshiki Arakawa, Benjamin Schmitt, Susumu Miyamoto, et al. Grading glial tumors with amide proton transfer mr imaging: different analytical approaches. *Journal of neuro-oncology*, 122 (2):339–348, 2015.

[165] Amandeep Salhotra, Bachchu Lal, John Laterra, Phillip Zhe Sun, Peter C M. van Zijl, and Jinyuan Zhou. Amide proton transfer imaging of 9l gliosarcoma and human glioblastoma xenografts. *NMR Biomed*, 21(5):489–497, Jun 2008. doi: 10.1002/nbm.1216. URL http://dx.doi.org/10.1002/nbm.1216.

[166] Kohei Sano, Takahito Nakajima, Peter L Choyke, and Hisataka Kobayashi. Markedly enhanced permeability and retention effects induced by photoimmunotherapy of tumors. *ACS nano*, 7(1):717–724, 2012.

[167] Rachel Scheidegger, Elena Vinogradov, and David C Alsop. Amide proton transfer imaging with improved robustness to magnetic field inhomogeneity and magnetization transfer asymmetry using saturation with frequency alternating rf irradiation. *Magnetic resonance in medicine*, 66(5):1275–1285, 2011.

[168] Rachel Scheidegger, Eric T. Wong, and David C. Alsop. Contributors to contrast between glioma and brain tissue in chemical exchange saturation transfer sensitive imaging at 3 tesla. *Neuroimage*, 99:256–268, Oct 2014. doi: 10.1016/j.neuroimage.2014.05.036. URL http://dx.doi.org/10.1016/j.neuroimage.2014.05.036.

[169] Christoph Schleich, Anja Müller-Lutz, Lisa Zimmermann, Johannes Boos, Benjamin Schmitt, Hans-Jörg Wittsack, Gerald Antoch, and Falk Miese. Biochemical imaging of cervical intervertebral discs with glycosaminoglycan chemical exchange saturation transfer magnetic resonance imaging: feasibility and initial results. *Skeletal radiology*, 45(1):79–85, 2016.

[170] Benjamin Schmitt, Moritz Zaiss, Jinyuan Zhou, and Peter Bachert. Optimization of pulse train presaturation for cest imaging in clinical scanners. *Magn Reson Med*, 65(6):1620–1629, Jun 2011. doi: 10.1002/mrm.22750. URL http://dx.doi.org/10.1002/mrm.22750.

[171] JN Scott, PMA Brasher, RJ Sevick, NB Rewcastle, and PA Forsyth. How often are nonenhancing supratentorial gliomas malignant? a population study. *Neurology*, 59(6):947–949, 2002.

[172] T. Shah, L. Lu, K. M. Dell, M. D. Pagel, M. A. Griswold, and C. A. Flask. Cest-fisp: a novel technique for rapid chemical exchange saturation transfer mri at 7 t. *Magn Reson Med*, 65(2):432–437, Feb 20042011. doi: 10.1002/mrm.22637. URL http://dx.doi.org/10.1002/mrm.22637.

[173] Jun Shen. Preserving the excitation profile of small flip angle rf pulses in the presence of rapid transverse relaxation. *Journal of Magnetic Resonance*, 224: 8–12, 2012.

[174] Anup Singh, Mohammad Haris, Kejia Cai, Victor B Kassey, Feliks Kogan, Damodar Reddy, Hari Hariharan, and Ravinder Reddy. Chemical exchange saturation transfer magnetic resonance imaging of human knee cartilage at 3 t and 7 t. *Magnetic resonance in medicine*, 68(2):588–594, 2012.

[175] Karim Snoussi, Jeff W M. Bulte, Maurice GuÃ©ron, and Peter C M. van Zijl. Sensitive cest agents based on nucleic acid imino proton exchange: detection of poly(ru) and of a dendrimer-poly(ru) model for nucleic acid delivery and pharmacology. *Magn Reson Med*, 49(6):998–1005, Jun 2003. doi: 10.1002/mrm.10463. URL http://dx.doi.org/10.1002/mrm.10463.

[176] DP Soares and M Law. Magnetic resonance spectroscopy of the brain: review of metabolites and clinical applications. *Clinical radiology*, 64(1):12–21, 2009.

[177] Chang W Song, HeonJoo Park, and Brian D Ross. Intra-and extracellular ph in solid tumors. In *Antiangiogenic agents in cancer therapy*, pages 51–64. Springer, 1999.

[178] Guodong Song, Chunmei Li, Xiaojie Luo, Xuna Zhao, Shuai Zhang, Yi Zhang,

Shanshan Jiang, Xianlong Wang, Yuhui Chen, Haibo Chen, Tao Gong, Jinyuan Zhou, and Min Chen. Evolution of cerebral ischemia assessed by amide proton transfer-weighted mri. *Frontiers in neurology*, 8:67, 2017. ISSN 1664-2295. doi: 10.3389/fneur.2017.00067.

[179] D. F. HillenbrandK. M. LoW. F. B. PunchardT. G. ReeseP. M. Starewicz. High-order mr shimming: a simulation study of the effectiveness of competing methods, using an established susceptibility model of the human head. *Applied Magnetic Resonance, 29(1): 39*, 2005.

[180] Jason P Stockmann, Thomas Witzel, Boris Keil, Jonathan R Polimeni, Azma Mareyam, Cristen LaPierre, Kawin Setsompop, and Lawrence L Wald. A 32-channel combined rf and b0 shim array for 3t brain imaging. *Magnetic resonance in medicine*, 75:441–451, January 2016. ISSN 1522-2594. doi: 10.1002/mrm.25587.

[181] A. S. Stodolna, A. Rouzee, F. Lepine, S. Cohen, F. Robicheaux, A. Gijsbertsen, J. H. Jungmann, C. Bordas, and M J J. Vrakking. Hydrogen atoms under magnification: direct observation of the nodal structure of stark states. *Phys Rev Lett*, 110(21):213001, May 2013. doi: 10.1103/PhysRevLett.110.213001. URL `http://dx.doi.org/10.1103/PhysRevLett.110.213001`.

[182] M. Stubbs, Z. M. Bhujwalla, G. M. Tozer, L. M. Rodrigues, R. J. Maxwell, R. Morgan, F. A. Howe, and J. R. Griffiths. An assessment of 31p mrs as a method of measuring ph in rat tumours. *NMR Biomed*, 5(6):351–359, 1992.

[183] Phillip Zhe Sun. Simplified and scalable numerical solution for describing multi-pool chemical exchange saturation transfer (cest) mri contrast. *Journal of magnetic resonance (San Diego, Calif. : 1997)*, 205:235–241, August 2010. ISSN 1096-0856. doi: 10.1016/j.jmr.2010.05.004.

[184] Phillip Zhe Sun. Simultaneous determination of labile proton concentration and exchange rate utilizing optimal rf power: radio frequency power (rfp) depend-

ence of chemical exchange saturation transfer (cest) mri. *Journal of magnetic resonance*, 202(2):155–161, 2010.

[185] Phillip Zhe Sun. Simplified quantification of labile proton concentration-weighted chemical exchange rate (kws) with rf saturation time dependent ratiometric analysis (questra): Normalization of relaxation and rf irradiation spillover effects for improved quantitative chemical exchange saturation transfer (cest) mri. *Magnetic resonance in medicine*, 67(4):936–942, 2012.

[186] Phillip Zhe Sun. "a method for accurate ph mapping with chemical exchange saturation transfer (cest) mri.". *Contrast media & molecular imaging 11.3 : 195-202.*, 2016.

[187] Phillip Zhe Sun and A Gregory Sorensen. Imaging ph using the chemical exchange saturation transfer (cest) mri: correction of concomitant rf irradiation effects to quantify cest mri for chemical exchange rate and ph. *Magnetic resonance in medicine*, 60(2):390–397, 2008.

[188] Phillip Zhe Sun, Peter CM van Zijl, and Jinyuan Zhou. Optimization of the irradiation power in chemical exchange dependent saturation transfer experiments. *Journal of magnetic resonance*, 175(2):193–200, 2005.

[189] Phillip Zhe Sun, Jinyuan Zhou, Weiyun Sun, Judy Huang, and Peter C M van Zijl. Suppression of lipid artifacts in amide proton transfer imaging. *Magnetic resonance in medicine*, 54:222–225, July 2005. ISSN 0740-3194. doi: 10.1002/mrm.20530.

[190] Phillip Zhe Sun, Christian T. Farrar, and A Gregory Sorensen. Correction for artifacts induced by b(0) and b(1) field inhomogeneities in ph-sensitive chemical exchange saturation transfer (cest) imaging. *Magn Reson Med*, 58(6):1207–1215, Dec 2007. doi: 10.1002/mrm.21398. URL `http://dx.doi.org/10.1002/mrm.21398`.

[191] Phillip Zhe Sun, Jinyuan Zhou, Judy Huang, and Peter van Zijl. Simplified quantitative description of amide proton transfer (apt) imaging during acute ischemia. *Magnetic Resonance in Medicine*, 57(2):405–410, 2007.

[192] Phillip Zhe Sun, Jinyuan Zhou, Weiyun Sun, Judy Huang, and Peter CM van Zijl. Detection of the ischemic penumbra using ph-weighted mri. *Journal of Cerebral Blood Flow & Metabolism*, 27(6):1129–1136, 2007.

[193] Phillip Zhe Sun, Thomas Benner, Ashok Kumar, and A Gregory Sorensen. Investigation of optimizing and translating ph-sensitive pulsed-chemical exchange saturation transfer (cest) imaging to a 3t clinical scanner. *Magnetic resonance in medicine*, 60(4):834–841, 2008.

[194] Phillip Zhe Sun, Yoshihiro Murata, Jie Lu, Xiaoying Wang, Eng H Lo, and A Gregory Sorensen. Relaxation-compensated fast multislice amide proton transfer (apt) imaging of acute ischemic stroke. *Magnetic resonance in medicine*, 59(5):1175–1182, 2008.

[195] Phillip Zhe Sun, Jerry S Cheung, Enfeng Wang, Thomas Benner, and A Gregory Sorensen. Fast multislice ph-weighted chemical exchange saturation transfer (cest) mri with unevenly segmented rf irradiation. *Magnetic resonance in medicine*, 65(2):588–594, 2011.

[196] Phillip Zhe Sun, Jerry S Cheung, Enfeng Wang, and Eng H Lo. Association between ph-weighted endogenous amide proton chemical exchange saturation transfer mri and tissue lactic acidosis during acute ischemic stroke. *Journal of Cerebral Blood Flow & Metabolism*, 31(8):1743–1750, 2011.

[197] Phillip Zhe Sun, Enfeng Wang, Jerry S. Cheung, Xiaoan Zhang, Thomas Benner, and A Gregory Sorensen. Simulation and optimization of pulsed radio frequency irradiation scheme for chemical exchange saturation transfer (cest) mri-demonstration of ph-weighted pulsed-amide proton cest mri in an animal model

of acute cerebral ischemia. *Magn Reson Med*, 66(4):1042–1048, Oct 2011. doi: 10.1002/mrm.22894. URL http://dx.doi.org/10.1002/mrm.22894.

[198] Phillip Zhe Sun, Enfeng Wang, and Jerry S Cheung. Imaging acute ischemic tissue acidosis with ph-sensitive endogenous amide proton transfer (apt) mri:correction of tissue relaxation and concomitant rf irradiation effects toward mapping quantitative cerebral tissue ph. *Neuroimage*, 60(1):1–6, 2012.

[199] Phillip Zhe Sun, Yu Wang, and Jie Lu. Sensitivity-enhanced chemical exchange saturation transfer (cest) mri with least squares optimization of carr purcell meiboom gill multi-echo echo planar imaging. *Contrast media & molecular imaging*, 9(2):177–181, 2014.

[200] PC Sundgren. Mr spectroscopy in radiation injury. *American journal of neuroradiology*, 30(8):1469–1476, 2009.

[201] Chris Tench. (https://www.nottingham.ac.uk/research/groups/clinicalneurology/neuroi.aspx).

[202] M Terpstra, PM Andersen, and R Gruetter. Localized eddy current compensation using quantitative field mapping. *Journal of Magnetic Resonance*, 131(ARTICLE): 139–143, 1998.

[203] Enzo Terreno, Mauro Botta, Patrizia Boniforte, Chiara Bracco, Luciano Milone, Bruna Mondino, Fulvio Uggeri, and Silvio Aime. A multinuclear nmr relaxometry study of ternary adducts formed between heptadentate gdiii chelates and l-lactate. *Chemistry-A European Journal*, 11(19):5531–5537, 2005.

[204] Enzo Terreno, Daniela Delli Castelli, and Silvio Aime. Encoding the frequency dependence in mri contrast media: the emerging class of cest agents. *Contrast media & molecular imaging*, 5:78–98, 2010. ISSN 1555-4317. doi: 10.1002/cmmi.369.

[205] Anna Tietze, Jakob Blicher, Irene Klærke Mikkelsen, Leif Østergaard, Megan K Strother, Seth A Smith, and Manus J Donahue. Assessment of ischemic penumbra in patients with hyperacute stroke using amide proton transfer (apt) chemical exchange saturation transfer (cest) mri. *NMR in Biomedicine*, 27(2):163–174, 2014.

[206] Osamu Togao, Takashi Yoshiura, Jochen Keupp, Akio Hiwatashi, Koji Yamashita, Kazufumi Kikuchi, Yuriko Suzuki, Satoshi O. Suzuki, Toru Iwaki, Nobuhiro Hata, Masahiro Mizoguchi, Koji Yoshimoto, Koji Sagiyama, Masaya Takahashi, and Hiroshi Honda. Amide proton transfer imaging of adult diffuse gliomas: correlation with histopathological grades. *Neuro Oncol*, 16(3):441–448, Mar 2014. doi: 10.1093/neuonc/not158. URL `http://dx.doi.org/10.1093/neuonc/not158`.

[207] S Umesh Rudrapatna, Fabian Fluerenbrock, Terence W Nixon, Robin A de Graaf, and Christoph Juchem. Combined imaging and shimming with the dynamic multi-coil technique. *Magnetic resonance in medicine*, 81(2):1424–1433, 2019.

[208] Peter van Zijl and Nirbhay N Yadav. Chemical exchange saturation transfer (cest): what is in a name and what isn't? *Magnetic resonance in medicine*, 65(4): 927–948, 2011.

[209] Peter van Zijl, Jinyuan Zhou, Noriko Mori, Jean-Francois Payen, David Wilson, and Susumu Mori. Mechanism of magnetization transfer during on-resonance water saturation. a new approach to detect mobile proteins, peptides, and lipids. *Magnetic resonance in medicine*, 49(3):440–449, 2003.

[210] Peter C M. van Zijl, Jinyuan Zhou, Noriko Mori, Jean-Francois Payen, David Wilson, and Susumu Mori. Mechanism of magnetization transfer during on-resonance water saturation. a new approach to detect mobile proteins, peptides,

and lipids. *Magn Reson Med*, 49(3):440–449, Mar 2003. doi: 10.1002/mrm.10398. URL http://dx.doi.org/10.1002/mrm.10398.

[211] Peter C M. van Zijl, Craig K. Jones, Jimin Ren, Craig R. Malloy, and A Dean Sherry. Mri detection of glycogen in vivo by using chemical exchange saturation transfer imaging (glycocest). *Proc Natl Acad Sci U S A*, 104(11):4359–4364, Mar 2007. doi: 10.1073/pnas.0700281104. URL http://dx.doi.org/10.1073/pnas.0700281104.

[212] Peter CM Van Zijl, Craig K Jones, Jimin Ren, Craig R Malloy, and A Dean Sherry. Mri detection of glycogen in vivo by using chemical exchange saturation transfer imaging (glycocest). *Proceedings of the National Academy of Sciences*, 104(11): 4359–4364, 2007.

[213] G Varma, RE Lenkinski, and E Vinogradov. Keyhole chemical exchange saturation transfer. *Magnetic resonance in medicine*, 68(4):1228–1233, 2012.

[214] P. Vaupel, F. Kallinowski, and P. Okunieff. Blood flow, oxygen and nutrient supply, and metabolic microenvironment of human tumors: a review. *Cancer Res*, 49(23):6449–6465, Dec 1989.

[215] B. Venu K. Denisov, V.P. & Halle. Water 1 h magnetic relaxation dispersion in protein solutions . a quantitative assessment of internal hydration , proton exchange , and cross-relaxation. *Nature 7863, 3122-3134*, 1997.

[216] Keith Wachowicz. Evaluation of active and passive shimming in magnetic resonance imaging. *Research and Reports in Nuclear Medicine*, 4:1–12, 2014.

[217] Stefan Walenta, Michael Wetterling, Michael Lehrke, Georg Schwickert, Kolbein Sundfør, Einar K Rofstad, and Wolfgang Mueller-Klieser. High lactate levels predict likelihood of metastases, tumor recurrence, and restricted patient survival in human cervical cancers. *Cancer research*, 60(4):916–921, 2000.

[218] Simon Walker-Samuel, Rajiv Ramasawmy, Francisco Torrealdea, Marilena Rega, Vineeth Rajkumar, S Peter Johnson, Simon Richardson, Miguel Gonçalves, Harold G Parkes, Erik Årstad, et al. In vivo imaging of glucose uptake and metabolism in tumors. *Nature medicine*, 19(8):1067–1072, 2013.

[219] Jihong Wang, Joseph Weygand, Ken-Pin Hwang, Abdallah SR Mohamed, Yao Ding, Clifton D Fuller, Stephen Y Lai, Steven J Frank, and Jinyuan Zhou. Magnetic resonance imaging of glucose uptake and metabolism in patients with head and neck cancer. *Scientific reports*, 6:30618, 2016.

[220] J. P. Wansapura, S. K. Holland, R. S. Dunn, and WS Ball, Jr. Nmr relaxation times in the human brain at 3.0 tesla. *J Magn Reson Imaging*, 9(4):531–538, Apr 1999.

[221] K. M. Ward and R. S. Balaban. Determination of ph using water protons and chemical exchange dependent saturation transfer (cest). *Magn Reson Med*, 44 (5):799–802, Nov 2000.

[222] K. M. Ward, A. H. Aletras, and R. S. Balaban. A new class of contrast agents for mri based on proton chemical exchange dependent saturation transfer (cest). *J Magn Reson*, 143(1):79–87, Mar 2000. doi: 10.1006/jmre.1999.1956. URL `http://dx.doi.org/10.1006/jmre.1999.1956`.

[223] Zhibo Wen, Shuguang Hu, Fanheng Huang, Xianlong Wang, Linglang Guo, Xianyue Quan, Silun Wang, and Jinyuan Zhou. Mr imaging of high-grade brain tumors using endogenous protein and peptide-based contrast. *Neuroimage*, 51(2):616–622, Jun 2010. doi: 10.1016/j.neuroimage.2010.02.050. URL `http://dx.doi.org/10.1016/j.neuroimage.2010.02.050`.

[224] Michael Wendt. Second order shimming of high field magnets. *Siemens Medical Solutions, USA*.

[225] James L Wilson, Mark Jenkinson, and Peter Jezzard. Optimization of static field

homogeneity in human brain using diamagnetic passive shims. *Magnetic Resonance in Medicine: An Official Journal of the International Society for Magnetic Resonance in Medicine*, 48(5):906–914, 2002.

[226] Johannes Windschuh, Moritz Zaiss, Jan-Eric Meissner, Daniel Paech, Alexander Radbruch, Mark E Ladd, and Peter Bachert. Correction of b1-inhomogeneities for relaxation-compensated cest imaging at 7t. *NMR in biomedicine*, 28:529–537, May 2015. ISSN 1099-1492. doi: 10.1002/nbm.3283.

[227] D. E. Woessner. Nuclear transfer effects in nuclear magnetic resonance pulse experiments. *J. Chem. Phys.*, 35:41, 1961.

[228] Sherry AD Woessner DE Zhang S, Merritt ME. Numerical solution of the bloch equations provides insights into the optimum design of paracest agents for mri. *Magn Reson Med. 53(4):790-9.*, 2005.

[229] S. D. Wolff and R. S. Balaban. Magnetization transfer contrast (mtc) and tissue water proton relaxation in vivo. *Magn Reson Med*, 10(1):135–144, Apr 1989.

[230] G. & Liepinsh WÃŒthrich K., Otting. Protein hydration in aqueous solution. *Science 254, 974-980*, 1992.

[231] B Wu, G Warnock, M Zaiss, C Lin, M Chen, Z Zhou, L Mu, D Nanz, R Tuura, and G Delso. An overview of cest mri for non-mr physicists. *EJNMMI physics*, 3:19, December 2016. ISSN 2197-7364. doi: 10.1186/s40658-016-0155-2.

[232] Renhua Wu. "quantitative description of radiofrequency (rf) power based ratiometric chemical exchange saturation transfer (cest) ph imaging.". *NMR in biomedicine 28.5 : 555-565.*, 2015.

[233] Renhua Wu, Gang Xiao, Iris Yuwen Zhou, Chongzhao Ran, and Phillip Zhe Sun. Quantitative chemical exchange saturation transfer (qcest) mri–omega plot analysis of rf-spillover-corrected inverse cest ratio asymmetry for simultaneous de-

termination of labile proton ratio and exchange rate. *NMR in biomedicine*, 28(3): 376–383, 2015.

[234] Gang Xiao, Phillip Zhe Sun, and Renhua Wu. Fast simulation and optimization of pulse-train chemical exchange saturation transfer (cest) imaging. *Physics in medicine and biology*, 60(12):4719, 2015.

[235] Junzhong Xu, Moritz Zaiss, Zhongliang Zu, Hua Li, Jingping Xie, Daniel F Gochberg, Peter Bachert, and John C Gore. On the origins of chemical exchange saturation transfer (cest) contrast in tumors at 9.4 t. *NMR in biomedicine*, 27(4): 406–416, 2014.

[236] Xiang Xu, Nirbhay N Yadav, Linda Knutsson, Jun Hua, Rita Kalyani, Erica Hall, John Laterra, Jaishri Blakeley, Roy Strowd, Martin Pomper, et al. Dynamic glucose-enhanced (dge) mri: translation to human scanning and first results in glioma patients. *Tomography: a journal for imaging research*, 1(2):105, 2015.

[237] Nirbhay N Yadav, Kannie WY Chan, Craig K Jones, Michael T McMahon, and Peter van Zijl. Time domain removal of irrelevant magnetization in chemical exchange saturation transfer z-spectra. *Magnetic resonance in medicine*, 70(2): 547–555, 2013.

[238] Nirbhay N Yadav, Craig K Jones, Jun Hua, Jiadi Xu, and Peter Zijl. Imaging of endogenous exchangeable proton signals in the human brain using frequency labeled exchange transfer imaging. *Magnetic resonance in medicine*, 69(4):966–973, 2013.

[239] Kun Yan, Zongming Fu, Chen Yang, Kai Zhang, Shanshan Jiang, Dong-Hoon Lee, Hye-Young Heo, Yi Zhang, Robert N Cole, Jennifer E Van Eyk, et al. Assessing amide proton transfer (apt) mri contrast origins in 9 l gliosarcoma in the rat brain using proteomic analysis. *Molecular Imaging and Biology*, 17(4): 479–487, 2015.

[240] Jing Yuan, Qinwei Zhang, Yi-Xiang Wang, Juan Wei, and Jinyuan Zhou. Accuracy and uncertainty of asymmetric magnetization transfer ratio quantification for amide proton transfer (apt) imaging at 3t: A monte carlo study. In *2013 35th Annual International Conference of the IEEE Engineering in Medicine and Biology Society (EMBC)*, pages 5139–5142. IEEE, 2013.

[241] Jing Yuan, Shuzhong Chen, Ann D King, Jinyuan Zhou, Kunwar S Bhatia, Qinwei Zhang, David Ka Wei Yeung, Juan Wei, Greta Seng Peng Mok, and Yi-Xiang Wang. Amide proton transfer-weighted imaging of the head and neck at 3 t: a feasibility study on healthy human subjects and patients with head and neck cancer. *NMR in Biomedicine*, 27(10):1239–1247, 2014.

[242] Moritz Zaiss and Peter Bachert. Chemical exchange saturation transfer (cest) and mr z-spectroscopy in vivo: a review of theoretical approaches and methods. *Physics in medicine and biology*, 58(22):R221, 2013.

[243] Moritz Zaiss and Peter Bachert. Chemical exchange saturation transfer (cest) and mr z-spectroscopy in vivo: a review of theoretical approaches and methods. *Physics in medicine and biology*, 58(22):R221, 2013.

[244] Moritz Zaiss, Benjamin Schmitt, and Peter Bachert. Quantitative separation of cest effect from magnetization transfer and spillover effects by lorentzian-line-fit analysis of z-spectra. *Journal of magnetic resonance*, 211(2):149–155, 2011.

[245] Moritz Zaiss, Patrick Kunz, Steffen Goerke, Alexander Radbruch, and Peter Bachert. Mr imaging of protein folding in vitro employing nuclear-overhauser-mediated saturation transfer. *NMR in biomedicine*, 26(12):1815–1822, 2013.

[246] Moritz Zaiss, Junzhong Xu, Steffen Goerke, Imad S Khan, Robert J Singer, John C Gore, Daniel F Gochberg, and Peter Bachert. Inverse z-spectrum analysis for spillover-, mt-, and t1-corrected steady-state pulsed cest-mri–application to ph-weighted mri of acute stroke. *NMR in biomedicine*, 27(3):240–252, 2014.

[247] Moritz Zaiss, Johannes Windschuh, Daniel Paech, Jan-Eric Meissner, Sina Burth, Benjamin Schmitt, Philip Kickingereder, Benedikt Wiestler, Wolfgang Wick, Martin Bendszus, Heinz-Peter Schlemmer, Mark E. Ladd, Peter Bachert, and Alexander Radbruch. Relaxation-compensated cest-mri of the human brain at 7t: Unbiased insight into noe and amide signal changes in human glioblastoma. *Neuroimage*, 112:180–188, May 2015. doi: 10.1016/j.neuroimage.2015.02.040. URL `http://dx.doi.org/10.1016/j.neuroimage.2015.02.040`.

[248] Moritz Zaiss, Zhongliang Zu, Junzhong Xu, Patrick Schuenke, Daniel F Gochberg, John C Gore, Mark E Ladd, and Peter Bachert. A combined analytical solution for chemical exchange saturation transfer and semi-solid magnetization transfer. *NMR in biomedicine*, 28:217–230, February 2015. ISSN 1099-1492. doi: 10.1002/nbm.3237.

[249] Moritz Zaiss, Johannes Windschuh, Steffen Goerke, Daniel Paech, Jan-Eric Meissner, Sina Burth, Philipp Kickingereder, Wolfgang Wick, Martin Bendszus, Heinz-Peter Schlemmer, Mark E Ladd, Peter Bachert, and Alexander Radbruch. Downfield-noe-suppressed amide-cest-mri at 7 tesla provides a unique contrast in human glioblastoma. *Magnetic resonance in medicine*, 77:196–208, January 2017. ISSN 1522-2594. doi: 10.1002/mrm.26100.

[250] Moritz Zaiss, Goran Angelovski, Eleni Demetriou, Michael T McMahon, Xavier Golay, and Klaus Scheffler. Quesp and quest revisited - fast and accurate quantitative cest experiments. *Magnetic resonance in medicine*, 79:1708–1721, March 2018. ISSN 1522-2594. doi: 10.1002/mrm.26813.

[251] Moritz Zaiss, Mark Schuppert, Anagha Deshmane, Kai Herz, Philipp Ehses, Lars FÃŒllbier, Tobias Lindig, Benjamin Bender, Ulrike Ernemann, and Klaus Scheffler. Chemical exchange saturation transfer mri contrast in the human

brain at 9.4t. *NeuroImage*, 179:144–155, October 2018. ISSN 1095-9572. doi: 10.1016/j.neuroimage.2018.06.026.

[252] Hong Zhang, Huiying Kang, Xuna Zhao, Shanshan Jiang, Yi Zhang, Jinyuan Zhou, and Yun Peng. Amide proton transfer (apt) mr imaging and magnetization transfer (mt) mr imaging of pediatric brain development. *European radiology*, 26:3368–3376, October 2016. ISSN 1432-1084. doi: 10.1007/s00330-015-4188-z.

[253] Lei Zhang, André F Martins, Yuyan Mai, Piyu Zhao, Alexander M Funk, M Veronica Clavijo Jordan, Shanrong Zhang, Wei Chen, Yunkou Wu, and A Dean Sherry. Imaging extracellular lactate in vitro and in vivo using cest mri and a paramagnetic shift reagent. *Chemistry-A European Journal*, 23(8): 1752–1756, 2017.

[254] Xiao-Yong Zhang, Feng Wang, Aqeela Afzal, Junzhong Xu, John C Gore, Daniel F Gochberg, and Zhongliang Zu. A new noe-mediated mt signal at around -1.6ppm for detecting ischemic stroke in rat brain. *Magnetic resonance imaging*, 34:1100–1106, October 2016. ISSN 1873-5894. doi: 10.1016/j.mri.2016.05.002.

[255] Xiaomeng Zhang, Yuxiang Lin, and Robert J. Gillies. Tumor ph and its measurement. *J Nucl Med*, 51(8):1167–1170, Aug 2010. doi: 10.2967/jnumed.109.068981. URL `http://dx.doi.org/10.2967/jnumed.109.068981`.

[256] Kuangcong Wu Zhang Shanrong and Dean Sherry. "a novel ph-sensitive mri contrast agent.". *Angewandte Chemie International Edition 38.21 : 3192-3194.*, 1999.

[257] Jason M Zhao, Yah-el Har-el, Michael T McMahon, Jinyuan Zhou, A Dean Sherry, George Sgouros, Jeff WM Bulte, and Peter CM van Zijl. Size-induced enhancement of chemical exchange saturation transfer (cest) contrast in liposomes. *Journal of the American Chemical Society*, 130(15):5178–5184, 2008.

[258] Xuna Zhao, Zhibo Wen, Fanheng Huang, Shilong Lu, Xianlong Wang, Shuguang Hu, Donglin Zu, and Jinyuan Zhou. Saturation power dependence of amide proton transfer image contrasts in human brain tumors and strokes at 3 t. *Magnetic resonance in medicine*, 66(4):1033–1041, 2011.

[259] Xuna Zhao, Zhibo Wen, Ge Zhang, Fanheng Huang, Shilong Lu, Xianlong Wang, Shuguang Hu, Min Chen, and Jinyuan Zhou. Three-dimensional turbo-spin-echo amide proton transfer mr imaging at 3-tesla and its application to high-grade human brain tumors. *Molecular Imaging and Biology*, 15(1):114–122, 2013.

[260] Xuna Zhao, Zhibo Wen, Chunmei Li, Min Chen, Yi Wang, and Jia-Hong Gao. Quantitative amide proton transfer imaging with reduced interferences from magnetization transfer asymmetry for human brain tumors at 3t. *Magn Reson Med*, Aug 2014. doi: 10.1002/mrm.25411. URL `http://dx.doi.org/10.1002/mrm.25411`.

[261] Shaokuan Zheng, Imramsjah MJ van der Bom, Zhongliang Zu, Guoxing Lin, Yansong Zhao, and Matthew J Gounis. Chemical exchange saturation transfer effect in blood. *Magnetic resonance in medicine*, 71(3):1082–1092, 2014.

[262] Iris Yuwen Zhou, Enfeng Wang, Jerry S Cheung, Xiaoan Zhang, Giulia Fulci, and Phillip Zhe Sun. Quantitative chemical exchange saturation transfer (cest) mri of glioma using image downsampling expedited adaptive least-squares (ideal) fitting. *Scientific reports*, 7(1):84, 2017.

[263] Jinyuan Zhou, Bachchu Lal, David A. Wilson, John Laterra, and Peter C M. van Zijl. Amide proton transfer (apt) contrast for imaging of brain tumors. *Magn Reson Med*, 50(6):1120–1126, Dec 2003. doi: 10.1002/mrm.10651. URL `http://dx.doi.org/10.1002/mrm.10651`.

[264] Jinyuan Zhou, Jean-Francois Payen, David A. Wilson, Richard J. Traystman, and Peter C M. van Zijl. Using the amide proton signals of intracellular proteins and

peptides to detect ph effects in mri. *Nat Med*, 9(8):1085–1090, Aug 2003. doi: 10.1038/nm907. URL http://dx.doi.org/10.1038/nm907.

[265] Jinyuan Zhou, David A. Wilson, Phillip Zhe Sun, Judith A. Klaus, and Peter C M. Van Zijl. Quantitative description of proton exchange processes between water and endogenous and exogenous agents for wex, cest, and apt experiments. *Magn Reson Med*, 51(5):945–952, May 2004. doi: 10.1002/mrm.20048. URL http://dx.doi.org/10.1002/mrm.20048.

[266] Jinyuan Zhou, Jaishri O. Blakeley, Jun Hua, Mina Kim, John Laterra, Martin G. Pomper, and Peter C M. van Zijl. Practical data acquisition method for human brain tumor amide proton transfer (apt) imaging. *Magn Reson Med*, 60(4):842–849, Oct 2008. doi: 10.1002/mrm.21712. URL http://dx.doi.org/10.1002/mrm.21712.

[267] Jinyuan Zhou, Erik Tryggestad, Zhibo Wen, Bachchu Lal, Tingting Zhou, Rachel Grossman, Silun Wang, Kun Yan, De-Xue Fu, Eric Ford, Betty Tyler, Jaishri Blakeley, John Laterra, and Peter C M. van Zijl. Differentiation between glioma and radiation necrosis using molecular magnetic resonance imaging of endogenous proteins and peptides. *Nat Med*, 17(1):130–134, Jan 2011. doi: 10.1038/nm.2268. URL http://dx.doi.org/10.1038/nm.2268.

[268] Jinyuan Zhou, Kun Yan, and He Zhu. A simple model for understanding the origin of the amide proton transfer mri signal in tissue. *Applied magnetic resonance*, 42(3):393–402, 2012.

[269] Jinyuan Zhou, Xiaohua Hong, Xuna Zhao, Jia-Hong Gao, and Jing Yuan. Apt-weighted and noe-weighted image contrasts in glioma with different rf saturation powers based on magnetization transfer ratio asymmetry analyses. *Magnetic resonance in medicine*, 70(2):320–327, 2013.

[270] Jinyuan Zhou, He Zhu, Michael Lim, Lindsay Blair, Alfredo Quinones-Hinojosa, Steven A Messina, Charles G Eberhart, Martin G Pomper, John Laterra, Peter B Barker, et al. Three-dimensional amide proton transfer mr imaging of gliomas: Initial experience and comparison with gadolinium enhancement. *Journal of Magnetic Resonance Imaging*, 38(5):1119–1128, 2013.

[271] He Zhu, Craig K. Jones, Peter C M. van Zijl, Peter B. Barker, and Jinyuan Zhou. Fast 3d chemical exchange saturation transfer (cest) imaging of the human brain. *Magn Reson Med*, 64(3):638–644, Sep 2010. doi: 10.1002/mrm.22546. URL `http://dx.doi.org/10.1002/mrm.22546`.

[272] Xiaopeng Zong, Ping Wang, Seong-Gi Kim, and Tao Jin. Sensitivity and source of amine-proton exchange and amide-proton transfer magnetic resonance imaging in cerebral ischemia. *Magnetic resonance in medicine*, 71(1):118–132, 2014.

[273] Zhongliang Zu. Ratiometric noe(-1.6) contrast in brain tumors. *NMR in biomedicine*, 31:e4017, December 2018. ISSN 1099-1492. doi: 10.1002/nbm.4017.

[274] Zhongliang Zu, Ke Li, Vaibhav A. Janve, Mark D. Does, and Daniel F. Gochberg. Optimizing pulsed-chemical exchange saturation transfer imaging sequences. *Magn Reson Med*, 66(4):1100–1108, Oct 2011. doi: 10.1002/mrm.22884. URL `http://dx.doi.org/10.1002/mrm.22884`.

[275] Zhongliang Zu, Ke Li, Vaibhav A Janve, Mark D Does, and Daniel F Gochberg. Optimizing pulsed-chemical exchange saturation transfer imaging sequences. *Magnetic resonance in medicine*, 66(4):1100–1108, 2011.

[276] Zhongliang Zu, Vaibhav A Janve, Ke Li, Mark D Does, John C Gore, and Daniel F Gochberg. Multi-angle ratiometric approach to measure chemical exchange in amide proton transfer imaging. *Magnetic resonance in medicine*, 68(3):711–719, 2012.